Forschungsbericht 2025-32

Influence of Powered Lift Systems on the Aerodynamics of a Turboprop Aircraft

Dennis Keller

Deutsches Zentrum für Luft- und Raumfahrt
Institut für Aerodynamik und Strömungstechnik
Braunschweig

Deutsches Zentrum
DLR für Luft- und Raumfahrt

Forschungsbericht 2025-32

Influence of Powered Lift Systems on the Aerodynamics of a Turboprop Aircraft

Dennis Keller

Deutsches Zentrum für Luft- und Raumfahrt
Institut für Aerodynamik und
Strömungstechnik
Braunschweig

139 Seiten
76 Bilder
10 Tabellen
125 Literaturstellen

Deutsches Zentrum
DLR für Luft- und Raumfahrt

Herausgeber:

Deutsches Zentrum
für Luft- und Raumfahrt e. V.
Wissenschaftliche Information
Linder Höhe
D-51147 Köln

ISSN 1434-8454
ISRN DLR-FB-2025-32
Erscheinungsjahr 2025
DOI: 10.57676/cmfw-nm22

Angewandte Aerodynamik, Propeller, aktive Strömungskontrolle, Zirkulationskontrolle, Grenzschichtkontrolle, Propelleranblasung, Hochauftrieb, Seitenbewegung, Numerische Strömungssimulation

Dennis KELLER
DLR, Institut für Aerodynamik und Strömungstechnik, Braunschweig

Einfluss von aktiven Systemen zur Auftriebserhöhung auf die Aerodynamik eines Turbopropflugzeugs
Technische Universität Braunschweig

Das Ziel der vorliegenden Arbeit ist, den Einfluss aktiver Systeme zur Auftriebserhöhung in Form von Zirkulationskontrolle und Flügelanblasung durch Propeller auf das aerodynamische Verhalten eines modernen Transportflugzeugs mit Kurzstart- und -landefähigkeit (STOL) zu untersuchen. Beide Technologien allein beeinflussen die Aerodynamik des Hauptflügels bereits derart, dass die Auftriebserzeugung verstärkt wird. Der gemeinsame Einsatz beider Technologien führt zu zusätzlichen Integrationseffekten. Zudem ist der Einfluss von Zirkulationskontrolle und Flügelanblasung nicht auf den Hauptflügel beschränkt. Durch die Änderung der Zirkulationsverteilung des Hauptflügels wird auch der Nachlauf des Hauptflügels beeinflusst. Infolgedessen ändern sich die Strömungsverhältnisse und letztlich das aerodynamische Verhalten des Leitwerks. Die Veränderungen des aerodynamischen Verhaltens des Hauptflügels und insbesondere des Leitwerks können ausgeprägte Auswirkungen auf die Steuerbarkeit und Stabilität des gesamten Flugzeugs haben, wie in Experimenten der NASA in den 1960er Jahren zu beobachten war. Die vorliegende Arbeit liefert eine aerodynamische Datenbasis, die ausführliche flugdynamische Analysen der untersuchten Flugzeugkonfiguration ermöglicht. Da die Ursachen für das veränderte Flugzeugverhalten in den früheren Untersuchungen meist unbekannt blieben, zielt die Arbeit außerdem darauf ab, aerodynamische Phänomene zu identifizieren, die zu den Auswirkungen von Zirkulationskontrolle und Flügelanblasung auf die Steuerbarkeit und Stabilität führen. Um diese Einflüsse auf das aerodynamische Verhalten zu untersuchen, wurden numerische Simulationen des gesamten Flugzeugs in Landekonfiguration auf der Grundlage der Reynolds-gemittelten Navier-Stokes Gleichungen durchgeführt.

Die vorliegende Studie führt für eine Flugzeugkonfiguration, die sowohl Zirkulationskontrolle als auch Flügelanblasung zur Verbesserung der Hochauftriebsleistung verwendet, zu einem maximalen Auftriebskoeffizienten in Landekonfiguration von bis zu 4,52. Werden die Propellereffekte nicht berücksichtigt, verschlechtert sich der maximale Auftriebskoeffizient aufgrund nachteiliger Auswirkungen der Triebwerksintegration deutlich. Dabei induziert die Triebwerksgondel starke Randwirbel, die stromab mit der Zirkulationskontrolle interagieren und somit ein Ablösen des Flügelnachlaufs von der Klappenströmung verursachen. Die Analyse der Längsbewegung zeigt zudem, dass der Einfluss von Zirkulationskontrolle und Propeller auf die statische und dynamische Stabilität eher gering ist. Während die Zirkulationskontrolle die Stabilität geringfügig erhöht, verringern Propellereffekte tendenziell die Stabilität. Hinsichtlich der Seitenbewegung ist der Einfluss von Zirkulationskontrolle und Propeller stärker ausgeprägt. Sowohl die Windfahnenstabilität als auch das Gierdämpfung-Derivativ sind in hohem Maße nichtlinear und hängen von verschiedenen Parametern wie Zirkulationskontroll-Modus, Propellerschub und Strömungsbedingungen ab. Sowohl die Zirkulationskontrolle als auch die Propeller können unter bestimmten Bedingungen eine erhebliche Verringerung der Stabilität verursachen. Dabei können Propellereffekte sogar zu Windfahneninstabilität und einem Vorzeichenwechsel des Gierdämpfungsderivativs führen. Als Ursache für dieses Verhalten wurde die Interaktion des Flügel-/Propellernachlaufs mit dem Rumpf ermittelt. Im Fall mit Zirkulationskontrolle und ohne Propellereffekte spielen hinsichtlich der Abnahme der Stabilität die inneren Klappenrandwirbel die entscheidende Rolle. Werden zudem Propellereffekte berücksichtigt, so sind komplexe Strömungsinteraktionen der inneren Klappenrandwirbel mit dem Propellernachlauf für die stärkere Verminderung der Stabilitätseigenschaften ursächlich. Die Zirkulationskontrolle verringert außerdem die statische Seitenstabilität ("V-Stellungseffekt"), während der Einfluss der Propeller von verschiedenen Parametern, wie der Propellerdrehrichtung und dem Schiebewinkel, abhängt. Neben zusätzlichen Einflüssen der Zirkulationskontrolle und der Propeller auf die Rolldämpfung und die anderen dynamischen Derivative der Seitenbewegung, zeigte die Untersuchung auch Kreuzkopplungseffekte zwischen

Seiten- und Längsbewegung, wie die Entstehung eines erheblichen Nickmoments durch Seitenwind.

applied aerodynamics, propeller, powered lift, active flow control, circulation control, boundary layer control, slipstream deflection, high-lift, STOL, lateral motion, numerical simulation

(Published in English)

Dennis KELLER
German Aerospace Center (DLR), Institute of Aerodynamics and Flow Technology, Braunschweig

Influence of Powered Lift Systems on the Aerodynamics of a Turboprop Aircraft

Technische Universität Braunschweig

The purpose of the present work is to evaluate the influence of active lift augmentation systems, in terms of circulation control and slipstream deflection, on the aerodynamic behavior of a state-of-the-art transport aircraft with short take-off and landing (STOL) capabilities. Both technologies individually affect the aerodynamics of the main wing in order to increase lift generation. Using both technologies together leads to additional integration effects. Moreover, the influence of circulation control and slipstream deflection is not limited to the main wing. Due to the alteration of the main wing's circulation distribution, the main wing wake is affected as well. The flow conditions, and thus the aerodynamic behavior of the tail, are therefore changed. The changes in the aerodynamic behavior of the main wing, and in particular the tail, can have a significant impact on the controllability and stability of the entire aircraft, as observed in experiments by NASA in the 1960s. The present work provides an aerodynamic data base that enables thorough flight dynamic analyses of the investigated aircraft configuration. As the root cause of the change in aircraft behavior mostly remained unknown in past investigations, the work also aims at identifying aerodynamic phenomena that lead to the effects of circulation control and slipstream deflection on the controllability and stability. In order to investigate these effects on the aerodynamic behavior, numerical simulations of the entire aircraft in landing configuration were carried out based on the Reynolds-averaged Navier-Stokes

equations.

The present investigation indicates a maximum lift coefficient in landing configuration of up to 4.52 for an aircraft utilizing both circulation control and slipstream deflection to enhance low-speed performance. With the propellers off, the maximum lift coefficient is degraded due to adverse engine integration effects. The nacelle thereby induces strong vortices, which interact with the circulation control downstream, causing local wake bursting. The analysis of the longitudinal motion further indicates that the effect of circulation control and the propellers on the static, as well as dynamic stability, is rather small. While circulation control slightly increases the stability, propeller effects tend to decrease the stability. In lateral motion, the influence of circulation control and the propellers has been found to be more severe. Directional stability, as well as the dynamic yaw damping derivatives, are highly non-linear, depending on various parameters such as circulation control mode, thrust, and freestream flow conditions. Both circulation control and the propellers may cause a significant decrease in stability under certain conditions. Propeller effects may even lead to directional instability and reversed yaw damping derivatives. Wake-fuselage interaction has been found to be the origin of this behavior. While the inner flap tip vortices play the dominating role concerning the decrease in stability in the case with circulation control and with propellers off, complex flow interactions of the inner flap tip vortices with the propeller slipstream cause the more severe degradation of stability, if the propellers are on. Circulation control also reduces the lateral static stability (dihedral effect), whereas the effect of the propellers depends on various parameters such as rotational direction of the propellers and sideslip angle. Besides additional influences of circulation control and the propellers on the roll damping and the other lateral dynamic derivatives, the investigation also revealed cross-coupling effects between lateral and longitudinal motion such as the creation of a considerable pitching moment due to crosswind.

TU Braunschweig – Niedersächsisches
Forschungszentrum für Luftfahrt

Berichte aus der Luft- und Raumfahrttechnik

Forschungsbericht 2025-14

Influence of Powered Lift Systems on the Aerodynamics of a Turboprop Aircraft

Dennis Keller

Deutsches Zentrum für Luft- und Raumfahrt
Institut für Aerodynamik und Strömungstechnik

Diese Veröffentlichung wird gleichzeitig in der Berichtsreihe „NFL - Forschungsberichte“ geführt.

Diese Arbeit erscheint gleichzeitig als von der Fakultät für Maschinenbau der Technischen Universität Carolo-Wilhelmina zu Braunschweig zur Erlangung des akademischen Grades eines Doktor-Ingenieurs genehmigte Dissertation.

Influence of Powered Lift Systems on the Aerodynamics of a Turboprop Aircraft

Von der Fakultät für Maschinenbau

der Technischen Universität Carolo-Wilhelmina zu Braunschweig

zur Erlangung der Würde

eines Doktor-Ingenieurs (Dr.-Ing.)

genehmigte Dissertation

von:	Dipl.-Ing. Dennis Keller
geboren in (Geburtsort):	Bonn

eingereicht am:	9. August 2024
mündliche Prüfung am:	11. Juli 2025

Vorsitz:	Prof. Dr.-Ing. Jens Friedrichs
Gutachter:	Prof. Dr.-Ing. Ralf Rudnik
	Prof. a.D. Dr.-Ing. Rolf Radespiel

2025

Acknowledgments

The present work was carried out during my tenure as a research associate at the Institute of Aerodynamics and Flow Technology of the German Aerospace Center (DLR).

First and foremost, I would like to express my gratitude to Prof. Dr.-Ing. R. Rudnik for providing me with the opportunity to write this thesis and for taking on the role of academic supervisor. His continuous support and guidance have been very valuable to me. I am also thankful to Prof. a.D. Dr.-Ing. R. Radespiel for acting as co-supervisor and Prof. Dr.-Ing. J. Friedrichs to serve as the chair of the examination committee.

Additionally, I would like to thank Dr.-Ing. J. H. Diekmann and Dr.-Ing. Tayson Weiss for the close collaboration within the framework of the SFB 880. Our discussions, both technical and non-technical, have not only broadened my understanding of the subject matter but also made the research experience more enjoyable.

My appreciation extends to my colleagues at the Institute of Aerodynamics and Flow Technology for the excellent working atmosphere and support. Special thanks go to Dr.-Ing. Arne Stürmer for his help and support.

Finally, I would like to thank my mother, my sister, and my friends for their constant support and encouragement. Their love and support were invaluable to me and helped me to complete the work.

Abstract

The purpose of the present work is to evaluate the influence of active lift augmentation systems, in terms of circulation control and slipstream deflection, on the aerodynamic behavior of a state-of-the-art transport aircraft with short take-off and landing (STOL) capabilities. Both technologies individually affect the aerodynamics of the main wing in order to increase lift generation. Using both technologies together leads to additional integration effects. Moreover, the influence of circulation control and slipstream deflection is not limited to the main wing. Due to the alteration of the main wing's circulation distribution, the main wing wake is affected as well. The flow conditions, and thus the aerodynamic behavior of the tail, are therefore changed. The changes in the aerodynamic behavior of the main wing, and in particular the tail, can have a significant impact on the controllability and stability of the entire aircraft, as observed in experiments by NASA in the 1960s. The present work provides an aerodynamic data base that enables thorough flight dynamic analyses of the investigated aircraft configuration. As the root cause of the change in aircraft behavior mostly remained unknown in past investigations, the work also aims at identifying aerodynamic phenomena that lead to the effects of circulation control and slipstream deflection on the controllability and stability. In order to investigate these effects on the aerodynamic behavior, numerical simulations of the entire aircraft in landing configuration were carried out based on the Reynolds-averaged Navier-Stokes equations.

The present investigation indicates a maximum lift coefficient in landing configuration of up to 4.52 for an aircraft utilizing both circulation control and slipstream deflection to enhance low-speed performance. With the propellers off, the maximum lift coefficient is degraded due to adverse engine integration effects. The nacelle thereby induces strong vortices, which interact with the circulation control downstream, causing local wake bursting. The analysis of the longitudinal motion further indicates that the effect of circulation control and the propellers on the static, as well as dynamic stability, is rather small. While circulation control slightly increases the stability, propeller effects tend to decrease the stability. In lateral motion, the influence of circulation control and the propellers has been found to be more severe. Directional stability, as well as the dynamic yaw damping derivatives, are highly non-linear, depending on various parameters such as circulation control mode, thrust, and freestream flow conditions. Both circulation control and the propellers may cause a significant decrease in stability under certain conditions. Propeller effects may even lead to directional instability and reversed yaw damping derivatives. Wake-fuselage interaction has been found to be the origin of this behavior. While the inner flap tip vortices play the dominating role concerning the decrease in stability in the case with circulation control and with propellers off, complex flow interactions of the inner flap tip vortices with the propeller slipstream cause the more severe degradation of stability, if the propellers are on. Circulation control also reduces the lateral static stability

(dihedral effect), whereas the effect of the propellers depends on various parameters such as rotational direction of the propellers and sideslip angle. Besides additional influences of circulation control and the propellers on the roll damping and the other lateral dynamic derivatives, the investigation also revealed cross-coupling effects between lateral and longitudinal motion such as the creation of a considerable pitching moment due to crosswind.

Kurzfassung

Das Ziel der vorliegenden Arbeit ist, den Einfluss aktiver Systeme zur Auftriebserhöhung in Form von Zirkulationskontrolle und Flügelanblasung durch Propeller auf das aerodynamische Verhalten eines modernen Transportflugzeugs mit Kurzstart- und -landefähigkeit (STOL) zu untersuchen. Beide Technologien allein beeinflussen die Aerodynamik des Hauptflügels bereits derart, dass die Auftriebserzeugung verstärkt wird. Der gemeinsame Einsatz beider Technologien führt zu zusätzlichen Integrationseffekten. Zudem ist der Einfluss von Zirkulationskontrolle und Flügelanblasung nicht auf den Hauptflügel beschränkt. Durch die Änderung der Zirkulationsverteilung des Hauptflügels wird auch der Nachlauf des Hauptflügels beeinflusst. Infolgedessen ändern sich die Strömungsverhältnisse und letztlich das aerodynamische Verhalten des Leitwerks. Die Veränderungen des aerodynamischen Verhaltens des Hauptflügels und insbesondere des Leitwerks können ausgeprägte Auswirkungen auf die Steuerbarkeit und Stabilität des gesamten Flugzeugs haben, wie in Experimenten der NASA in den 1960er Jahren zu beobachten war. Die vorliegende Arbeit liefert eine aerodynamische Datenbasis, die ausführliche flugdynamische Analysen der untersuchten Flugzeugkonfiguration ermöglicht. Da die Ursachen für das veränderte Flugzeugverhalten in den früheren Untersuchungen meist unbekannt blieben, zielt die Arbeit außerdem darauf ab, aerodynamische Phänomene zu identifizieren, die zu den Auswirkungen von Zirkulationskontrolle und Flügelanblasung auf die Steuerbarkeit und Stabilität führen. Um diese Einflüsse auf das aerodynamische Verhalten zu untersuchen, wurden numerische Simulationen des gesamten Flugzeugs in Landekonfiguration auf der Grundlage der Reynolds-gemittelten Navier-Stokes Gleichungen durchgeführt.

Die vorliegende Studie führt für eine Flugzeugkonfiguration, die sowohl Zirkulationskontrolle als auch Flügelanblasung zur Verbesserung der Hochauftriebsleistung verwendet, zu einem maximalen Auftriebskoeffizienten in Landekonfiguration von bis zu 4,52. Werden die Propellereffekte nicht berücksichtigt, verschlechtert sich der maximale Auftriebskoeffizient aufgrund nachteiliger Auswirkungen der Triebwerksintegration deutlich. Dabei induziert die Triebwerksgondel starke Randwirbel, die stromab mit der Zirkulationskontrolle interagieren und somit ein Ablösen des Flügelnachlaufs von der Klappenströmung verursachen. Die Analyse der Längsbewegung zeigt zudem, dass der Einfluss von Zirkulationskontrolle und Propeller auf die statische und dynamische Stabilität eher gering ist. Während die Zirkulationskontrolle die Stabilität geringfügig erhöht, verringern Propellereffekte tendenziell die Stabilität. Hinsichtlich der Seitenbewegung ist der Einfluss von Zirkulationskontrolle und Propeller stärker ausgeprägt. Sowohl die Windfahnenstabilität als auch das Gierdämpfung-Derivativ sind in hohem Maße nichtlinear und hängen von verschiedenen Parametern wie Zirkulationskontroll-Modus, Propellerschub und Strömungsbedingungen ab. Sowohl die Zirkulationskontrolle als auch die Propeller können unter bestimmten Bedingungen eine erhebliche Verringerung der Stabilität verursachen.

Dabei können Propellereffekte sogar zu Windfahneninstabilität und einem Vorzeichenwechsel des Gierdämpfungsderivativs führen. Als Ursache für dieses Verhalten wurde die Interaktion des Flügel-/Propellernachlaufs mit dem Rumpf ermittelt. Im Fall mit Zirkulationskontrolle und ohne Propellereffekte spielen hinsichtlich der Abnahme der Stabilität die inneren Klappenrandwirbel die entscheidende Rolle. Werden zudem Propellereffekte berücksichtigt, so sind komplexe Strömungsinteraktionen der inneren Klappenrandwirbel mit dem Propellernachlauf für die stärkere Verminderung der Stabilitätseigenschaften ursächlich. Die Zirkulationskontrolle verringert außerdem die statische Seitenstabilität ("V-Stellungseffekt"), während der Einfluss der Propeller von verschiedenen Parametern, wie der Propellerdrehrichtung und dem Schiebewinkel, abhängt. Neben zusätzlichen Einflüssen der Zirkulationskontrolle und der Propeller auf die Rolldämpfung und die anderen dynamischen Derivative der Seitenbewegung, zeigte die Untersuchung auch Kreuzkopplungseffekte zwischen Seiten- und Längsbewegung, wie die Entstehung eines erheblichen Nickmoments durch Seitenwind.

Contents

List of Figures **xiii**

List of Tables **xix**

Nomenclature **xxi**

1 Introduction **1**

1.1 State of the Art 3

1.2 Objectives and Outline 7

2 High-Lift Enhancement, Geometric Model and Mesh Generation **9**

2.1 Principles of Circulation Control and Slipstream Deflection 9

2.2 Geometric Model 12

2.3 Mesh Generation 15

3 Numerical Methods **19**

3.1 Governing Equations 19

3.2 Reynolds-Averaged Navier-Stokes Equations 21

3.2.1 Spalart-Allmaras Turbulence Model 24

3.2.2 SSG/LRR-g Turbulence Model 26

3.2.3 Actuator Disc 27

3.3 Flow Solver 28

3.3.1 Spatial Discretization 29

3.3.2 Time Stepping 30

3.3.3 Convergence Criteria and Averaging 30

3.4 Force and Moment Evaluation 30

3.5 Determination of Stability Derivatives 31

4 Verification and Validation **33**
4.1 Validity of the Numerical Approach for High-Lift Configurations 33
4.2 Meshing Influence 34
4.3 Turbulence Modeling 39
4.4 Simulation of Propeller Effects 43

5 Results **47**
5.1 Longitudinal Motion 47
5.1.1 Lift Generation and Stall Mechanism of the Wing-Body 48
5.1.2 Wake Evolution and Flow Conditions at the HTP 61
5.1.3 Controllability 69
5.1.4 Static Stability 71
5.1.5 Dynamic Stability 75
5.2 Lateral Motion 77
5.2.1 Aerodynamic Behavior under Crosswind Conditions 77
5.2.2 Static Directional Stability 98
5.2.3 Static Lateral Stability 102
5.2.4 Cross-Coupling of Static Longitudinal and Lateral Behavior 105
5.2.5 Dynamic Stability 105

6 Conclusions and Outlook **115**

Own Publications and Author Contributions **119**

Bibliography **121**

Appendix A Referenced Wind Tunnel Tests and Flight Experiments **131**

Appendix B Stall Behavior **133**

Appendix C Lateral Stability **135**

Appendix D Directional Stability **137**

List of Figures

1.1 Powered lift concepts 2

2.1 Flap with circulation control 10
2.2 Lift coefficient depending on momentum coefficient 10
2.3 Lift generation by means of circulation control in conjunction with slipstream deflection 12
2.4 Geometry overview with basic parameters of the CAD model used in the simulations 14
2.5 Circulation control airfoil with droop nose, deflected flap, and blowing slot geometry 15
2.6 Definition of propeller's rotational sense 15
2.7 Aircraft geometry with surface mesh and HTP module 16
2.8 Surface mesh and volume mesh at the slot exit in Y=const-cutting plane . 17

3.1 Blade section [86] 28

4.1 Surface mesh of REF2013-0 wing-body-nacelle model in landing configuration 36
4.2 Influence of mesh resolution on main wing's lift distribution 37
4.3 Longitudinal force and moment coefficients depending on mesh resolution 37
4.4 Influence of mesh resolution on local downwash at HTP position 38
4.5 Influence of mesh resolution on slipstream in terms of total pressure contours at HTP position 38
4.6 Testcase geometry 40
4.7 Flow topology (SA-RC), as viewed looking upstream from a location aft of the flap trailing edge 41
4.8 Total pressure loss due to vortex within main wing boundary layer at $\xi = 0.72$ (looking upstream) 42
4.9 Influence of vortex-circulation control interaction on flap suction peak . . 43

4.10 Streamwise velocity distribution in a X-cutting-plane at $X/r = 1$ downstream of the actuator disk 45
4.11 Spanwise velocity distribution in a X-cutting-plane at $X/r = 1$ downstream of the actuator disk 45

5.1 Comparison of the pressure coefficient and force distribution between airfoil without and with circulation control at $\alpha = 0°$ 49
5.2 Surface pressure distribution, skin friction lines, and visualization of nacelle vortices by streamlines and total pressure loss at $C_\mu = 0$, $\alpha = 6°$ 50
5.3 Visualization of nacelle vortices by streamlines and total pressure loss at $C_\mu = 0.03$, $\alpha = 6°$ 51
5.4 Visualization of nacelle vortices by streamlines and total pressure loss at $C_\mu = 0.03$, $\alpha = 10°$ 52
5.5 Distribution of minimum pressure coefficient along the trailing edge devices and lift distribution of the full wing for various angles of attack at $C_\mu = 0.03$ 53
5.6 Pressure coefficient distribution and skin friction lines on the main wing at post stall with circulation control ($C_\mu = 0.03$, $\alpha = 21°$) 54
5.7 Impact of nacelle and circulation control on lift curve of wing-body configuration 55
5.8 Visualization of nacelle vortices by streamlines and total pressure loss at $C_\mu = 0.03$, $\alpha = 6°$, and propeller on 56
5.9 Influence of circulation control and the propeller on pressure coefficient distribution at $\eta = 0.25$, $\alpha = 6°$ 57
5.10 Influence of circulation control and the propeller on lift distribution at $C_\mu = 0.03$ and $\alpha = 6°$ 58
5.11 Pressure coefficient distribution and skin friction lines on the main wing at $C_\mu = 0.03$, $\alpha = 18°$, and propeller on 59
5.12 Pressure coefficient distribution and skin friction lines on the main wing at post stall in the case with the propeller on ($C_\mu = 0.03$, $\alpha = 20°$) 60
5.13 Impact of the propeller on lift curve 61
5.14 Wake topology with most important flow features regarding flow conditions at the tail planes 63
5.15 Vortex core position at HTP streamwise location ($\xi = 5.07$) for $C_\mu = 0$ (propeller off) 64
5.16 Vortex core position at HTP streamwise location ($\xi = 5.07$) for $C_\mu = 0.03$ (propeller off) 65
5.17 Vortex core position at HTP streamwise location ($\xi = 5.07$) for $C_\mu = 0.03$ with propeller on 66

5.18 Inner flap tip vortex position visualized by iso-surfaces of $kvn = 2$ and influence on surface pressure coefficient at the rear fuselage for $C_\mu = 0.03$ (propeller off) . . . 67
5.19 Change in local angle of attack due to change in global angle of attack at HTP's aerodynamic center . . . 68
5.20 Impact of circulation control and the propeller on the wing-body's pitching moment curve . . . 72
5.21 Impact of circulation control and the propeller on HTP's pitching moment curve . . . 73
5.22 Impact of circulation control and the propeller on aircraft's pitching moment curve . . . 74
5.23 Influence of cross flow on lift distribution at $\alpha = 0°$ and $\beta = 5°$ for varying circulation control modes (propellers off) . . . 79
5.24 Shift of propeller slipstream and its influence on the main wing's lift distribution due to crosswind . . . 81
5.25 Propeller load shift due to crosswind ($C_\mu = 0.03$, $\alpha = 0°$, $\beta = 5°$) . . . 82
5.26 Slipstream impingement on the lower side of the main wing for symmetrically rotating propellers (inboard up) at $C_\mu = 0.03$, $\alpha = 0°$, and $\beta = 0°$ . . . 83
5.27 Slipstream impingement on the lower side of the main wing for symmetrically rotating propellers (inboard up) at $C_\mu = 0.03$, $\alpha = 0°$, and $\beta = 5°$ . . . 84
5.28 Influence of crosswind on lift distribution for symmetrically rotating propellers (inboard up) at $C_\mu = 0.03$ and $\alpha = 0°$ . . . 85
5.29 Influence of crosswind on lift distribution for symmetrically rotating propellers (inboard down) at $C_\mu = 0.03$ and $\alpha = 0°$ . . . 86
5.30 Evolution of main wing wake at $\alpha = 0°$ and $\beta = 5°$ (propellers off) . . . 87
5.31 Evolution of induced spanwise velocities due to trailing vortices at $C_\mu = 0$, $\alpha = 0°$, and $\beta = 5°$ (propellers off) . . . 89
5.32 Evolution of induced spanwise velocities due to trailing vortices at $C_\mu = 0.03$, $\alpha = 0°$, and $\beta = 5°$ (propellers off) . . . 89
5.33 Evolution of induced spanwise velocities due to trailing vortices at $C_\mu = 0.03$, $\alpha = 10°$, and $\beta = 5°$ (propellers off) . . . 91
5.34 Wake topology and resulting induced secondary flow for activated circulation control at positive sideslip angle and high angles of attack (propellers off) . . . 92
5.35 Evolution of main wing wake with symmetrically rotating propellers (inboard up) at $C_\mu = 0.03$, $\alpha = 0°$, and $\beta = 5°$ . . . 94

5.36 Evolution of induced spanwise velocities due to trailing vortices and slipstream in the case with circulation control and symmetrically rotating propellers (inboard up) at $\alpha = 0°$ and $\beta = 5°$ 95
5.37 Surface pressure coefficient distribution and skin friction lines for propellers rotating symmetrically inboard up at $C_\mu = 0.03$, $\alpha = 0°$, and $\beta = 5°$ 96
5.38 Schematic view of significant flow phenomena and crossflow topology at the aft fuselage in the case with circulation control and symmetrically rotating propellers (inboard up) at $\alpha = 0°$ and $\beta = 5°$ 97
5.39 Yawing moment depending on sideslip angle for varying circulation control modes and angles of attack with propellers off 99
5.40 Yawing moment of components and entire aircraft depending on sideslip angle for $C_\mu = 0.03$ and propellers on (I/B up) 100
5.41 Rolling moment depending on sideslip angle for varying circulation control modes and angles of attack (propellers off) 103
5.42 Rolling moment of components and entire aircraft depending on sideslip angle for symmetrically rotating propellers (I/B up), $C_\mu = 0.03$, and $\alpha = 0°$ 104
5.43 Pitching moment coefficient with respect to sideslip angle for symmetrically rotating propellers (I/B up), $C_\mu = 0.03$, and $\alpha = 0°$ 104
5.44 Differences in surface pressure coefficient due to a quasi-steady roll motion at $p = 15°/s$, $C_\mu = 0.03$ and $\alpha = 6°$ (propellers off) 106
5.45 Influence of circulation control on force vectors at $p = 15°/s$ and $\alpha = 6°$ (propellers off) 107
5.46 Evolution of main wing wake with circulation control at $r = 15°/s$ 110
5.47 Influence of circulation control and the propellers on yawing moment with respect to the yaw rate 111
5.48 Influence of circulation control and propellers on aircraft's yawing moment with respect to the yaw rate 113
5.49 Pitching moment variation due to yaw rate at $C\mu = 0.03$, $\alpha = 0°$, and propellers on 113

B.1 Visualization of nacelle vortices by streamlines and total pressure loss at $C_\mu = 0.03$, $\alpha = 10°$, and propeller on 133
B.2 Begin of stall at the wing root visualized by total pressure loss and streamlines ($C_\mu = 0.03$, $\alpha = 19°$, and propeller on) 134

C.1 Change in spanwise jet momentum distribution and suction peak distributions due to crosswind $C_\mu = 0.03$, props off, $\alpha = 0°$, and $\beta = 5°$ (LE = leading edge, TE = trailing edge) 135

D.1 Evolution of main wing wake with symmetrically rotating propellers (inboard down) at $C_\mu = 0.03$, $\alpha = 0°$, and $\beta = 5°$ 137
D.2 Slipstream evolution with symmetrically rotating propellers (inboard down) at $C_\mu = 0.03$, $\alpha = 10°$, and $\beta = 10°$ 138
D.3 Yawing moment with respect to sideslip angle for symmetrically rotating propellers (inboard down) at $C_\mu = 0.03$ and $\alpha = 10°$ 139

List of Tables

2.1 Aerodynamic parameters of the reference aircraft 13
2.2 Overview of used model configurations 15

5.1 Simulation boundary conditions 47
5.2 HTP trim angles 71
5.3 Static margins 74
5.4 Dynamic derivatives of wing-body, HTP and full aircraft 77
5.5 Dynamic moment derivatives of the full aircraft due to roll rate 109
5.6 Lateral dynamic derivatives of the main wing due to yaw rate 109
5.7 Lateral dynamic derivatives of the VTP 112

A.1 Overview of models, similar to present configuration, which were used in experiments and flight tests 131

Nomenclature

C_{p} pressure coefficient, $\frac{p-p_\infty}{q_\infty}$

C_μ jet momentum coefficient, $\frac{\dot{m}_{\mathrm{jet}} V_{\mathrm{jet}}}{q_\infty S_{\mathrm{ref}}}$

$C_{D\alpha}$ drag coefficient derivative due to angle of attack

C_D drag coefficient, $\frac{\text{drag}}{q_\infty S_{\mathrm{ref}}}$

$C_{L'}$ sectional lift coefficient, $\frac{\text{sectional lift}}{q_\infty c_{\mathrm{ref}}}$

$C_{L\alpha}$ lift curve slope

C_L lift coefficient, $\frac{\text{lift}}{q_\infty S_{\mathrm{ref}}}$

C_T propeller thrust coefficient, $\frac{\text{thrust}}{q_\infty S_{\mathrm{ref}}}$

$C_{Z'}$ sectional vertical force coefficient, $\frac{\text{sectional vertical force}}{q_\infty c_{\mathrm{ref}}}$

C_{lp} dynamic roll damping derivative

C_{lr} dynamic rolling moment derivative due to yaw rate

C_l aircraft rolling moment coefficient, $\frac{2 \cdot \text{rolling moment}}{q_\infty S_{\mathrm{ref}} b}$

$C_{m\alpha}$ static pitching moment derivative due to angle of attack

$C_{m\dot{\alpha}}$ dynamic pitching moment derivative due to angle of attack rate

C_{mq} dynamic pitch damping derivative

C_m aircraft pitching moment coefficient, $\frac{\text{pitching moment}}{q_\infty S_{\mathrm{ref}} l_{\mathrm{ref}}}$

C_{np} dynamic yawing moment derivative due to roll rate

C_{nr} dynamic yaw damping derivative

C_n aircraft yawing moment coefficient, $\frac{2 \cdot \text{yawing moment}}{q_\infty S_{\mathrm{ref}} b}$

D'	sectional drag	$\frac{N}{m}$
D_{prop}	propeller diameter	m
E	total specific energy	J
H	total specific enthalpy	J
L'	sectional lift	$\frac{N}{m}$
M	Mach number	
N	Number of mesh points	
O	order of convergence	
R	specific gas constant	$J/(mol \cdot K)$
S	surface	m^2
S_{ref}	reference Area	m^2
T	temperature	K
T_S	Sutherland temperature	K
V	velocity magnitude	m/s
V_c	control volume	m^3
X	streamwise/roll axis	m
X_{CoG}	X-location of the center of gravity	m
X_{N}	X-location of the aircraft's neutral point	m
$X_{\text{ref}_{\text{HTP}}}$	X-location of 25% mean aerodynamic chord (HTP)	m
$X_{\text{ref}_{\text{WB}}}$	X-location of 25% mean aerodynamic chord (main wing)	m
Y	spanwise/pitch axis	m
Z	vertical/yaw axis	m
$Z_{\text{ref}_{\text{HTP}}}$	Z-location of 25% mean aerodynamic chord (HTP)	m
$Z_{\text{ref}_{\text{WB}}}$	Z-location of 25% mean aerodynamic chord (main wing)	m
$\bar{\bar{F}}$	flux density tensor	
$\bar{\bar{I}}$	unit tensor	
$\overline{\overline{S}}$	strain rate tensor	$1/s$

$\vec{V}$	velocity vector	m/s
$\vec{W}$	vector of conservative flow variables	
b	wing span	m
c	chord	m
c_p	specific heat coefficient at constant pressure	$J/(mol \cdot K)$
c_v	specific heat coefficient at constant volume	$J/(mol \cdot K)$
c_{ref}	mean aerodynamic chord length (main wing)	m
e	specific internal energy	J
f_n	normal sectional force	$\frac{N}{m}$
f_t	tangential sectional force	$\frac{N}{m}$
g_h	grid spacing	m
g_r	grid refinement ratio	
h	specific enthalpy	J
h_{AC}	aircraft height	m
i_{HTP}	horizontal tail plane trim angle	$^\circ$
kvn	kinematic vorticity number, $\frac{\lvert\bar{\bar{\omega}}\rvert}{\lvert\bar{\bar{S}}\rvert}$	
$\dot{m}$	mass flow rate	kg/s
n	rotational velocity of propeller	RPM
n_b	number of propeller blades	
p	pressure	Pa
p	roll rate	$^\circ/s, rad/s$
p_t	total pressure, $p_t = p(1 + \frac{\kappa-1}{2}M^2)^{\frac{\kappa}{\kappa-1}}$	Pa
q	dynamic pressure, $\frac{\rho V^2}{2}$	Pa
q	pitch rate	$^\circ/s, rad/s$
r	yaw rate	$^\circ/s, rad/s$
r_b	radial coordinate in actuator disc coordinate system	m

t	time	s
u	x-wise velocity component	m/s
v	y-wise velocity component	m/s
w	z-wise velocity component	m/s
Γ	circulation	m^2/s
Ω_m	rotation velocity of the reference system	rad/s
Ω_{AD}	angular velocity of propeller	rad/s
Θ	angular coordinate in actuator disc coordinate system	rad
α	angle of attack	$^\circ$
β	sideslip angle	$^\circ$
δ	trailing edge device deflection angle	$^\circ$
ϵ	Downwash angle	$^\circ$
ϵ_{ijk}	alternating tensor	
η	dimensionless half span, $\frac{2Y}{b}$	
γ	glide slope	$^\circ$
κ	adiabatic index	
λ	thermal conductivity coefficient	$W/(m \cdot K)$
λ_b	velocity of control volume	m/s
μ	dynamic viscosity	$Pa \cdot s$
μ_l	laminar viscosity	$Pa \cdot s$
μ_t	turbulent eddy viscosity	$Pa \cdot s$
ν_l	kinematic viscosity	m^2/s
ω	specific turbulence dissipation rate	$1/s$
$\overline{\overline{\omega}}$	vorticity tensor	$1/s$
ϕ	sweep angle	$^\circ$
ρ	density	m^3/kg
τ	turbulent shear stress	Pa

ξ	dimensionless length, $\frac{(X-X_{\text{ref}_{\text{WB}}})}{c_{ref}}$ with $X_{\text{ref}_{\text{WB}}} = 0$ in 2-dimensional cases	
ζ	dimensionless height, $\frac{Z}{h_{AC}}$	
g	turbulence length scale $1/\sqrt{\omega}$	$s^{1/2}$

Abbreviations, Subscripts

∞	freestream
AC	aerodynamic center
jet	blowing jet
a	aileron
A/C	aircraft (airframe including propeller forces)
CC	circulation control
CoG	center of gravity
f	flap
HTP	horizontal tail plane
IBF	internally blown flap
IFT	inner flap tip vortex
MLW	maximum landing weight
OFT	outer flap tip vortex
RANS	Reynolds-averaged Navier-Stokes
STOL	short take-off and landing
TED	trailing edge device
VTP	vertical tail plane
WB	wing-body
WT	wing tip vortex

1 Introduction

About 100 years ago, Tony Jannus conducted the world's first commercial flight by transporting one passenger from St. Petersburg, Florida to the 23 miles distant Tampa. Since then, the development of air traffic has been impressive. One passenger became five hundred passengers and 23 miles became 9000 miles. Technical achievements and the resulting cost reductions led to an exponential growth in air traffic. However, its success is also one of aviation's biggest challenges today. While planning and approval of large infrastructure projects is increasingly difficult, existing airports that can handle modern passenger aircraft become bottlenecks, limiting efficiency and future growth. Furthermore, the huge amount of today's daily flights has led the industry and authorities to focus on environmental aspects, as well. In 2001, the Advisory Council for Aeronautics Research in Europe (ACARE) was founded with the aim of developing a strategic research agenda to be better prepared for tackling rising challenges and meeting society's needs. Besides the reduction of CO_2, NO_x and noise emissions, their latest vision *Flightpath 2050* [8] also manifests the aim of reducing travel time within Europe.

Against the background of limited airport capacity, new concepts have to be found to achieve these goals without choking off growth. One idea is to start utilizing existing airport infrastructure, which is not capable of handling today's large passenger aircraft due to its limited runway lengths. Therefore, new aircraft concepts are necessary that require less runway length due to improved high-lift performance. As a side effect, the resulting reduced take-off and landing speeds are also thought to lead to a reduction of airframe noise, as its intensity increases proportionally to the 5th power of the flow velocity [9]. Furthermore, using additional infrastructure can reduce door-to-door travel time, CO_2 and NO_x emissions, as the decentralization helps to reduce travel distance to the airport, and unclog congested airports.

Many approaches exist in order to increase an aircraft's high-lift performance and to achieve so-called short take-off and landing (STOL) capabilities. The most obvious way is to enhance the performance of the high-lift devices. However, as the maximum lift coefficient of conventional passive devices increases, so does system complexity and weight. Furthermore, additional increases beyond a maximum lift coefficient of about 3 are limited due to flow separation [10]. To further increase the high-lift performance, parts of the engine power can be used for lift generation instead of thrust generation. This approach is referred to as powered-lift, if it is used to achieve vertical take-off and landing (VTOL) or at least STOL capabilities. Figure 1.1 depicts some of the powered-lift concepts for subsonic

fixed-wing aircraft. The combination of active flow-control technologies, such as blowing and high-lift devices, is a promising approach to increase the high-lift performance, as it may also reduce system complexity [11].[1] Moreover, applying active-flow control can lead to additional benefits in terms of noise reduction as multi-elements with slots and gaps, which are thought to be a major noise source may become obsolete. The use of active flow control devices may, however, introduce new noise sources, which have to be investigated. If circulation control is regarded as an example, hints on this matter were given by Salikuddin et al., who measured noise from a circulation control wing with upper surface blowing in 1985. According to them, the used high-lift system did not cause "any significant noise problem" [12]. More detailed investigations of the aeroacoustics of a high-aspect ratio jet, as it would be ejected by circulation control, found that the jet noise is proportional to the 8^{th} power of the jet velocity [13]. Furthermore, proportionalities to the slot height and the slot width were found. More recently, Pott-Pollenske et al. compared the noise emissions from a slatless airfoil with circulation control to a conventional 3-element high-lift configuration in a wind tunnel [14]. At model scale, the noise was reduced by about 3dB to 6dB in the frequency range of 2kHz to 20kHz due to the use of the airfoil with circulation control. Aeroacoustics is currently also a research topic within the *Collaborative Research Center 880* (CRC 880) [15].

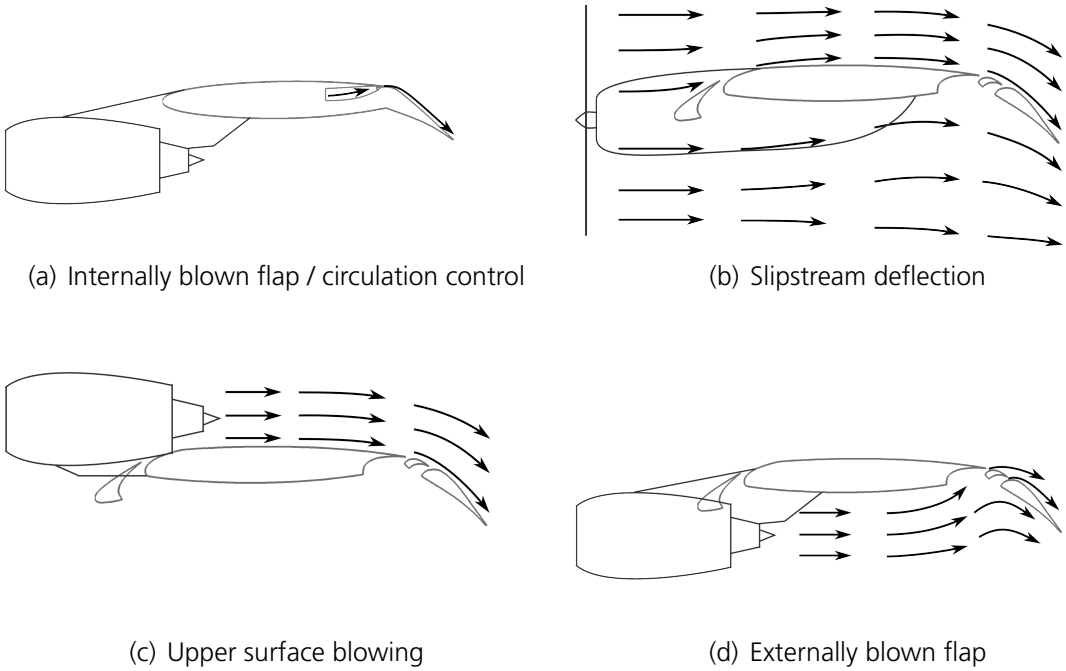

(a) Internally blown flap / circulation control

(b) Slipstream deflection

(c) Upper surface blowing

(d) Externally blown flap

Figure 1.1: Powered lift concepts

Due to its potential of lowering take-off and landing speeds and reducing noise emissions,

[1] The combination of active flow-control technologies and high-lift does not necessarily belong to the powered-lift domain in the classical sense, but an overlap clearly exists.

the use of active flow control for increasing high-lift capabilities is a promising approach to fulfill important aims of *Flightpath 2050*.

1.1 State of the Art

The beginnings of active flow-control date back to 1904, when Ludwig Prandtl showed that flow separation behind a circular cylinder can be reduced by introducing a suction slot into its surface [16]. The earliest use of blowing was mentioned in 1929, when Knight and Bamber successfully tested an airfoil with a backward opening slot [17]. Around the year 1940, Lyon et al. conducted a series of experiments on the blowing over a trailing edge flap [18, 19, 20, 21]. In Germany, the first wind tunnel tests with blowing over a trailing edge flap date back to 1938 and were performed by Hagedorn and later by Schwier (1941) [20, 22, 23, 24]. According to Williams, flight tests with boundary layer control on an Arado 232, Dornier Do-24, and Messerschmidt Me-109 were conducted at that time in Germany [20]. After world war II, investigations of boundary layer control were continued by Williams in England and Poisson-Quinton et al. in France [25]. However, with the emergence of jet engines, the focus progressively shifted from suction to blowing. The latter was more convenient due to the availability of engine bleed air [10, 24].

At the beginning of the cold war, several countries were looking for new high-speed fighters with short take-off and landing (STOL) capabilities to equip their aircraft carriers. This led to the development of the Breguet Vultur prototype in 1951, which used internally blown flaps (IBF). IBF systems blow out a jet sheet from inside of the wing. Usually, the jet sheet is blown over a trailing edge flap, as illustrated in Figure 1.1(a). However, the definition also refers to the jet flap, which simply blows air out of the wing's trailing edge at a certain angle in order to increase the effective chord and camber of the wing. More jet fighters with IBF followed later, including the Blackburn Buccaneer, Mikojan-Gurewitsch MiG-21PFS and the Lockheed F-104, which all went into mass production.

In the late 1950s, research on boundary layer control gathered further momentum when interest in military transport aircraft with STOL capabilities arose. Thereupon, NASA started large scale wind-tunnel tests of propeller-driven airplanes with boundary-layer control flaps [26, 27, 28, 29]. The idea was to further increase the lift production by additional exploitation of the propeller slipstream (slipstream deflection). The main effect here is higher dynamic pressure within the propeller slipstream, which increases the local wing load (Figure 1.1(b)). Fink conducted tests with $50°$ flap deflection whilst suction and blowing was applied to the inboard and outboard wing sections, respectively. This type of boundary layer control resulted in an increase in maximum lift coefficient from 2 to 2.76 in windmill-power condition. With the engines running at full power, the maximum lift coefficient was increased to 4.8. However, the high-lift performance gains were to some extend accompanied by significant impairments of the aircraft's stability behavior. Fink investigated the longitudinal static stability of the aircraft and found that "boundary-layer control application caused a moderate increase in the basic airplane stability", whereas propeller

thrust reduced the longitudinal static stability [26]. Griffin tested a similar configuration with blowing, only [28]. He proved an increase in $\alpha_{(C_{L,max})}$ of 4-5 degrees due to the use of a drooped leading edge in combination with the blown flaps. In the following year, Weiberg tested the same configuration with four propellers. Based on the results of these tests, he calculated downwash angles (the deflection angle of the flow around the pitch axis due to the main wing) from the measured tail pitching moment and dynamic pressure [29]. Later on, Weiberg examined possible stability and control problems and found reduced static longitudinal stability due to an increase in the change of downwash angle with the angle of attack at the HTP position when thrust is applied [30]. Since the configuration had a conventional tail, it was assumed that the situation could be improved if the horizontal tail plane was located higher. Weiberg also reported lateral static instability in case of flap deflection ($60°$) and high thrust coefficients, which was deemed unacceptable [30].

Meanwhile, NASA commenced flight tests with a Stroukoff YC-134 and a Lockheed C-130B, both propeller-driven high-wing transport aircraft with two and four engines, respectively. The flight tests mainly served to investigate handling qualities at low speed. The YC-134, which flew with suction at the trailing edge flap, showed "unsatisfactory" static directional stability[2] beyond $10°$ of sideslip. Furthermore, the roll due to sideslip behavior[3] was considered unsatisfactory [31]. Even though the flight tests with the C-130B showed a similar static directional stability behavior, the latter began at a higher sideslip angle of $\beta = 18°$. Since this is also a characteristic of the basic C-130B airplane, the lift augmentation systems did not appear to have any adverse impact here [32].

The french Brequet Aircraft Company also started an extensive research program on propeller-driven transport aircraft with blown flaps in the late 1950's. Initial studies demonstrated acceptable STOL performance and handling qualities, whereupon NASA also performed flight tests with the Brequet 941. Directional static stability was tested up to $\beta = 30°$. Even though directional static stability was found to be low, the aircraft remained stable [33].

In the late sixties, the Japanese company Shin Meiwa developed a similar STOL aircraft configuration with blown flaps and propeller engines, known as the Shin Meiwa US-1. NASA tested a prototype of this aircraft (UF-XS). The aircraft's handling qualities were rated unsatisfactory in terms of longitudinal static stability, large sideslip excursions, and stability of the spiral mode. However, with an integrated "Automatic Stabilization Equipment" (ASE) turned on, the handling qualities were found to be satisfactory [34].

Investigation of active flow control was not limited to propeller aircraft at that time. A few years before, in the early sixties, Boeing started the first tests with internally blown flap systems on a high-speed transport aircraft, the Boeing 707. The flight tests demonstrated a landing speed reduction to less than 85 knots. Lateral directional problems were also encountered with this type of aircraft. However, they could be improved by "stability augmentation" [35]. The stability augmentation added artificial dutch roll damping

[2] the aircraft's ability to yaw back to its original sideslip angle after a disturbance

[3] the aircraft's tendency to rotate around its roll axis due to a sideslip angle

by increasing rudder deflection proportional to sideslip rate. Furthermore, rudder inputs proportional to aileron deflection and roll rate were added in order to help the pilot fly coordinated turns.

Beginning in 1969, the US Navy did extensive research on circulation controlled wings [36]. The idea was to reduce system complexity of previous powered-lift concepts by simply turning the flow around a bluff trailing edge of an airfoil via tangential blowing. The circulation control wing concept was tested on a Grumman A-6A model and delivered a maximum lift coefficient that was 2.2 times as high as that of the conventional high-lift system [37, 38]. The successful wind-tunnel tests also led to flight tests with a Grumman A-6A [36]. However, since the blunt trailing edge led to high drag during cruise flight, the development shifted towards a tangentially blown plain flap, the dual radius flap [39]. The dual radius flap is a very short chord blown flap with its hinge line lying on the wing's lower surface. The front of the flap's upper surface is a circular arc with the radius being the local wing's thickness at the position of the hinge line. The aft of the upper surface is shaped with another circular arc at a much larger radius. As a result, the jet can be deflected around the trailing edge at high angles, whereas the trailing edge is thin if the flap is retracted. While the term circulation control originally referred to a wing with bluff trailing edge that is tangentially blown, it is used more generally nowadays, also referring to wings with tangentially blown flaps.

The focus shifted to upper surface blowing as noise became a concern. With an integration of the engine above the wing, the jet noise is shielded by the main wing (Figure 1.1(c)). NASA's latest experimental aircraft with STOL capabilities was the Quiet Short-Haul Research Aircraft (QSRA) [40], a modified de Havilland C-8A Buffalo with upper surface blowing, which did its last research flight in the early eighties.

NASA's latest experimental aerodynamic research on circulation control are the wind-tunnel test campaigns with the FAST-MAC model in the NASA-LaRC[4] National Transonic Facility. The half model was equipped with a 15% chord plain flap and 4 independent plenums. It was primarily used to investigate Reynolds number effects and provide a circulation control benchmark database at realistic flight Reynolds numbers for CFD validations [41]. Furthermore, the model was used to successfully demonstrate the application of circulation control in order to beneficially alter the shockwave pattern on the upper wing surface and thus reduce flow separation [41].

In addition to their own research, NASA contracted the California Polytechnic State University (CalPoly) under a NASA Research Announcement (NRA) to investigate a cruise efficient short take-off and landing (CESTOL) aircraft configuration. In 2012, CalPoly conducted a large-scale wind-tunnel test with their CESTOL configuration AMELIA (Advanced Model for Extreme Lift and Improved Aeroacoustics). The AMELIA model was equipped with blown trailing edge flaps as well as over-the-wing mounted turbine propulsion simulators and also incorporated tangential leading edge blowing [42]. Again, one of the main goals of the investigations was to provide a database for CFD validations and advance the state-of-the-art in prediction capabilities [42].

[4]NASA Langley Research Center

In the same year, Petrov compiled TsAGI's recent activities regarding STOL airplanes with powered-lift [43]. Accordingly, TsAGI conducted wind-tunnel tests with the experimental aircraft "Photon", which was equipped with either a circulation controlled bluff trailing edge, similar to the circulation control wing concept [38], or a boundary layer controlled plain flap. The latter can be compared to the dual radius flap [39], even though a second circular arc region on the flap is not mentioned. Furthermore, the aircraft used tangential blowing at the leading edge in order to delay leading edge separation. The configuration with the boundary layer controlled flap led to increases in the lift coefficient of up to $\Delta C_{L,max} \approx 2.5$ at a flap deflection of 60 degrees. Furthermore, TsAGI tested a large-scale model of the Antonov-10 with powered-lift by means of slipstream deflection and blown flaps. The combined system led to a maximum lift coefficient increase from 1.8 to 5.4 at 40 degrees flap deflection and a jet momentum coefficient of 0.02. Flight tests with an Antonov An-70, which was equipped with propfans and only used slipstream deflection, yielded lift coefficients even larger than 7 for high propfan loading coefficients [43].

With increasing CFD capabilities in the last two decades, numerous numerical investigations were carried out on circulation control configurations. Besides validation efforts and improvements in methodology [44, 45, 46, 47], most of them were focusing on improving maximum lift performance and efficiency of the lift gains [48, 49, 50, 51, 52]. At the Technische University of Braunschweig, several studies investigated design parameters such as slot height, flap length, and flap deflection [47, 53, 49]. Furthermore, the use of a leading edge device for IBF applications, such as the flexible droop nose, was investigated [51]. The results laid the basis of the high-lift design used in the present investigation. However, simulations of entire aircraft configurations with circulation controlled high-lift systems remain scarce. One configuration, which has to be mentioned in this context, is the AMELIA configuration, which was simulated with a RANS approach by CalPoly [54, 55].

In recent years, research has focused on active flow control concepts other than circulation control [56], since they promise considerable high-lift performance improvements at low power requirements. Even though these concepts are highly efficient and easier to realize, they cannot deliver the maximum lift increases circulation control can yield, especially in conjunction with slipstream deflection, nor do they have similar potential to enhance control surface efficiency. The combination of circulation control and slipstream deflection therefore remains one of the most promising approaches to allow STOL capabilities. Nevertheless, the investigations, carried out in the 1950's and 1960's, also revealed critical issues regarding flight mechanical stability and controllability that have to be addressed in order to use the concept.

The influence of conventional high-lift systems on the stability in lateral motion of propeller-driven aircraft is a known issue for decades. In 1943 Pitkin carried out freeflight wind-tunnel tests with a twin-engine airplane model with deployed (conventional) flaps [57]. His tests indicated a pronounced effect of flap deflection on lateral stability. Pitkin also observed an influence of the direction of propeller rotation on the stability characteristics with the propellers rotating inboard up being more critical regarding directional stability. In conjunction with airflow patterns measured by Stüper [58] and Sveberg [59], Pitkin

suspected direct slipstream–tail interaction to be the reason for the observed behavior. According to them, the concentration of high velocities on the down-going side of the propeller leads to higher tail effectiveness for inboard down rotation and lower effectiveness for inboard up rotation. Rogallo et al. confirmed Pitkin's findings regarding the effect of the direction of propeller rotation and flap settings on the directional stability with their wind-tunnel investigation of the XB-28 [60]. Mannée [61] and more recently, Schroijen et al. [62] investigated the effect of the propeller slipstream on the lateral controllability under one engine inoperative conditions (OEI). Despite the conditions in these studies being materially different from the ones in the present investigation (OEI vs. all engines operative), the resulting fundamental aerodynamic phenomena are at least closely related as previous work indicates [1]. Mannée as well as Schroijen et al. observed extra yawing moments that cannot be attributed to the product of thrust and thrust arm under OEI conditions. Both assumed asymmetric vortex evolution caused by asymmetric lift distributions at the main wing to be the main cause. They also found a minor contribution to the yawing moment from the fuselage.

1.2 Objectives and Outline

As Gratzer pointed out, it is important to consider the integration of powered-lift systems at an early stage of the design process, as it often has a critical influence on aspects which determine stability and control characteristics [63]. This statement was sufficiently proven by NASA's wind-tunnel and flight tests and led among other aspects to the formation of the CRC 880. It's aim is to advance active high-lift solutions for future civil aircraft by means of a multi-disciplinary approach. For this purpose, aspects from the fields of aerodynamics, aeroacoustics, flight mechanics, light-weight structure, material science, turbomachinery, and micro-technology are investigated. The results are then exchanged and evaluated for a state-of-the-art civil aircraft design. In order to contribute to society's needs, the aims postulated by ACARE, i.e. reduction of CO_2 and noise emissions, travel time reduction, etc., have been closely considered during the aircraft design process.

The present study focuses on the aerodynamic aspects of the integration of active high-lift systems to a state-of-the-art civil transport aircraft and, in particular, their influence on the aircraft stability. With the latest advances in computational fluid dynamics, new approaches exist in terms of numerical flow simulations, which can help to advance in that matter. However, it first has to be shown that these approaches can reproduce the known stability issues of such configurations. If this is the case, only numerical flow simulations with their unique flow analysis potential allow to identify the origins of the problems, which were encountered during wind-tunnel and flight tests, and yet were not fully understood due to limited evidence. Hence, three main research hypothesis can be derived, which shall be examined in this thesis:

- The aerodynamic characteristics and stability issues of a full aircraft configuration, known from wind-tunnel tests and flight experiments can be reproduced by the

chosen numerical approach[5];

- Detailed information about the aerodynamic properties of a state-of-the-art design of a transport aircraft with propellers and circulation control can be derived. The results lay the basis for flight dynamic evaluations that are intended to verify known stability and handling quality issues;

- The analyis of flowfield and surface data will illustrate the influence circulation control and the propeller slipstream have on the aerodynamic behavior of the aircraft. In particular, the analysis will lead to an improved understanding of the complex interaction effects of circulation control and the propeller slipstream. As a result, the (aerodynamic) sources of the stability issues can be identified. The knowledge about the aerodynamic phenomena, which lead to stability issues, is a prerequisite to improve the aircraft behavior of this type of configuration in the future.

The thesis is organized as follows:

Following this introduction in Chapter 1, the second chapter will introduce the geometric model that is used for the numerical simulations. Furthermore, details regarding the computational meshes are given. The third chapter will present the numerical approach which was followed within the numerical investigation. The fourth chapter addresses the numerical uncertainties that accompany the selected approach. Particularly, influences of the computational mesh, turbulence modeling, and modeling of the propeller effects are the methodical aspects which are thought to have the biggest influence on accuracy. Besides validation data from literature, two preliminary studies are presented that shall support the assessment of the uncertainties of the investigation. In the fifth chapter, the results of the numerical study on the impact of circulation control and slipstream deflection on the aerodynamic properties of a novel aircraft configuration are presented. The chapter is organized into two main parts, the longitudinal behavior and the lateral behavior with both parts being subdivided into two sections, one addressing the static, and the other one addressing the dynamic behavior. All aspects will be examined regarding their influence by circulation control and the propeller slipstream. The final chapter will summarize the findings, previously discussed.

[5] An overview of similar test configurations previously used in wind tunnel tests and flight experiments is given in Table A.1.

2 High-Lift Enhancement, Geometric Model and Mesh Generation

2.1 Principles of Circulation Control and Slipstream Deflection

In order to increase the lift generation of a high-lift configuration with plain flaps, constant tangential blowing can be applied at the rounded part of the deployed trailing edge flap; an approach referred to as circulation control. The wall jet entrains the surrounding fluid while being bound by the flap's upper surface on the lower side. As a result, a pressure gradient across the jet is enforced, which keeps the jet attached to the flap. This effect was first observed by Henri Coandă and is therefore called "Coandă effect" [64]. Due to the momentum transfer, the surrounding flow – i.e. the wake caused by the boundary layer leaving the wing's main element at the trailing edge above the blowing slot – is also accelerated. Consequently, the jet as well as the main element's wake can overcome higher adverse pressure gradients, which occur due to the flap deflection. To what extent the flow can withstand an adverse pressure gradient without separating from the flap surface mainly depends on the amount of blowing. For comparison purposes, the blowing momentum is typically expressed as the ratio between the thrust, generated by the jet, and the reference dynamic pressure multiplied by the reference area:

$$C_\mu = \frac{\dot{m}_{jet} V_{jet}}{\frac{\rho_\infty}{2} V_\infty^2 S_{ref}} \tag{2.1}$$

The definition for C_μ was first introduced by Poisson-Quinton [65] and is known as the jet momentum coefficient.

Considering an airfoil with plain flap and modest flap deflection, the application of tangential blowing can be classified into different operating modes based on the blowing coefficient. If no blowing is applied, the flow will eventually separate from the flap's upper surface in proximity to the flap knuckle (Figure 2.1(a)). If tangential blowing is activated at a rather low blowing rate, i.e. a low value for the jet momentum coefficient, the separation point will move towards the rear with the amount of flow separation depending on the amount of blowing (Figure 2.1(b)). As a result, the airfoil's lift is increased. This type of application is called boundary layer control (BLC) and is most efficient in terms

of lift increase compared to the necessary jet momentum. The ratio of lift increase vs. applied jet momentum is called lift gain factor. If the momentum coefficient is further increased, the flow will be fully attached to the flap at some point (Figure 2.1(c)). This is the point which divides the boundary layer control regime from the super circulation (SC) regime. From this point, the separation point cannot be shifted further to the rear of the flap. Yet, the airfoil's circulation is still altered as the jet now virtually increases the flap length (Figure 2.1(d)). Consequently, the lift is still increased when the blowing is increased, but its efficiency is reduced. Therefore, the critical point between boundary layer control and super circulation is very favorable, as it gives the highest lift increase at the highest possible efficiency (Figure 2.2).

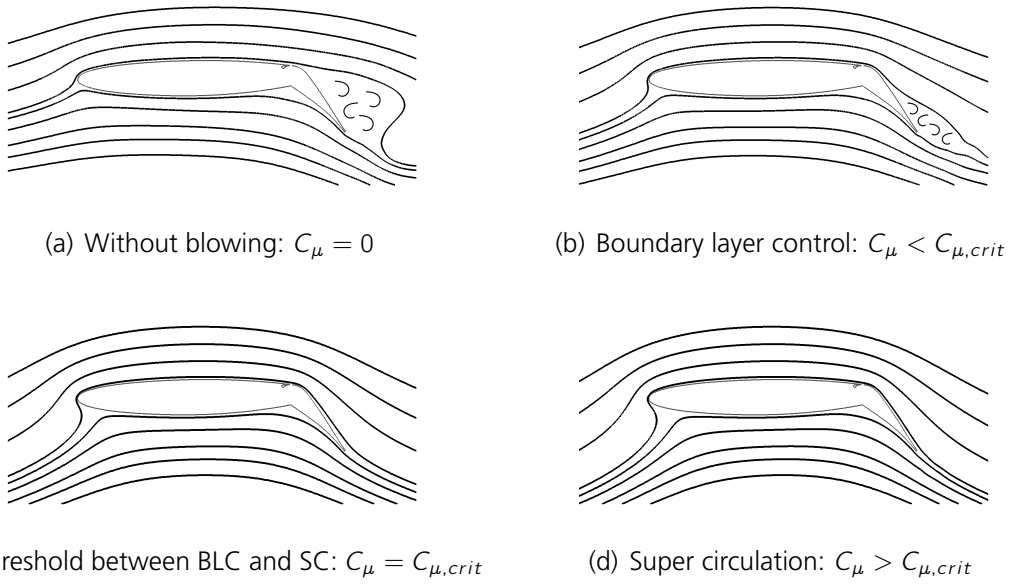

(a) Without blowing: $C_\mu = 0$

(b) Boundary layer control: $C_\mu < C_{\mu,crit}$

(c) Threshold between BLC and SC: $C_\mu = C_{\mu,crit}$

(d) Super circulation: $C_\mu > C_{\mu,crit}$

Figure 2.1: Flap with circulation control

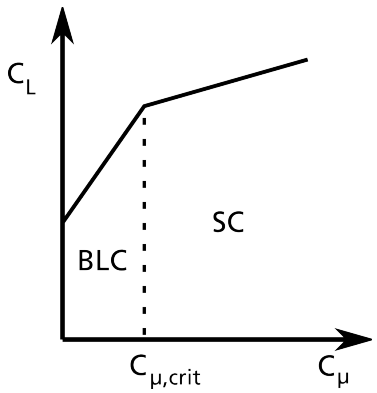

Figure 2.2: Lift coefficient depending on momentum coefficient

Another way to increase the lift of a high-lift configuration is to make use of slipstream

effects, which is easily possible for a wing-mounted propeller engine in tractor configuration. Mounting a propeller in front of the wing has two main effects. Firstly, the reaction force of the propeller locally increases the dynamic pressure within the fluid, with the increase in dynamic pressure depending on the propeller's thrust. Assuming that the aerodynamic properties of the wing in terms of effective camber (which may vary due to flow separation) are not altered by the slipstream, the load of the wing section, that is affected by the slipstream is therefore raised. Consequently, the increase in load due to the dynamic pressure increase is dependent on the thrust and the aerodynamic properties of the wing section, i.e. the force coefficients. Secondly, the swirl of the propeller slipstream leads to a change in the local angles of attack with the magnitude of the change depending on the swirl of the propeller and the radial position. The sign of the change depends on the spanwise position with respect to the propeller axis. On one side of the propeller, where the blades are turning in an upward direction, the local angles of attack are increased behind the propeller (upwash). On the other side of the propeller, where the blades are rotating downwards, the local angles of attack are reduced (downwash). The change in local angles of attack obviously also alters the local load of the main wing. The change depends on the force gradients with respect to the angle of attack, i.e. the static force derivatives.

In summary, it can be concluded that the impact of the propeller on the lift generation of the main wing depends on the propeller characteristics as well as the main wing properties. Thus, wing sections with high circulation, for example due to circulation control, can profit in particular from the use of slipstream deflection to increase lift generation. The synergetic effect of circulation control in conjunction with slipstream deflection is illustrated in Figure 2.3 based on the Kutta–Joukowski theorem. With neither circulation control, nor slipstream deflection, the flow eventually separates from the flap as shown in the left picture and the sectional circulation is low. With circulation control, the flow remains attached to the flap and in turn the sectional lift is increased due to higher circulation (middle picture). If the wing section with circulation control is located downstream of a propeller, the propeller slipstream additionally increases the onset flow velocity and thus the sectional lift (right picture). The onset flow velocity and the sectional circulation are thereby factors of the sectional lift according to the Kutta–Joukowski theorem.

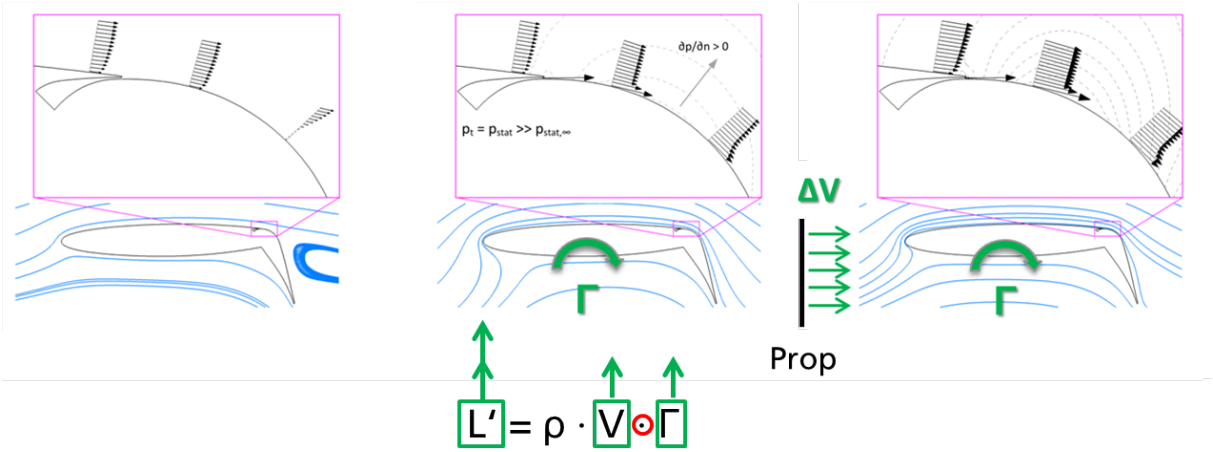

Figure 2.3: Lift generation by means of circulation control in conjunction with slipstream deflection

2.2 Geometric Model

The basis of the investigations is the landing configuration (REF2-2013) of a generic short range transport aircraft, which was designed with the preliminary aircraft design tool PrADO [66] in the course of the CRC 880 [67]. With a maximum payload corresponding to 100 passengers, the mission range is around 2000 km at a cruise Mach number of $M_{cr} = 0.74$. Table 2.1 and Figure 2.4 give some of the main geometric aircraft parameters. In order to achieve the targeted maximum take-off and landing distance of less than 800m, the aircraft is powered by turboprop engines and equipped with internally blown plain flaps and ailerons. The relative chord length of the flaps and ailerons is $c_f/c = c_a/c = 0.25$ and has been chosen on the basis of an earlier study by Jensch et. al [49], who investigated the aerodynamic influence of the flap length. They found that even though longer flaps lead to higher lift coefficients, they also reduce the lift gain factor, i.e. the lift increase for a given amount of blowing. Furthermore, longer flap chord lengths reduce the possible wing tank volume and can have a negative impact on structural weight.
The tangential blowing of the flaps is realized by the integration of a high-pressure plenum into the main wing above the flap kink, which is located at a relative chord length of $c_f/c = 0.75$ (Figure 2.5). For optimal efficiency of the circulation control, the plenum along the wing span is separated into six sections that can be independently pressurized to adjust the blowing to the local flow conditions.
In landing configuration, the flaps are deflected by $\delta_f = 65°$ and the ailerons are drooped by $\delta_a = 45°$. Unless otherwise noted, the total pressure within the plenums is tuned to obtain fully attached flow on the flaps and ailerons for $\alpha = 6°$ at the smallest possible amount of blowing. The resulting global blowing coefficient equates to $C_\mu = 0.03$.
Due to the very high effective camber, the position of the leading edge stagnation line is shifted far downstream on the main wing's lower side. Initial results without leading

Reference wing area	95 m^2
Wing span	28.775 m
Mean aerodynamic chord	3.428 m
Aerodynamic center	(13.131m|0|1.563 m)
Wing leading edge sweep	10°
Basic main wing airfoil	DLR F15
HTP area	27 m^2
HTP span	11.023 m
Relative tail volume (HTP)	1.487
VTP area	27 m^2
VTP span	5.692 m
Relative tail volume (VTP)	0.296
HTP airfoil	NACA0010

Table 2.1: Aerodynamic parameters of the reference aircraft

edge device showed massive leading edge separation at low angles of attack [2]. In order to circumvent leading edge separation, the aircraft is also equipped with a flexible droop nose [68, 69, 70, 51].

The centerline of the engine is located at $\eta = 0.35$. The propeller has a diameter of $D_{prop} = 5.0\,m$ and was designed as part of the *CRC 880* project. The propeller effects are modeled by an actuator disk. Since the approach uses the blade element theory, local flow conditions are considered for the calculation of the blade loads, thrust, and swirl (see Section 3.2.3). The engine settings are set to balance out the drag at a landing glideslope of $\gamma = -3°$. At $M_\infty = 0.15$, the propeller's rotational speed of $n = 975RPM$ results in a blade tip Mach number of $M_{tip} = 0.77$. The propellers' sense of rotation is also a subject of the present investigation. However, unless otherwise noted, the propellers are rotating symmetrically in inboard up direction (Figure 2.6).

Since circulation control and slipstream deflection are used for lift augmentation, they obviously also impact the pitching moment balance. Therefore, the horizontal tail plane (HTP) is trimmed for the varying conditions at $\alpha = 6°$ with respect to the center of gravity position at maximum landing weight and maximum payload (CoG_{MLW}).

In the course of the investigations, a study on the use of nacelle strakes demonstrated the potential of a significant increase in the maximum lift coefficient under certain conditions. Therefore, the subsequent investigations, namely the analysis of the longitudinal and lateral stability, were conducted with a modified geometry that includes a nacelle strake (REF2-2013S) as summarized in Table 2.2.

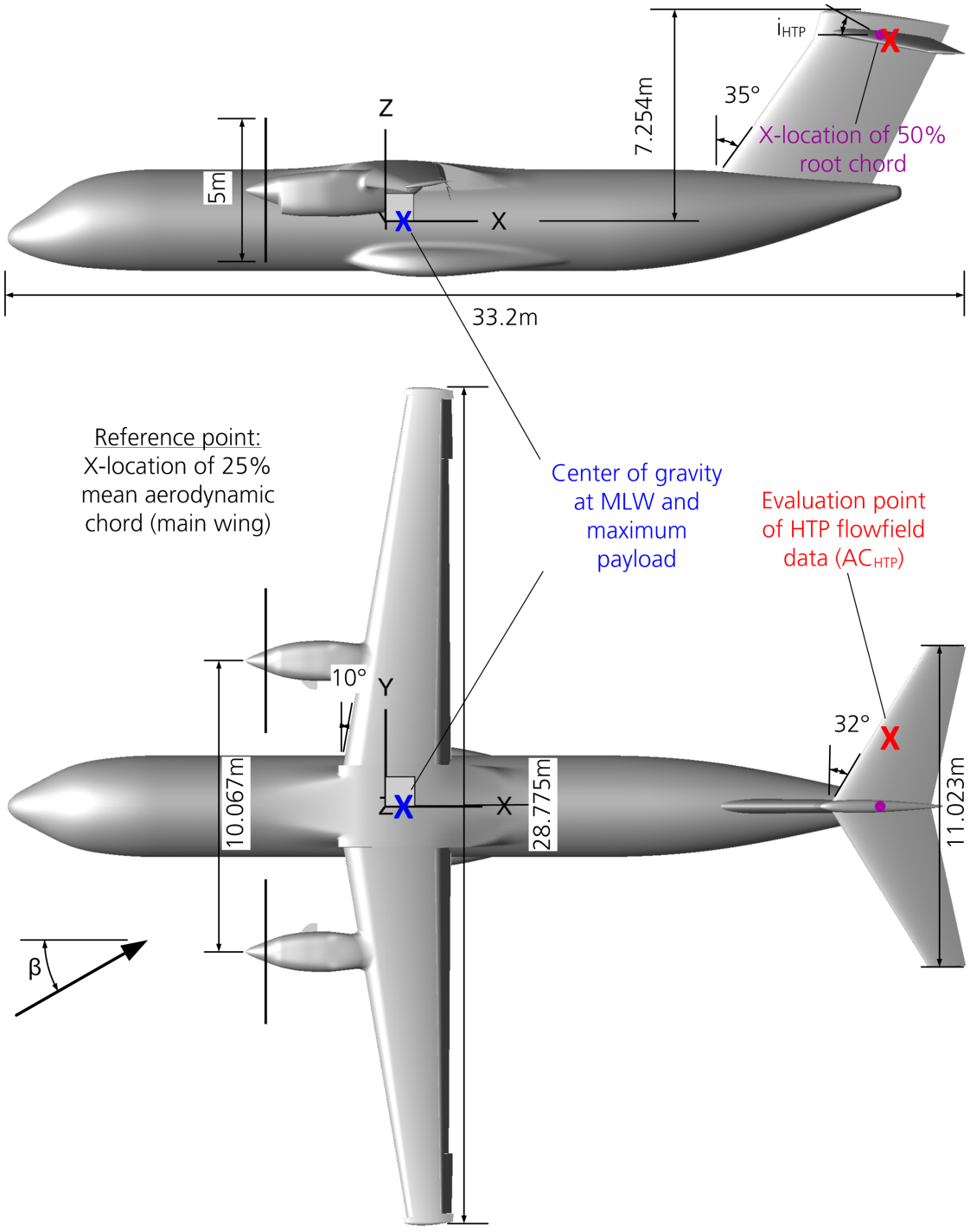

Figure 2.4: Geometry overview with basic parameters of the CAD model used in the simulations

Type of investigation	Configuration	Configuration name
Stall behavior	Wing-body (with engine)	REF2-2013
Wake evolution	Wing-body (with engine / with strake)	REF2-2013S
Longitudinal stability	Wing-body-tail (with engine / with strake)	REF2-2013S
Lateral stability	Wing-body-tail (with engine / with strake)	REF2-2013S

Table 2.2: Overview of used model configurations

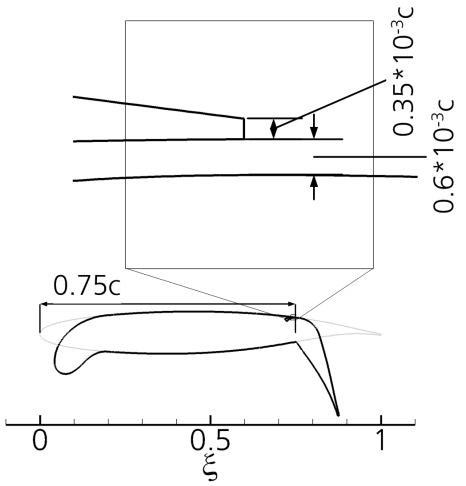

Figure 2.5: Circulation control airfoil with droop nose, deflected flap, and blowing slot geometry

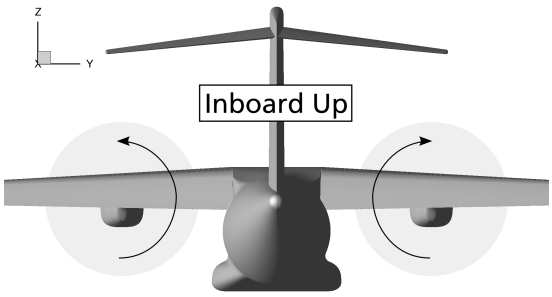

Figure 2.6: Definition of propeller's rotational sense

2.3 Mesh Generation

Mesh generation plays a key role in numerical investigations based on the RANS approach, as mesh resolution and quality impact the results. Since discretization errors inversely correlate with mesh resolution, a trade-off between result accuracy and computation costs has to be made. A common method to do so is to choose the mesh cell sizes based on a grid convergence study. For this type of configuration, meshing studies in 2D as well as 3D have been performed (see Section 4.2). The computational mesh for the present investigation was then built based on the outcome of these studies. For this purpose, the semi-automated meshing software Centaur [71] was used. The software typically creates hybrid meshes, which are intended to combine the positive aspects of structured and unstructured meshes. The mesh generation is carried out in three steps. In the first step, the surface mesh is built. During the second step, the mesh generator builds structured layers in proximity to viscous surfaces in order to properly resolve boundary layers. In the final step and if not otherwise defined, the rest of the computational domain is filled with unstructured tetrahedra, which provides the mesh the flexibility of fully unstructured meshes. The meshing software also features modular meshing, which means that the

computational domain is split up into two or more sub-domains, and each sub-domain can be remeshed individually without having to remesh the entire computational domain. This feature was used for large trim deflections of the HTP, whereas small adaptions during the trim routine were realized by TAU mesh deformation [72]. Figure 2.7 illustrates the modular box around the HTP.

The basic surface discretization of the main wing with refinement zones at the leading edge, the slot region, the flap knuckle, and the trailing edges is based on a two-dimensional grid convergence study [2]. Additionally, refinements in regions of slipstream and three-dimensional flow features are added. The final surface mesh of the half model with tail has approximately 1.2 million points and can be seen in Figure 2.7.

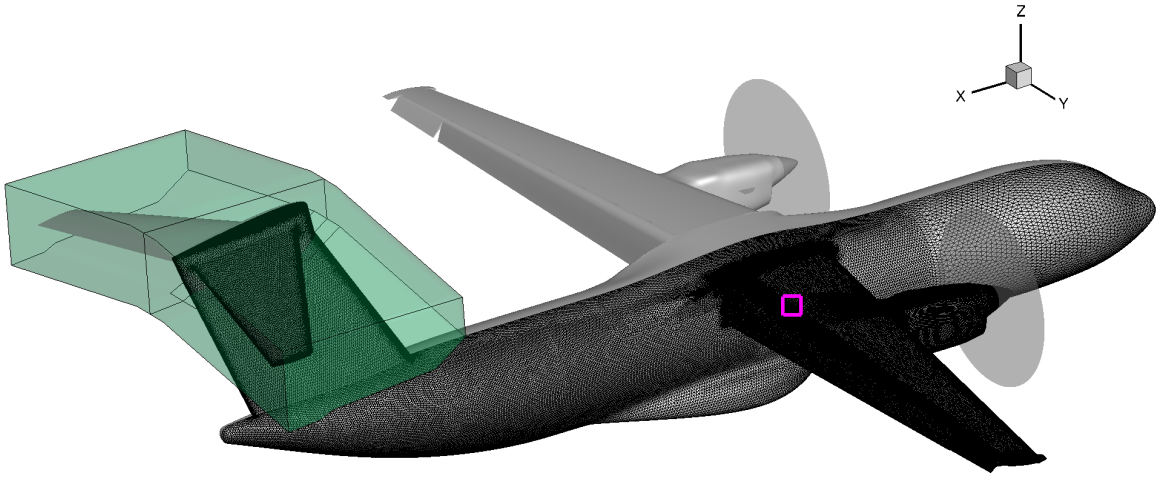

Figure 2.7: Aircraft geometry with surface mesh and HTP module

Even though the hybrid meshing approach works well for boundary layers, it leads to difficulties in case of free shear layers due to the rigid O-type topology. Consequently, the meshing of the slot exit is one of the main challenges of the investigated configuration. Its relatively small size compared to the aircraft dimensions makes the meshing process even more difficult. However, the two dimensional meshing studies demonstrated that the hybrid approach is suitable for such type of investigations. A comparison of a hybrid mesh with O-type topology at the slot exit and a mesh, that is structured and in H-type topology at the slot exit, showed almost identical results. With comparable cell sizes, the difference in maximum lift was less than $\Delta C_l = 0.001$ at identical angle of attack.

Figure 2.8 depicts the mesh topology at the slot exit, as realized for the three dimensional geometry (detail marked by the magenta square in Figure 2.7). It shows that the number of prism layers (blue lines) is reduced (chopped down) from 37 to 23 in front of the main element's trailing edge, and the prismatic elements then wrap around the trailing edge and continue into the plenum. The chosen number of prism layers within the plenum is

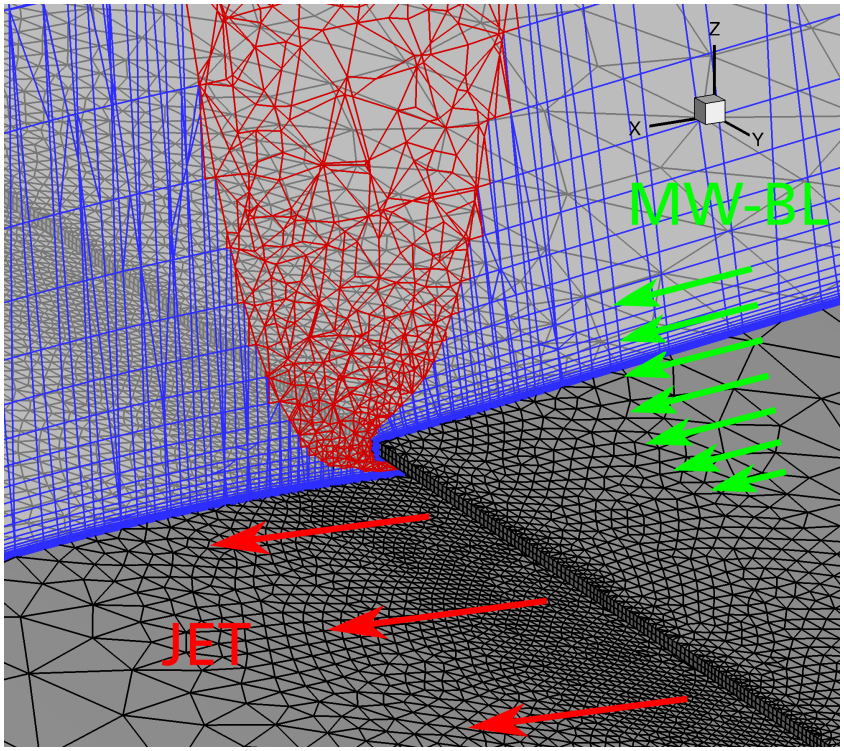

Figure 2.8: Surface mesh and volume mesh at the slot exit in Y=const-cutting plane

a good compromise between high boundary layer resolution and adequate cell sizes at the interface with the adjacent tetrahedra. At the lower side of the plenum the prism layers quickly increase from 23 to 39 on the flap and the aileron in order to provide sufficient boundary layer resolution downstream. The space between the prism layers is filled with tetrahedra (red lines). The prism height as well as the initial layer thickness were first estimated based on the theory of a flat plate turbulent boundary layer [73, 74]. Afterwards, they were adapted based on the results of the first RANS computations. However, the high circulation around the main wing and the high jet exit velocity lead to large differences in local velocities which in turn result in strongly varying initial layer thicknesses, if a non-dimensional wall distance of $y^+ = 1$ shall be fulfilled. Even though the initial layer thickness is adapted along the plenum exit, the initial layer's wall distance locally reaches values of up to $y^+ \approx 2.3$ at the slot exit. A two-dimensional study on the influence of the initial layer's wall distance yielded a difference of $\Delta C_{l,max} = 0.005$ at $C_\mu = 0.039$ for the selected first layer heights compared to a mesh with first layers heights not exceeding $y^+ = 1$, which is considered acceptable. The maximum angle of attack remained unchanged.
The remaining volume is filled with tetrahedra with the region behind the wing being refined in order to capture the wake phenomena. The refined zone extends behind the tail. The final volume mesh of the half model with tail consists of approximately 49 million nodes.

The analysis of the longitudinal motion was carried out on the half model. A full model

for asymmetric flow conditions was obtained by mirroring the mesh of the half model in order to examine the lateral motion.

3 Numerical Methods

3.1 Governing Equations

For aeronautical applications, the atmosphere can be considered a continuum, allowing to apply the conservation laws of fluid mechanics. Since air can also be treated as a Newtonian fluid, the Navier-Stokes equations are valid for this type of application. For a control volume V_c and a moving coordinate system, the conservation of mass, momentum, and energy can be written as

$$\frac{d}{dt}\iiint_{V_c} \vec{W}\,dV_c + \iint_S \left(\overline{\overline{F}} - \vec{W}\cdot\vec{\lambda}_b\right)\cdot\vec{n}\,dS + \iiint_{V_c}\vec{G}\,dV_c = 0 \qquad \text{with}$$
$$\vec{W} = \begin{bmatrix}\rho\\ \rho\vec{V}\\ \rho E\end{bmatrix}. \tag{3.1}$$

Here, the change of the conservative flow variables $\vec{W}$ within the control volume V_c is compensated by the fluxes over the control volume's surface S and a source term $\vec{G}$ which results from the change from an inertial coordinate system to a rotating (e.g. body-fixed) one [75]. The fluxes over the control volume's surface are expressed by the flux density tensor $\overline{\overline{F}}$ and the local normal vector $\vec{n}$ of the surface element dS. Since the flux density tensor is formulated with the absolute velocity $\vec{V}$, the fluxes have to be reduced by the share which is related to the motion of the control volume's surface $\vec{\lambda}_b$ in the case of moving grids. Furthermore, the flux density tensor can be split into a convective part $\overline{\overline{F_c}}$ and a viscous or diffusive part $\overline{\overline{F_v}}$:

$$\begin{aligned}
\overline{\overline{F}} &= \overline{\overline{F_c}} - \overline{\overline{F_v}}\\
\overline{\overline{F_c}} &= \begin{bmatrix}\rho\vec{V}\\ \rho\vec{V}\otimes\vec{V} + \bar{\bar{I}}p\\ \rho H\vec{V}\end{bmatrix}\\
\overline{\overline{F_v}} &= \begin{bmatrix}0\\ \bar{\bar{\tau}}\\ \vec{V}\bar{\bar{\tau}} + \lambda\nabla T\end{bmatrix}
\end{aligned} \tag{3.2}$$

In order to solve this set of equations, a few additional relations have to be introduced. With Newton's correlation between shear stress and the shear strain rate and considering Stoke's hypothesis regarding the bulk viscosity being zero, the shear stress tensor $\overline{\overline{\tau}}$ in the momentum equations can be expressed by the spatial velocity derivatives and the dynamic viscosity μ [76]:

$$\overline{\overline{\tau}} = \mu \left(\nabla \otimes \vec{V} + \left(\nabla \otimes \vec{V} \right)^T - \frac{2}{3} \overline{\overline{I}} \left(\nabla \cdot \vec{V} \right) \right) \tag{3.3}$$

The dependency of the dynamic viscosity on the temperature T is represented by Sutherland's law with the Sutherland temperature being $T_S = 110.4K$:

$$\frac{\mu}{\mu_\infty} = \left(\frac{T}{T_\infty} \right)^{\frac{3}{2}} \frac{T_\infty + T_S}{T + T_S} \tag{3.4}$$

In the energy equation, the total specific energy E and the total specific enthalpy H were introduced. The first can be derived from the specific internal energy e and the specific kinetic energy:

$$E = e + \frac{1}{2}\vec{V}^2 \tag{3.5}$$

Assuming a calorically perfect gas, the specific internal energy can be calculated with a constant specific heat capacity at constant volume c_v as following

$$e = c_v T. \tag{3.6}$$

The specific total enthalpy is then derived by

$$H = E + \frac{p}{\rho}. \tag{3.7}$$

Due to the assumption of calorically perfect gas, the ideal-gas law

$$p = \rho R T \tag{3.8}$$

can be applied as well. With the introduction of the adiabatic index κ and the specific gas constant R

$$\begin{aligned} \kappa &= \frac{c_p}{c_v} \\ R &= c_p - c_v = \frac{\kappa - 1}{\kappa} c_p, \end{aligned} \tag{3.9}$$

the total specific energy E can finally be expressed by a relation of the pressure p, the density ρ and the velocity vector $\vec{V}$:

$$E = \frac{1}{\kappa - 1}\frac{p}{\rho} + \frac{\vec{V}\cdot\vec{V}}{2} \tag{3.10}$$

The heat flux can be computed with the relation between the viscous diffusion rate and the thermal diffusion rate with the Prandtl number being set to $Pr = 0.72$ for air:

$$Pr = \frac{\mu c_p}{\lambda} \tag{3.11}$$

3.2 Reynolds-Averaged Navier-Stokes Equations

Based on the Navier-Stokes equations, several approaches exist to compute real flow behavior which vary in terms of their demand on computational resources and complexity. However, analytic solutions only exist for particular flow phenomena. The highest level of effort to solve the Navier-Stokes equations numerically is the direct numerical simulation (DNS), which is too costly for complex flows, especially at high Reynolds numbers as the CPU-time scales as Re^3 [77]. If one is not interested in resolving all scales of turbulence, as is mostly the case in aerodynamic problems at the aircraft level, turbulence effects can be approximated to various extents through modeling. Large eddy simulations only resolve large eddies and model small scale turbulence. In order to further reduce the computational cost, the entire bandwidth of turbulence scales can be modeled. For this purpose, the flow variable ϕ is decomposed into time-averaged mean $\overline{\phi}$ and fluctuating part ϕ', of which the time average is zero ($\overline{\phi'} = 0$), as was presented by Reynolds in 1895 for incompressible flows [78]:

$$\phi = \overline{\phi} + \phi' \tag{3.12}$$

In the case of compressible flows, the fluctuations in density lead to additional non-linear terms, which can be avoided by applying a mass-weighted (Favre) averaging to certain flow variables:

$$\phi = \widetilde{\phi} + \phi'', \qquad \text{with} \qquad \widetilde{\phi} = \frac{\overline{\rho\phi}}{\overline{\rho}} \tag{3.13}$$

Here, the mass-weighted average of the fluctuations is zero ($\widetilde{\phi''} = 0$), whereas the time-average is not zero ($\overline{\phi''} \neq 0$). Decomposing the variables of the Navier-Stokes equations, averaging, and neglecting terms cubic in fluctuating quantities, yields the so-called Reynolds-averaged Navier-Stokes (RANS) equations

$$\frac{d}{dt}\iiint_{V_c} \overline{\vec{W}}\,dV_c + \iint_S \left(\overline{\overline{\vec{F}}} - \overline{\vec{W}}\cdot\vec{\lambda}_b\right)\cdot\vec{n}\,dS + \iiint_{V_c} \vec{G}\,dV_c = 0 \tag{3.14}$$

with the Reynolds- and Favre-averaged conservative variable vector $\overline{\vec{W}}$ and flux density tensor $\overline{\overline{\vec{F}}}$:

$$\vec{W} = \begin{bmatrix} \overline{\rho} \\ \overline{\rho}\widetilde{\vec{V}} \\ \overline{\rho}\widetilde{E} \end{bmatrix}, \qquad \overline{\overline{\vec{F}}} = \overline{\overline{\vec{F}_c}} - \overline{\overline{\vec{F}_v}} \tag{3.15}$$

The convective $\overline{\overline{\vec{F}_c}}$ and viscous $\overline{\overline{\vec{F}_v}}$ components of the flux density tensor now yield

$$\begin{aligned} \overline{\overline{\vec{F}_c}} &= \begin{bmatrix} \overline{\rho}\widetilde{\vec{V}} \\ \overline{\rho}\widetilde{\vec{V}} \otimes \widetilde{\vec{V}} + \overline{\rho\vec{V}'' \otimes \vec{V}''} + \overline{\overline{I}}\overline{p} \\ \overline{\rho}\widetilde{H}\widetilde{\vec{V}} + \overline{\rho\vec{V}''h''} + \overline{\rho\vec{V}'' \otimes \vec{V}''}\widetilde{\vec{V}} + \frac{1}{2}\overline{\rho\vec{V}''\left(\vec{V}'' \otimes \vec{V}''\right)} \end{bmatrix} \text{ and} \\ \overline{\overline{\vec{F}_v}} &= \begin{bmatrix} 0 \\ \overline{\overline{\tau}} \\ \widetilde{\vec{V}}\overline{\overline{\tau}} + \overline{\overline{\tau}\vec{V}''} + \lambda\nabla\widetilde{T} \end{bmatrix}. \end{aligned} \tag{3.16}$$

After introducing the Favre-averaged turbulent kinetic energy $\widetilde{k}$ and generally defining the Favre-averaged total energy $\widetilde{E}$ and total enthalpy $\widetilde{H}$ as

$$\widetilde{E} = \widetilde{e} + \frac{\widetilde{V}^2}{2} + \widetilde{k} \;\text{ and }\; \widetilde{H} = \widetilde{h} + \frac{\widetilde{V}^2}{2} + \widetilde{k} \;\text{ with }\; \widetilde{k} = \frac{1}{2}\widetilde{\vec{V}''\vec{V}''}, \tag{3.17}$$

three additional terms remain in the components of the flux density tensor compared to the initial Navier-Stokes equations. These terms represent fluctuations of the flow variables and do not vanish due to their non-linear nature:

- $\overline{\rho\vec{V}'' \otimes \vec{V}''}$ describes the transport of momentum due to the turbulent fluctuations and is called Reynolds stress tensor;
- $\overline{\rho\vec{V}''h''}$ corresponds to the transport of heat due to turbulent fluctuations and is therefore called turbulent heat-flux tensor;
- $\overline{\overline{\tau}\vec{V}''} - \frac{1}{2}\overline{\rho\vec{V}''\left(\vec{V}'' \otimes \vec{V}''\right)}$ represent the molecular diffusion and turbulent transport of turbulence kinetic energy, respectively [79].

In order to close the RANS equations, formulations for these terms have to be defined with the Reynolds stress tensor typically thought to be the most important one. Various approaches exist on how to do so. Reynolds stress models (RSM) directly compute the six components of the symmetric Reynolds stress tensor by solving transport equations for them. An additional transport equation, for example for the length scale is needed. RSM

are called second-order closure models and are thought to be the most complex of the classical RANS turbulence models. Eddy viscosity models (EVM) relate the Reynolds stresses to the averaged velocity gradients by introducing a so-called turbulent eddy viscosity. They are known as first-order closure models. The most common EVM are the linear EVM, which rely on the Boussinesq hypothesis, assuming a relation between the turbulent shear stress and the mean strain rate in analogy to laminar flow:

$$\overline{\overline{\tau_t}} = -\overline{\rho\vec{V}'' \otimes \vec{V}''} = \mu_t \left(\nabla \otimes \widetilde{\vec{V}} + \left(\nabla \otimes \widetilde{\vec{V}} \right)^T - \frac{2}{3}\overline{\overline{I}} \left(\nabla \cdot \widetilde{\vec{V}} \right) \right) - \frac{2}{3}\overline{\overline{I}} \left(\overline{\rho}\widetilde{k} \right) \tag{3.18}$$

Based on the Reynolds analogy, the modeling of the turbulent transport of heat becomes

$$\overline{\rho\vec{V}''h''} = -\lambda_t \nabla \widetilde{T}, \tag{3.19}$$

whereas the turbulent thermal conductivity coefficient λ_t is defined as

$$\lambda_t = c_p \frac{\mu_t}{Pr_t} \tag{3.20}$$

with $Pr_t = 0.9$ for air. The terms representing the molecular diffusion and the turbulent transport of turbulence kinetic energy are modeled in different ways and are sometimes neglected. One example how to model these terms is

$$\overline{\overline{\tau}\vec{V}''} - \frac{1}{2}\overline{\rho\vec{V}'' \left(\vec{V}'' \otimes \vec{V}'' \right)} = \left(\mu_l + \frac{\mu_t}{\sigma_k} \right) \nabla \widetilde{k}, \tag{3.21}$$

with σ_k being dependent on the modeling of the turbulence kinetic energy $\widetilde{k}$.

Applying the Boussinesq hypothesis in conjunction with the Reynolds analogy leaves the eddy viscosity μ_t and the turbulence kinetic energy $\widetilde{k}$ (and σ_k) as the remaining unknowns. How these unknowns are determined depends on the turbulence model. Generally, one can distinguish between three types of linear EVM: Zero-, one-, and two-equation models, depending on the number of additional transport equations. Zero-equation (or algebraic) turbulence models do not use an additional transport equation and calculate the missing variables directly from the mean flow variables. One-equation turbulence models solve one additional transport equation, usually for the turbulent kinetic energy or the eddy viscosity. Two-equation models solve two additional transport equations, typically for the turbulent kinetic energy and a variable reflecting the scale of the turbulence.

Equation 3.18 reveals a fundamental deficit all of the linear EVM imply. Even though the Reynolds stress tensor receives an artificial anisotropy from the mean strain rate, any information about the actual anisotropy of the fluctuations is lost. However, since these models can deliver sufficiently high accuracy for many problems at a low computational cost, they are widely used.

3.2.1 Spalart-Allmaras Turbulence Model

The Spalart-Allmaras (SA) turbulence model is a one-equation linear EVM, which solves for a transported quantity that is closely related to the eddy viscosity [80]. The model evolved from the need to better model detached and multiple shear layers than algebraic turbulence models did at a time when two-equation models were too costly and unstable for many purposes. The transported quantity $\widetilde{\nu}$ equals the kinematic eddy viscosity except in the viscous region which is realized with the introduction of the function f_{v1}:

$$\mu_t = \rho\widetilde{\nu} f_{v1} \quad \text{with} \quad f_{v1} = \frac{\chi^3}{\chi^3 + {c_{v1}}^3} \quad \text{and} \quad \chi = \frac{\rho\widetilde{\nu}}{\mu} \tag{3.22}$$

The transport equation for the viscosity variable $\widetilde{\nu}$ is then composed of its temporal change, convection and viscous fluxes, and a source term on the right-hand side:

$$\begin{aligned} &\iiint_{V_c} \frac{\partial \rho\widetilde{\nu}}{\partial t} dV_c + \iint_S \left(\rho\widetilde{\nu} \left(\widetilde{\vec{V}} - \vec{\lambda}_b \right) - \left(\frac{\mu_l + \rho\widetilde{\nu}}{\sigma} \right) \nabla\widetilde{\nu} \right) \cdot \vec{n} dS \\ &= \iiint_{V_c} \left(c_{b1} \left(1 - f_{t2}\right) \widetilde{S} \rho\widetilde{\nu} + \frac{c_{b2}}{\sigma} \nabla \left(\rho\widetilde{\nu}\right) \cdot \nabla\widetilde{\nu} - \left(c_{w1} f_w - \frac{c_{b1}}{k^2} f_{t2} \right) \rho \frac{\widetilde{\nu}^2}{d^2} \right) dV_c \end{aligned} \tag{3.23}$$

The production term $c_{b1}\left(1 - f_{t2}\right)\widetilde{S}\rho\widetilde{\nu}$ is proportional to a sum of the magnitude of the vorticity $|\overline{\overline{\omega}}|$ and a term which shall improve its log-layer behavior and is related to the nearest wall distance d:

$$\widetilde{S} = |\overline{\overline{\omega}}| + \frac{\rho\widetilde{\nu}}{k^2 d^2} f_{v2} \quad \text{with} \quad \overline{\overline{\omega}} = \nabla \otimes \overline{\vec{V}} - \left(\nabla \otimes \overline{\vec{V}} \right)^T \quad \text{and} \quad f_{v2} = 1 - \frac{\chi}{1 + \chi f_{v1}} \tag{3.24}$$

For the destruction term, the wall function f_w is defined as

$$f_w = g \left[\frac{1 + {c_{w3}}^6}{g^6 + {c_{w3}}^6} \right]^{\frac{1}{6}} \quad \text{with} \quad g = r + c_{w2}\left(r^6 - r\right) \quad \text{and} \quad r = \frac{\widetilde{\nu}}{\widetilde{S} k^2 d^2} \ , \tag{3.25}$$

with r being limited to a maximum of 10 ($r = min\left(r, 10\right)$).
Furthermore, the tripping function f_{t2}, which is used in the production and destruction terms of the general SA formulation, and which shall provide control over the laminar regions of the shear layers [80], is defined as

$$f_{t2} = c_{t3} exp\left(-c_{t4}\chi^2\right) \tag{3.26}$$

The constants of the model used in the present study are:

$$
\begin{aligned}
c_{b1} &= 0.1355 \quad , \quad c_{b2} = 0.622 \quad , \quad \sigma = 2/3 \quad , \quad k = 0.41 \\
c_{v1} &= 7.1 \quad , \quad c_{t3} = 0 \quad , \quad c_{t4} = 0.5 \\
c_{w1} &= \frac{c_{b1}}{k^2} + \frac{1 + c_{b2}}{\sigma} \quad , \quad c_{w2} = 0.3 \quad , \quad c_{w3} = 2
\end{aligned}
$$

Due to $c_{t3} = 0$ instead of $c_{t3} = 1.2$, the f_{t2} terms are removed from the transport equation. As a result, the pseudo-laminar behavior, which occurs at low free stream values of $\widetilde{\nu}$, vanishes independently of the $\widetilde{\nu}_\infty$ according to Rumsey [81].

The SA model neglects the turbulence kinetic energy and the terms representing the molecular diffusion and the turbulent transport of turbulence kinetic energy:

$$
\begin{aligned}
\widetilde{k} &= 0 \\
\overline{\overline{\tau}\vec{V}''} - \frac{1}{2}\overline{\rho\vec{V}''\left(\vec{V}'' \otimes \vec{V}''\right)} &= 0
\end{aligned}
\tag{3.27}
$$

Rotational and Curvature Correction (SARC)

The basic formulation of the Spalart-Allmaras turbulence model does not account for effects of system rotation and streamline curvature. Considering a vortex, the model in fact contradicts what is known about the rather laminar behavior of the vortex core [82], since its production term is proportional to the magnitude of the vorticity, which is obviously very high within the core. Therefore, Spalart and Shur introduced a modification to the model's production term in order to improve its behavior in the case of system rotation and streamline curvature [83]. The modification of the original SA turbulence model is simply achieved by multiplying its production term $c_{b1}\left(1 - f_{t2}\right)\widetilde{S}\rho\widetilde{\nu}$ with a rotation function f_{r1} [84]:

$$
f_{r1} = \left(1 + c_{r1}\right)\frac{2r^*}{1 + r^*}\left(1 - c_{r3}\tan^{-1}\left(c_{r2}\widetilde{r}\right)\right) - c_{r1} \tag{3.28}
$$

Here, the ratio of the strain rate and the vorticity magnitude

$$
r^* = \frac{|\overline{\overline{S}}|}{|\overline{\overline{\omega}}|} \tag{3.29}
$$

plays an important role, as it is used as a sensor. In shear layers, the strain rate is of similar magnitude as the vorticity, leading to a ratio of $r^* \approx 1$. Therefore, the production term is fully active. In contrast, the deformation gradient within a vortex core is strongly dominated by rotation, leading to very small values of $r^* << 1$. As a result, the production term is strongly reduced in vortex cores. The variable $\widetilde{r}$ in the rotation function f_{r1} is defined as

$$
\widetilde{r} = 2\omega_{ik}S_{jk}\left(\frac{DS_{ij}}{Dt} + \left(\epsilon_{imn}S_{jn} + \epsilon_{jmn}S_{in}\right)\Omega_m\right)/D^4 \tag{3.30}
$$

with

$$S_{ij} = 0.5\,(u_{i,j} + u_{j,i}) \quad , \quad \omega_{gh} = 0.5\,((u_{g,h} - u_{h,g}) + 2\epsilon_{mhg}\Omega_m \tag{3.31}$$

and

$$D^2 = 0.5\left(|\overline{\overline{S}}|^2 + |\overline{\overline{\omega}}|^2\right) \tag{3.32}$$

Note that the rotation tensor ω is modified by considering the rotation velocity of the reference system Ω_m. The constants are defined as follows:

$$c_{r1} = 1.0 \quad , \quad c_{r2} = 12 \quad , \quad c_{r3} = 1.0 \tag{3.33}$$

3.2.2 SSG/LRR-g Turbulence Model

The SSG/LRR-g turbulence model belongs to the group of Reynolds stress models. Therefore, it does not rely on the Boussinesq approximation, but instead computes each component of the Reynolds stress tensor, separately. As a result, the anisotropic nature of turbulence is thought to be captured. Especially in the cases where multiple Reynolds stresses are important, for example secondary flow, the model promises better approximations of the Reynolds stress tensor. The SSG-LRR-g is based on the typical approach of transport equations, with the source term consisting of a production term $\overline{\rho}P_{ij}$, a pressure-strain correlation $\overline{\rho}\Phi_{ij}$, a dissipation term $\overline{\rho}\epsilon_{ij}$, a diffusion term $\overline{\rho}D_{ij}$, and a system rotation term $\overline{\rho}F_{ij}$. The mass flux term is usually neglected. For the six independent Reynolds stresses, the transport equation reads

$$\begin{aligned} &\frac{d}{dt}\iiint_{V_c} \overline{\rho}\widetilde{u_i'' u_j''}\,dV_c + \iint_S \overline{\rho}\widetilde{u_i'' u_j''}\left(\widetilde{\vec{V}} - \vec{\lambda}_b\right)\cdot\vec{n}\,dS \\ &= \iiint_{V_c} \left(\overline{\rho}P_{ij} + \overline{\rho}\Phi_{ij} - \overline{\rho}\epsilon_{ij} + \overline{\rho}D_{ij} + \overline{\rho}F_{ij}\right)\cdot dV_c \ . \end{aligned} \tag{3.34}$$

The production term and the system rotation term can be exactly computed, whereas the other terms are modeled. The pressure-strain correlation term is a combination of the LRR for the near wall region and the SSG formulation away from the wall, as is also done by the Menter Baseline model for ω and ϵ. Instead of ω, the SSG/LRR-g model uses $g = 1/\sqrt{\omega}$ as length-scale variable. As a result, the dependency of the solution on y_1^+ resolution is reduced [85]. To close the system of equations, the transport equation for the length scale variable g is solved with $\overline{\rho}P^g$, $\overline{\rho}\epsilon^g$, $\overline{\rho}D^g$, $\overline{\rho}C_D^g$ and $\overline{\rho}G^g$ being the production, destruction, diffusion, cross-diffusion, and additional gradient term, respectively:

$$\begin{aligned} &\frac{d}{dt}\iiint_{V_c} \overline{\rho} g dV_c + \iint_S \overline{\rho} g \left(\widetilde{\vec{V}} - \vec{\lambda}_b\right) \cdot \vec{n} dS \\ &= \iiint_{V_c} \left(\overline{\rho} P^g - \overline{\rho}\epsilon^g + \overline{\rho} D^g + \overline{\rho} C_D^g + \overline{\rho} G^g\right) \cdot dV_c \end{aligned} \tag{3.35}$$

Further details on the used RSM can be found in [85].

3.2.3 Actuator Disc

In order to estimate the propeller influence on the fluid without fully resolving the unsteady propeller blades rotation, the propeller can be modeled by a so-called actuator disk. The idea can be traced back to Rankine's momentum theory. Rankine proposed to model propeller effects by discontinuous pressure jumps over a disk of zero thickness. The theory was later advanced by Froude by calculating the blade load distribution in order to estimate the propeller's forces acting on the fluid. The blade load distributions are calculated based on sectional geometric and aerodynamic data of the blade and the local flow conditions, where the sectional data can be defined by the user:

$$\begin{aligned} L'_{(r_b,\Theta)} &= \frac{\rho_{(r_b,\Theta)}}{2} v^2_{e(r_b,\Theta)} c_{(r_b)} C_L(\alpha_{e(r_b,\Theta)}) \\ D'_{(r_b,\Theta)} &= \frac{\rho_{(r_b,\Theta)}}{2} v^2_{e(r_b,\Theta)} c_{(r_b)} C_D(\alpha_{e(r_b,\Theta)}) \end{aligned} \tag{3.36}$$

The geometric data include the sectional chord length c and the blade twist β. Considering the local blade twist, the effective local angle of attack of the blade becomes

$$\alpha_{e(r_b,\Theta)} = \beta_{(r_b)} - \alpha_{i(r_b,\Theta)} \qquad \text{with} \qquad \alpha_{i(r_b,\Theta)} = \arctan\left(\frac{-v_{n(r_b,\Theta)}}{v_{t(r_b,\Theta)} - \Omega_{AD} r_b}\right) \tag{3.37}$$

The inflow angle $\alpha_{i(r_b,\Theta)}$ is thereby calculated from the local rotational speed $\Omega_{AD} r_b$ and the relative velocity components $v_{n(r_b,\Theta)}$ and $v_{t(r_b,\Theta)}$. The relation between the velocities and the angles is depicted in Figure 3.1. The magnitude of the effective velocity $v_{e(r_b,\Theta)}$ is derived from the velocity components:

$$v_{e(r_b,\Theta)} = \sqrt{\left(v_{t(r_b,\Theta)} - \Omega_{AD} r_b\right)^2 + v^2_{n(r_b,\Theta)}} \tag{3.38}$$

The reaction forces to the sectional lift and drag are transformed into normal and tangential sectional force components of the disk coordinate system:

$$\begin{aligned} f_{n(r_b,\Theta)} &= \left(-L'_{(r_b,\Theta)}\right)\cos\left(\alpha_{i(r_b,\Theta)}\right) - \left(-D'_{(r_b,\Theta)}\right)\sin\left(\alpha_{i(r_b,\Theta)}\right) \\ f_{t(r_b,\Theta)} &= \left(-L'_{(r_b,\Theta)}\right)\sin\left(\alpha_{i(r_b,\Theta)}\right) + \left(-D'_{(r_b,\Theta)}\right)\cos\left(\alpha_{i(r_b,\Theta)}\right) \end{aligned} \tag{3.39}$$

Based on the sectional forces, the time-averaged forces, which are applied to a grid cell's surface S on the actuator disk, are

$$F_{Sn} = f_{n(r_b,\Theta)} \frac{n_b}{2\pi} \int_S \frac{1}{r_b} dS$$
$$F_{St} = f_{t(r_b,\Theta)} \frac{n_b}{2\pi} \int_S \frac{1}{r_b} dS \tag{3.40}$$

with n_b being the number of blades and r_b being the local radial position. As a result, the actuator disk model can calculate local changes in velocity magnitude and direction based on the propeller input parameters and local flow conditions.

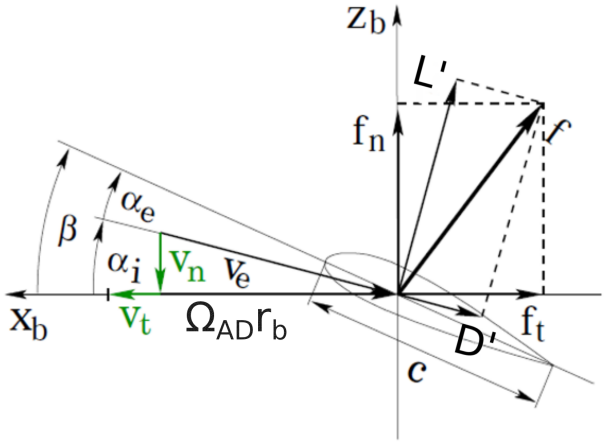

Figure 3.1: Blade section [86]

3.3 Flow Solver

For the present study, the DLR TAU-code was used. It solves for the three-dimensional, compressible RANS-equations with a finite-volume approach. The flow solver uses a cell-vertex metric based on a dual grid approach. Therefore, the control volumes, for which the RANS-equations are solved, are built around the vertices of the primary grid by connecting the surrounding primary grid's cell centers and cell face centers.

Assuming the conservative flow variables to be constant for a control volume V_c and the flux density tensor to be uniform over the cell face, Equation 3.14 can be written as

$$\frac{d}{dt}\vec{W}^n = -\frac{1}{V_c}\left(\vec{F}^{*n} + \vec{G}^*\right) = -\vec{R}^n(\vec{W}^n) \quad \text{with} \quad \vec{F}^{*n} = \sum_{i=1}^{m}\left(\vec{F}^*_{c,i} - \vec{F}^*_{v,i}\right) \ , \tag{3.41}$$

where $\vec{F}^{*n}$ comprises the fluxes over the control volume's m boundary faces and $\vec{G}^*$ is the additional source term in the case of a rotating coordinate system. The fluxes are con-

structed with finite difference formulations. The user is thereby able to select from various options. For the present study, a second order central scheme with scalar dissipation according to the method of Jameson, Schmidt and Turkel [87] was used for the convective mean flow fluxes and the viscous fluxes. The convective turbulent fluxes were discretized with a second order Roe upwind scheme.

The flow solution is advanced in time from an initial solution to the final solution with an iterative time stepping scheme. The temporal differences of the conservative flow variables, which are also called residuals $\vec{R}^n$, should thereby converge towards zero with its minimum values depending on the machine accuracy.

3.3.1 Spatial Discretization

Central discretization

For the present study, the fluxes which are constructed with a central scheme, are computed by the average of fluxes from the left and right state. Generally, this is second order accurate in space. However, since a simple central difference is built by an average of the adjacent cell values and therefore does not consider the direction of propagation of information, the stability of the approach is not guaranteed. Furthermore, the approach tends to oscillations at shock waves. In order to improve these problems, an artificial dissipation term $\vec{D}_i$, which consists of a second difference and a fourth difference term, is added to the convective fluxes. In smooth regions, the latter is activated in order to counteract odd-even decoupling and thus improve the stability with minimum dissipation. The scheme remains second-order accurate. In regions of large pressure gradients, i.e. shocks, a pressure sensor switches from the fourth difference term to the second difference term to limit overshoots, reducing the scheme to a first-order accurate one. The second- and fourth difference terms are scaled with the scaling coefficients $k^{(2)}$ and $k^{(4)}$, respectively. For the present study, $k^{(2)}$ is set to $\frac{1}{2}$ and $k^{(4)}$ equals $\frac{1}{64}$. Furthermore, the entire dissipation term is scaled with the maximum eigenvalue of the flux Jacobian $\lambda^*_{c,i}$ for the face i and a term f_ϕ, which accounts for the local grid stretching.

$$\vec{F}^*_{c,i} = \frac{1}{2}\left(\vec{F}_{c,i}(\vec{W}_R) + \vec{F}_{c,i}(\vec{W}_L)\right) - \frac{1}{2}\lambda^*_{c,i} f_\phi \vec{D}_i \tag{3.42}$$

Upwind Discretization

In the case of the Roe upwind scheme, the propagation direction of information has to be determined. Therefore, a linearized model of the Riemann problem is solved. According to Roe [88], the flux $\vec{F}^*_{c,i}$ can then be expressed as

$$\vec{F}^*_{c,i} = \frac{1}{2}\left(\vec{F}_{c,i}(\vec{W}_R) + \vec{F}_{c,i}(\vec{W}_L)\right) - \frac{1}{2}|\overline{\overline{A}}^*_i|\left(\vec{W}_R - \vec{W}_L\right) \tag{3.43}$$

with $\overline{\overline{A_i^*}}$ representing the flux Jacobian based on so-called Roe-averaged variables at the cell face. The lower indices L and R denote the variables to the left and right state of the cell face. For second order accuracy, gradients of the flow variables have to be computed in order to extrapolate the variables from the cell center to the cell face. In the present study, these gradients are evaluated with the Green-Gauss divergence theorem.

3.3.2 Time Stepping

In order to advance the solution from an initial state to the final state, a (pseudo) time stepping scheme has to be chosen. In traditional explicit schemes, the time step size is limited by the Courant-Friedrichs-Levy (CFL) condition for stability reasons. Implicit time stepping schemes, such as the Backward-Euler method, which was used in the present study, allow significantly larger time step sizes at the cost of large memory requirements and higher CPU-time per iteration. For this method, a large system of equations has to be solved, which is done with the Lower-Upper Symmetric Gauss-Seidel method proposed by Jameson and Turkel [89]. In order to accelerate convergence, local time stepping and multigrid methods were applied.

3.3.3 Convergence Criteria and Averaging

The complex geometry and model set-up in the present study introduce unsteady flow behavior (e.g. due to local flow separation and vortices) that cannot be resolved by the chosen RANS approach and eventually leads to the residuals $\vec{R}^n$ being greater than machine precision. Even at the final state, differences within the flow solution remain between the iterations that are reflected in oscillations of the integral force and moment values. In the present study, the amplitude of those oscillations was typically less than $0.5\,\%$ of the corresponding averaged integral value. The maximum observed amplitude of the lift coefficient for example was less than 0.01. For this reason, the averaged integral coefficients were assessed to determine the state of convergence. The computations were assumed to have reached the final state when the integral coefficients demonstrated ergodic behavior.

3.4 Force and Moment Evaluation

The force and moment coefficients for the longitudinal and lateral motion are computed based on the integration of the forces acting on the aircraft's surfaces. The surfaces are thereby treated depending on their boundary condition. Accordingly, the forces of the viscous walls are computed from the pressure and shear stress acting on the surfaces. The forces of the actuator disks (thrust and circumferential force) are the reaction forces to the normal and tangential forces introduced to the computational domain (see 3.2.3).
For the determination of the airframe's force and moment coefficients, the forces of the

viscous walls were considered. The surfaces inside the plenums of the blowing jets were thereby excluded. With regard to the airframe's moments, comparisons with and without plenum forces showed that the plenum forces are negligible. The jet momentum coefficient was derieved by integrating the flow quantities in a plane normal to the jet nozzle exit:

$$C_\mu = \frac{1}{q_\infty S_{ref}} \int\limits_{S_{slot}} |\vec{V}| \rho \vec{V} \vec{n} dS \tag{3.44}$$

The thrust coefficient was computed from the normal forces acting on the actuator disks, with the forces from the spinners being considered in the airframe and thus being excluded from the thrust (coefficient). The aircraft's force and moment coefficients consist of the contributions from the airframe and the actuator disks.

3.5 Determination of Stability Derivatives

The definition of freestream flow conditions and the evaluation of the moment coefficients and derivatives are based on the body-fixed TAU coordinate system as depicted in Figure 2.4. The definition of a positive sideslip angle and the signs of the lateral moments therefore differ from the ones in the LN9300 standardized coordinate system.[1]

Dynamic Derivatives

For the determination of the dynamic derivatives, quasi-steady motions with a moving grid were performed. In the case of the pitch motion, the grid is constantly rotated around a point, which is located above the aircraft's center of gravity at a distance r_p in the inertial system. In contrast to typical RANS computations, the free stream velocity at the aircraft is not induced by a given farfield velocity but results from the grid movement as

$$V_\infty = r_p \cdot q \ , \tag{3.45}$$

with q being the angular velocity of the grid. Furthermore, the angle of attack and sideslip angle can be defined by additional constant rotation angles (without angular velocity) of the body-fixed system to the inertial system. Similar to the pitch motion, the yaw motion can be simulated by a rotation at constant angular velocity around a point which is located to the side of the aircraft's center of gravity at a distance r_r. In the case of the roll motion, the grid is rotated around the center of gravity, with the free stream velocity being given by the farfield boundary conditions.

[1] The definition of the sideslip angle β is analogous to that used in the LN9300 coordinate system and therefore yields the same signs for the stability derivatives.

Based on the quasi-steady simulations, the dynamic derivatives can be calculated. Assuming linear behavior, the dynamic derivative for the force or moment i is the ratio between the difference in the force or moment coefficient C_i at varying angular velocities and the difference of the non-dimensional angular velocities q^*,p^*, and r^*, themselves [90, 91, 92]

$$\begin{aligned} C_{iq} &= \frac{\partial C_i}{\partial q^*} \approx \frac{C_{i,q2} - C_{i,q1}}{q_2^* - q_1^*} \\ C_{ip} &= \frac{\partial C_i}{\partial p^*} \approx \frac{C_{i,p2} - C_{i,p1}}{p_2^* - p_1^*} \\ C_{ir} &= \frac{\partial C_i}{\partial r^*} \approx \frac{C_{i,r2} - C_{i,r1}}{r_2^* - r_1^*} \end{aligned} \tag{3.46}$$

The non-dimensional angular velocities are defined as

$$\begin{aligned} q^* &= q\frac{c_{ref}}{V_\infty} \\ p^* &= p\frac{b}{2V_\infty} \\ r^* &= r\frac{b}{2V_\infty} \ , \end{aligned} \tag{3.47}$$

with the pitch rate q^* being non-dimensionalized with the reference length c_{ref}, and the roll and yaw rate are non-dimensionalized with the semi-span $\frac{b}{2}$.

4 Verification and Validation

Prior to investigating the aerodynamic behavior of the full aircraft configuration, the reliability of the chosen simulation approach shall be assessed for the presented problem. Since there is no validation data of a similar test case available, the capabilities of the numerical approach to simulate complex high-lift configurations in general is first assessed. Additionally, aspects, which are thought to have the largest impact on accuracy in this particular investigation are addressed. These additional aspects are mesh discretization, the modeling of turbulence, and the modeling of propeller effects. The chosen procedure shall build and support confidence in the accuracy of the numerical approach for the present case.

4.1 Validity of the Numerical Approach for High-Lift Configurations

The validity of high-lift simulations performed with the TAU solver and the basic numerical approach has been studied in many past investigations. Two particular projects shall be highlighted here. The high-lift prediction workshop is the most notable collaborative effort of RANS validation for high-lift cases. Several computation cases with varying geometrical complexity are defined and shared among the participants who then compare the performance of their CFD codes with each other and with experimental results. The focus is laid on the correct prediction of the lift coefficient in the linear range and that of the maximum lift coefficient. Furthermore, capabilities of capturing separation phenomena and wake effects can be verified. The DLR's TAU code has been validated in all three workshops and showed respectable results [93, 94, 95]. The results computed with the SA turbulence model were consistent with those of the other participants. While the prediction of the lift coefficient agreed well with the experimental results in the linear range, it was off by up to 5% for the maximum lift coefficient at low Reynolds numbers [96]. At high Reynolds numbers the deviation in maximum lift coefficient was even smaller.

In 2010, the HINVA project was initiated with the aim to enhance the accuracy and reliability of RANS computations of civil transport aircraft with deployed flaps [97]. For this purpose, RANS simulations were compared to wind tunnel as well as flight test experiments. While data evaluation is still in progress, simulations of a stall maneuver found $C_{L,max}$ to be in the range given by the flight data systems during flight test [98].

With the participation in the high-lift prediction workshops, the HINVA project, and other similar activities [99, 100, 101, 102, 103], the TAU code demonstrated its basic suitability for simulating complex high-lift configurations.

4.2 Meshing Influence

The use of meshes with finite cell sizes introduces errors to the solution compared to the exact analytical solution of the system of partial differential equations. These discretization errors generally scale with the order of the selected scheme of spatial discretization. However, numerical models and boundary conditions also affect the discretization errors. Mesh convergence studies can be performed in order to estimate the discretization errors. For this purpose, the problem has to be solved on a mesh family, which consists of several meshes with identical topology and varying refinement levels (self-similar meshes). A common way to obtain a mesh family for a structured mesh is to create a fine mesh first. Then, a coarser mesh is created by removing every other grid line in each coordinate direction [104]. For a two-dimensional mesh, this approach leads to a mesh with one fourth of the number of cells of the fine mesh. For a three-dimensional mesh, the number of cells would be reduced to one eighth of the fine mesh. This procedure can then be repeated to obtain even coarser meshes. After the mesh family has been created and computations of the problem have been performed, the Richardson extrapolation can be used to obtain the exact analytical solution for a quantity f, with f_1, f_2, and f_3 being the solutions of this quantity on meshes with varying cell sizes [105]:

$$f_{exact} = f_1 + (f_1 - f_2)/(g_r^O - 1) \tag{4.1}$$

$$g_r = g_{h_2}/g_{h_1} = g_{h_3}/g_{h_2} \tag{4.2}$$

The exact analytical solution depends on the grid refinement ratio g_r, given by the grid spacing g_h and the order of convergence o. Equation 4.3 demonstrates that it needs at least three meshes at a constant grid refinement ratio to obtain the order of convergence o.

$$O = In(\frac{f_3 - f_2}{f_2 - f_1})/In(g_r) \tag{4.3}$$

It has to be noted that the creation of a mesh family for hybrid meshes will introduce inconsistencies with respect to the refinement ratio of the cells due to the characteristics of these meshes and the way they are created.

For the present investigation, a 2D as well as a 3D meshing study were carried out. First, a 2D mesh convergence study was performed on a wing section of the present configuration for both structured and unstructured meshes [2]. The mesh resolution of the 3D mesh was then chosen based on these results. This approach should lead to an appropriate mesh resolution with the exception of a possible strong impact of specific 3D

features. Comparing the results of a 2-dimensional hybrid mesh with the topology of the 3-dimensional mesh and similar cell sizes with the exact solution from the Richardson extrapolation based on the 2-dimensional structured meshes, yields differences of $\frac{\Delta C_L}{C_{L,exact}} = 2.2\%$, $\frac{\Delta C_D}{C_{D,exact}} = 21.3\%$, and $\frac{\Delta C_m}{C_{m,exact}} = 2.5\%$ for the lift, drag, and pitching moment coefficient, respectively.

In order to estimate the mesh influence on 3D features, a meshing study of the 3D wing-body-nacelle model of the REF2013-0[1] landing configuration was conducted. The meshing study also demonstrates the influence of mesh resolution on the wake evolution, which is dominated by 3D features such as vortices. The resulting mesh family consists of the base mesh, a coarse mesh, which has about half the number of points of the base mesh, and a fine mesh that is about twice as big as the base mesh. Therefore, the cells' edge lengths of the coarse and the fine meshes are selected to be $2^{1/3}$ and $\frac{1}{2^{1/3}}$ times as large as those of the base mesh, respectively. However, due to the chosen unstructured meshing approach, not every single cell size is user defined, but instead is a result of the input given by the user and the underlying meshing algorithms. The effective refinement ratios of the mesh family are therefore not identical and the mesh sizes result in 22.1 million, 36.6 million, and 65.9 million points for the coarse, base, and fine mesh, respectively. Figure 4.1 gives an overview of the surface meshes in the main wing region. In order to distinguish between mesh influence and influences from turbulence modeling, the wall distance of the first mesh layer at viscous walls was kept constant.

[1]The REF2013-0 configuration is the CRC 880's initial design of the turboprop aircraft. The main differences between the REF2013-2 and the REF2013-0 are the added droop nose, the modified nacelle, the altered main wing's angle of incidence, and the increased empennage size.

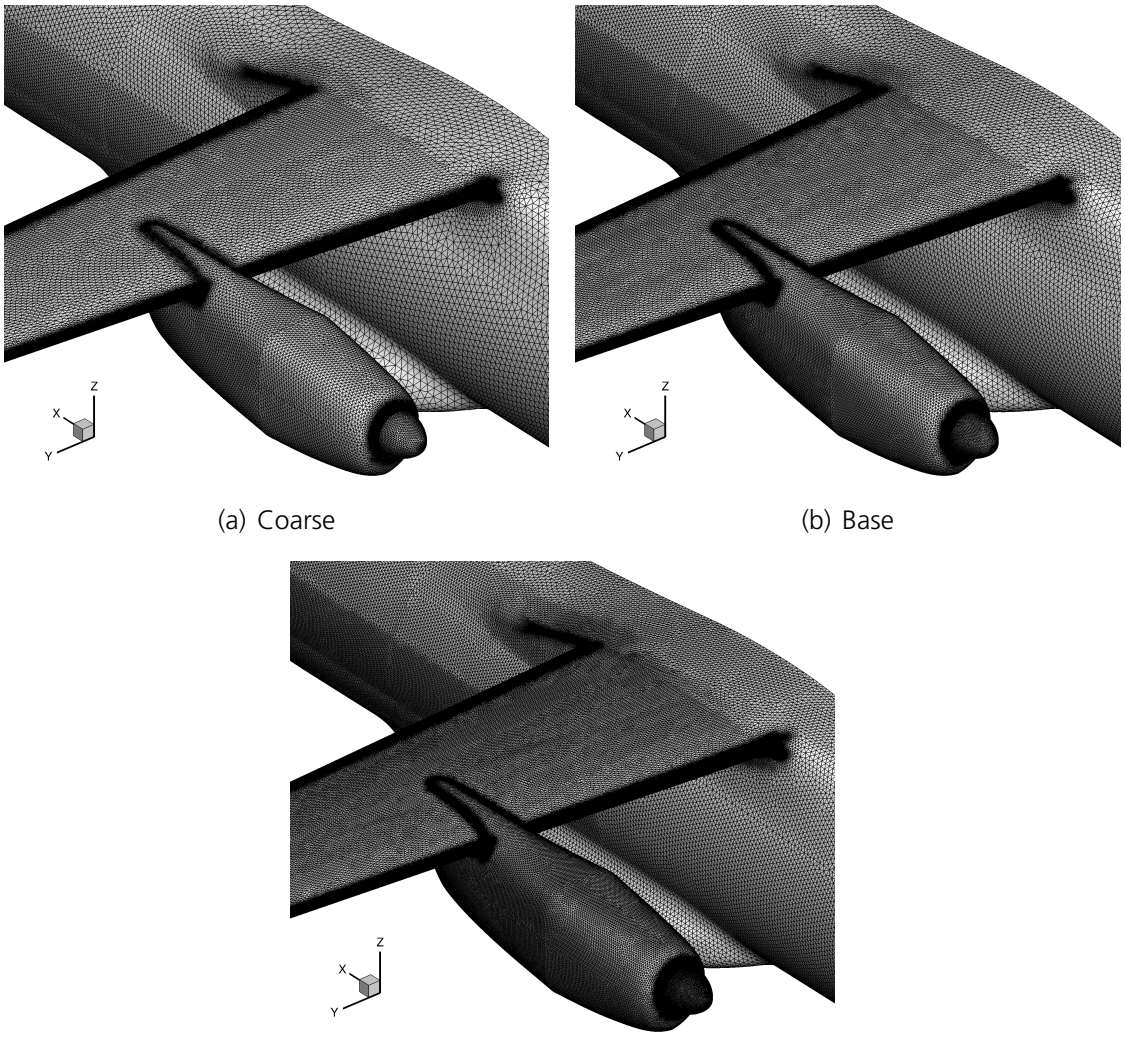

(a) Coarse (b) Base

(c) Fine

Figure 4.1: Surface mesh of REF2013-0 wing-body-nacelle model in landing configuration

Figure 4.2 compares the lift distributions for the varying mesh sizes at a jet momentum coefficient of $C_\mu = 0.033$ and $\alpha = 0°$. In the outboard region, the influence of the mesh refinement on the local lift is marginal. The trend is as expected from the results of the two-dimensional grid convergence study, with the finest mesh yielding the highest lift as the flow velocity along the surface is affected less by artificial dissipation. The sensitivity of the local lift with respect to the change in cell sizes is, however, lower compared to the two-dimensional test case. When comparing these two test cases, it has to be noted that, despite the global angle of attack being identical, the local flow conditions differ notably between the two-dimensional and the three-dimensional test case due to the induced angle of attack and the twist angle. The local angle of attack, and thus the leading edge suction peak, is significantly lower in the outboard region of the three-dimensional test case compared to the one of the two-dimensional case. The difference in the suction peak due to mesh refinement is therefore most likely smaller, as well. Furthermore, the

induced angle of attack is affected by the mesh refinement. The local flow conditions are therefore not even identical on the different meshes of the three-dimensional case. Both effects influence the impact of increased flow velocities along the surface due to less artificial dissipation and therefore lead to an altered sensitivity of the local lift in the outboard region with respect to the mesh cell sizes.

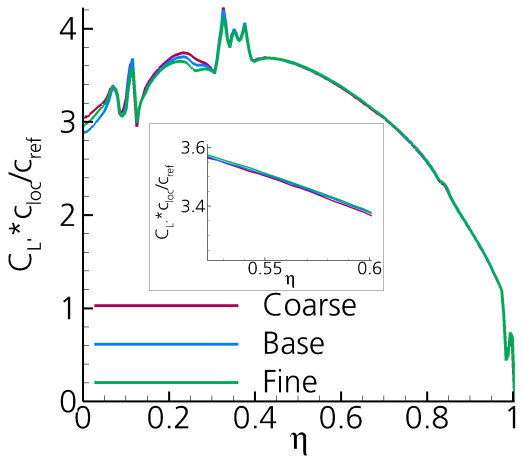

Figure 4.2: Influence of mesh resolution on main wing's lift distribution

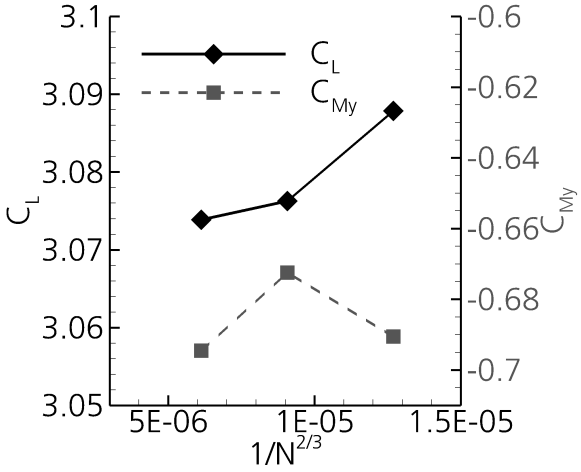

Figure 4.3: Longitudinal force and moment coefficients depending on mesh resolution

The largest influence on the lift distribution can be observed at the inboard side of the nacelle. Here, the local lift decreases with increasing mesh resolution. The reason behind this behavior is the inner nacelle vortex, which becomes stronger with increasing mesh resolution due to lower artificial dissipation. The nacelle vortex causes a decrease in the local lift. The phenomenon of the inner nacelle vortex is further investigated and explained in Section 5.1.1 (see Figure 5.3). Figure 4.3 depicts the global lift and pitching moment coefficients over the number of mesh points to the power of $-2/3$.[2] It demonstrates that the lift coefficient continuously decreases with increasing mesh resolution due to the influence of the inner nacelle vortex. However, the curve does not have a constant gradient.[3] The lift coefficient ranges between $3.074 \leq C_L \leq 3.088$, which is a variation of 0.5% of the lift coefficient of the base mesh. The pitching moment coefficient does not show a clear trend. It ranges between $-0.695 \leq C_{My} \leq -0.672$, resulting in a

[2] In theory, the discretization errors of a second-order discretization scheme applied to a three-dimensional mesh behave proportional to $N^{-2/3}$. The illustration of global coefficients and their errors with respect to $N^{-2/3}$ should therefore yield straight lines.

[3] The reasons for the non-linear behavior are manifold. As known from the two-dimensional test case, the discretization errors of the global coefficients do not scale with the cell length to the power of two. Moreover, the self-similarity of the meshes is flawed due to the chosen meshing approach. Additional effects such as flow separation, and thus convergence behavior as well as numerical modeling approaches are also known to impact the grid convergence behavior.

variation of 3.4% of the pitching moment coefficient of the base mesh. For comparison, the lift and the pitching moment coefficient of the wing-body model range between $2.45 < C_L < 3.45$ and $-0.73 < C_{My} < -0.35$, respectively. Consequently, the differences due to grid resolution equate to $\frac{\Delta C_{L,GR}}{\Delta C_{L,Range}} = 1.4\%$ and $\frac{\Delta C_{My,GR}}{\Delta C_{My,Range}} = 6\%$ of the lift coefficient and pitching moment coefficient ranges, respectively.

Since the investigation of wake-tail interference effects is an essential part of the study, the meshing influence on the flow conditions at the tail shall be discussed, as well. Figure 4.4 plots the local downwash[4] angle along the HTP's quarter chord line. The local downwash does not show a clear trend, either. The differences between the meshes are rather small with a maximum variation of $\Delta\epsilon_{max} = 0.15°$ or 1.5% of the maximum downwash at $\alpha = 0°$.

The mesh resolution was also investigated regarding its influence on the slipstream evolution. Figure 4.5 compares the slipstream for the different meshes in a X-cutting plane at the HTP position in terms of total pressure iso-lines. Even though small differences exist, the shape and size of the slipstream is very similar at the aircraft's tail. In particular, the total pressure iso-lines of the base mesh do not show any significant differences to the ones of the fine mesh. The resolution of the base mesh is therefore thought to be appropriate for the analysis of the wake flow.

The results of the meshing studies lead to the conclusion that the base mesh has a sufficient resolution for the purpose of the investigation and is therefore selected for the simulations.

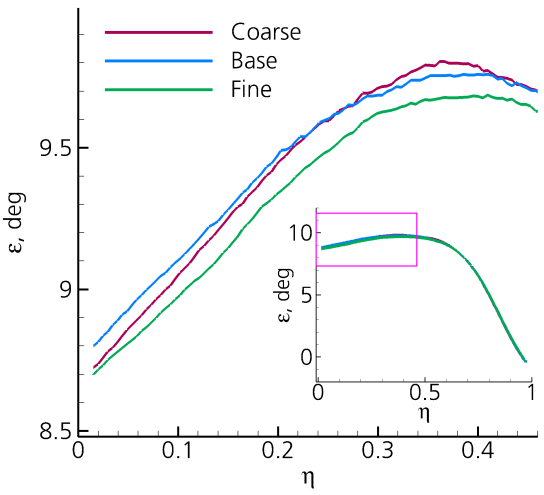

Figure 4.4: Influence of mesh resolution on local downwash at HTP position

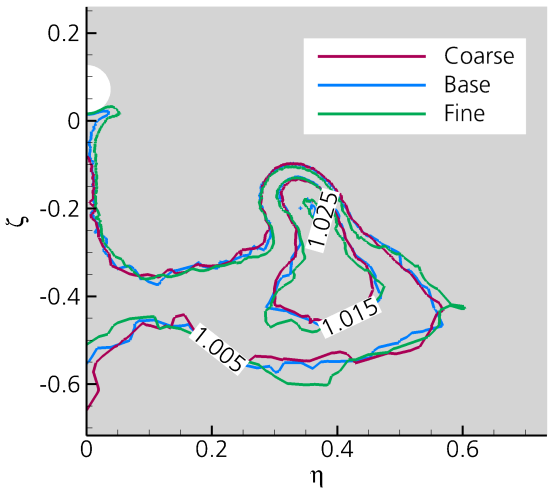

Figure 4.5: Influence of mesh resolution on slipstream in terms of total pressure contours at HTP position

[4]Flow induced by the aircraft and its wake phenomena in downward direction

4.3 Turbulence Modeling

Due to the use of circulation control, attached flow on highly deflected surfaces is an important flow feature. As Shur et al. point out, turbulent shear flows are strongly altered by system rotation and/or streamline curvature [84]. Therefore, rotation and curvature (RC) corrections are expected to have a favorable effect on the simulation of cases with circulation control. Swanson et al. demontrated the importance of including curvature effects when computing CC airfoil flows for a CC wing section with round trailing edge [44]. Further comparisons of SA variations and other RANS turbulence models for the simulation of circulation control airfoils, with experiments by Pfingsten et al. on the identical test case, and by Allan et al. on a similar test case, confirm these findings [47, 106]. Pfingsten et al. demonstrated a notable improvement of boundary layer velocity profiles along the round trailing edge of the investigated CC airfoil and the resulting impact on surface pressure distributions due to the application of rotation and curvature corrections to the SA model. Allan et al.'s comparison of turbulence models with a wind tunnel experiment also showed an improvement in surface pressure distributions and lift coefficients due to the use of RC. As already seen in other studies, those cases with high blowing rates are particularly challenging. Allan et al. were able to reduce the difference in lift coefficients between experiment and simulation from 70% to 46% for a blowing rate as high as $C_\mu = 0.115$ due to the use of RC [106].

Since vortices play an important role in the underlying investigation, their proper reproduction is another key aspect for accurate results. Many studies have shown that the turbulence model has a significant impact on this matter. A well known flaw of the SA turbulence model is the overproduction of eddy viscosity in the vortex core as discussed in Section 3.2.1. This overproduction of eddy viscosity leads to a faster dissipation of the vortex. The rotational correction is thought to improve this behavior, as was shown by Nichols and Churchfield et al. [107, 108]. They examined the behavior of a wing tip vortex simulated with different turbulence models and compared it to experimental results. On sufficiently resolved grids, the vortex centerline static pressure was predicted to be within 9.4% of that of the experiment by the use of SA-RC [108]. The centerline axial velocity differed only 0.6% from the one measured in the the experiment [108]. Furthermore, the core radius remained nearly unchanged along the vortex path and therefore resembles the behavior seen in the experiment more closely than the other investigated turbulence models [108].

The interaction of vortices with circulation control is one of the most important flow features the present 3D configuration shows compared to less complex circulation control configurations, as it impacts the stall behavior of the investigated configuration in several ways. No documented studies were found on this particular phenomenon. However, it is known that adverse pressure gradients promote vortex breakdown, as was demonstrated by means of a diverging duct by Sarpkaya [109]. Due to circulation control and the resulting large achievable circulation, the main wing features very high adverse pressure gradients as well as various trailing vortices. When it comes to RANS simulations of these

type of flow features, it is expected that mesh resolution and turbulence modeling have a significant impact, as vortices are accompanied by large velocity gradients. The influence of mesh resolution on a vortex interacting with circulation control was already presented in Section 4.2. In order to get a more detailed picture of the meshing influence and of the influence of turbulence modeling on the particular phenomenon, a preliminary study on vortex-circulation control interaction was perfomed on a simplified test case (Figure 4.6). The test case consisted of a rectangular wing with a representative airfoil section of the investigated aircraft's landing configuration. Symmetry plane boundary conditions were applied on both sides of the wing. A rectangular wing based on a NACA0012 airfoil section with an aspect ration of $AR = 5$ was positioned ahead of the wing at a distance of one chord length. The wing had half the spanwidth of the one located further downstream and is attached to the symmetry plane on the starboard side. In an effort to isolate and focus on the influence of the turbulence model, a fully structured mesh was used. In addition, the meshing influence was examined for the use of an unstructured mesh which is representative of the meshes used for the present aircaft simulations in terms of topology and resolution.

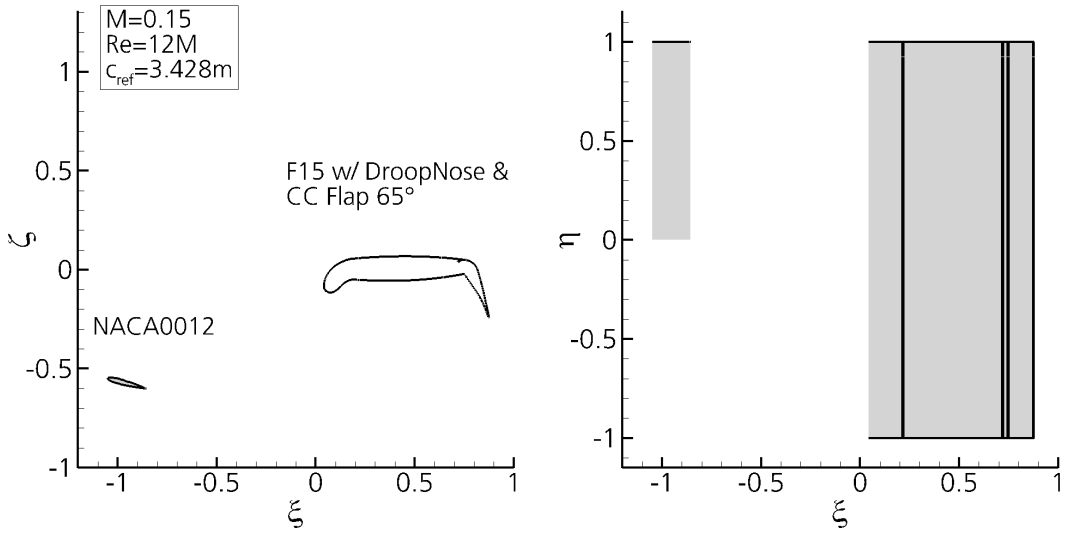

Figure 4.6: Testcase geometry

Figure 4.7 depicts the computed flow topology of the test case in terms of total pressure loss and surface pressure distribution. The front wing induces a wing tip vortex, which travels along the upper surface of the main wing, as seen by the total pressure loss within the vortex core. Above the flap, vortex bursting occurs due to the adverse pressure gradient, which results from the pressure recovery at the flap trailing edge.

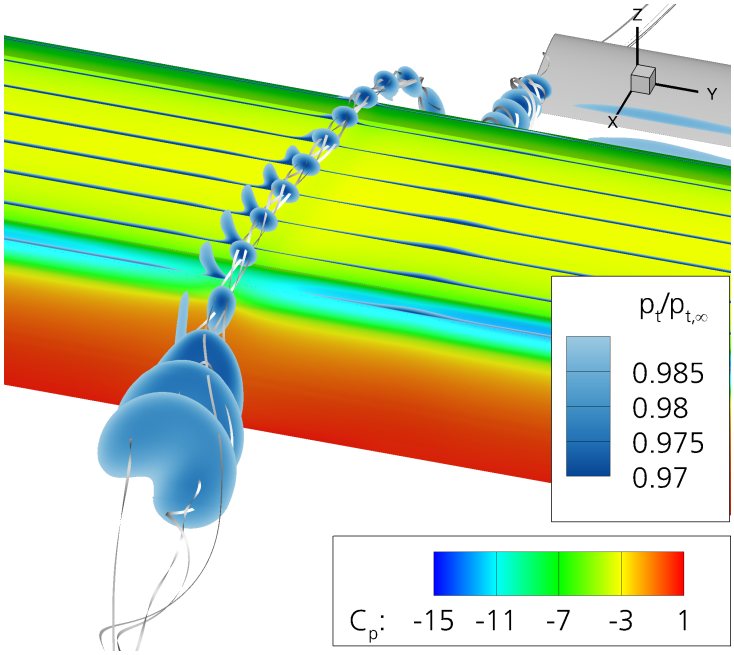

Figure 4.7: Flow topology (SA-RC), as viewed looking upstream from a location aft of the flap trailing edge

Figure 4.8 compares the influence of the turbulence model and mesh type on the total pressure loss near the main wing's upper surface at $\xi = 0.72$ in the vicinity of the vortex. In the case of the SA model (Figure 4.8(a)), the total pressure loss is strongly smeared out and the actual vortex core cannot be identified. At the lower left side of the expected vortex core position, a region with particularly high total pressure losses can be identified. In the case of SA with rotational correction, the vortex appears to be resolved better (Figure 4.8(b)). Two destinct regions of large total pressure losses can be identified. The first one is directly caused by the high shear stresses within the core. The second one is located on the lower left side of the vortex core. The induced velocities from the vortex cause low momentum fluid from the boundary layer below the vortex core to be transported to the upwash side, where it leads to an increased region of total pressure losses. Similar to the case without rotational correction, the highest total pressure losses can be found at this position. The SSG-LRR turbulence model leads to a similar total pressure loss distribution as the SA model with rotational correction (Figure 4.8(c)). However, the losses at the upwash side are spread along the surface and are not transported as far away from the surface. Within the vortex core, the losses are slightly higher than in the case of SA-RC. Furthermore, the vortex core is located closer to the surface. Figure 4.8(d) plots the total pressure losses in the case of SA-RC on the unstructed grid. As expected, the vortex core is less well-resolved than it is on the structured mesh. The vortex core is flattened and the losses seem more smeared. However, the two distinct regions of total pressure losses are still visible with the highest losses close to the surface at the upwash side of the vortex core.

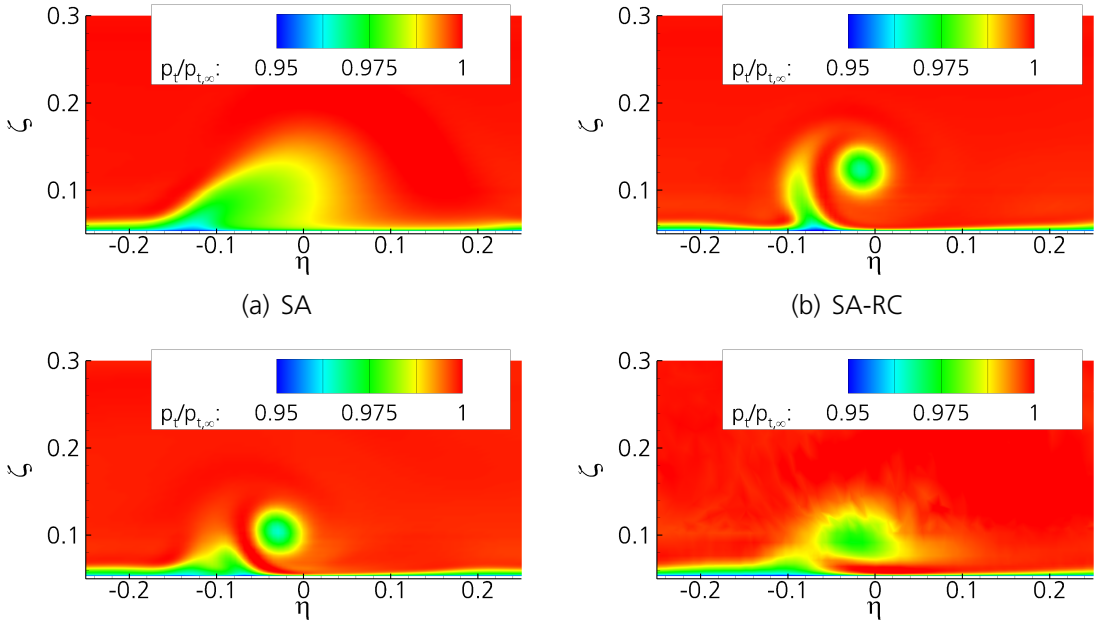

(a) SA (b) SA-RC

(c) SSG-LRR (d) SA-RC (Unstructured mesh)

Figure 4.8: Total pressure loss due to vortex within main wing boundary layer at $\xi = 0.72$ (looking upstream)

In order to judge the impact of the vortex on the high-lift performance, Figure 4.9 compares the flap suction peak distribution for the different cases. All cases show a significant increase in pressure in the region of the vortex. However, the quantity and position varies for the different cases. The SA model delivers the largest surface pressure increase. If the suction peak level at the symmetry wall at $\eta = -1$ is assumed to be the ideal suction peak, which can be achieved without disturbance, the influence of the vortex leads to a reduction of the suction peak by 63%. The region most strongly affected by the vortical flow is located at the position of the maximum total pressure loss, as can be seen in Figure 4.8(a). In the case of the SSG-LRR model, the suction peak is reduced by 44%. Compared to the SA case, it is shifted in positive spanwise direction, as is also the case for the maximum total pressure loss. Additionally, a kink can be observed in the flap suction peak distribution at $-0.05 < \eta < 0$. Thus, the kink is located at the position of the vortex core and reflects its negative impact on the flap suction peak. The SA-RC model results in the smallest reduction of the suction peak level due to the vortex interaction. On the structured grid, the reduction amounts to 24% of the ideal value. On the unstructed mesh, this value is slightly lower with 17%. Again, the locations of the surface pressure peaks correlate with the positions of the maximum total pressure losses within the boundary layer.

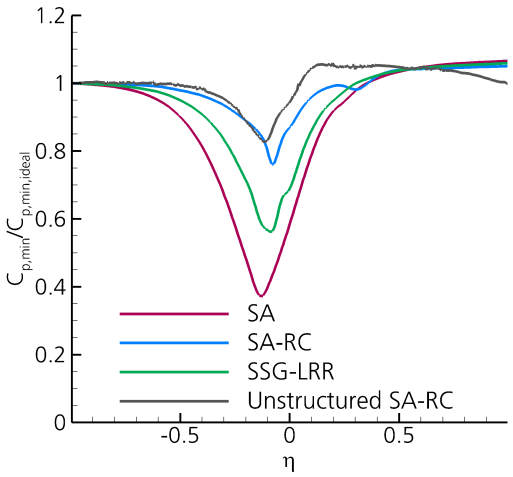

Figure 4.9: Influence of vortex-circulation control interaction on flap suction peak

It can be concluded that all investigated turbulence models predict a significant effect of the vortex on the flap suction peak. The negative effect is more directly caused by the pile up of low momentum fluid from the boundary layer due to the vortex sidewash than by the vortex core and its inherent instability. The resulting local velocity deficit within the main element's wake increases the velocity gradient between the jet and the wake and thus increases the shear stresses. As a result, the momentum transfer to the wake is raised, causing a reduction in the jet momentum, and in turn a local static pressure increase on the surface. The strength of the effect is highly dependent on the turbulence model and varies strongly. The SA-RC turbulence model, which is used in this thesis, is showing the least influence especially on the mesh type used for the complex cases. Consequently, it is anticipated that the interaction effects, seen in the aircraft simulations, might rather be underpredicted than overpredicted.

4.4 Simulation of Propeller Effects

As a more efficient alternative to resolving the rotation of every single propeller blade with transient simulations, the effects of the propeller can be modeled via actuator disk, as described in Section 3.2.3. The actuator disk does not account for transient phenomena such as blade tip vortices and other time-dependent circumferential inhomogeneities. However, the time-averaged forces, which act on the flow due to the propellers, are represented quite well by this approach as various test cases show. Marquez et al. compared actuator disk simulations for an isolated and semi-installed contra-rotating open rotor with unsteady simulations, which fully resolved the propellers' motion [110]. The isolated test case showed deviations of 1.5% and 6.69% in the thrust coefficients of the front and aft rotor, respectively. The same accuracy was observed for the wake velocity profiles [110].

A test case more similar to the present study was investigated by Lenfers et al. [111]. They compared RANS simulations of a wing section with plain flap, circulation control,

and wing mounted propeller with wind tunnel experiments. The investigated wing section was also based on the F15 airfoil with a flap length of $c_f = 0.25 c_{Ref}$ and a deflection of $\delta_f = 65°$, which is similar to the high-lift configuration under investigation here. Furthermore, the numerical set-up was closely related to the set-up used in the current study. Their results showed very good aggreement with the data from their wind tunnel experiment, in particular in terms of surface pressure distributions behind the propeller [111]. Based on the results from these studies, it is expected that the actuator disk approach can generally reproduce the flow phenomena that are most important for the investigation of the aircraft's aerodynamic properties and that this approach is therefore suitable for the present study.

Actuator Disk Approach for Grids in Motion

For the estimation of the dynamic behavior, moving grids have to be used. However, the original formulation of the actuator disk boundary condition in the TAU code does not consider moving grids. In order to allow for the use of moving grids, two functions of the boundary condition were modified in the course of this thesis. The first one relates to the computation of the inflow angle α_i (Equation 3.37), where the relative velocity components $v_{n(r_b,\Theta)}$ and $v_{t(r_b,\Theta)}$ now include the local grid velocity λ_b. The second one evaluates the conservative variables at the actuator disk exit based on the conservation laws of momentum and energy, considering the actuator disk's force and work, respectively. Again, the inflow and exit velocity components at the actuator disk boundary condition now include the local grid velocity λ_b. The new implementation developed in the context of the present investigation was verified on an isolated actuator disk with blade parameters identical to the ones used for the investigation of the full aircraft. In order to increase the effect of the freestream velocity, the freestream Mach number was $M_\infty = 0.5$ in the test case as opposed to $M_\infty = 0.15$ in the main study. The test case was first simulated with a farfield Mach number of $M_{FF} = 0.5$ and no grid motion. Then, the case was simulated with $M_{FF} = 0$ at the farfield, while moving the grid at a Mach number of $M_b = 0.5$. The angle of attack in the testcase was set to $20°$ and thus higher than any angle of attack simulated with the motion module in the main study. Analogous to the Mach number, the angle of attack was introduced via farfield boundary condition in the case without grid motion. In the case with moving grid, the angle of attack was given via motion module.

Figure 4.10 compares the streamwise velocity u at a distance of one propeller radius behind the actuator disk for the case without motion, the case with motion and original actuator disk implementation, and the case with motion and modified actuator disk implementation. The distribution of the relative velocity u_{rel} in the case with motion and the original actuator disk formulation (Figure 4.10(b)) thereby strongly differs from the velocity distribution in the case without motion (Figure 4.10(a)) in terms of velocity magnitude. In contrast, the relative velocity distribution of the case with motion and the modified actuator disk formulation is identical to the velocity distribution of the case without motion.
The same trend can be observed for the distributions of the lateral velocity v, as seen in Figure 4.11. The spanwise velocity distribution of the case with grid motion and origi-

nal actuator disk formulation (Figure 4.11(b)) differs significantly from the one without motion. In contrast, the spanwise velocity distribution of the case with grid motion and modified actuator disk formulation (Figure 4.11(c)) is identical with the one of the case without motion (Figure 4.11(a)). The resulting thrust in the case with grid motion and modified actuator disk is also identical to the one in the case without motion. It can therefore be concluded that the reformulation of the actuator disk boundary condition will allow the use of moving grids.

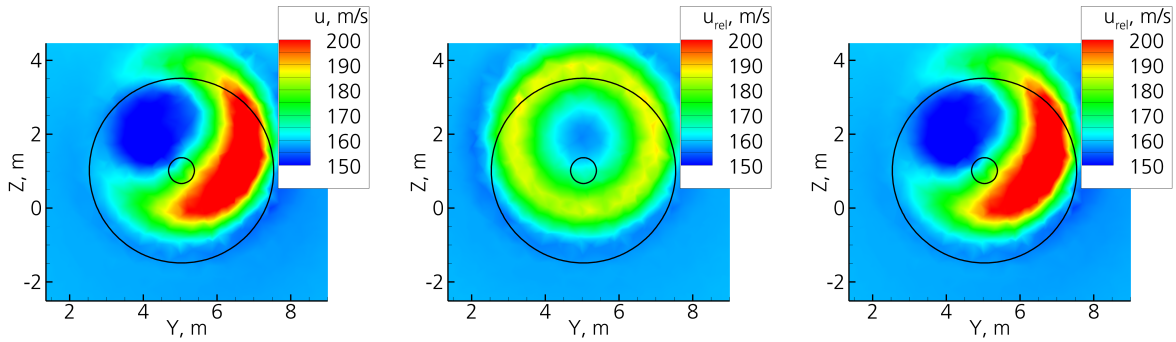

(a) without motion

(b) with motion (original actuator disk implementation)

(c) with motion (modified actuator disk implementation)

Figure 4.10: Streamwise velocity distribution in a X-cutting-plane at $X/r = 1$ downstream of the actuator disk

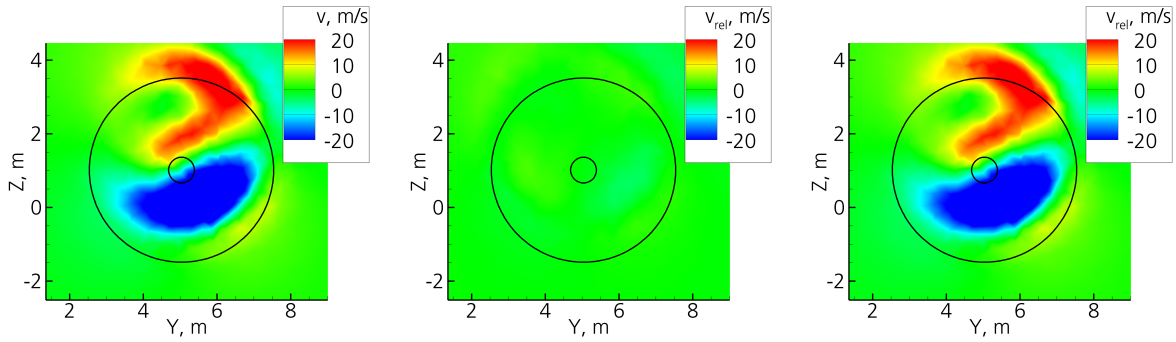

(a) without motion

(b) with motion (original actuator disk implementation)

(c) with motion (modified actuator disk implementation)

Figure 4.11: Spanwise velocity distribution in a X-cutting-plane at $X/r = 1$ downstream of the actuator disk

5 Results

This chapter presents the results on the aerodynamic behavior and its impact on the aircraft stability of the CRC 880's REF2-2013(S) landing configuration. The chapter is divided into results discussing the longitudinal motion and results concerning the lateral motion. Both sections are structured similarly. They begin with a study of the influence of circulation control and the propeller(s) on the flowfield, pressure distribution, and resulting forces. Aerodynamic phenomena, which are crucial for understanding the static and dynamic behavior of the entire aircraft, are thereby illustrated. Subsequently, their implications on the aircraft's moments balance and its static and dynamic stability will be discussed. The underlying boundary conditions for the simulations are summarized in Table 5.1. All simulations that are discussed in this chapter have been performed with the SARC turbulence model.

Case	$C_\mu = 0.0$ prop(s) off	$C_\mu = 0.03$ prop(s) off	$C_\mu = 0.03$ prop(s) on
Mach number M_∞	0.15	0.15	0.15
Reynolds number Re_∞	$11.97 * 10^6$	$11.97 * 10^6$	$11.97 * 10^6$
Jet momentum coefficient C_μ	0.0	0.03	0.03
Propeller thrust coefficient C_T	-	-	0.53
Propeller rotational speed	-	-	$975\,RPM$

Table 5.1: Simulation boundary conditions

5.1 Longitudinal Motion

The aerodynamic behavior in longitudinal motion is examined based on the REF2-2013(S) configuration. The first section illustrates the influence of circulation control and propeller effects[1] on the lift generation and stall behavior of the wing-body configuration. Changes in the main wing's lift distribution alter the main wing's wake and eventually affect the flow development downstream. Since changes in the flow conditions at the HTP can have a notable impact on its pitching moment contribution, the relevant flowfield characteristics at the position of the HTP are analyzed. Drawing on these discussions, the pitching

[1] In the cases with the propeller on, the propeller rotates symmetrically inboard up.

moment balance and the static longitudinal stability are examined based on the contributions from the wing-body and the HTP. Finally, the chapter gives a short summary of the dynamic longitudinal behavior.[2]

5.1.1 Lift Generation and Stall Mechanism of the Wing-Body

The first question, which is being addressed, is how circulation control, the propeller, and their configurational implementations affect lift generation in longitudinal motion and stall behavior of the main wing. For this purpose, the high-lift capabilities of the landing configuration were investigated in three consecutive steps. First, the wing-body half-model was simulated without engine in order to assess the influence of circulation control on the aerodynamic behavior of the main wing. The behavior without engine has been the subject of previous investigations [2, 5],[112] and is not discussed here. In a second step, the engine was integrated with the propeller being off. In doing so, effects related to the geometric change due to the engine integration could be analyzed. In a third step, the propeller was added in order to investigate the propeller's slipstream effect in conjunction with circulation control. The following sections illustrate the influence of circulation control and the propeller – i.e. the resulting propeller slipstream and the forces on the propeller – on the force generation and stall mechanism based on the wing-body configuration with engine.

Influence of Circulation Control

The main effects of circulation control can be demonstrated by comparing the pressure coefficient distribution and the directivity of the resulting surface pressure forces of a representative two-dimensional airfoil for the cases without and with circulation control at a constant angle of attack. It has to be kept in mind, however, that the local angle of attack of the wing-body configuration strongly varies along the span due to the wing twist and the induced angle of attack. More importantly, it also differs between the case without circulation control and the case with circulation control. Figure 5.1 compares the pressure coefficient distribution at $\alpha = 0°$, which is thought to be representative for the selected flow conditions and reflects the basic trends. The magnitude and effective direction of the local surface pressure coefficient are represented by the length and orientation of the thin arrows, beginning at the surface. Without circulation control, the pressure coefficient distribution is rather flat except for the droop nose, as depicted by the gray arrows. Here, the load is slightly increased due to the convex shape and the position of the stagnation point. The position is indicated by the arrow of maximum length that is directed inwards. On the flap's upper surface, the arrow length is constant for the most part, indicating the existing flow separation and lack of pressure recovery.
With circulation control, the load significantly increases over the entire upper surface, as displayed by the blue arrows. The flow is fully attached to the flap, which leads to the

[2] Parts of the results in sections 5.1.1, 5.1.3, and 5.1.4 have already been published in [3, 4].

strong load increase at the flap knuckle. Analysis reveals that the stagnation point at the leading edge is moved towards the rear, adding additional load along the upper side of the droop nose. The increased load is also reflected by the position and the magnitude of the force vectors of the droop nose (orange), main element (green), and flap sections (purple), which are illustrated by the thick arrows. All three force vectors strongly increase in magnitude as compared to the case without circulation control. The origin of the main element's force vector, which contributes the largest share to the lift, is only slightly shifted towards the rear, whereas the origins of the other two force vectors are notably shifted towards the front. As a result, the center of pressure at $\alpha = 0°$ is located at $\xi = 0.452$ in both cases, and thus is almost unchanged by circulation control.

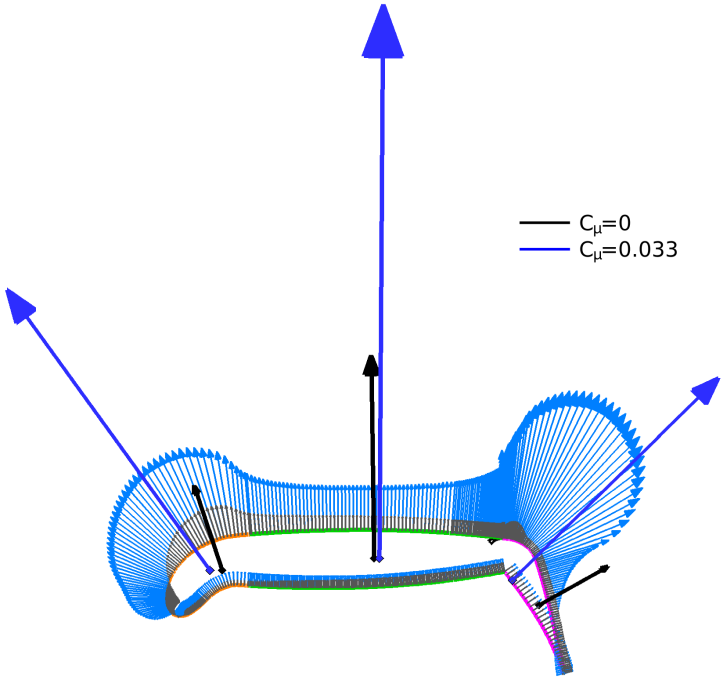

Figure 5.1: Comparison of the pressure coefficient and force distribution between airfoil without and with circulation control at $\alpha = 0°$

After illustrating the basic influence of circulation control on an airfoil, its impact on the lift generation of the wing-body configuration is discussed. The influence on the aerodynamic behavior in the linear range is demonstrated by comparing the case with no circulation control to the case with circulation control at the reference angle of attack of $\alpha = 6°$. Figure 5.2 depicts the contour of the surface pressure coefficient and skin friction lines of the main wing in the region of the nacelle with no circulation control and the propeller off at $\alpha = 6°$. The aircraft's behavior in longitudinal motion at the chosen angle of attack is representative for its behavior in the linear region of its lift curve. Furthermore, total pressure losses are visualized in various X-cutting planes above the main wing. The skin friction lines indicate that the flow is fully separated from the flap. The surface

pressure coefficient is homogeneously distributed on the flap's upper surface ($C_p \approx -0.5$), without showing a distinct flap suction peak. Due to the large flap deflection in landing configuration, the high wing camber and the resulting adverse pressure gradient above the flap are too large for the flow to remain attached, even at low angles of attack. The flow therefore detaches from the upper side at the flap knuckle. Since the flow does not follow the flap contour, the effective camber of the wing is low. This, in turn, leads to rather high surface pressures and low suction peaks, as the surface pressure contour reveals. The streamlines indicate rotational flow on both sides of the nacelle, which cause total pressure losses above the main wing to increase slightly, as demonstrated by the X-cutting planes. The rotational flow can be attributed to the nacelle, which acts as a lifting body for local angles of attack greater than zero. As a result, tip vortices emanate from both sides of the nacelle.

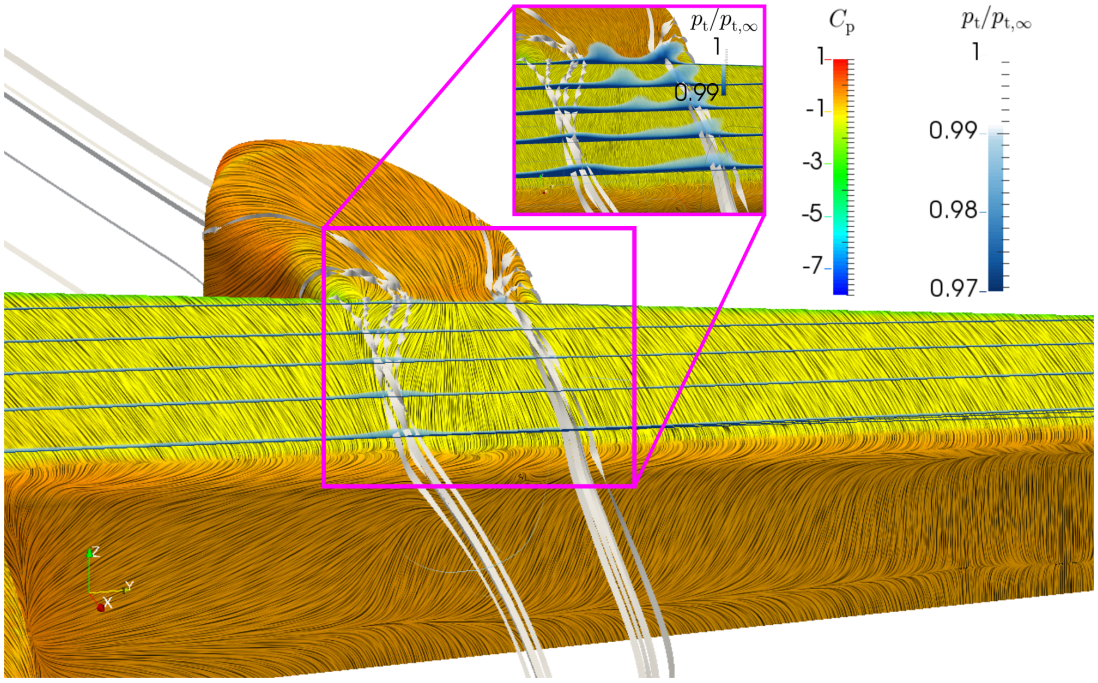

Figure 5.2: Surface pressure distribution, skin friction lines, and visualization of nacelle vortices by streamlines and total pressure loss at $C_\mu = 0$, $\alpha = 6°$

With circulation control, the flow is completely attached to the flap at a jet momentum coefficient of $C_\mu = 0.03$, as illustrated by the skin friction lines in Figure 5.3. The resulting increase in effective camber of the main wing is evidenced by a significantly increased flap suction peak and improved pressure recovery along the trailing edge flap, as indicated by the surface pressure distribution. The higher circulation causes stronger upwash in front of the main wing. As a consequence, the local (effective) angle of attack at the position of the nacelle is raised. This is illustrated by the skin friction lines on the inner side of the nacelle. Here, the skin friction lines are directed further upwards compared to the case without circulation control. Due to the increased local angle of attack, the pressure difference between the upper and lower side of the nacelle, and thus the strength of the

nacelle vortices is increased. The X-cutting planes indicate that the increased strength of the nacelle vortices causes higher total pressure losses along the vortex paths. Similarly to the vortex-circulation control interaction that was discussed in Section 4.3, the nacelle vortices locally reduce the effectiveness of the circulation control behind the nacelle, evidenced by a locally reduced flap suction peak. The jet as well as the main element's wake are, however, still attached to the flap as indicated by the skin friction lines and the streamlines.

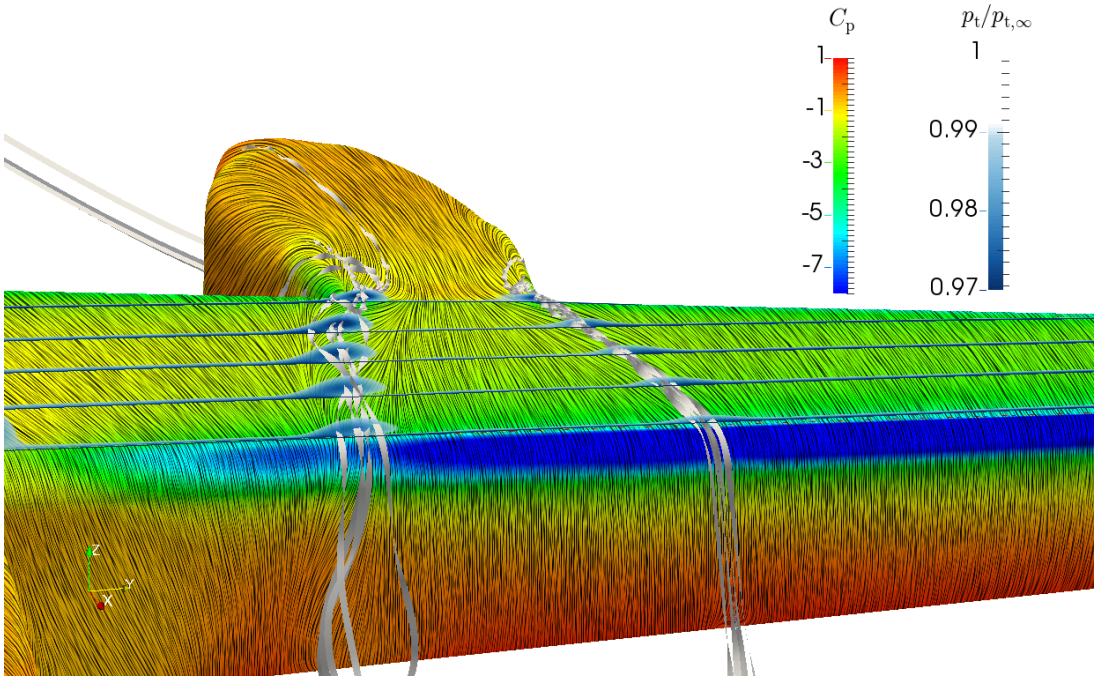

Figure 5.3: Visualization of nacelle vortices by streamlines and total pressure loss at $C_\mu = 0.03$, $\alpha = 6°$

The nacelle vortices evidently have a notable impact on the surface pressure distribution of the main wing. The evolution of the nacelle vortices with an increase in the angle of attack is therefore studied in more detail. Figure 5.4 shows the evolution of the nacelle vortices at $\alpha = 10°$. Compared to $\alpha = 6°$, the X-cutting planes indicate higher total pressure losses within the nacelle vortex cores. The increased total pressure losses point to an increased strength of the vortices, which can be attributed to the higher angle of attack. The visualization of the total pressure losses along the inner nacelle vortex also demonstrates the two distinct regions of strong losses caused by a vortex in the vicinity of a boundary layer (see Figure 4.8(b)). The first region of high total pressure losses is located slightly above the surface and is directly caused by the nacelle vortex. The second region is located to the lower left side of the first region and is originated by the sidewash of the vortex in conjunction with the boundary layer (see Section 4.3). As a result, a wide area of reduced flap suction peak can be observed in the region of the inner nacelle vortex. Additionally, the increased total pressure losses within the vortex core cause vortex bursting above the flap, as indicated by the vortex core streamlines. The accompanied

separation of the outer flow from the jet above the flap results in a further reduction of the local flap suction peak. It shall be noted that the blowing jet remains attached to the flap despite vortex bursting and despite the resulting detachment of the main element's wake, as evidenced by the skin friction lines in Figure 5.4.

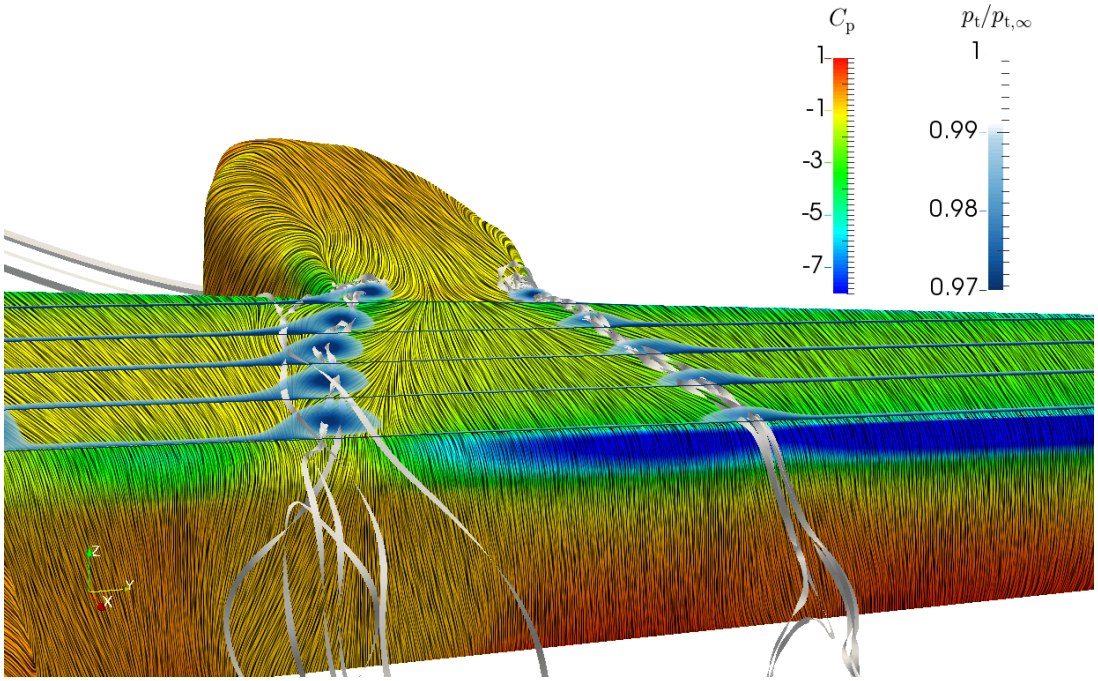

Figure 5.4: Visualization of nacelle vortices by streamlines and total pressure loss at $C_\mu = 0.03$, $\alpha = 10°$

Figure 5.5 provides a more detailed picture of the nacelle vortices' influence on the flap suction peak and its correlation with the lift distribution in the case with circulation control. The top graph shows the spanwise distribution of the suction peak – i.e. the smallest pressure coefficient value – of the trailing edge devices for various angles of attack. The bottom graph depicts the main wing lift distribution (including fuselage and nacelle). At $\alpha = 0°$ (black line), the flap suction peak distribution shows a rather monotonous increase from an inboard to the mid-span position ($\eta \approx 0.7$). Further outboard, the suction peak decreases as the flap ends and the less deflected aileron begins. At $\eta \approx 0.3$, the distribution shows a small dip caused by the influence of the nacelle vortices. The lift distribution at $\alpha = 0°$ (black line) steadily increases from the center of the fuselage to the position of the nacelle, which is indicated by two peaks. These peaks arise due to the flow around the round edges along the upper side of the nacelle. The turning of the flow leads to local flow acceleration and, consequently, to increased lift. At $\alpha = 6°$ (blue line), the flap suction peak at the outer and mid span ($0.5 \lesssim \eta \lesssim 0.85$) is almost unchanged compared to the one at $\alpha = 0°$. In the inboard region between $0.1 \lesssim \eta \lesssim 0.5$, the flap suction peak decreases. At $\eta \approx 0.25$ and $\eta \approx 0.4$, the suction peak is notably reduced, indicating the position of the nacelle vortices. The lift distribution at $\alpha = 6°$ shows locally higher values across the span than at $\alpha = 0°$. However, it does show a minor drop at

the position of the inner nacelle vortex. At $\alpha = 10°$ (red line), the local reduction of the flap suction peak due to the nacelle vortices is significantly amplified. Furthermore, the reduction affects regions even further outboard. At $\alpha = 10°$, the local loss of flap load is also clearly evidenced by the lift distribution, which is reduced in proximity to the engine. The region inboard of the nacelle is particularly affected, whereas the lift is still rising in the outer part of the wing. It can be concluded that the nacelle vortices significantly impact the evolution of the flap suction peak, and thus the lift distribution with rising angle of attack. Moreover, the influence of the nacelle vortices is not limited to the two locations where they directly interact with the circulation control system. The vortices also affect the flap suction peak in their proximity. As a result, the lift generation of the main wing is limited. Even though conditions with zero thrust might not be common during flight operations, they are still relevant in terms of safety aspects regarding the one engine inoperative case. Additional studies indicate that the adverse effect of nacelle vortices can be successfully reduced by nacelle strakes [4].

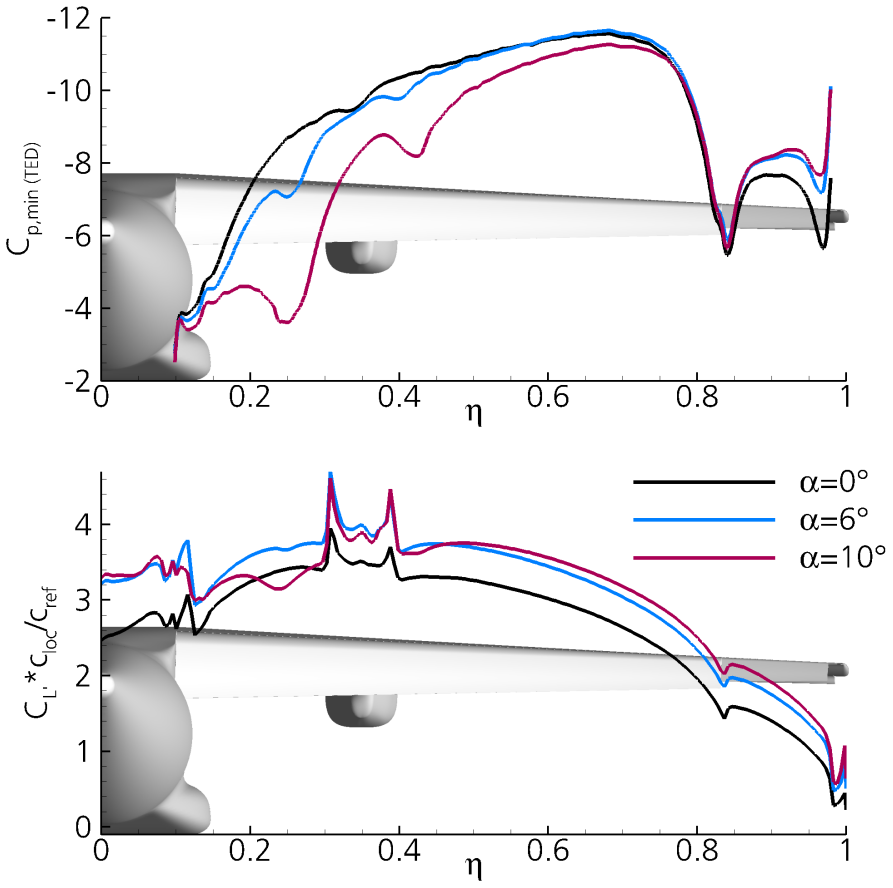

Figure 5.5: Distribution of minimum pressure coefficient along the trailing edge devices and lift distribution of the full wing for various angles of attack at $C_\mu = 0.03$

Even though, the nacelle vortices significantly reduce the local lift generation at $\alpha = 10°$, the lift of a large part of the main wing still increases with rising angle of attack up to $\alpha = 20°$. Figure 5.6 depicts the surface pressure distribution and skin friction lines at

$\alpha = 21°$. The skin friction lines indicate a leading edge flow separation across the entire inboard section. As a result, the leading edge suction peak is strongly reduced in the inboard section. On the flap, the skin friction lines indicate fully attached flow. However, the surface pressure is almost constant in the entire inboard region, neither showing a meaningful flap suction peak, nor pressure recovery at the trailing edge.

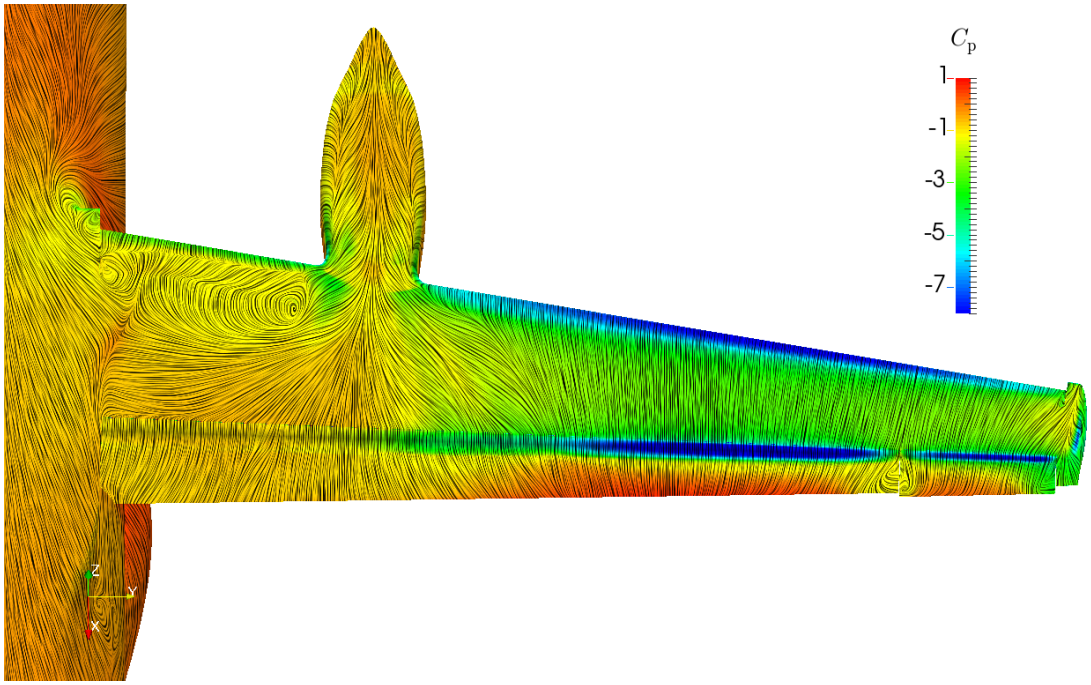

Figure 5.6: Pressure coefficient distribution and skin friction lines on the main wing at post stall with circulation control ($C_\mu = 0.03$, $\alpha = 21°$)

Figure 5.7 demonstrates the influence of circulation control on the lift coefficient with respect to the angle of attack for the wing-body model of the landing configuration. Furthermore, the influence of the nacelle integration is illustrated. The case without nacelle and without circulation control is represented by the green line. With circulation control (red line), the curve is shifted upwards due to the increase of the effective camber, leading to an increase in the maximum lift coefficient by $\Delta C_L = 1.35$. The maximum angle of attack is slightly raised by $\Delta\alpha = 1°$. The black and blue lines represent the lift curves of the wing-body configuration with nacelle for the cases without and with circulation control, respectively. While the integration of the nacelle has nearly no influence on the lift curve without circulation control, the impact is significant with circulation control. In the latter case, the lift is slightly reduced by $\Delta C_L = 0.04$ at low angles of attack ($\alpha \leq 6°$), with $C_{L\alpha}$ remaining unchanged. At $\alpha > 6°$, the influence of the nacelle and the accompanied vortices increases, leading to a reduction of α_{max} by 15° to $\alpha = 8°$ and a reduction of $C_{L,max}$ by 0.53 compared to the case without nacelle. Once, α_{max} is reached, the lift coefficient slightly degrades until $\alpha = 20°$, as the effect of the nacelle vortices overcompensates the lift increase at the outer main wing. Increasing the angle of attack further causes a lift breakdown due to the leading edge stall in the inboard region.

In summary, the investigation of the stall behavior of the landing configuration with the propeller off indicates a significant increase in the maximum lift coefficient due to the use of circulation control. This increase is adversely impacted by the integration of the engine nacelle due to the interaction of the nacelle vortices with the blowing jet of the circulation control. These results agree well with the observations made by Fink, who experienced "rough flow at the wing and nacelle junctures", which led to stall on a similar configuration [26]. A reduction of the nacelle size or counter measures such as the use of nacelle strakes can have a beneficial effect on the maximum lift coefficient, as demonstrated in a recent numerical study [4].

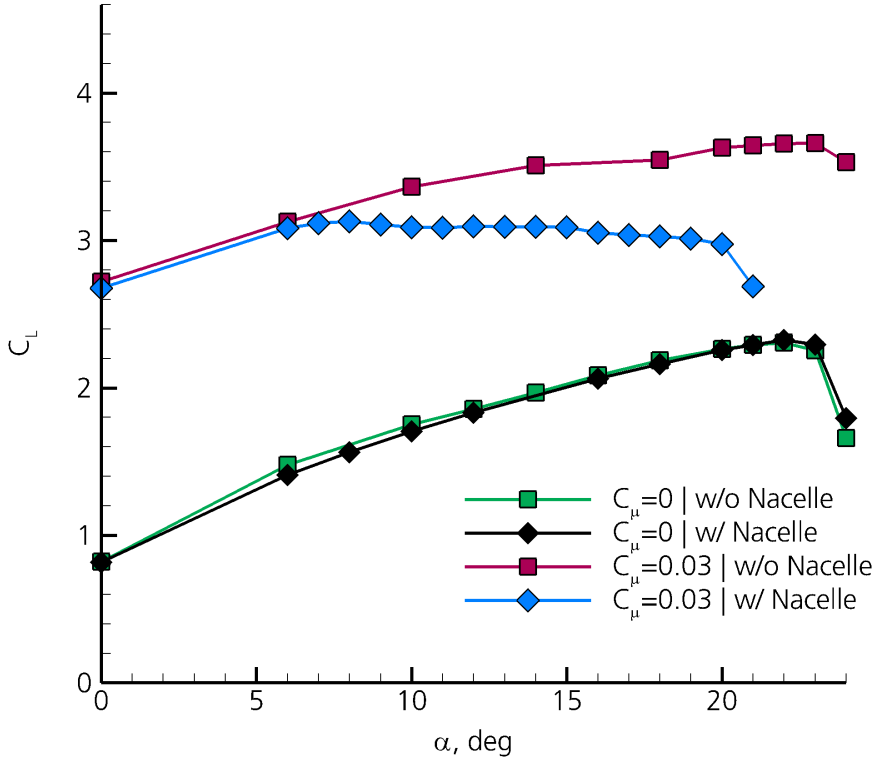

Figure 5.7: Impact of nacelle and circulation control on lift curve of wing-body configuration

Influence of the Propeller

According to Newton's third law of motion, the actuator disks have to exert forces on the fluid equal to thrust and tangential forces, when the engines are active.[3] The resulting slipstream has two main effects on the flowfield of the main wing downstream of the actuator disks. Firstly, the dynamic pressure within the flow is increased. Secondly, the local flow direction is altered due to the swirl. Both effects vary along the wing span since the force distribution of the actuator disk is calculated via blade element theory and

[3]Radial forces are assumed to be negligible and are not considered by the actuator disk model.

therefore depends on the local flow conditions and the radial distribution of the propeller blade characteristics [6].

Figure 5.8 illustrates the surface pressure distribution and nacelle vortex evolution at $\alpha = 6°$ for the case with circulation control and the propeller on. The skin friction lines reveal five different zones of flow behavior on the flap. In the wing root section, the skin friction lines indicate attached flow to the flap. However, the main element's wake is detached from the blowing jet, as is shown by the streamlines in this region. The flap suction peak is rather small, here. Inboard and outboard of the nacelle, flow separation can be observed on the flap. Between these two zones, a small region with attached flow exists. Despite the partial flap separation, the flap suction peak is significantly increased in the region behind the propeller as compared to the case with the propeller off. Outboard of the region with the propeller, the flow is fully attached, again.

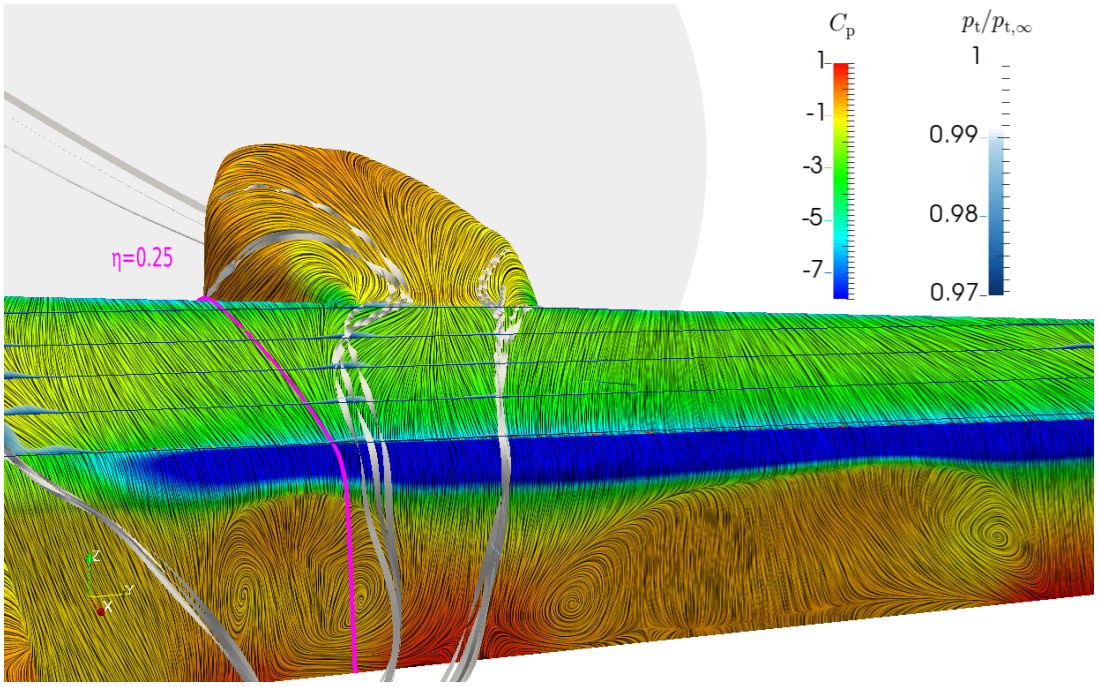

Figure 5.8: Visualization of nacelle vortices by streamlines and total pressure loss at $C_\mu = 0.03$, $\alpha = 6°$, and propeller on

Figure 5.9 depicts the influence of circulation control and the propeller on the pressure distribution in a spanwise section at $\eta = 0.25$, which is located in the propeller upwash region.[4] Compared to the case without circulation control (black line), the pressure coefficient with circulation control is considerably reduced across the entire upper surface except for the flap trailing edge (blue line). In particular, the flap suction peak is significantly increased. At the trailing edge, the pressure coefficient is slightly increased due to the pressure recovery caused by the attached flow. The stagnation point at the leading edge is slightly moved towards the rear due to the increased circulation. With the propeller

[4]The influence of propeller upwash and downwash on the pressure distribution is compared in [6].

on (red line), the surface pressure coefficient is further reduced along the upper surface. In particular, the suction peaks at the droop nose and the flap are notably increased. At the flap trailing edge, the pressure coefficient is reduced since the flap separation prevents pressure recovery. On the lower side, the deceleration of the slipstream causes an increase in the pressure coefficient. Particularly, the stagnation pressure at the leading and trailing edge is significantly increased. Furthermore, the leading edge stagnation point slightly moves towards the front, compared to the case with circulation control and the propeller off (blue line). The waviness of the pressure distribution on the lower side is caused by recirculation regions, as discussed in [6].

The higher velocities due to the propeller slipstream lead to an increase of the flap suction peak and stagnation pressure. The adverse pressure gradient above the flap is thereby raised. Since the jet momentum is not significantly changed by the slipstream, it no longer suffices to overcome the adverse pressure gradient and the flow separates from the flap as seen in Figure 5.8 and 5.9. The circulation control is operating in boundary layer control mode in this region. The lift can therefore be increased effectively, if the jet momentum is locally raised until the flow is fully attached to the flap again [6]. In other words, the boundary layer control regime, which is most efficient, is extended to higher lift coefficients.

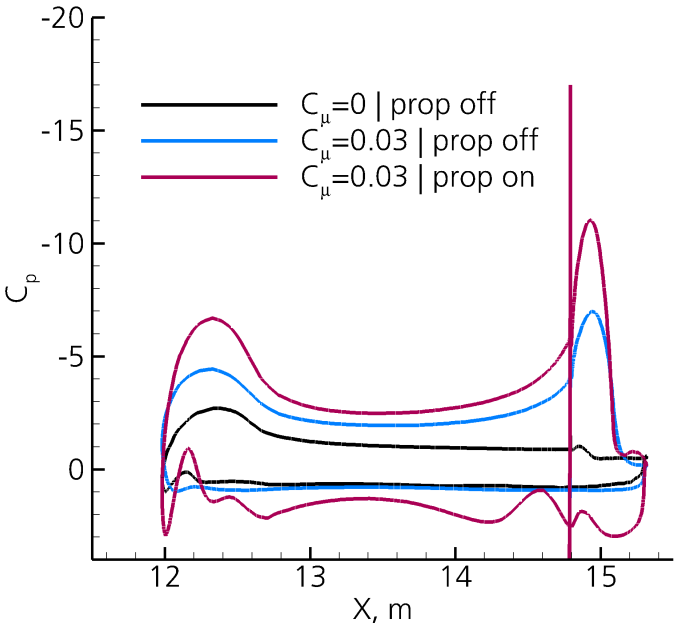

Figure 5.9: Influence of circulation control and the propeller on pressure coefficient distribution at $\eta = 0.25$, $\alpha = 6°$

Although nacelle vortices are indicated by the streamlines in Figure 5.8, the total pressure losses with respect to the freestream total pressure, which are illustrated by the X-cutting planes, are considerably reduced with the propeller on compared to the case without propeller. The additional dynamic pressure caused by the propeller slipstream counteracts the total pressure losses, here.

It is important to note that the flap separation caused by slipstream effects and the wake bursting due to vortex-circulation control interaction (as seen in Figure 5.4) are two different separation mechanisms. In the first case, the jet momentum is insufficient to compensate for the momentum losses within the main element's boundary layer and to overcome the adverse pressure gradient at the same time. As a result, the jet itself detaches from the flap. The main element's boundary layer is however rather thin and the momentum losses are moderate. This means that flap separation can be avoided by increasing the blowing rate. In the second case, the momentum losses within the main element's boundary layer are high. Furthermore, losses also occur at a larger distance to the surface due to the influence of the vortex. For this reason, the jet is unable to transfer sufficient momentum to the regions in deficit, and the remaining velocity deficit in the wake causes wake bursting. Due to the limitations regarding momentum transfer and the location of the momentum deficit in higher layers, this type of separation cannot be avoided by increased blowing as easily as in the first case. The two types of separation are analogous to the different separation mechanisms of circulation controlled airfoils, as discussed by Burnazzi [113].

Figure 5.10 illustrates the influence of circulation control and the propeller on the main wing's lift distribution at $\alpha = 6°$. Due to circulation control (blue line), the lift is significantly increased over the entire wing as compared to no circulation control (black line). With the propeller on and circulation control, the lift is primarily increased in the region of the propeller, which is affected by the slipstream. Particularly on the inboard side of the nacelle, which is the upwash side of the propeller in this case, the lift is raised considerably. The lift is also increased at the position of the nacelle due to flow entrainment of the fluid behind the center of the actuator disk. At the downwash side of the propeller the local angle of attack is reduced by the swirl of the slipstream. Consequently, the lift increase is rather small. However, the local lift is still positively altered due to the large sectional $C_{L'(\alpha=0°)}$. In summary, the lift generation is strongly increased behind the propeller despite the flow separating from the flap.

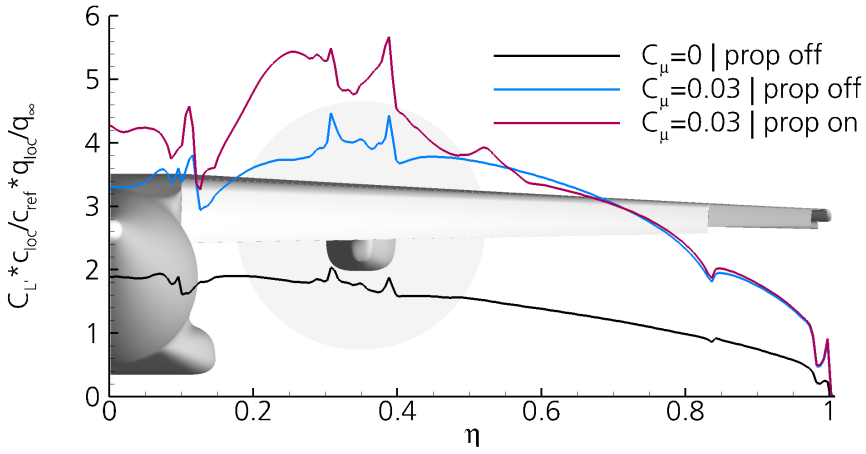

Figure 5.10: Influence of circulation control and the propeller on lift distribution at $C_\mu = 0.03$ and $\alpha = 6°$

Figure 5.11 shows the surface pressure distribution and skin friction lines for the case with

circulation control and the propeller on at $\alpha = 18°$. Again, the total pressure losses are visualized in terms of $p_t/p_{t,\infty}$ in X-cutting planes. Similarly to $\alpha = 6°$, the skin friction lines on the flap indicate attached flow at the wing root section and flow separation behind the propeller. The skin friction lines on the main wing illustrate the extent of the propeller slipstream due to a sudden change in flow direction. Outboard of the propeller slipstream, the skin friction lines indicate the onset of trailing edge flow separation on the flap. Inboard of the slipstream tube, flow reversal can be observed at the leading edge. With the local angle of attack being raised in the propeller's upwash region and the local circulation being proportional to $C_{L'} \cdot V_{loc}$, it is reasonable to assume that the main wing circulation is locally increased due to the slipstream. As a consequence, the local induced angle of attack is changed towards positive values outside of the slipstream tube, increasing the local angle of attack here, as well. Hence, leading edge flow separation is most likely occurring prematurely. The visualization of the total pressure ratio illustrates increased total pressure losses between the wing-root and the nacelle, which can be attributed to the leading edge separation. Significant total pressure losses also occur downstream of the unprotected inner wing leading edge. As discussed in [5], these total pressure losses can be attributed to the vortex emanating from the side-edge of the unprotected leading edge, which supports the detachment of the main element's wake from the blowing jet. The contour indicating the surface pressure coefficient shows strong suction peaks at the leading edge and the flap. At the wing root, the flap suction peak is degraded due to the detachment of the main element's wake. In the area influenced by the propeller slipstream, the suction peaks are more pronounced, mainly due to the increased dynamic pressure.

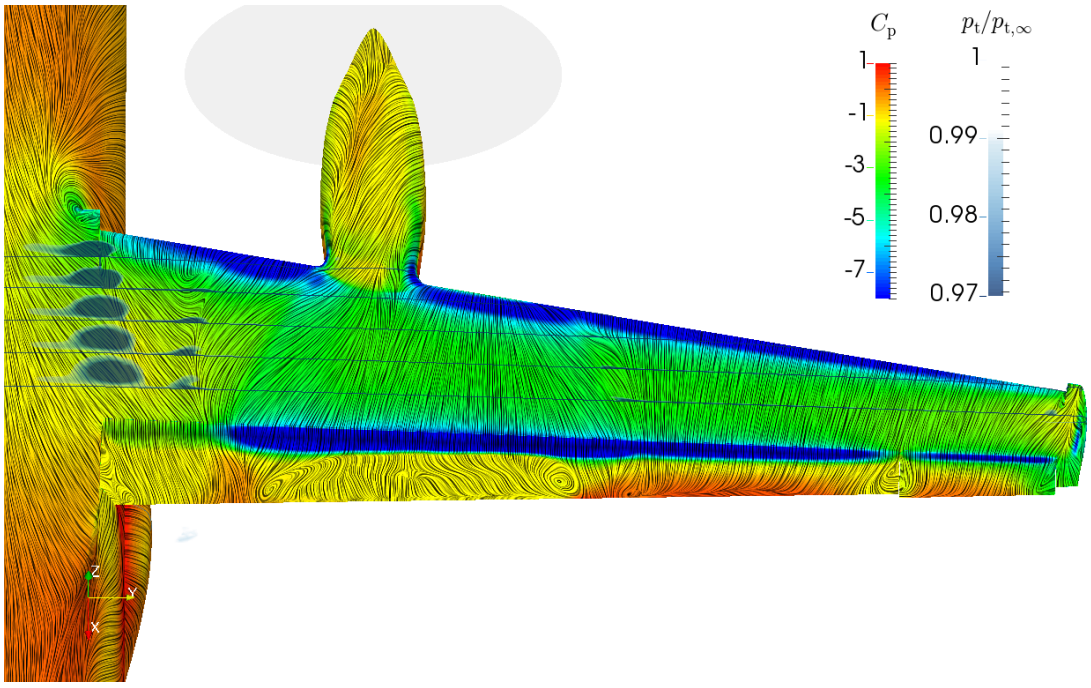

Figure 5.11: Pressure coefficient distribution and skin friction lines on the main wing at $C_\mu = 0.03$, $\alpha = 18°$, and propeller on

With rising global angle of attack, the leading edge separation in the inboard region increases, as Figure 5.12 shows. At $\alpha = 20°$, the skin friction lines indicate that the leading edge separation spreads out across the entire region between the wing root and the nacelle. As a result, the suction peaks of the leading edge and the flap break down in the inboard region.

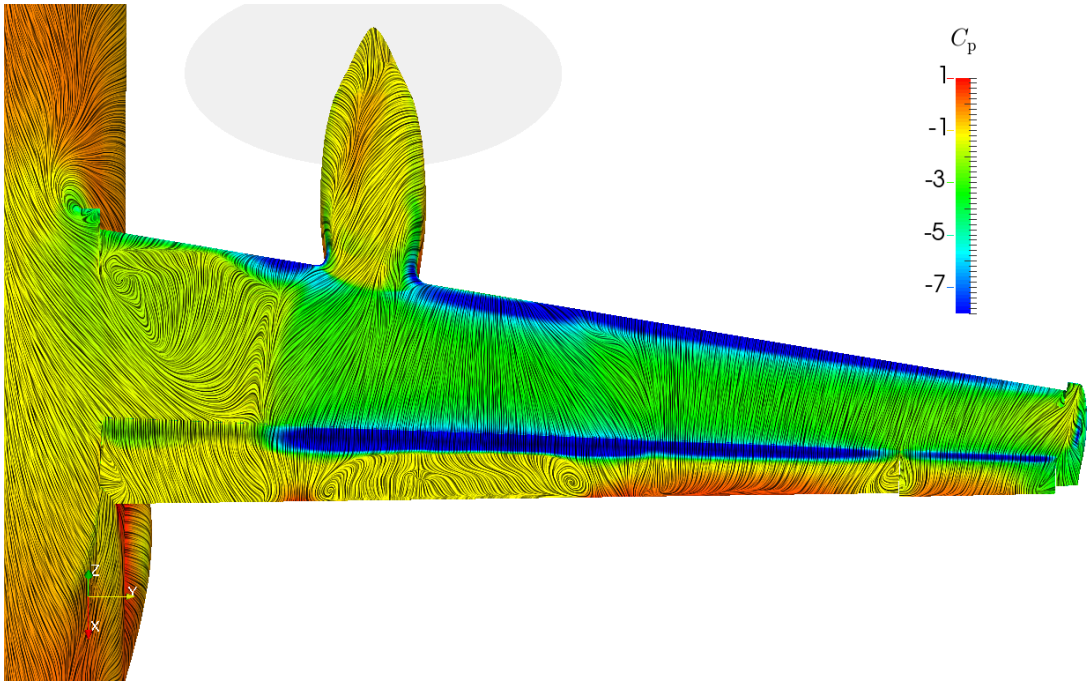

Figure 5.12: Pressure coefficient distribution and skin friction lines on the main wing at post stall in the case with the propeller on ($C_\mu = 0.03$, $\alpha = 20°$)

A comparison of the lift curves (Figure 5.13) demonstrates the significant impact, the propeller has on both the maximum angle of attack and maximum lift coefficient. The blue and black lines represent the cases with the propeller off, as illustrated in Figure 5.7. If the propeller is added to the case with circulation control (red line), the lift slope is increased due to the additional dynamic pressure behind the propeller, leading to an increased $C_{L,\alpha=0°}$. The limitation of α_{max} resulting from the nacelle vortices is also removed. Hence, α_{max} and $C_{L,max}$ are raised by 11° and 1.39, respectively. The maximum effective lift coefficient of the aircraft is $C_{L,eff,max} = 4.78$, when also considering the forces on the propeller. $C_{L,eff,max}$ is therefore 0.26 higher than the maximum lift coefficient of the airframe.

In summary, circulation control significantly increases the maximum lift coefficient due to an increase of the effective wing camber. However, the potential of lift gain is notably reduced due to the adverse engine integration effects. Propeller effects increase the maximum lift coefficient further. The adverse engine integration effects seen for the case with the propeller off do not occur. Additionally, the critical blowing coefficient is shifted to higher values allowing for higher lift coefficients at optimal efficiency.

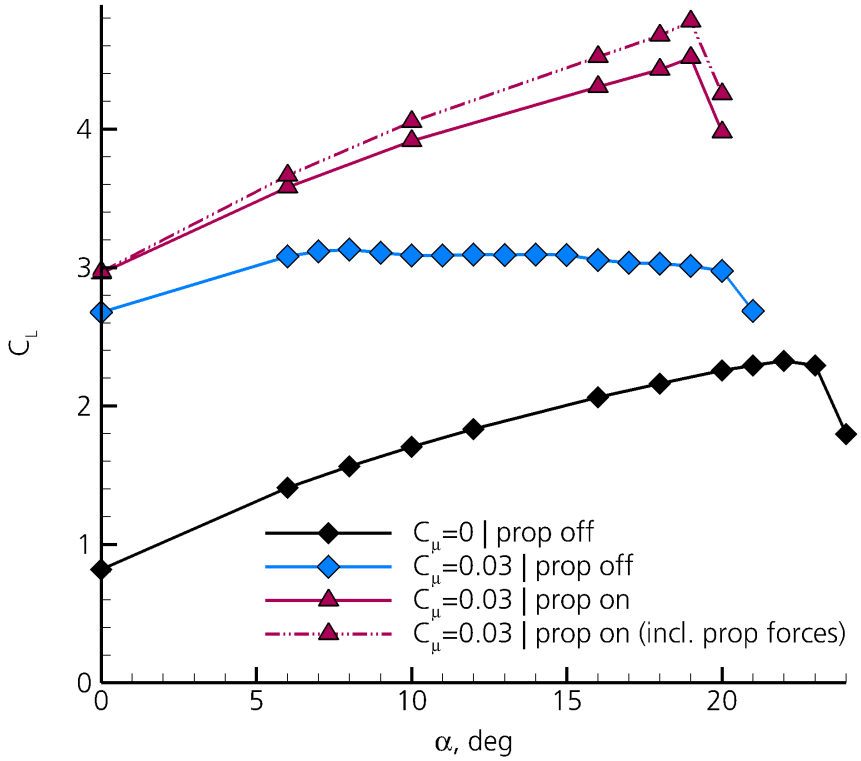

Figure 5.13: Impact of the propeller on lift curve

5.1.2 Wake Evolution and Flow Conditions at the HTP

Along with the wing-body components, the HTP is the main contributor to the pitching moment and thus has a significant influence on the aircraft's controllability and stability in longitudinal motion. The HTP's pitching moment contribution strongly depends on the local flow conditions – namely the local angle of attack and dynamic pressure – at the position of the HTP. The following section will therefore discuss the influence of circulation control and the propeller on the wake evolution and the resulting flow conditions at the HTP position. In order to exclude the influence of the HTP itself on the local flow conditions, the analysis of the latter is based on the simulations of the wing-body model (with engine).

For the controllability of the aircraft, the influence of circulation control and the propeller on the local angle of attack at the HTP α_{HTP} (at constant global angle of attack) is of importance. In contrast, the change of α_{HTP} due to an α change ($d\alpha_{HTP}/d\alpha$) is vital for the longitudinal static stability. Furthermore, the local dynamic pressure at constant angle of attack is important for controllability and stability[5]. The local angle of attack is comprised of the global angle of attack, the HTP trim angle, and the downwash angle ϵ:

[5]The stability is also affected by the change in local dynamic pressure due to a change in angle of attack. However, $dq_{HTP}/d\alpha$ is thought to be negligible.

$$\alpha_{HTP} = \alpha + i_{HTP} - \epsilon \tag{5.1}$$

Several aspects can therefore influence α_{HTP} and $d\alpha_{HTP}/d\alpha$. Firstly, α_{HTP} obviously dependends on the main wing circulation and thus on its lift coefficient. Analogously, $d\alpha_{HTP}/d\alpha$ depends on $C_{L\alpha}$. Secondly, the local angle of attack also depends on the main wing's circulation distribution, according to lifting line theory and the law of Biot-Savart. $d\alpha_{HTP}/d\alpha$ is therefore affected by $d\Gamma_{(y)}/d\alpha$ (the change in the circulation distribution due to a change in angle of attack). In reality, changes in circulation strength and distribution may even lead to an alteration of the main wing wake topology. Furthermore, the relative positions of the main wing wake phenomena with respect to the HTP location depend on α, as the vortices tend to follow the freestream flow direction in absence of aircraft influences. A severe impact on the longitudinal static stability can be expected if trailing vortices or the propeller slipstream move to the position of the HTP. Both, local angle of attack and dynamic pressure can then be significantly altered. Even if this is not the case, wake phenomena may affect longitudinal controllability and stability due to a change in strength or position.

Figure 5.14 illustrates the most important flow features of the port sided main wing wake with regard to the flow conditions at the tail planes. On the starboard side, the flow features are represented by increased values of kvn in a X-cutting plane at the location of the HTP's aerodynamic center AC_{HTP}[6] ($\xi = 5.07$). The colors of the vortex representations on the port side illustrate the vortices' sense of rotation. Red stands for a positive rotational sense and blue for a negative rotational sense. The strongest vortex is the wing tip vortex (WT), which exist in all computed cases, but varies in strength. At both flap side edges, flap tip vortices (IFT, OFT) emanate, which increase in strength due to circulation control. The slipstream (S1) is obviously linked to the cases with the propeller on. In those cases, an additional vortex (S2) emanates from the midboard of the wing, correlating with the position of the sudden increase in lift distribution that is caused by the slipstream.

[6] the location of AC_{HTP} is illustrated in Figure 2.4

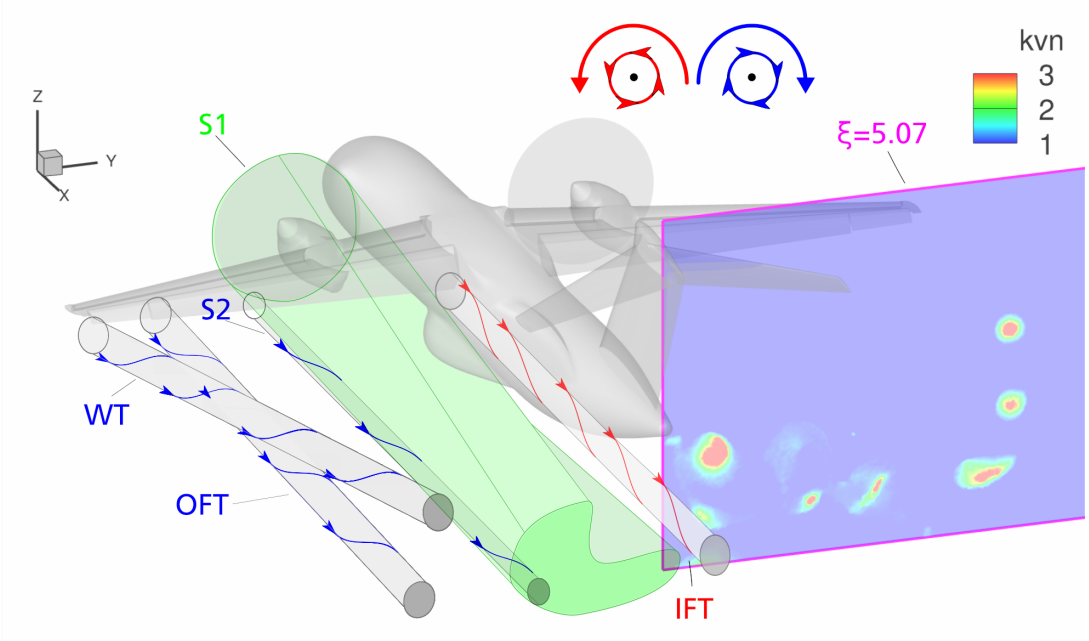

Figure 5.14: Wake topology with most important flow features regarding flow conditions at the tail planes

The following Figures (5.15, 5.16, and 5.17) illustrate the locations of the slipstream and the most significant trailing vortices at the streamwise position of the HTP (see Figure 5.14). The blue curves (ω_X-iso lines)[7] represent their locations at $\alpha = 6°$. The locations of the features at α_{max} of the corresponding case are shown by red lines[7]. The resulting trajectories due to a change in α are represented by dashed arrows. Additionally, the strength of the vortex at α_{max} is visualized by the X-component of the vorticity (ω_X). The box in proximity to the HTP illustrates the induced downwash in terms of ϵ in this region at α_{max}.

Without circulation control (Figure 5.15), three vortices can be identified that are relevant for the flow conditions at the HTP. The strongest one is the wing tip vortex (WT), which already occurs at $\alpha = 6°$. With rising angle of attack, the vortex moves in upward direction. As a result, the vortex is located above the HTP position at α_{max}. Due to its sense of rotation, the wing tip vortex induces a downwash at the position of the HTP. At high angles of attack, a vortex pair (INT and ONT) arises, which cannot be observed at $\alpha = 6°$. The two vortices can be traced back to the nacelle-wing junctions, one at the inboard side (INT), and one at the outboard side (ONT). Both vortices pass the HTP on its lower side at α_{max}. While the ONT vortex has a positive sense of rotation, like the wing tip vortex, the INT vortex has a negative sense of rotation. As a result, they induce downwash in the region in between them and upwash in the region outside of the vortex system. Due to their proximity to the HTP position, these two vortices lead to a notable variation of the local angle of attack along the HTP, as demonstrated by the ϵ contour. While the downwash angle is rather low in the inner and the outer region of the HTP, ϵ is notably higher

[7]The iso-lines for the identification of the vortex cores represent a cut-off value of $|\omega_X| = 20\ 1/s$.

in the midboard region.

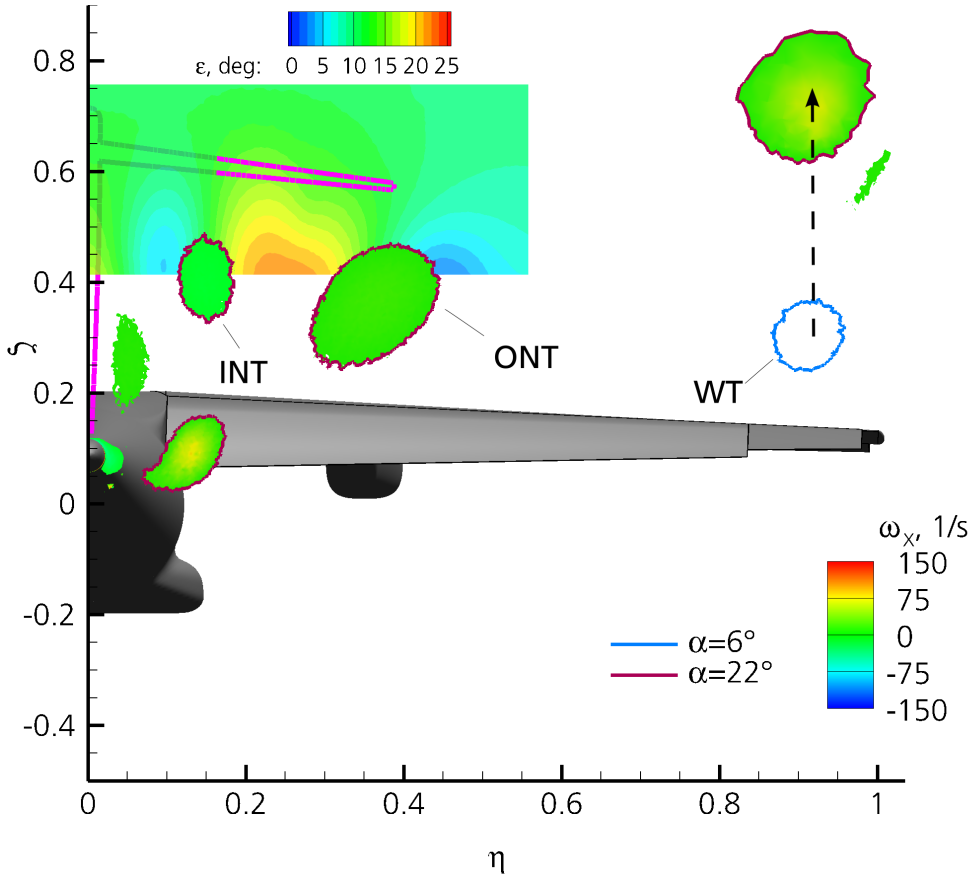

Figure 5.15: Vortex core position at HTP streamwise location ($\xi = 5.07$) for $C_\mu = 0$ (propeller off)

With circulation control, the wing tip vortex (WT) is significantly stronger, as indicated by the ω_x contour at α_{max} in Figure 5.16. Furthermore, the outer flap tip (OFT) vortex and the inner flap tip (IFT) vortex can be identified in this case. Even at α_{max}, the vortices are located far away from the HTP position. In particular, the IFT vortex does not move significantly with change in α, which can be attributed to the increase in downwash from the main wing. As a result, the variation of ϵ along the HTP span is rather small. However, the trend of an increasing ϵ towards the lower outboard side indicates the influence of the WT and OFT vortices.

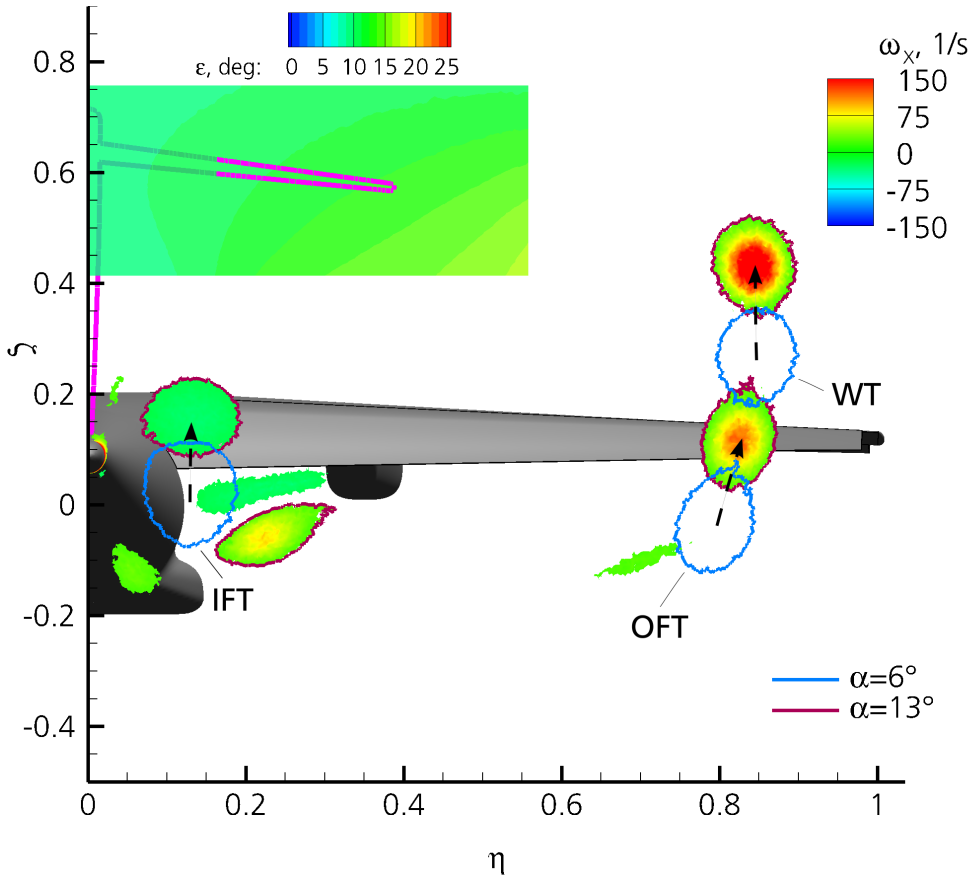

Figure 5.16: Vortex core position at HTP streamwise location ($\xi = 5.07$) for $C_\mu = 0.03$ (propeller off)

With circulation control and the propeller on, the wake topology becomes more complex (Figure 5.17). In addition to the vortices seen with the propeller off, the S2 vortex can be identified at low angles of attack with the propeller on. With rising angle of attack, the S2 and OFT vortices merge to one vortex. The IFT vortex is located slightly lower at $\alpha = 6°$ compared to the case with circulation control and the propeller off, indicating stronger downwash from the main wing. Furthermore, the IFT vortex does not move significantly upwards with rising angle of attack, as already seen for the case with the propeller off. Behind the propeller, the location of the slipstream can be identified by $p_t = \text{const.}$-curves (S1). Like the IFT vortex, the slipstream does not move upwards significantly. As a result, the HTP does not appear to directly interact with the IFT vortex or the slipstream. However, the ϵ contour reflects increased downwash at the outboard side of the IFT vortex and reduced downwash at the inboard side of it, indicating the influence of the IFT vortex. At the HTP tip, ϵ reaches a maximum of $\epsilon = 21.3°$. Towards the HTP root, ϵ decreases by $\Delta\epsilon_{max} = -4.8°$.

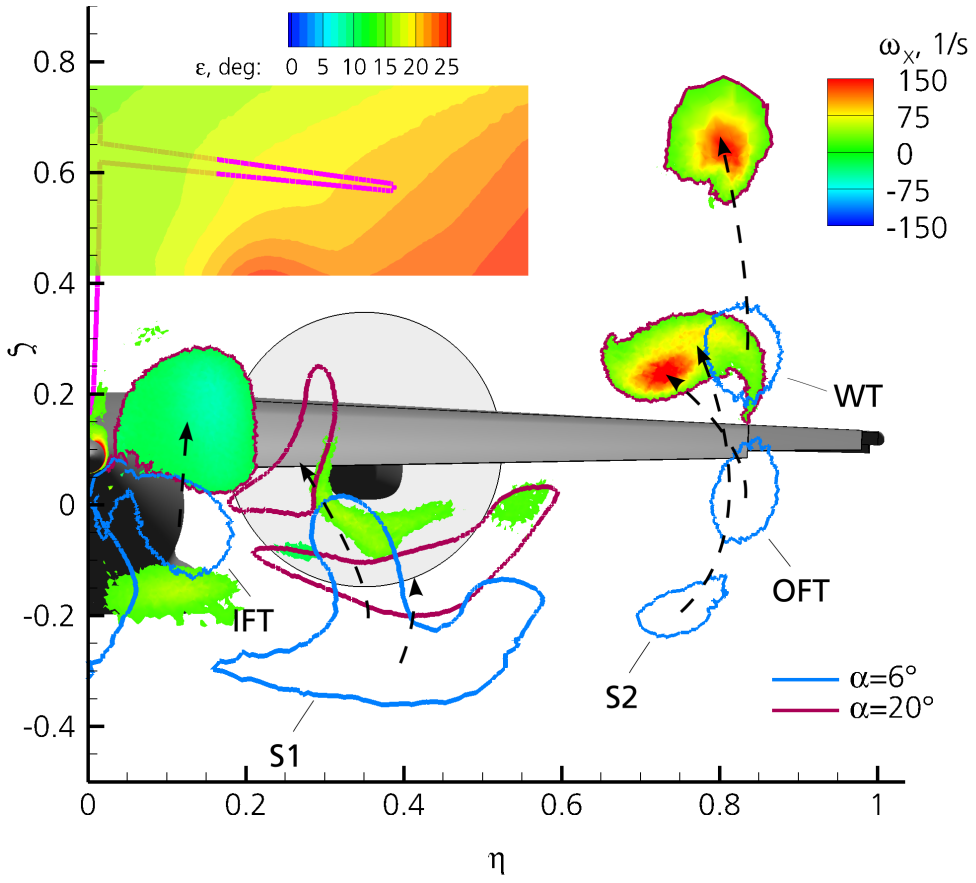

Figure 5.17: Vortex core position at HTP streamwise location ($\xi = 5.07$) for $C_\mu = 0.03$ with propeller on

It can be concluded that due to the strong wing downwash in the case with circulation control, no interaction between the HTP and trailing vortices or slipstream is to be expected. Therefore, the most critical case regarding vortex-HTP interaction is the case without circulation control. However, even though no vortex-HTP interaction is to be expected with circulation control, the trailing vortices still influence the local flow conditions at the HTP due to their strength. In particular, the case with the propeller on indicates a strong inhomogeneity in the ϵ distribution along the HTP span.

Besides the HTP, the inner flap tip vortex directly affects the pressure distribution of the fuselage. Figure 5.18 depicts a close-up view of the rear fuselage. The inner flap tip vortex is visualized by an iso-surface of $kvn = 2$, and the surface contour represents the pressure coefficient. The surface pressure is lower along the vortex path, indicating the footprint of the inner flap tip vortex. At $\alpha = 0°$ (Figure 5.18(a)), the inner flap tip vortex is located below the aft fuselage due to its conical shape. Consequently, the reduced pressure also acts on the lower side of the fuselage, leading to a force in downward direction. As the angle of attack increases, the position of the inner flap tip vortex is shifted upwards, as seen for $\alpha = 6°$ in Figure 5.18(b). As a result, the impact of the inner flap tip vortex on the fuselage's lower side diminishes, and the vertical force is removed. Since the inner

flap tip vortex is weaker without circulation control, the effect does not occur under these conditions.

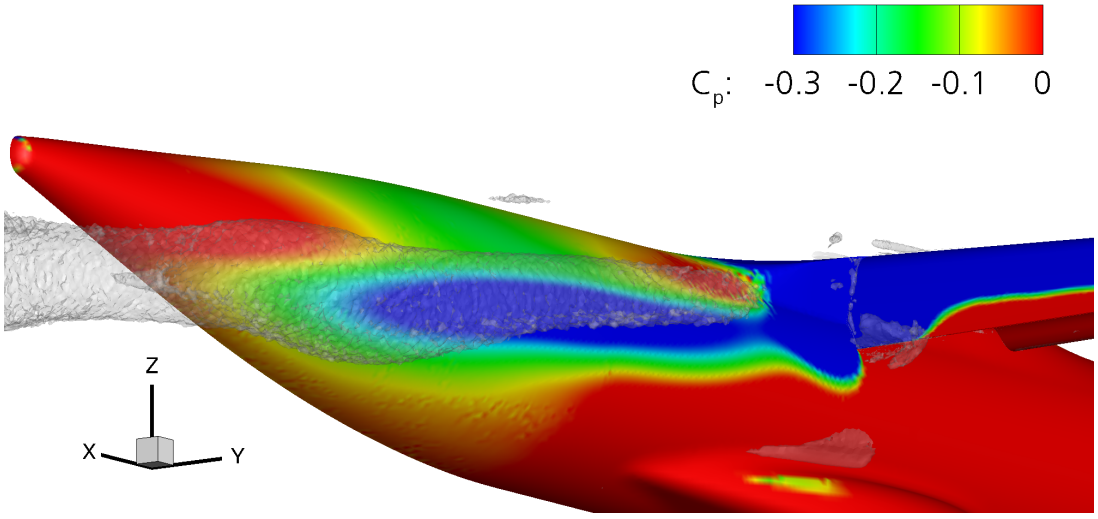

(a) $\alpha = 0°$

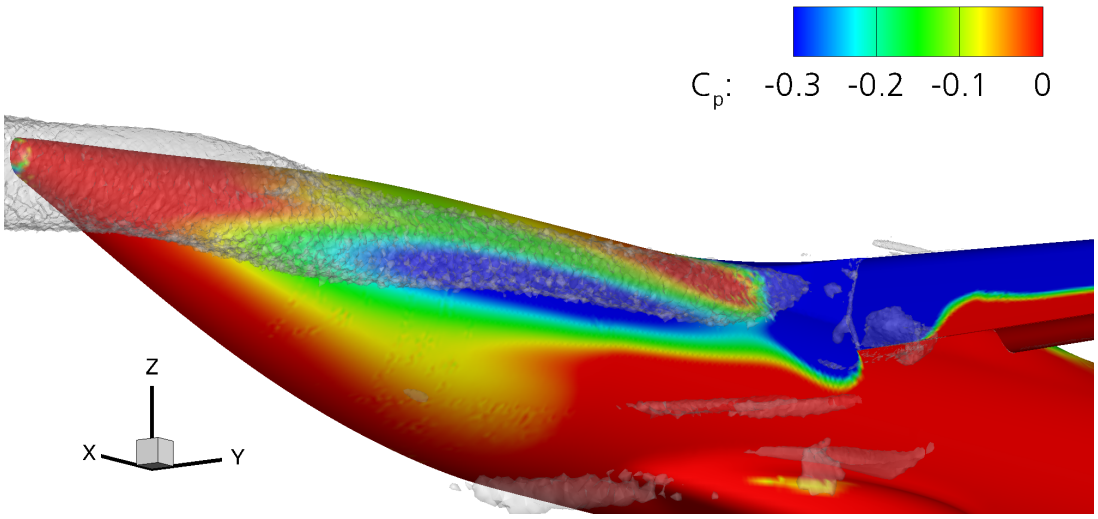

(b) $\alpha = 6°$

Figure 5.18: Inner flap tip vortex position visualized by iso-surfaces of $kvn = 2$ and influence on surface pressure coefficient at the rear fuselage for $C_\mu = 0.03$ (propeller off)

Returning to the flow conditions at the HTP position, the influence of circulation control and the propeller are evaluated in more detail by comparing the local angle of attack at the position of the HTP's aerodynamic center at constant angle of attack. At $\alpha = 6°$, circulation control and the propeller significantly increase the local downwash. The local angle of attack at AC_{HTP} is therefore reduced by $\Delta\alpha_{HTP} = -3.3°$ due to circulation control and by $\Delta\alpha_{HTP} = -5.3°$, if propeller effects are additionally considered. Consequently, circulation control and the propeller lead to additional downward forces at the HTP.

In order to evaluate if these effects influence $d\alpha_{HTP}/d\alpha$, the local angle of attack gradient is evaluated at the position of the HTP's aerodynamic center AC_{HTP}. Figure 5.19 depicts the gradient of the local angle of attack with respect to the global angle of attack. Without circulation control and the propeller off (black line), $d\alpha_{HTP}/d\alpha$ ranges between $0.58 \leq d\alpha_{HTP}/d\alpha \leq 0.67$ for $\alpha < 22°$. Once α_{max} is reached, $d\alpha_{HTP}/d\alpha$ reaches values above one, since the lift decreases with rising angle of attack. Consequently, the downwash decreases, which results in additional HTP effectiveness in terms of $d\alpha_{HTP}/d\alpha$. At low angles of attack, circulation control has a comparatively small effect on $d\alpha_{HTP}/d\alpha$, as the blue line demonstrates. The gradient of the local angle of attack ranges between $0.63 \leq d\alpha_{HTP}/d\alpha \leq 0.71$ for $\alpha < 8°$. A comparison of the gradients at $\alpha = 6°$ shows that $d\alpha_{HTP}/d\alpha$ slightly increases with rising C_μ from $d\alpha_{HTP}/d\alpha_{C_\mu=0} = 0.65$ to $d\alpha_{HTP}/d\alpha_{C_\mu=0.03} = 0.69$, a change of 7.1%. At higher angles of attack ($\alpha > 8°$), the gradient significantly increases mainly due to the decreasing lift gradient $C_{L\alpha}$, which causes a reduction of additional downwash, and thus an increase of $d\alpha_{HTP}/d\alpha$. Since the maximum angle of attack is reduced due to circulation control, the onset of the increase in $d\alpha_{HTP}/d\alpha$ due to the decreasing lift gradient $C_{L\alpha}$ is also shifted to lower angles of attack compared to the case without circulation control.

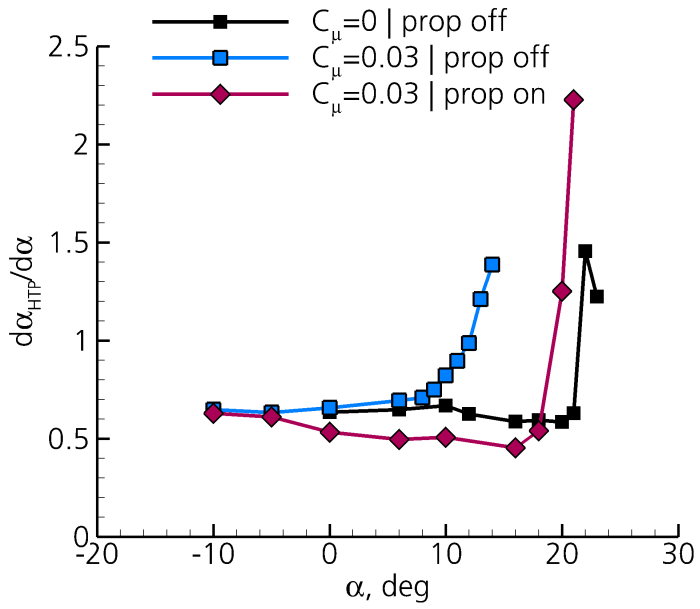

Figure 5.19: Change in local angle of attack due to change in global angle of attack at HTP's aerodynamic center

In contrast to circulation control, the propeller has a significant influence on $d\alpha_{HTP}/d\alpha$ at moderate angles of attack ($0° \leq \alpha \leq 16°$). Here, the gradient for the case with the propeller on and circulation control (red line) ranges between $0.45 \leq d\alpha_{HTP}/d\alpha \leq 0.53$. At $\alpha = 6°$, $d\alpha_{HTP}/d\alpha$ is reduced by 27.5% from 0.69 to 0.50 due to the propeller.

In summary, circulation control has a slightly beneficial impact on the HTP's effectiveness in terms of change in effective angle of attack, whereas the propeller notably reduces the

effectiveness.

For comparison, Weiberg reported downwash gradients of $d\epsilon/d\alpha \approx 0.5$ at a thrust coefficient of $C_T = 0.15$ and $d\epsilon/d\alpha \approx 0.7$ at $C_T = 1.15$ for the configuration with blown flaps ($\delta_f = 60°$), conventional tail, and four propellers [29]. This would yield local angle of attack gradients of $d\alpha_{HTP}/d\alpha = 0.5$ and $d\alpha_{HTP}/d\alpha = 0.3$, respectively. Considering the differing number of propellers and the different HTP position, the results agree well. Especially, the negative influence of the propeller on the local angle of attack gradient $d\alpha_{HTP}/d\alpha$ correlates well. Weiberg explained the effect by means of the increased lift curve slope, which he found to be "roughly proportional" to the increase in $d\epsilon/d\alpha$ [29]. With the change in the downwash gradient due to the propeller being $\approx 61\%$ and the change in the lift curve slope due to the propeller being $\approx 49\%$ (at $C_\mu = 0.03$ and $\alpha = 6°$), a rough proportionality exists in the present computations, as well. However, other influences, such as change of wake topology and its proximity to the HTP, enhance the effect of the increase in the lift curve slope.
Furthermore, $d\alpha_{HTP}/d\alpha$ strongly depends on the angle of attack. The present simulations indicate that at very low angles of attack ($\alpha \leq -5°$), $d\alpha_{HTP}/d\alpha$ of the case with the propeller on rises to values similar to the values in the case with the propeller off. This tendency is documented by Weiberg [29], as well. His data points to an increased $d\alpha_{HTP}/d\alpha$ at low angles of attack for the tests with $\delta_f = 80°$.

The second important parameter regarding the effectiveness of the HTP is the local dynamic pressure, which was also investigated. The analysis of those results, not shown here, indicates that circulation control and the propeller have a slightly beneficial impact on the HTP's effectiveness due to an increase in dynamic pressure. Circulation control increases q_{HTP}/q_∞ by one to two percent compared to the freestream dynamic pressure. The reason for this is the additional velocity induced by the increased local main wing circulation upstream of the HTP [6]. The propeller has a minor effect on q_{HTP}/q_∞ at low angles of attack. However, as the angle of attack rises, q_{HTP}/q_∞ increases up to a value of 1.03. It can be concluded that the impact of circulation control and the propeller on q_{HTP}/q_∞ is rather small compared to their influence on $d\alpha_{HTP}/d\alpha$.

5.1.3 Controllability

The influence of circulation control and the propeller on the controllability of the configuration (REF2-2013S) is demonstrated by evaluating the HTP trim angles – necessary for a balanced pitching moment ($C_m = 0$) – at constant angle of attack of $\alpha = 6°$. The trim angle is mainly affected by the pitching moment contributions from the wing-body and the HTP. As indicated in Sections 5.1.1 and 5.1.2, the force generation of the wing-body components and the flow conditions downstream at the HTP are notably influenced by circulation control and the propeller, which eventually impacts the pitching moment contributions of these components.

Recalling the pressure distribution of the representative airfoil (Figure 5.1), circulation control causes a significant increase in forces. As a result, the pitching moment coefficient

of the airfoil with respect to the geometric aerodynamic center ($\xi = 0.25$) more than triples from $C_{m,C_\mu=0} = -0.30$ to $C_{m,C_\mu=0.039} = -0.93$ despite the change in the center of pressure being negligible. For comparison, the pitching moment at cruise conditions is $C_{m,Cr} = -0.066$.
Considering the wing-body configuration at $\alpha = 6°$, the center of pressure is shifted from $\xi = 0.129$ to $\xi = 0.176$ due to circulation control. Again, the difference in pitching moment with respect to the geometric aerodynamic center is larger than the shift in the center of forces may suggest due to the increase in the force's magnitude. From $C_{m,C_\mu=0} = -0.21$ in the case without circulation control, it almost triples to $C_{m,C_\mu=0.03} = -0.61$. The pitching moment gradient with respect to C_L is $\frac{\Delta C_m}{\Delta C_L} = -0.232$. Changing the global blowing coefficient from $C_\mu = 0.02$ in the boundary layer control regime to $C_\mu = 0.04$ in the super-circulation control regime leads to pitching moments of $C_{m,C_\mu=0.02} = -0.53$ and $C_{m,C_\mu=0.04} = -0.63$, respectively.
With the propeller on, additional load is created due to the propeller (as illustrated in Figure 5.10). The main wing's center of pressure is thereby shifted in inboard direction compared to the cases with the propeller off. However, the impact on the streamwise movement of the center of pressure due to propeller effects is marginal with $\Delta\xi_{C_\mu=0.03} = 0.015$ in the case with circulation control. Regarding the fuselage, the change of the force due to the propeller is considerable when circulation control is active. In this case, the deflected slipstream below the inner part of the main wing interacts with the fuselage, as discussed in [6].
For the entire wing-body configuration, the influence of the propeller on the pitching moment coefficient due to changes in force magnitude and position sums up to $\Delta C_m = -0.204$ ($\frac{\Delta C_m}{\Delta C_L} = -0.533$) when circulation control is active. It can be therefore concluded that circulation control as well as the propeller lead to a notable pitch down moment. While the effect of circulation control on the pitching moment is significantly stronger than the effect of the propeller, the relative increase in pitching moment with respect to the lift coefficient is larger due to the propeller.

Due to the changes in the wing-body pitching moment and to altered flow conditions at the HTP, as illustrated in Section 5.1.2, circulation control and the propeller affect the HTP trim angle, as depicted in Table 5.2. The change in trim angle due to circulation control and the propeller is thereby lower than the change in local downwash angle at the HTP. While the additional downwash, caused by circulation control and the propeller, leads to a pitch up tendency, the wing-body pitching moment decreases, causing a pitch down tendency. Furthermore, the increase of the local dynamic pressure slightly increases the effectiveness of the HTP, and the downwash varies along the HTP span. The effect of circulation control and the propeller on the wing-body's pitching moment therefore counteracts the effect on the HTP's pitching moment due to changing flow conditions. As a result, the trim angle has to be only moderately adjusted for each of the cases.

Case	HTP trim angle
$C_\mu = 0$ | prop off	0.68°
$C_\mu = 0$ | prop on	2.63°
$C_\mu = 0.03$ | prop off	3.46°
$C_\mu = 0.03$ | prop on	4.78°

Table 5.2: HTP trim angles

5.1.4 Static Stability

The longitudinal static stability[8] of the reference aircraft was investigated based on the REF2-2013S model. Besides the main wing, the HTP is the main determinant for longitudinal stability. The impact of circulation control and the propeller on the wing-body's contribution as well as the HTP's contribution to the longitudinal static stability is therefore examined.

Wing-Body Contribution

While the static pitching moment of the wing-body at a constant angle of attack is important for the controllability of the aircraft, the pitching moment's gradient with respect to the angle of attack is decisive for the aircraft's static stability. Figure 5.20 depicts the wing-body's pitching moment with respect to the center of gravity at maximum landing weight (CoG_{MLW}) over the angle of attack. The curves representing the cases with circulation control generally lie below the curve of the case without circulation control, indicating a stronger pitch down tendency, as already discussed for $\alpha = 6°$. This tendency is increased in conjunction with the propeller on. The plot also shows that the unstable trend of the wing-body configuration, indicated by the positive stability gradient $C_{m\alpha}$, remains if circulation control is active and/or the propeller is on. However, with circulation control, the gradient is smaller compared to the case without circulation control. The stabilizing effect is mainly caused by the wake-fuselage interference, discussed in Section 5.1.2. The change in vertical forces at the rear fuselage due to a change in the angle of attack leads to an additional pitch down moment with rising angle of attack. The pitching moment gradient $C_{m\alpha}$ of the wing-body is therefore reduced.

Comparing the case with circulation control and the propeller off (blue line) to the one with circulation control and the propeller on (red line) in Figure 5.20 shows little difference in the curves' gradients in the linear range. This means that in contrast to circulation control, the propeller slipstream has almost no impact on the stability behavior of the wing-body in the linear range. At higher angles of attack, the curves diverge, as separation sets in at different angles of attack for the different cases and the respective stall mechanisms differ. Although, the comparison of the wing-body considers the slipstream effect on the main wing, it does not include propeller forces. If these are considered, the

[8] For an aircraft being longitudinally (static) stable, the pitching moment derivative has to fulfill $C_{m\alpha} < 0$ with $C_{m_{(C_L=0)}} > 0$ [90].

pitching moment gradient becomes steeper, as depicted by the dash-dotted red line. The reason for the additional destabilizing moment lies in the P-factor[9], which is discussed in more detail in [3].

It can be concluded that circulation control influences the longitudinal static stability derivative due to wake-fuselage interference. In the present case, it has a stabilizing effect on the wing-body configuration in a certain range of angles of attack. In contrast, the propeller has an adverse influence on the main wing stability if the forces acting on the propeller are considered.

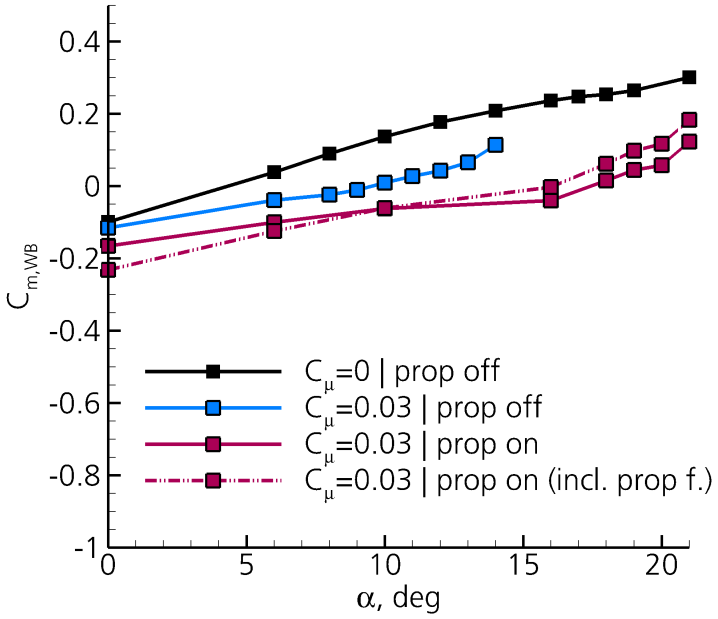

Figure 5.20: Impact of circulation control and the propeller on the wing-body's pitching moment curve

HTP Contribution

Based on the analysis of the wake flow characteristics of the wing-body configuration in Section 5.1.2, the influence of the wake on the HTP's pitching moment and its contribution to the static stability of the full aircraft are examined.

Figure 5.21 illustrates the HTP's pitching moment with respect to the angle of attack. The negative slopes of the HTP's pitching moment curves demonstrate that the HTP has a stabilizing effect in all investigated cases even beyond α_{max}. However, the magnitude of the gradient differs from case to case. While circulation control has little effect on the stability derivative, the propeller reduces the magnitude of the derivative considerably. Comparing the cases at $\alpha = 6°$, circulation control increases $C_{m\alpha}$ by 3.2%, whereas the

[9]When a propeller is operated under an incident angle, the local angle of attack and the local relative velocity of the propeller blades depend on the blade's angular position. The propeller load therefore becomes asymmetric, causing additional longitudinal and lateral moments.

propeller reduces it by 34% if circulation control is active. Without circulation control, $C_{m\alpha}$ is reduced by 27.2% due to the propeller (not shown). Considering the inhomogeneity of the flow conditions along the HTP span and the influence of the local dynamic pressure, the trends of $C_{m\alpha}$ correlate well with the behavior of $d\alpha_{HTP}/d\alpha$ at the HTP's aerodynamic center.

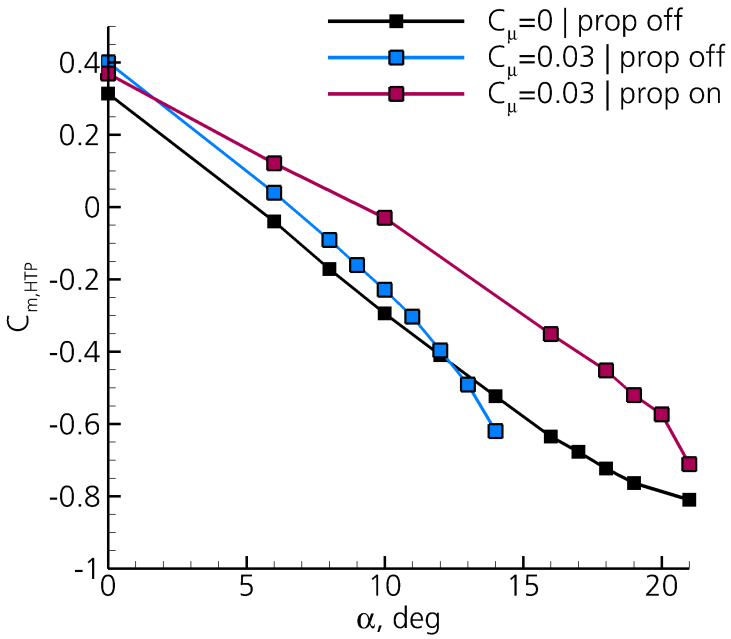

Figure 5.21: Impact of circulation control and the propeller on HTP's pitching moment curve

Full Aircraft

Having analyzed the main contributors to the aircraft's longitudinal static stability in the previous sections, Figure 5.22 illustrates the static stability behavior of the entire aircraft. Since the aircraft was trimmed for a constant angle of attack of $\alpha = 6°$, all curves (except that representing the powered case without an accounting of the forces on the propeller) intersect each other at this angle of attack and $C_m = 0$. All cases have negative gradients, which means that the aircraft is stable for the underlying conditions. However, the curve in the case with circulation control and the propeller off is steeper than the one without circulation control. This leads to the conclusion that circulation control tends to increase the static stability for this configuration. The effect is mainly caused by the wing-body behavior. In contrast, the propeller reduces the stability due to the resulting effects on the HTP. Both trends are also reflected in the static margins[10] for the investigated center of gravity in Table 5.3. The margin ranges between $-0.52 \leq \Delta\xi_{SM,CoG_{MLW}} \leq -0.12$, being the lowest without circulation control and the propeller on, and being the highest with

[10]The static margin is a measure for the pitch stiffness. It is defined as $\xi_{SM} = \frac{X_{CoG} - X_N}{c_{ref}} = \frac{C_{m\alpha}}{C_{A\alpha}}$ [90].

Case	Static margin
$C_\mu = 0$ | prop off	-0.32
$C_\mu = 0$ | prop on	-0.12
$C_\mu = 0.03$ | prop off	-0.52
$C_\mu = 0.03$ | prop on	-0.19

Table 5.3: Static margins

circulation control and the propeller off. According to [90], a static margin of $|\xi_{SM}| \geq 0.05$ is generally required.

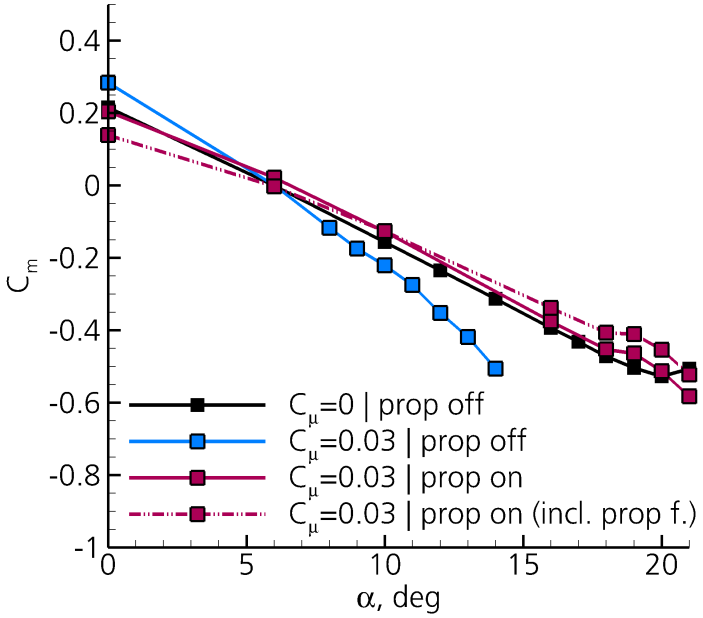

Figure 5.22: Impact of circulation control and the propeller on aircraft's pitching moment curve

With circulation control increasing the stability, and the propeller reducing the stability, the simulations show the same tendencies that Fink et al. found for their two-propeller model in their wind-tunnel test [26]. They documented the stability margin "for the full power condition being approximately half the values for the windmill conditions" [26]. Weiberg et al. also reported reduced static longitudinal stability with increasing thrust from his wind-tunnel test with the four-propeller model with blown flaps [30]. A few years later, Quigley experienced static longitudinal instability at high angles of attack during his flight tests with the C-130B with blown flaps [32]. However, it has to be kept in mind that a major difference between the tested configurations previously mentioned and the underlying configuration of this study is the position of the HTP, which can have a strong impact. Furthermore, the flight tests with the YC-134A did not show any problems regarding static longitudinal stability [31].

5.1.5 Dynamic Stability

A comprehensive understanding of the aircraft's dynamic behavior would necessitate a complete and in-depth flight mechanics investigation. Nevertheless, the analysis of the aerodynamic behavior already gives some insight into its dynamic stability. Besides the static aerodynamic parameters, the damping-in-pitch or pitch damping derivatives C_{mq} and $C_{m\dot{\alpha}}$ are typically the main aerodynamic influence parameters regarding the longitudinal modes of motion. Most importantly, they directly affect the damping of the short period mode according to Brockhaus [90]. If the pitch damping derivative is negative, the short period mode will be damped.[11] For conventional aircraft, C_{mq} is the dominating derivative and can be estimated by simulations of quasi-steady pitch motions. Therefore, the investigation of the influence of circulation control and the propeller on the dynamic stability of the present configuration (REF2-2013S) is performed using this type of simulation. Since the long period mode (phugoid mode) is mainly influenced by the glide ratio and not by the dynamic derivatives, it will not be discussed here. In the present context, longitudinal dynamic stability refers to the stability of the longitudinal short period mode.

Wing-Body Contribution

The investigation of the dynamic longitudinal behavior at $\alpha = 6°$ shows little influence of circulation control and the propeller on the wing-body contribution (Table 5.4). The biggest impact can be observed for $C_{\mathrm{Lq,WB}}$. While the dynamic derivative of the lift force is rather small without circulation control and the propeller off, it is notably higher if circulation control is active and/or the propeller is on. The increase in $C_{\mathrm{Lq,WB}}$ due to circulation control is caused by reduced surface pressures on the main wing due to the (positive) pitch motion (not shown). The table also shows increased pitch damping derivative values, especially when circulation control is active. Analogous to the static behavior (Section 5.1.4), the increased pitch damping derivatives can be attributed to the wake-fuselage interaction. Comparable to an increase in the angle of attack, the positive pitch motion also leads to an upward shift of the inner flap tip vortex position, which in turn results in a pitch down momentum as described in Section 5.1.4.

It can be expected that the influence of circulation control and the propeller becomes more significant at higher angles of attack, since the wake phenomena move closer to the HTP and the strength of the trailing vortices increases. Therefore, a quasi-steady pitch motion was simulated at an angle of attack of $\alpha = 18°$ with circulation control and the propeller on. As seen in Section 5.1.1, the flow is already partially separated in the inboard region at $\alpha = 18°$. Due to the positive pitch motion, the leading edge separation is reduced, leading to an increase in C_{lq} and C_{mq}. However, this effect is slightly offset by the reduced wake-fuselage interaction. As a result, the contributions of the wing-body on the dynamic

[11] The pitch damping derivative must not necessarily be negative for the short period mode being damped. The case of an undamped harmonic oscillation depends on several parameters such as $C_{L\alpha}$,$C_{D\alpha}$ and C_D. Considering these parameters being greater than zero, the short period mode will be damped with $C_{mq} + C_{m\dot{\alpha}} < 0$ [90].

derivatives are only slightly altered compared to $\alpha = 6°$, as shown in Table 5.4.

HTP Contribution

At low and moderate angles of attack, circulation control leads to stronger flap tip and wing tip vortices, which move in upward direction towards the HTP in case of a positive pitch motion. The additional lift of the main wing due to the motion ($C_{\mathrm{Lq,WB}}$) is slightly increased due to circulation control. This results in an increased local downwash at the HTP position, which in turn leads to a reduced damping effect of the HTP. The HTP contribution to C_{mq} is thereby slightly reduced at $\alpha = 6°$, as seen in Table 5.4. With the propeller on, the reduction of the local angle of attack at the HTP is larger due to the stronger inner flap tip vortex. However, at global angles of attack, at which the wing tip vortex moves above the HTP, the local downwash at the HTP decreases due to the (positive) pitch motion. As a result, the dynamic pitch damping value is considerably increased, as seen for $\alpha = 18°$ in Table 5.4.

Full Aircraft

The longitudinal dynamic derivatives of the full aircraft are dominated by the dynamic derivatives of the wing-body components and the HTP. However, small contributions are also made by the VTP, which make up for the differences between the dynamic derivatives of the wing-body and the HTP on one hand, and the aircraft on the other hand in Table 5.4[12]. The table illustrates that the dynamic derivatives of the lift force and the pitching moment slightly increase due to circulation control, despite a reduction in the contributions from the HTP. This reduction is more than offset by the contribution from the wing-body.
Considering propeller effects reduces the dynamic pitch damping derivative, regardless of whether circulation control is active or not. In the case with circulation control and the propeller, the pitch damping value increases when the angle of attack is raised to $\alpha = 18°$, mainly due to the impact of the HTP.

It can be concluded that the configuration exhibits longitudinal dynamic stability for all investigated cases, even at high angles of attack close to α_{max}.

[12] The individual components on their own are unclosed surfaces. With regard to the VTP, an aerodynamic force acts on the upper side, whereas the VTP is open towards the lower side with no aerodynamic force acting from below.

C_μ	Propeller	α,deg	$C_{Lq,WB}$	$C_{Lq,HTP}$	$C_{Lq,A/C}$	$C_{mq,WB}$	$C_{mq,HTP}$	$C_{mq,A/C}$
0	prop off	6.0	0.6	5.1	5.8	−0.5	−25.6	−26.5
0	prop on	6.0	2.0	4.8	6.8	−1.1	−23.7	−25.2
0.03	prop off	6.0	2.1	4.9	6.6	−2.7	−24.0	−27.1
0.03	prop on	6.0	2.0	4.7	6.8	−2.9	−23.2	−26.5
0.03	prop on	18.0	2.6	5.3	7.9	−2.4	−27.4	−30.4

Table 5.4: Dynamic derivatives of wing-body, HTP and full aircraft

5.2 Lateral Motion

In the following section, the aerodynamic behavior in lateral motion of the REF2-2013S is discussed. Firstly, flow phenomena and the generation of forces under crosswind conditions are analyzed. The aerodynamic behavior under crosswind conditions is the basis for static directional and static lateral stability. Furthermore, the generation of forces under crosswind conditions illustrates the fundamental principles of cross flow effects on this particular configuration. These effects also play a key role when investigating the dynamic behavior in yawing motion. Having examined the aerodynamic phenomena under crosswind conditions, their impact on the static directional stability and the static lateral stability is discussed. The analysis of the static behavior is completed with the investigation of cross-coupling effects. In this context, cross-coupling effects refer to a coupling of the lateral and longitudinal motion caused by induced longitudinal forces due to crosswind. Finally, the chapter illustrates the influence of circulation control and the propellers on the dynamic stability in rolling and yawing motion.[13]

It is evident that the rotational sense of the propellers can have a notable influence on the aerodynamic behavior in lateral motion. The analysis of the propeller effects will focus on the case of propellers rotating symmetrically in inboard up direction. Alterations in the behavior due to the rotational sense will be only briefly discussed.

5.2.1 Aerodynamic Behavior under Crosswind Conditions

The investigation of the aerodynamic behavior under crosswind conditions is essential for an analysis of the stability in lateral motion. In addition to its obvious significance for the directional static stability, it determines the lateral static stability and influences the stability of the dutch roll and the spiral mode [90]. Besides the VTP, the main wing and the fuselage are the main contributors of forces and moments due to crosswind. The investigations revealed that the aerodynamic behavior under crosswind conditions, in particular of the tail, is highly dependent on the angle of attack and the sideslip angle. The discussion will focus on the cases at $\alpha = 0°$ as it demonstrates the characteristics of the configuration with propellers.

[13] Parts of the results in sections 5.2.1 and 5.2.2 have already been published in [1].

Main Wing

This subsection covers the influence of circulation control and the propellers on the aerodynamic behavior of the main wing under crosswind.

Influence of Circulation Control Figure 5.23 compares the influence of crosswind on the main wing's lift distribution along the wing span for the case with circulation control (blue lines) and the one without circulation control (black lines). The lift distributions (Figure 5.23(a)) indicate little differences between the windward and leeward side of the wing at first sight. Besides asymmetries at the position of the fuselage ($|\eta| \lesssim 0.12$), the largest differences can be observed at the nacelles ($0.3 \lesssim |\eta| \lesssim 0.4$). Here, the peaks in the lift distribution, which also exist at zero crosswind (see Section 5.1.1), are increased on the windward side and reduced on the leeward side. The asymmetry is caused by the crosswind in conjunction with positive local angles of attack induced by the main wing. In this case, the crosswind supports the flow around the nacelles on the upper windward sides and the lower leeward sides, whereas it counteracts the flow around the nacelles on the lower windward sides and the upper leeward sides. This causes a change in the velocity distribution of the flow around the nacelles, which in turn increases the local lift on the windward side of the components and reduces it on the leeward side of the components. Since the local angles of attack ahead of the main wing are increased by circulation control, the effect is stronger in this case compared to the case without circulation control.
Notable asymmetries can also be observed in both cases in the regions between the fuselage and the nacelles. Here, the lift of the main wing on the windward side increases, whereas it decreases on the main wing's leeward side. The effect can be attributed to the fuselage in conjunction with the high wing configuration. As a part of the cross flow is deflected around the fuselage towards the upper side, it induces an increased angle of attack on the windward side in proximity to the fuselage, and a decreased angle of attack on the leeward side. The lift distribution is thereby changed.

For a more detailed analysis, Figure 5.23(b) shows the difference in lift distributions due to crosswind. The plot confirms that the changes at the position of the nacelles, in particular on the windward side, are larger with circulation control compared to the case without circulation control. In contrast, the changes between the fuselage and the nacelles are similar in both cases, as they solely depend on the local lift gradient $C_{L'\alpha} \cdot c_{loc}/c_{ref}$ and the change in local angle of attack. While Figure 5.23(b) does not show any further significant differences in the lift distribution without circulation control, it reveals notable differences for the entire wing outboard of the nacelles in the case with circulation control. On the windward side, the local lift is reduced due to the crosswind for $-1 < \eta < -0.4$, whereas it increases on the leeward side for $0.6 < \eta < 1$.

Generally, negative dihedral (as is the case for the investigated configuration) in conjunction with crosswind leads to higher lift on the leeward side compared to the windward side due to a change in the local effective angle of attack. In contrast, positive wing

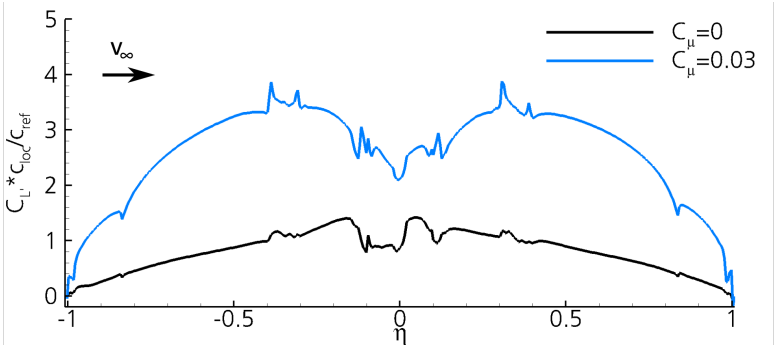

(a) Lift distribution

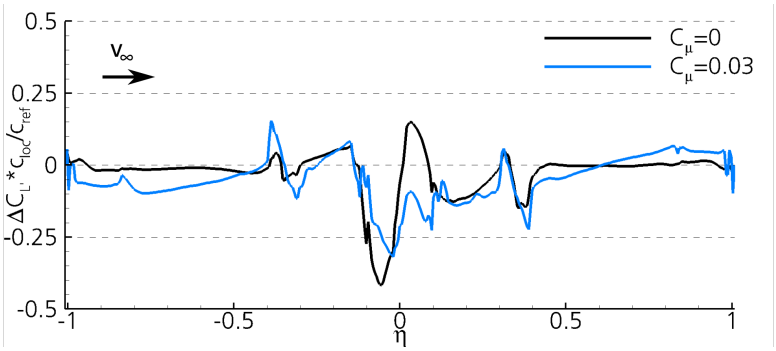

(b) Lift increment due to sideslip ($\Delta C_{L'} \cdot \frac{c_{loc}}{c_{ref}} = (C_{L'}|_{\beta=5°} - C_{L'}|_{\beta=0°}) \cdot \frac{c_{loc}}{c_{ref}}$)

Figure 5.23: Influence of cross flow on lift distribution at $\alpha = 0°$ and $\beta = 5°$ for varying circulation control modes (propellers off)

sweep causes the opposite effect due to the altered freestream velocity normal to the quarter chord line (effective freestream velocity) [114]. In the present case, both dihedral and sweep angle are comparatively small. The small difference in the main wing's lift distribution outboard of the nacelle in the case without circulation control is therefore reasonable. The larger differences on the outboard wing with circulation control cannot be explained by these two effects. The negative dihedral effect, which leads to lower lift on the windward side, depends on the lift slope. The lift slope is nearly unaffected by circulation control. In contrast, the sweep effect due to the altered effective freestream velocity depends on the local lift coefficient, which is significantly raised by circulation control. This effect would therefore counteract the trend of increased lift on the leeward side in the case with circulation control. The influence of higher main wing load due to flap deflection on the main wing's behavior under crosswind conditions has been investigated by Tucker [114]. He examined the influence of flap deflection on a fighter model with a quarter chord sweep angle of $\phi_{.25c} = -2.6°$ in a wind-tunnel. His results indicate a reduced dihedral effect due to deployed flaps, which correlates with a shift of the lift distribution towards the leeward side, as it is also seen in the present case with circulation

control.[14] Williams et al. performed wind-tunnel experiments with various configurations with IBF and reported a significant anhedral effect (shift of lift distribution towards the leeward side) due to blowing that was "not predicted by conventional arguments" [115]. Kuhn also concludes an anhedral effect by IBF from a summary on lateral/directional characteristics of distributed jet STOL configurations [116]. Most notably he found correlations between wing dihedral, flap deflection angle, and jet deflection on the one hand, and anhedral effect on the other hand based on his compilation of datasets. A "shift in total wing-flap vortex system" was mentioned by Kuhn as a possible cause for the anhedral effect of flap deflection [116]. Flow field analysis of the present configuration confirms that the trailing vortex system is altered as it is transported towards the leeward side by the crosswind (not shown). It also reveals that the jet flow downstream of the slot is skewed towards the leeward side, beginning at about 50 % of the flap chord. This effect can only be observed outboard of the nacelles and therefore correlates with the lift redistribution. In addition, the jet momentum distribution along the circulation control exit slot is affected by the crosswind (see Appendix C). However, the local changes in the jet momentum with respect to the jet momentum without crosswind are smaller than 0.7 %.[15]

Influence of the Propellers The influence of the propellers on the main wing subject to crosswind conditions can be mainly attributed to two effects. First, local flow conditions at the propellers are altered. The normal velocity component of the onset flow is reduced, which generally increases the effective angle of attack of the blade (see Figure 3.1). The in-plane velocity component is also changed, depending on the position of the blade. In the region where the blade rotates against the crosswind, the relative in-plane velocity component increases, which in turn increases the effective angle of attack. In contrast, the relative in-plane velocity is reduced at the position where the blade rotates with the direction of the crosswind, leading to a reduction in the effective angle of attack. The change in relative in-plane velocities evidently leads to a locally varying dynamic pressure, which increases in the region where the blade rotates against the crosswind and decreases in the region where it rotates with the crosswind. Due to the alteration of the local effective angle of attack and dynamic pressure, the propeller load is shifted within the propeller plane, the so-called P-factor. Generally, this leads to an increase of load at the position where the blades rotate against the crosswind. The propeller's sense of rotation therefore determines if the increased load occurs in the lower or upper part. The change in propeller loads affects the dynamic pressure in the slipstream, which in turn affects the lift distribution of the main wing.

The second effect of the crosswind in conjunction with propellers is the shift of its slip-

[14] According to Tucker, this behavior is caused by the flap hinge lines being swept forward and the resulting effect on the effective onset velocity at the flap. This argumentation however is not valid in the present case, as the flap hinge lines of the present configuration are swept back.

[15] Evaluation of flow field and surface data indicates that the local lift gain factor at $\eta = -0.75$ would be 1146, when it is assumed that the change in lift is solely caused by the change in the jet momentum coefficient. Typical lift gain factors for the present type of circulation control set-up and C_μ value are not higher than 100 [113].

stream, as illustrated in Figure 5.24. The slipstream is transported with the crosswind and therefore its region of impact on the main wing changes. The plus signs indicate an increase in local lift, and the minus signs indicate a decrease in local lift. The magnitude of the local lift change mainly depends on the velocities induced by the propeller and the local lift coefficient itself. This means that the change in local lift is primarily driven by the propeller's rotational sense and will generally be larger in the propeller's upwash region than in the downwash region, despite effects of varying sectional C_L' and chord length.

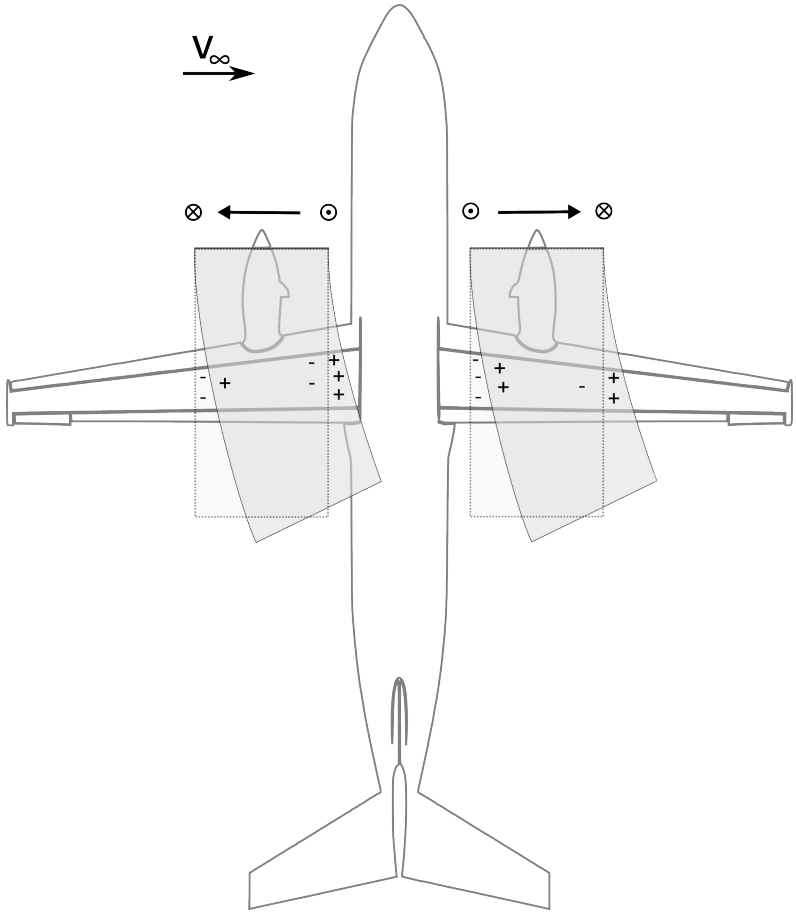

Figure 5.24: Shift of propeller slipstream and its influence on the main wing's lift distribution due to crosswind

Symmetric Inboard Up As discussed previously, the propeller load increases in those regions where the blade movement opposes the crosswind and decreases in the regions where the blade moves with the crosswind. Figure 5.25 illustrates the shift of the sectional thrust ($X\text{-}load = f_{n(r_b,\Theta)}$) when propellers symmetrically rotate in inboard up direction with crosswind from the port side. The plus signs and red contour within the figure represent an increase in local propeller load with respect to the average load. The minus signs and blue contour symbolize a reduction in local load. The load is increased in the upper half of the propeller on the windward side and in the lower half of the propeller on the leeward side. On the opposite sides, the load is reduced. The regions are phase shifted in

the direction of the rotational sense, causing higher load on the windward sides of both propellers.

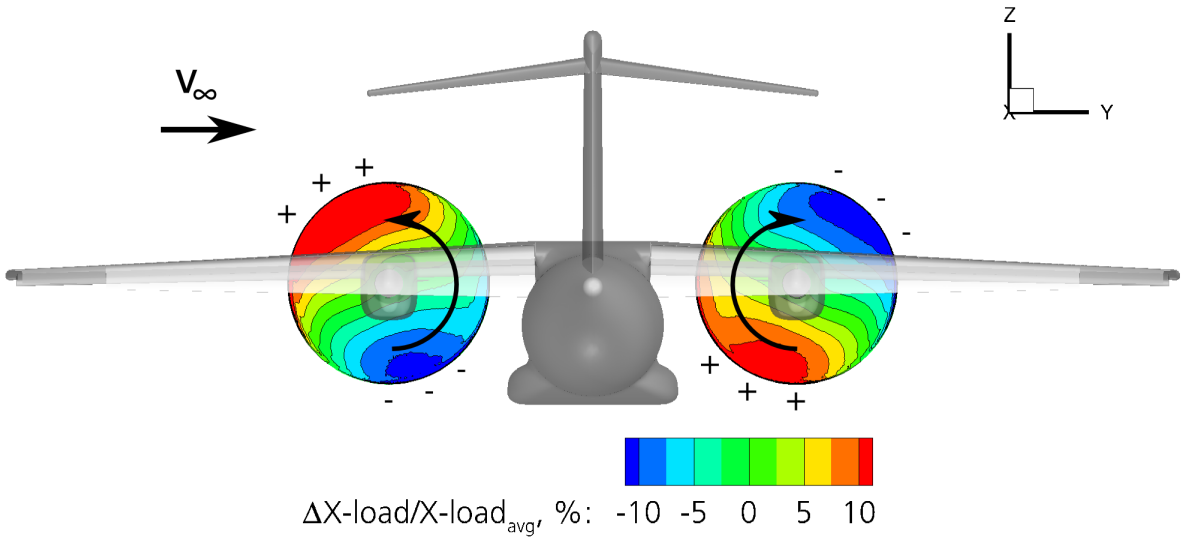

Figure 5.25: Propeller load shift due to crosswind ($C_\mu = 0.03$, $\alpha = 0°$, $\beta = 5°$)

Besides the two basic phenomena of the crosswind in conjunction with propellers, a third one can be observed on the lower side of the main, wing which is specific to the present configuration. Figure 5.26 depicts the slipstream in terms of streamlines and the surface C_p distribution on the configuration's lower side for the case of propellers rotating inboard up at $\alpha = 0°$ and $\beta = 0°$. The red color indicates that the C_p distribution on the lower side of the main wing is notably altered due to the slipstream as discussed in [6]. On the propeller's upwash side, the incidence angle of the slipstream with respect to the main wing is rather high, and the slipstream-main wing impingement leads to a high static pressure, especially at the rear part of the wing's main element and the flap. In the flap kink, the slipstream recirculates and is transported in spanwise direction to both sides. On the propeller's downwash side, the incidence angle of the slipstream is significantly smaller. The small incidence angle in conjunction with the droop nose causes leading edge separation on the lower side of the main wing. As the separated flow moves downstream, it is deflected by the flap towards the wing tip before it passes below the flap trailing edge. Along its path, the circulating separated flow reduces the surface pressure at the lower side of the main wing.

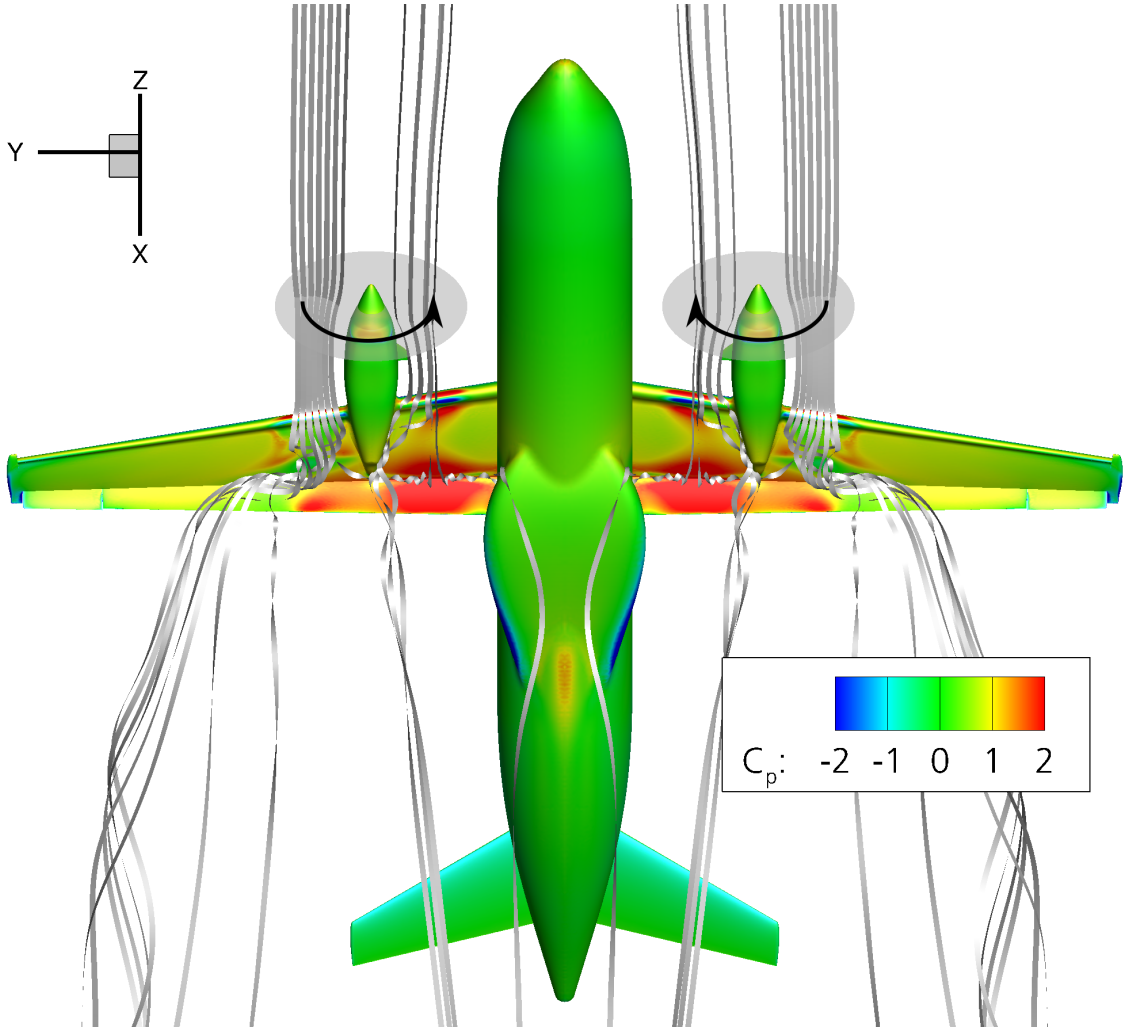

Figure 5.26: Slipstream impingement on the lower side of the main wing for symmetrically rotating propellers (inboard up) at $C_\mu = 0.03$, $\alpha = 0°$, and $\beta = 0°$

Figure 5.27 illustrates the slipstream and the surface C_p distribution on the configuration's lower side in the case of crosswind (I/B up, $\alpha = 0°$ and $\beta = 5°$). While the slipstream-main wing impingement at the inboard side remains rather unaffected by crosswind, the trajectory of the separated flow at the the outboard of the engine nacelle is changed. The impact is particularly big at the leeward side, where the separated flow below the main wing travels in crosswind direction to the outer side edge of the flap, before it passes below the flap trailing edge. The low pressure region caused by the separated flow is thereby also expanded in outboard direction.

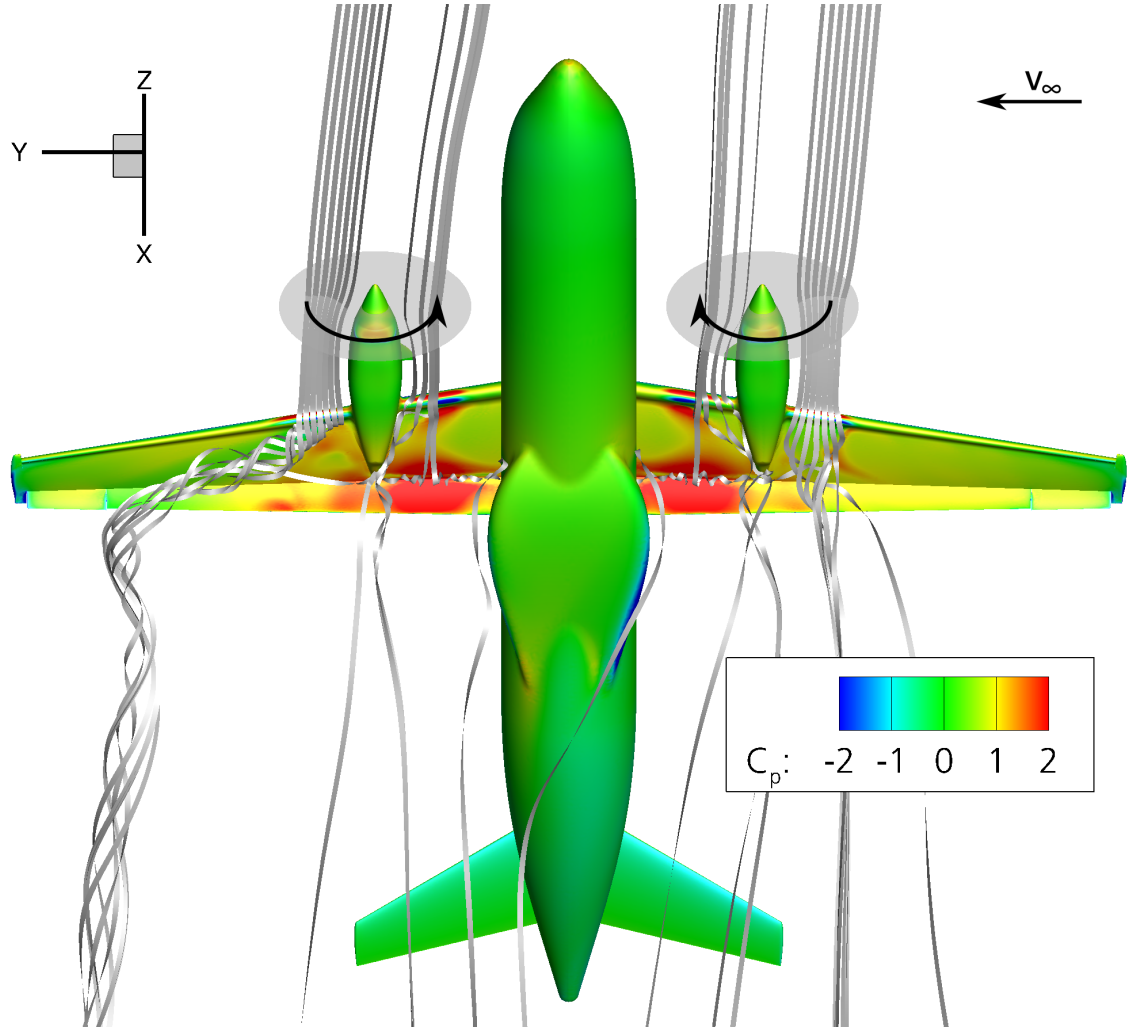

Figure 5.27: Slipstream impingement on the lower side of the main wing for symmetrically rotating propellers (inboard up) at $C_\mu = 0.03$, $\alpha = 0°$, and $\beta = 5°$

Due to the various effects that partially amplify and partially counteract each other, the impact of crosswind on the main wing's lift distribution is complex and non-linear, as illustrated in Figure 5.28. In the outboard region of the windward side, the local lift is slightly reduced similar to the case without propellers. At $\eta \approx -0.5$, the local lift is increased due to the increased thrust, as illustrated in Figure 5.25. In the middle of the slipstream region, the local lift is mainly affected by the reduced thrust in the lower part of the propeller. As a result, the stagnation pressure, and thus the surface pressure on the lower side of the the main wing, is reduced. Further inboard, the reduction in the local lift is counteracted by the fuselage influence. Furthermore, the local lift is increased here due to the transportation of the slipstream by the crosswind towards the fuselage.
On the leeward side, the effect of slipstream transportation in spanwise direction and the fuselage effect counteract an increase in lift in the inboard region which would occur due to the increased thrust in the propeller's upwash region. More importantly, however, the change of the low pressure region due to the separated flow on the lower side leads to a

notable reduction in lift between $0.55 \lesssim \eta \lesssim 0.8$.

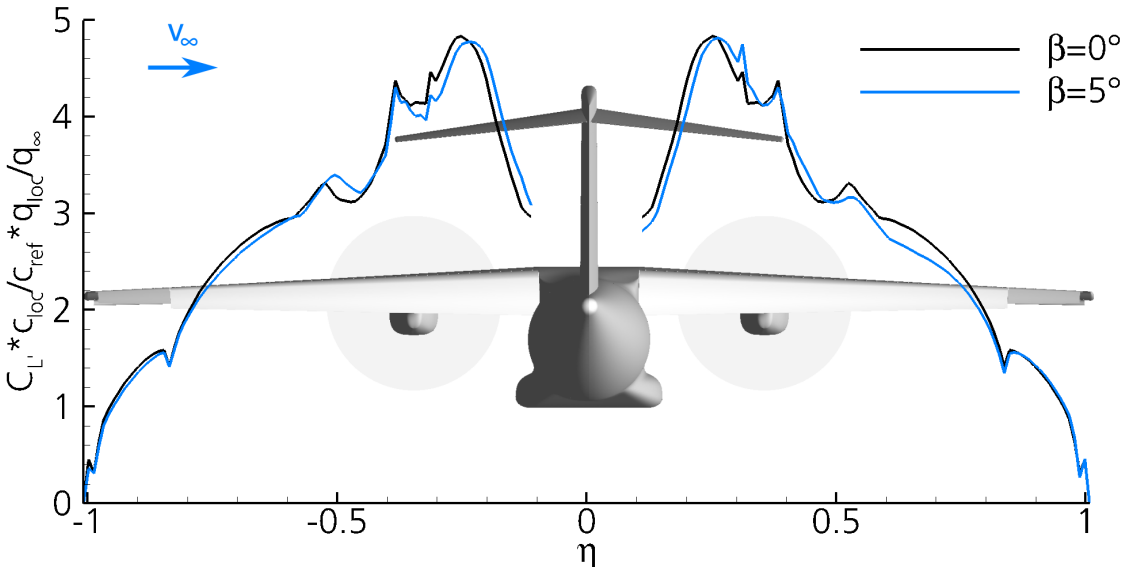

Figure 5.28: Influence of crosswind on lift distribution for symmetrically rotating propellers (inboard up) at $C_\mu = 0.03$ and $\alpha = 0°$

Symmetric Inboard Down In contrast to the case of symmetric inboard up rotation, the slipstream trajectory on the lower side of the main wing does not significantly change due to crosswind with the propellers rotating symmetrically inboard down (not shown). As a result, the change in the lift distribution is dominated by the effects of the propeller load shift and the shift of the slipstream in crosswind direction. The changes with respect to the sideslip angle therefore follow a clear trend, as Figure 5.29 demonstrates. Again, the outboard regions are dominated by the effect already seen in the case with propellers off. In the proximity to the propellers, the load is shifted towards the leeward side due to transportation of the slipstream. Furthermore, the lift is increased in the upwash region at the windward side and decreased in the upwash region at the leeward side due to the altered propeller load distribution. Inboard of the nacelles, the fuselage effect dominates the effect of the propeller load shift, leading to a slight lift increase at the windward side and a decrease at the leeward side.

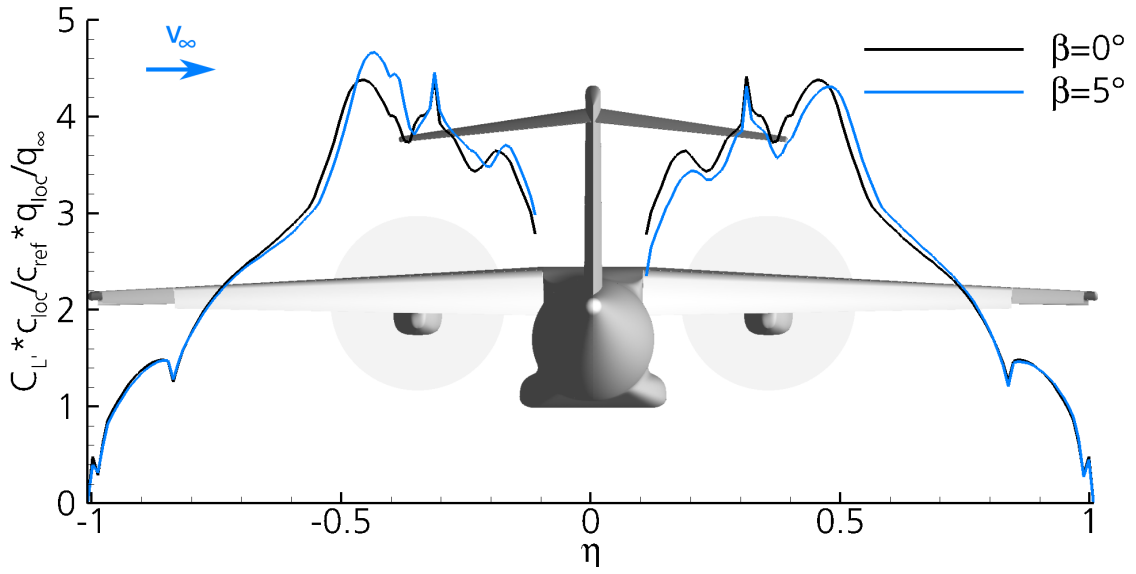

Figure 5.29: Influence of crosswind on lift distribution for symmetrically rotating propellers (inboard down) at $C_\mu = 0.03$ and $\alpha = 0°$

Asymmetric Rotational Direction With the propellers rotating asymmetrically, the propeller load shift behaves as known from the symmetric cases, i.e., increased thrust in those regions where the blade rotation is opposed to the crosswind and reduced thrust in those regions where the blades are rotating with the crosswind. The influence of crosswind on the slipstream evolution at the lower side of the main wing is also similar. Crosswind has therefore little influence on the slipstream evolution at the windward side and/or if the propeller is rotating inboard down. A notable influence can only be observed at the leeward side if the propeller is rotating inboard up, here. In summary, the trends in the lift distributions with respect to crosswind in the case of asymmetrically rotating propellers agree well with the trends seen for the symmetric cases.

It can be concluded that at the main wing, circulation control, in combination with crosswind, leads to a reduced lift on the outer wing of the windward side and an increased lift on the outer wing of the leeward side. With propellers on, the influence is complex and depends on the propeller's sense of rotation. Besides changes due to altered propeller loads distributions and a shift in the slipstream's area of influence, a change in slipstream induced flow separation below the main wing impacts the main wing's force generation the most. The latter notably reduces the local lift in the midspan region of the leeward-sided main wing, if the propeller on this side rotates in inboard up direction.

Fuselage and Tail

The VTP obviously plays a key role for the stability behavior in lateral motion. Additionally, the rear part of the fuselage is important due to its distance to the center of gravity. The flow conditions at the rear, and thus the generation of forces, are influenced by the main

wing's wake. Circulation control and propellers can have a significant impact on the wake evolution, as seen in Section 5.1.4. The following sections therefore cover the influence of circulation control and the propellers on the flow conditions behind the main wing and their effects on the surface pressure distribution in case of crosswind.

Influence of Circulation Control Figure 5.30 visualizes the main wing's wake in terms of streamlines colored by the Mach number at $\alpha = 0°$, $\beta = 5°$, and propellers off. Without circulation control (Figure 5.30(a)), the color of the streamlines is entirely blue, indicating low Mach numbers due to the fully separated flow above the flaps. Furthermore, the rotation of the flowfield behind the wing tips and at the inner flap tips is low, as the streamlines demonstrate. With circulation control (Figure 5.30(b)), the wake generally shows higher local Mach numbers. The trailing vortices are more distinct, indicating stronger circulation and thus a stronger variation of the circulation along the wing span, which in turn leads to higher induced velocities within the wake. Due to the crosswind, the inner flap tip vortex at the windward side is moved towards the fuselage. The one at the leeward side is transported away from the fuselage. At the rear end, where the fuselage begins to taper, the windward vortex moves below the fuselage and thus is displaced further towards the leeward side.

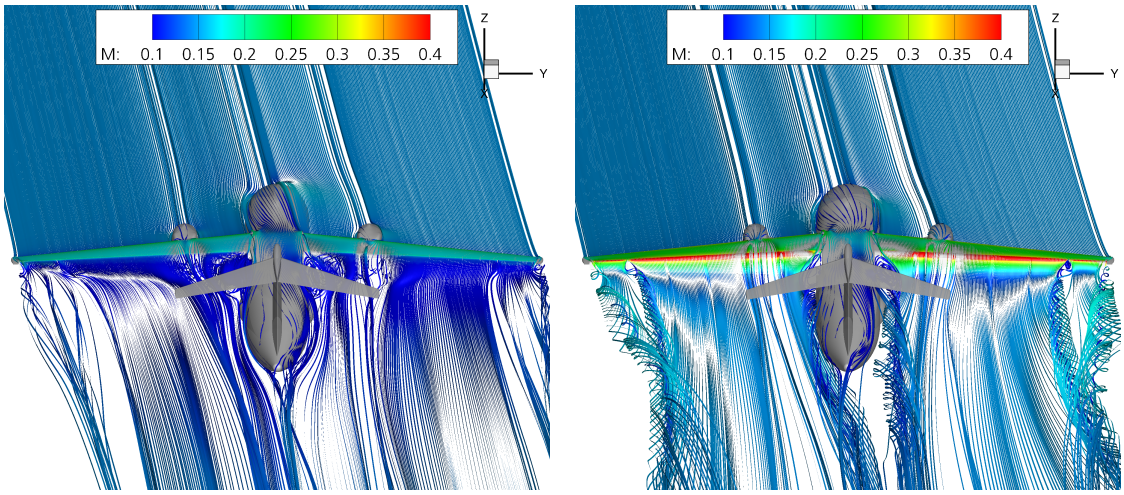

(a) Without circulation control (b) With circulation control

Figure 5.30: Evolution of main wing wake at $\alpha = 0°$ and $\beta = 5°$ (propellers off)

As indicated in Figure 5.30, the vortex system induces flow normal to the freestream direction. With regards to the static stability in lateral motion, the induced flow in spanwise direction at the rear part of the aircraft is of particular interest. It affects the local sideslip angle at the VTP and the rear fuselage, and thus may alter the generation of forces in spanwise direction, leading to significant changes in moments. The flow in spanwise direction which is induced by the trailing vortices can be approximated by subtracting the

crosswind from the absolute spanwise velocity[16]:

$$v_{ind} = v - sin(\beta) \cdot V_\infty \tag{5.2}$$

Figure 5.31 and 5.32 compare the evolution of v_{ind} behind the main wing for the cases without circulation control and with circulation control at $\alpha = 0°$ and $\beta = 5°$. Regions with significant negative induced velocities ($v_{ind} \leq -5$ m/s), which indicate induced flow against the crosswind direction, are colored in blue. The red color represents regions where cross flow in crosswind direction is notably enhanced by induced flow ($v_{ind} \geq 5$ m/s). Vortical structures are visualized by iso-surfaces of the kinematic vorticity number (kvn $= 1.5$) and appear green. Without circulation control (Figure 5.31), the induced spanwise velocities are rather low due to the low main wing circulation with low spanwise gradients of circulation. Focusing on the region along the fuselage, the visualization shows negative induced velocities at the lower leeward (starboard) side of the fuselage and slightly positive induced velocities on the upper leeward side. Both are mainly caused by the inner flap tip vortex. The induced velocities at the lower side of the fuselage are further enhanced by the lower part of the main wing horse shoe vortex[17]. Due to the symmetry of the vortex topology, the induced flow along the fuselage on the windward (port) side is heading in opposite direction. However, the regions of induced velocities are not fully symmetric. At the upper side, the region with high induced velocities on the leeward side appears to be closer to the aircraft's symmetry plane. The impression may be misleading, since v_{ind} is also affected by the displacement effect of the fuselage and, in particular, that of the VTP. The indication of v_{ind} in proximity to the VTP, for instance, is caused by deflection and thus cannot be considered induced flow that is caused by trailing vortices. Keeping this in mind, the visualization demonstrates that the VTP is not significantly affected by induced velocities from the trailing vortices.

[16]The approximation of v_{ind} does not consider additional effects such as the influence of the fuselage on the flow.

[17]The horse shoe vortex occurs due to the boundary layer of the fuselage approaching the main wing. Its evolution is described in more detail in [5].

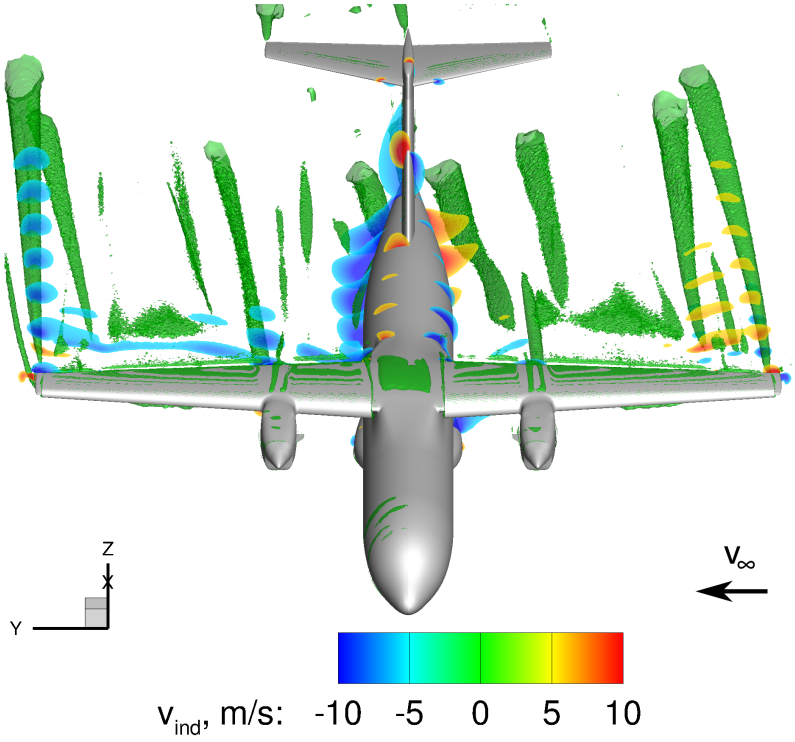

Figure 5.31: Evolution of induced spanwise velocities due to trailing vortices at $C_\mu = 0$, $\alpha = 0°$, and $\beta = 5°$ (propellers off)

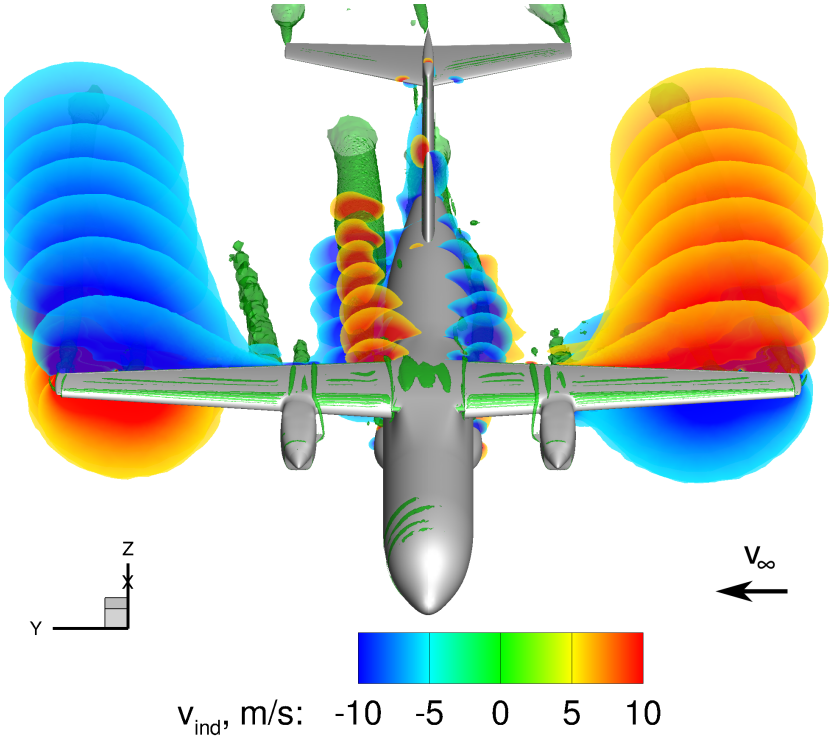

Figure 5.32: Evolution of induced spanwise velocities due to trailing vortices at $C_\mu = 0.03$, $\alpha = 0°$, and $\beta = 5°$ (propellers off)

With circulation control, the induced spanwise velocities downstream of the main wing increase considerably, as shown in Figure 5.32. The increased magnitude of v_{ind} is generally caused by the higher intensity of the trailing vortices, resulting from the higher main wing circulation and the accompanied larger spanwise gradients. Again, focusing on the region close to the fuselage, the inner flap tip vortex is well resolved on the leeward side, causing strong positive induced spanwise velocities above the vortex and negative ones below the vortex. As illustrated in Figure 5.30(b), the vortex is transported away from the fuselage along its path at the leeward side. The regions of high spanwise induced velocities are therefore shifted away from the fuselage and their impact on the incidence angle of the flow at the VTP is reduced. On the windward side, the diameter of the kvn isosurface which represents the inner flap tip vortex is considerably smaller than the one on the leeward side. The regions of significant v_{ind} values also appear smaller. This indicates decreased strength of the inner flap tip vortex on the windward side compared to the leeward side. In addition to the slightly lower lift at the inboard region of the windward side compared to the leeward side, the vortex evolution is thought to be the reason for this. The vortex core on the leeward side is further away from the fuselage compared to the one at the windward side. Furthermore, due to the rotational sense of the vortex, the position where its induced flow opposes the crosswind is located below the vortex core. Here, the crosswind is disturbed by the fuselage. Above the vortex, where the flow field is fully influenced by the crosswind, the induced flow is in crosswind direction. In contrast, the rotational sense of the vortex on the windward side is opposite. The direction of the induced flow is therefore opposed to the crosswind direction above the vortex. Both the smaller distance to the fuselage and the higher difference in velocities between the freestream and the induced flow above the vortex lead to higher shear stresses and thus to higher viscous and turbulent losses. These increased losses are expected to be a cause for the lower vortex strength on the windward side.

Due to the transportation of the inner flap tip vortex towards the fuselage on the windward side, the region with meaningful induced spanwise velocities is significantly closer to the aircraft's symmetry plane and the VTP. It therefore appears that the negative induced spanwise flow above the inner flap tip vortex on the windward side has a bigger influence on the VTP incidence angle than the positive induced spanwise flow above the leeward-sided inner flap tip vortex.

With rising angle of attack, the strength of the trailing vortices increases, as illustrated for the case with circulation control at $\alpha = 10°$ in Figure 5.33. Although both IBF vortices move in upward direction, the vertical position of the vortex on the leeward side is considerably higher than the position of the one on the windward side adding to the asymmetry of the vortex system already seen for $\alpha = 0°$ (Figure 5.32). Due to the altered positions of the inner flap tip vortices, the flow conditions above the fuselage are now dominated by the induced flow from the lower side of the leeward-sided inner flap tip vortex and the induced flow from the upper side of the windward-sided inner flap vortex. Both oppose the crosswind.

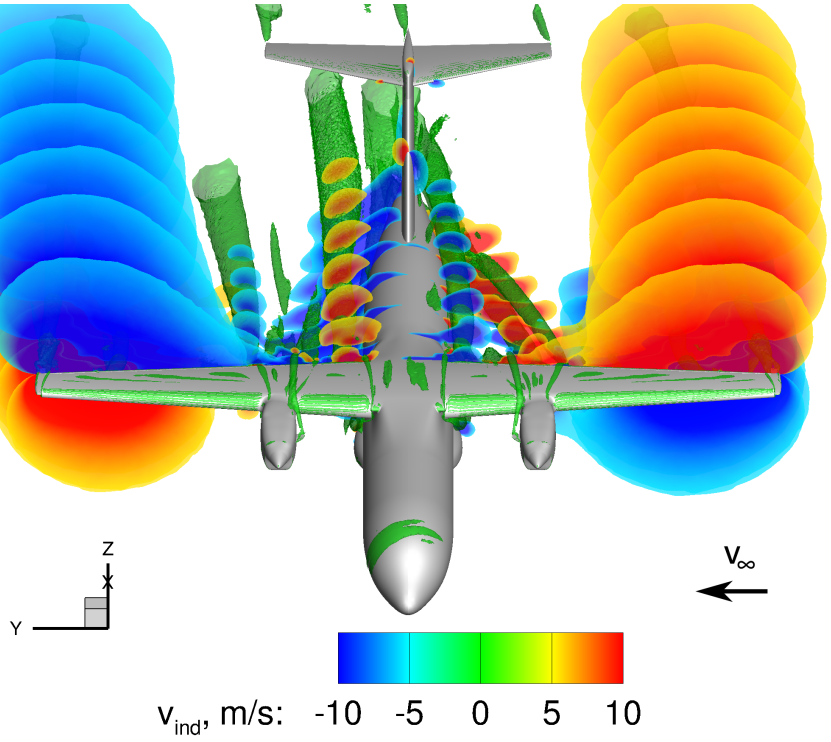

Figure 5.33: Evolution of induced spanwise velocities due to trailing vortices at $C_\mu = 0.03$, $\alpha = 10°$, and $\beta = 5°$ (propellers off)

Taking into consideration the observations made from the vortex visualization and the in-plane flow illustrations, it can be concluded that in contrast to the case without circulation control, the inner flap tip vortices have a significant effect on the flow conditions at the VTP with circulation control. For all investigated angles of attack, the vortices are transported towards the leeward side. As a result, the region above the fuselage, particularly at the position of the VTP, is located within the negative sidewash of the windward-sided vortex. At small angles of attack, the inner flap tip vortices do not affect the oncoming flow at the VTP significantly, as they are not strong enough and positioned too low with respect to the VTP. However, with rising angle of attack, the strength of the vortices intensifies, and the vortex system moves in upward direction. Furthermore, the inner flap tip vortices start to diverge vertically with rising angle of attack. As a result, the negative sidewash at the VTP root is intensified by the leeward-sided vortex. Figure 5.34 illustrates the trailing vortex system, the induced flow, and the resulting influence on the surface pressure distribution for the case with circulation control at high angles of attack. The basic downward direction of the induced flow is caused by the main wing's downwash. In proximity to the fuselage, the flow is then affected by the inner flap tip vortices, as described above. The incidence angle of the VTP is therefore reduced at its root, which in turn reduces the surface pressure on the windward side and increases the surface pressure on the leeward side of the VTP. Furthermore, the core of the inner flap tip vortex on the windward side reduces the surface pressure on the fuselage along its path due to its proximity to the fuselage. In summary, the vertical forces of the VTP and the fuselage under

crosswind conditions are reduced with circulation control for two reasons: the strength of the inner flap tip vortices and their asymmetric displacement due to the crosswind. It is also important to note that the induced velocities at the position of the VTP originate from trailing vortices rather than pressure differences above the main wing.

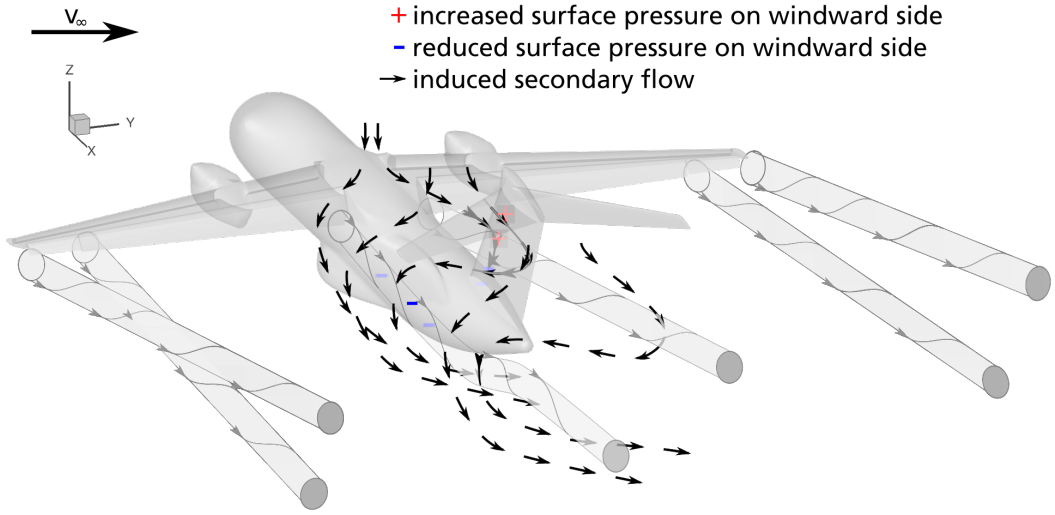

Figure 5.34: Wake topology and resulting induced secondary flow for activated circulation control at positive sideslip angle and high angles of attack (propellers off)

Influence of the Propellers As demonstrated in Section 5.1.4, the use of wing-mounted propeller engines also has an impact on the wake evolution that has to be assessed for crosswind conditions, as well. On the one hand, the propeller slipstream directly changes the flow conditions at the rear fuselage and the VTP. On the other hand, the change in lift distribution due to the interaction of the slipstream with the main wing leads to an altered trailing vortex system. As a result, the propeller slipstream is expected to play a significant role for the flow conditions at the rear fuselage and the VTP.

The evolution of the slipstream is influenced by three main factors. Firstly, the direction of the onset flow is important as it determines the basic direction the slipstream is transported to. Secondly, the slipstream evolution is affected by the trailing vortices and vice versa. Thirdly, the slipstream and also the trailing vortex evolution are strongly dependent on engine parameters such as the rotational sense of the propellers. Again, the discussion of the propeller effects focuses on the case with the propellers rotating symmetrically in inboard up direction, whereas the cases with propellers either rotating symmetrically inboard down or asymmetrically are described in less detail.

Symmetric Inboard Up Figure 5.35(a) visualizes the slipstream evolution in terms of an iso-surface for the total pressure ratio of $p_t/p_{t,\infty} = 1.02$[18] for the case with circulation control and propellers symmetrically rotating inboard up at $\alpha = 0°$ and $\beta = 5°$. The iso-surface indicates that the slipstream is transported towards the starboard side due to the crosswind. When it reaches the main wing, the slipstream tube of each propeller is split into two parts. The upper part can pass the wing with little resistance and therefore retains its shape. Further downstream the iso-surface begins to contract due to momentum diffusion and dissipation. Due to the crosswind, the upper part of the slipstream on the port side tends to move towards the starboard side. However, its swirl and the sidewash of the inner flap tip vortex prevent it from moving closer to the fuselage. At the starboard side, the swirl and the sidewash of the inner flap tip vortex support the transportation towards the wing tip.
Below the main wing, the slipstream is partially blocked by the flap and is therefore deflected to the sides. Here, the propeller's rotational direction and the induced velocities of the inner flap tip vortices below the vortex cores transport the slipstream towards the fuselage. As a result, the slipstream moves below the fuselage downstream of the main wing. On the windward side, this effect is supported by the crosswind, whereas it is counter-acted by the crosswind on the leeward side.

The influence of the propeller slipstream on the wake evolution is illustrated in Figure 5.35(b) in terms of streamlines. In the outboard regions of the wing, the wake looks similar to the one with propellers off (Figure 5.30(b)). However, behind the propellers and in proximity to the fuselage, the wake evolution is significantly altered. The propellers lead to higher Mach numbers, which is indicated by the color of the streamlines. The changes in the lift distribution introduced by the slipstream (see Figure 5.10) also cause additional vortical structures, as discussed in Section 5.1.2. Parts of the accelerated flow on the windward side are entrained by the inner flap tip vortex and pass below the fuselage.

[18] A total pressure ratio of $p_t/p_{t,\infty} > 1$ indicates flow with momentum in excess of the freestream momentum that is introduced via propeller forces and/or circulation control. The cut-off value $p_t/p_{t,\infty} = 1.02$ ensures the visualization of the slipstream core while its definition is somewhat arbitrary.

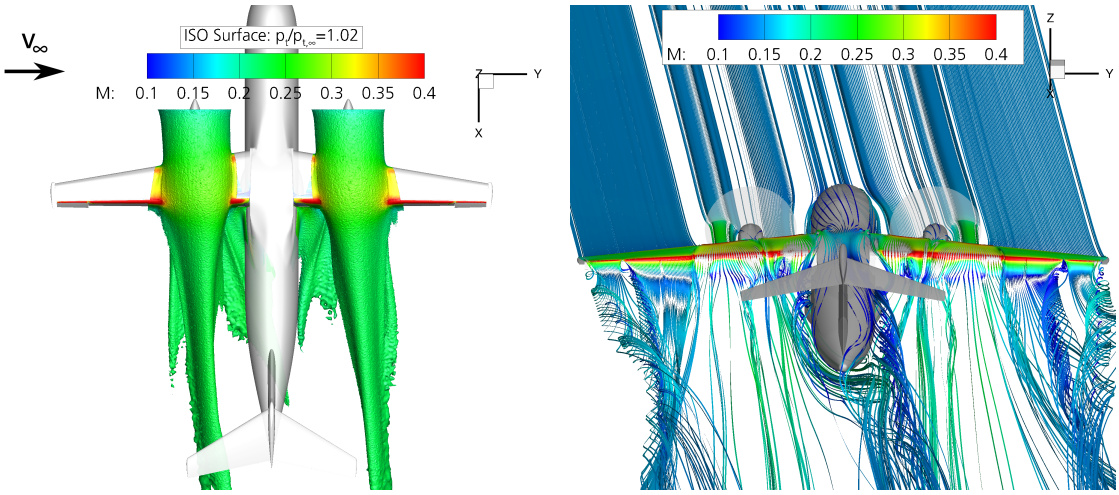

(a) Slipstream (b) Main wing boundary layer

Figure 5.35: Evolution of main wing wake with symmetrically rotating propellers (inboard up) at $C_\mu = 0.03$, $\alpha = 0°$, and $\beta = 5°$

The vortex evolution and the resulting spanwise induced velocities are depicted in Figure 5.36. Compared to the corresponding case with propellers off (Figure 5.32), the lateral displacement of the inner flap tip vortices is notably bigger. Furthermore, the region of negative induced spanwise flow above the inner flap tip vortex at the windward side appears considerably larger due to the influence of the slipstream swirl. The flow conditions at the VTP are therefore dominated by induced flow in negative spanwise direction.

The visualization of the wake evolution and the induced spanwise velocities demonstrate that the flow conditions at the tail are significantly altered by the propellers. In order to illustrate their impact on the generation of forces at the tail, contour plots of the surface pressure coefficient with skin friction lines are shown. Figure 5.37(a) depicts the surface pressure coefficient and the skin friction lines at the windward side. On the fuselage, three characteristic low pressure regions exist at the rear, which lead to a negative side force. The first one results from the inner flap tip vortex core, which can be easily identified by its separation and attachment lines. The second one is directly related to the slipstream. When the lower part of the slipstream from the windward side passes below the fuselage (Figure 5.35), the fluid near the fuselage is entrained, which in turn leads to a pressure deficit at the surface. A third low pressure region exists at the end of the fuselage below the VTP. Here, the flow coming from above the fuselage is accelerated by the inner flap tip vortex of the windward side, which has moved below the fuselage and therefore induces a downwash at this location.

The VTP surface pressure distribution, in particular in the root region, is affected by the negative induced spanwise velocities above the fuselage. Here, the pressure coefficient reaches negative values at the position of the VTP's maximum thickness despite being on the windward side. Furthermore, the high pressure zone at the nose indicates a movement of the stagnation line towards the front compared to the case without crosswind (not

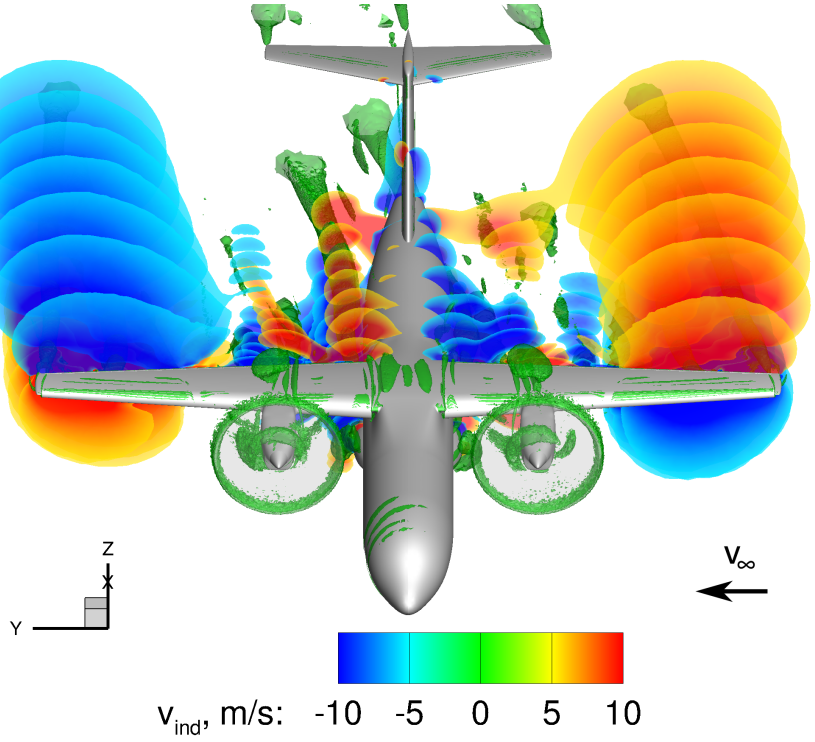

Figure 5.36: Evolution of induced spanwise velocities due to trailing vortices and slipstream in the case with circulation control and symmetrically rotating propellers (inboard up) at $\alpha = 0°$ and $\beta = 5°$

shown).

At the leeward side (Figure 5.37(b)), only one significant low pressure zone exists on the fuselage. As already indicated by Figure 5.36, the C_p distribution confirms that the inner flap tip vortex on the leeward side is stronger than the one at the windward side. However, when traveling downstream, the vortex core moves away from the fuselage, reducing its footprint. Contrary to the windward side, the skin friction lines below the vortex core point in upward direction due to the tapering of the fuselage, which is supported by the upwash of the inner flap tip vortex. The skin friction lines above the vortex core point in downward direction first, as they are dominated by the downwash. Further downstream, when the inner flap tip vortex of the windward side moves below the tapering fuselage, the skin friction lines change their direction upwards, as they are now influenced by the upwash of both of the inner flap tip vortices. The strong impact of the inner flap tip vortex on the windward side is also evidenced by the VTP's pressure distribution on the leeward side. The VTP's suction peak at the leading edge, which is caused by the sideslip angle, is degraded particularly at the root region due to the adverse cross flow that is induced mainly by the inner flap tip vortex on the windward side.

Based on the findings of the analysis of the wake evolution and the pressure coefficient contour plots with skin friction lines, Figure 5.38 sketches the most significant flow phenomena and the resulting topology of the induced flow at the aft fuselage. Accordingly,

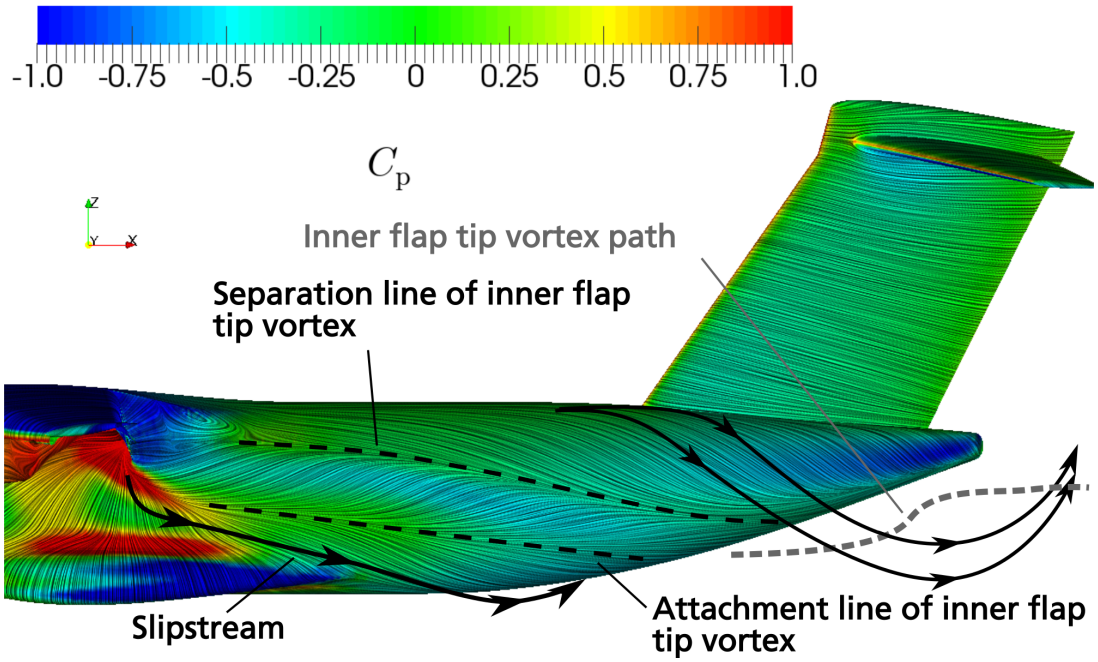

(a) Windward side

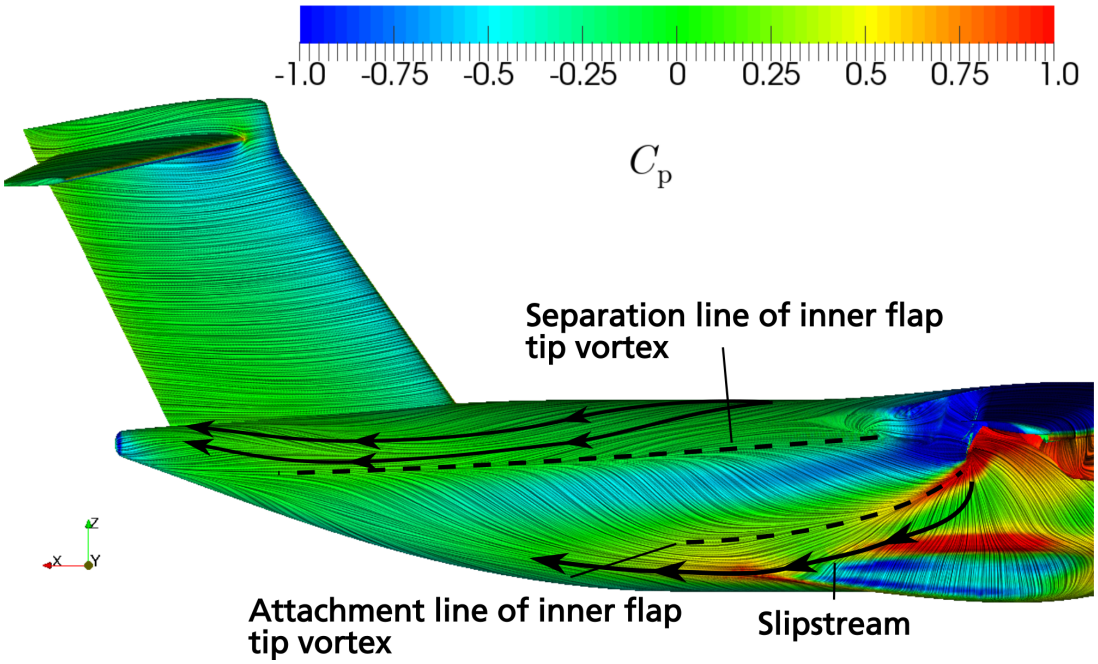

(b) Leeward side

Figure 5.37: Surface pressure coefficient distribution and skin friction lines for propellers rotating symmetrically inboard up at $C_\mu = 0.03$, $\alpha = 0°$, and $\beta = 5°$

the inner flap tip vortex on the windward side (red) and the one on the leeward side (blue) are transported towards the leeward side due to the crosswind, as discussed before. As

a result, the vortex on the windward side moves below the fuselage after the latter begins to taper. The lower part of the slipstream (green arrows) on the windward side is also directed towards the leeward side due to its swirl and the crosswind. This tendency is further enhanced by the inner flap tip vortex on the windward side as it induces flow in positive spanwise direction on its lower side. When the slipstream passes below the fuselage, it entrains the fluid in proximity to the fuselage and thus attaches to the latter (Cõanda effect). Due to the attachment to the fuselage and the induced upwash of the inner flap vortex on the leeward side, the slipstream is directed in upward direction once it has passed below the fuselage. The slipstream from the windward side supports the displacement of the inner flap tip vortex on the leeward side towards the wing tip caused by the crosswind. The behavior of the inner flap tip vortices and the slipstream leads to additional induced flow due to momentum transfer and resulting pressure differences, which is symbolized by black arrows. In particular, the inner flap tip vortex and the slipstream on the windward side induce flow around the fuselage including negative induced cross flow above the aft fuselage, as demonstrated in Figure 5.36. The induced flow alters the pressure distribution on the rear fuselage and the VTP, as indicated by the plus and minus signs and illustrated in more detail in Figure 5.37.

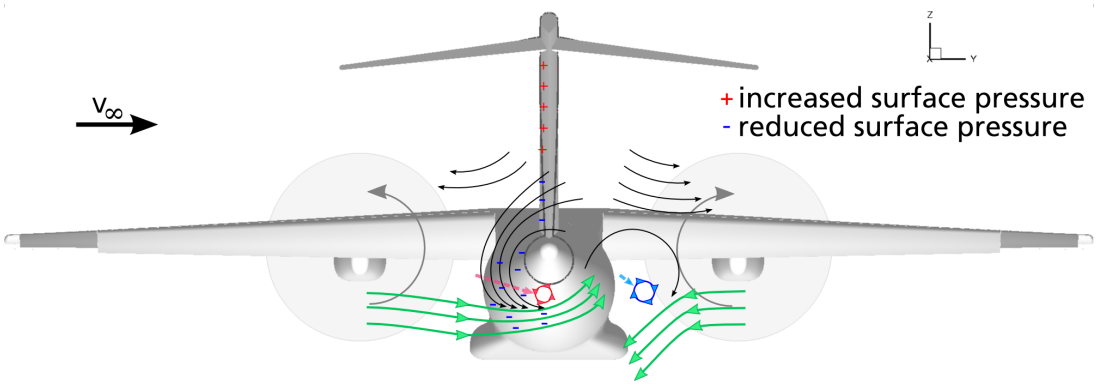

Figure 5.38: Schematic view of significant flow phenomena and crossflow topology at the aft fuselage in the case with circulation control and symmetrically rotating propellers (inboard up) at $\alpha = 0°$ and $\beta = 5°$

Symmetric Inboard Down Switching the propellers' sense of rotation to inboard down has several effects that affect the flow conditions at the rear fuselage. Firstly, the lift distribution of the main wing is altered with the peak in lift now being located in the midboard region of the wing (see Figure 5.29). This results in reduced strength of the inner flap tip vortices. Secondly, the lower part of the slipstream of the windward side does not attach to the fuselage as its direction points away from the fuselage due to the swirl. Thirdly, the direction of swirl counteracts the lateral displacement of the inner flap tip vortex on the leeward side, causing it to be located closer to the fuselage compared to symmetric inboard up rotation. However, the upper part of the slipstream from the windward side can attach to the fuselage and thereby adversely affect the directional stability under certain

conditions, e.g. if the angle of attack and sideslip angle are increased.[19]

Asymmetric Rotational Direction The behavior of the main wing wake and the slipstream with asymmetrically rotating propellers is highly dependent on the propeller's sense of rotation at the windward side. When the propeller turns inboard up at the windward side, the behavior is similar to the one at symmetric inboard up rotational sense. In contrast, if the sense of rotation of the propellers is reversed to inboard down on the windward side and inboard up on the leeward side, the behavior is similar to the one at symmetric inboard down rotation. Due to the asymmetry in slipstream development, these cases already impact the flow conditions at the tail at zero crosswind. The topologies of the induced velocities at zero crosswind are identical to the ones seen for $\beta = 5°$ of the corresponding cases with symmetrically rotating propellers.

The analysis of the flowfield behind the main wing demonstrates that circulation control notably alters the local flow conditions at the VTP position due to the increased strength of the inner flap tip vortices. With rising angle of attack, the local sideslip angles at the VTP due to crosswind are increasingly affected by induced spanwise cross flow, which opposes the crosswind. With propellers on, additional phenomena may occur, depending on several parameters such as the angle of attack, the sideslip angle, and the sense of rotation of the propellers. At $\alpha = 0°$, $\beta = 5°$, and propellers rotating inboard up, the slipstream in conjunction with the inner flap tip vortices lead to a pronounced asymmetric pressure distribution on the rear fuselage.

5.2.2 Static Directional Stability

Static directional stability is defined as the ability to recover "from a skid with the rudder free" [117]. The aircraft's yawing moment in response to crosswind is therefore essential for natural static directional stability[20]. Based on the aerodynamic phenomena caused by crosswind (Section 5.2.1), this section covers the influence of circulation control and the propellers on the static directional stability. Since the vertical tail plane and the fuselage are the main contributors to the yawing moment due to sideslip, these components are discussed in detail.

Influence of Circulation Control

Figure 5.39(a) depicts the yawing moment coefficient of the VTP with respect to the sideslip angle for varying circulation control settings and varying angles of attack with propellers off. Without circulation control and $\alpha = 0°$, the yawing moment changes with

[19] The evolution of the slipstream, the main wing wake, and the resulting yawing moments for symmetric thrust and propellers rotating inboard down are illustrated in Appendix D.

[20] For the aircraft being directionally stable, the yawing moment derivative with respect to the sideslip angle has to fulfill $C_{n\beta} > 0$ with $C_{n_{(\beta=0°)}} = 0$ [90].

rising sideslip angle at a nearly constant positive slope, showing a stabilizing behavior. Simulations at $\alpha = 6°$ indicate that the yawing moment contribution from the VTP is not affected by a change in α in the case without circulation control (not shown). With circulation control, the magnitude of the yawing moment at $\beta = 5°$ is reduced due to the flow conditions that are altered by the main wing wake (see Section 5.2.1). If the angle of attack is raised to $\alpha = 10°$, the yawing moment coefficient at $\beta = 5°$ is significantly lower than in the other cases, leading to a reduced $C_{n\beta}$ at low sideslip angles. The reduced yawing moment contribution from the VTP can be attributed to the increased asymmetric flow induced by the inner flap tip vortices at the VTP position (Figure 5.33). The higher yawing moment at $\beta = 10°$ indicates that $C_{n\beta}$ increases at larger sideslip angles.

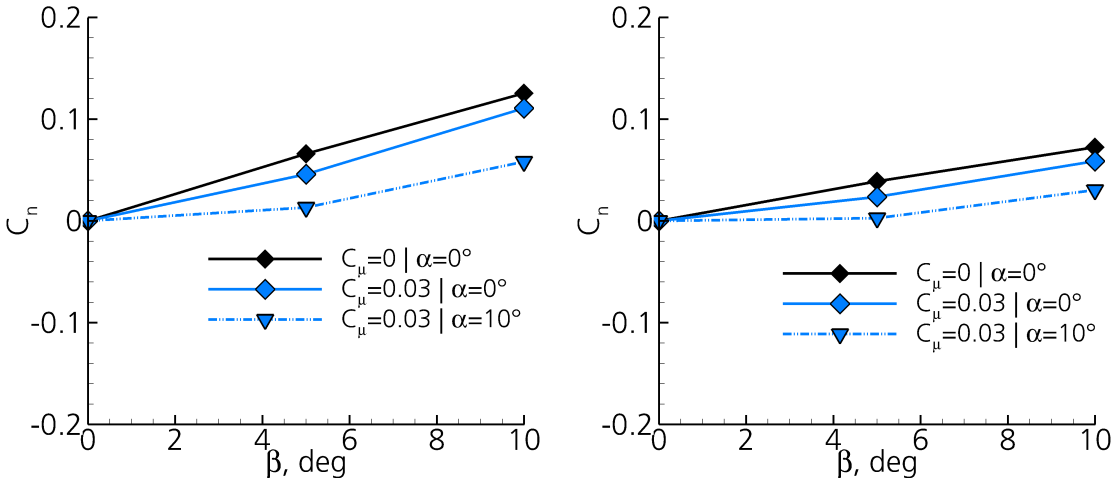

(a) VTP (b) Airframe

Figure 5.39: Yawing moment depending on sideslip angle for varying circulation control modes and angles of attack with propellers off

Compared to the yawing moment contributions from the VTP, the yawing moment curves for the complete airframe are shifted further towards the stability limit (Figure 5.39(b)). In particular, the contributions from the fuselage, which arise due to the proximity of the inner flap tip vortex to the fuselage on the windward side (Figure 5.34), adversely impact the stability. With rising angle of attack, the vortex path moves in upward direction, increasing the interference length with the fuselage due to its conical shape at the rear. In addition, the vortex strength increases with rising angle of attack. This results in a yawing moment coefficient of only $C_n = 0.02$ at $\alpha = 10°$ and $\beta = 5°$.

Influence of the Propellers

Figure 5.40 depicts the yawing moment contribution of the VTP, the fuselage, and the resulting entire aircraft due to sideslip at $C_\mu = 0.03$ and $\alpha = 0°$ with propellers that are rotating inboard up. At low sideslip angles, the yawing moment contribution from the VTP is rather small, with the yawing moment at $\beta = 2°$ being even negative. The

effect can be attributed to the induced spanwise flow at the VTP position, as sketched for $\beta = 5°$ in Figure 5.38. For $\beta > 2°$, the yawing moment steadily increases. In contrast, the yawing moment of the fuselage steadily decreases with rising sideslip angle, yielding a destabilizing effect in terms of directional stability. Similar to the behavior of the VTP's yawing moment curve, the most destabilizing behavior of the fuselage occurs at low sideslip angles and is caused by the effects discussed before (Section 5.2.1). The yawing moment of the entire aircraft is mainly driven by the fuselage and the VTP. The influence of the forces on the propellers is negligible ($|C_{n,prop}| < 0.005$). As a result, the yawing moment becomes negative at $\beta = 2°$, indicating unstable behavior at low sideslip angles. At higher sideslip angles, the slope of the C_n-β curve becomes positive, indicating a stable behavior in terms of directional stability. The directional stability with propellers on is strongly dependent on the angle of attack, as computations at $\alpha = 6°$ reveal. With rising α, the sideslip range of directional instability is shifted to higher sideslip angles.

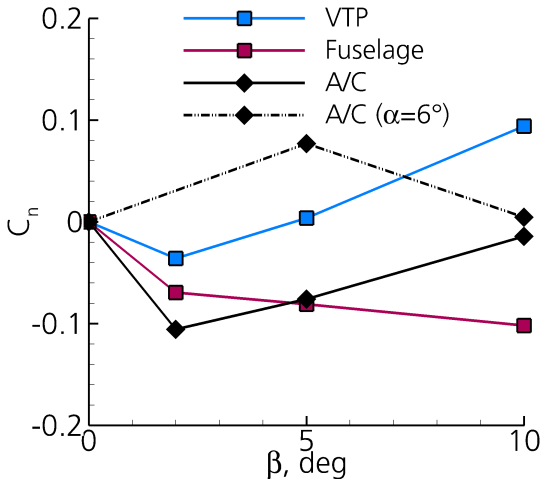

Figure 5.40: Yawing moment of components and entire aircraft depending on sideslip angle for $C_\mu = 0.03$ and propellers on (I/B up)

If the rotational direction of the propeller is switched to symmetric inboard down (not shown), the aircraft is even more stable than without circulation control and with propellers off.[21] However, simulations at $\alpha = 10°$ indicate that the directional stability is significantly degraded at higher angles of attack (see Figure D.3 of the Appendix D). Similar to the behavior observed with the propellers rotating inboard up, $\alpha = 0°$, and low sideslip angles (see Figure 5.40), the fuselage contributes a large destabilizing yawing moment under these conditions, as the upper part of the slipstream on the windward side leads to a low pressure zone at the rear fuselage (see Figure D.2).

As discussed before, the behavior of the main wing wake and the slipstream of the asymmetric cases is determined by the rotational sense of the propeller on the windward side. The yawing moments at $\beta = 5°$ therefore correlate with the corresponding symmetric

[21] A comparison of the VTP's C_p distribution and stagnation pressure between the different cases indicates an increased dynamic pressure due to circulation control and/or propeller slipstream to be the reason for higher stability.

cases. However, the gradients are switched due to the non-zero yawing moments[22] at $\beta = 0°$. Consequently, the aircraft is directionally unstable if the propeller at the windward side rotates inboard down, and it is stable, if the propeller rotates inboard up on the windward side. In other words, the flow conditions under which the configuration is directionally unstable shift to another region of sideslip angles.

The noted stability concerns only exist for the combination of active circulation control with propellers on. Without circulation control (not shown), the directional stability is also preserved with propellers on due to the lower strength of the inner flap tip vortices.

In summary, circulation control has an adverse effect on the directional static stability mainly due to the asymmetric evolution of the inner flap tip vortices and the resulting induced velocities at the VTP. The unfavorable impact on the directional stability increases with rising angle of attack. Nevertheless, the configuration remains stable for the investigated cases.

The influence of the propellers on the directional stability depends on several factors such as angle of attack, sideslip angle, rotational sense of the propellers, and circulation control mode. While the configuration is directionally stable for most of the cases, the case with circulation control and the propellers rotating symmetrically inboard up at small angles of attack and small sideslip angles is found to be one of the most critical ones. In this case, the configuration is directionally unstable. The analysis of the flow field at the rear fuselage indicates that the interaction of the propeller slipstream with the inner flap tip vortices and with the fuselage leads to several effects, which cause destabilizing forces at the rear fuselage and the VTP. For higher angles of attack, the directional instability occurs at higher sideslip angles. Changing the propellers' sense of rotation also shifts the most critical case to higher angles of attack and sideslip angles. Based on these findings, a separate numerical study has been performed, which indicates a notable improvement of the directional stability due to the integration of tail fences to the fuselage [1].

The basic trends of the present simulation results agree well with NASA's findings from wind-tunnel and flight tests during the 1960's. When Weiberg et al. tested a transport model configuration with four wing-mounted propellers and boundary layer control, they experienced static directional instability for 60° flap deflection and high thrust coefficients [30]. The model's propellers were all rotating "right-hand-side". The instability was encountered asymmetrically at sideslip angles of $\beta > 4°$. Flight tests with the two-propeller YC-134A also indicated that the "lateral-directional damping may decrease to unacceptable values." The documented rudder control force required for steady-state sideslip was extremely nonlinear and "considered unsatisfactory beyond 10° sideslip" [31]. Both observations agree well with the behavior identified in the present simulations with asymmetrically turning propellers. Furthermore, the instability during Weiberg's wind-tunnel test vanished when the flaps were retracted or the thrust was reduced [30]. The present simulations with strongly reduced main wing circulation due to deactivated circulation control (not shown) indicate increased stability compared to the case with circulation control, as

[22] The yawing moment due to asymmetrically rotating propellers at $\beta = 0°$ ($C_n = 0.15$) is equivalent to the yawing moment due to rudder deflection of approximately 18 degrees based on recent studies [7].

well. Again, the experimental investigations by NASA did not reveal the cause of the aircraft's unsatisfying behavior. Due to the flowfield analysis of the simulation results, causes for the similar behavior of the present configuration have been found. The favorable correlations with the experimental results from NASA strengthens their reliability.

5.2.3 Static Lateral Stability

In contrast to a disturbance in angle of attack or sideslip angle, aircraft do not directly create a restoring moment due to a change in roll angle. However, if an aircraft in level flight starts to bank, the lift vector is tilted with respect to the gravity force vector. The resulting force imbalance in spanwise direction leads to a sideslip angle. If the sideslip angle then causes the aircraft to roll back, the aircraft is considered to be laterally stable[23]. Typically, the main contributors to a stabilizing rolling moment due to sideslip ($C_{l\beta}$) – also known as dihedral effect – are the main wing and the VTP. The following sections will discuss the influence of circulation control and the propellers on the static lateral stability.

Influence of Circulation Control

As seen in Section 5.2.1, crosswind leads to an asymmetric lift distribution on the main wing. The asymmetric lift distribution due to sideslip creates a rolling moment, which is depicted in Figure 5.41(a) for the cases with propellers off. Without circulation control, the rolling moment coefficient is negative for $\beta > 0°$. With the magnitude increasing with rising sideslip angle, the main wing contribution is stabilizing. With circulation control, the main wing creates a positive, destabilizing rolling moment due to the asymmetric load at the outboard wing (Figure 5.23). The rolling moment coefficient increases nearly linearly with rising sideslip angle. The trend is unchanged at $\alpha = 10°$, with the magnitude of the rolling moment coefficient being increased slightly.
In addition to the main wing, the VTP contributes with a stabilizing rolling moment in all cases (Figure 5.41(b)). Analogous to the yawing moment coefficient (Figure 5.39(a)), the rolling moment coefficient is degraded with circulation control due to the wake-VTP interaction discussed in Section 5.2.1. Furthermore, the magnitude of the rolling moment coefficient decreases with rising angle of attack when circulation control is active. The influence of the angle of attack on the rolling moment coefficient is therefore of similar importance as it is for the yawing moment coefficient.
The rolling moment coefficient with respect to the sideslip angle of the entire airframe is shown in Figure 5.41(c). Due to the stabilizing influence of the main wing and the VTP, the entire airframe is stable without circulation control. With circulation control, the static lateral stability is reduced. At $\alpha = 0°$, C_l at $\beta = 5°$ is approximately zero. At higher sideslip angles, the rolling moment coefficient slightly increases in magnitude, leading to

[23] For the aircraft being laterally (static) stable, the rolling moment derivative with respect to the sideslip angle has to fulfill $C_{l\beta} < 0$ with $C_{l_{(\beta=0°)}} = 0$ [118].

higher static lateral stability. At $\alpha = 10°$, the rolling moment becomes positive, resulting in a positive slope $C_{l\beta}$, i.e. static lateral instability.

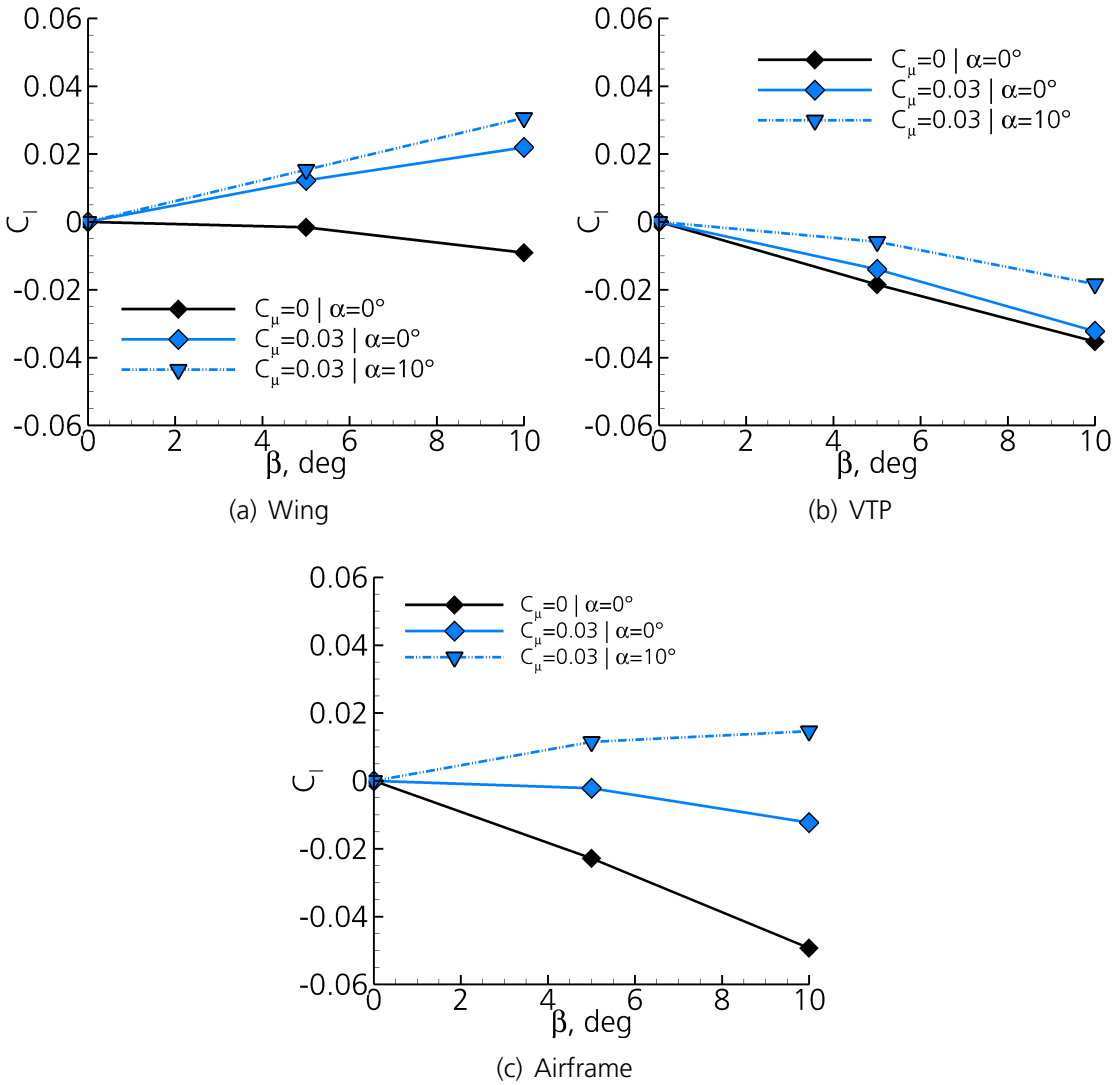

Figure 5.41: Rolling moment depending on sideslip angle for varying circulation control modes and angles of attack (propellers off)

Influence of the Propellers

The varying effects of the propeller slipstream in conjunction with circulation control, which were discussed in Section 5.2.1, lead to a rolling moment coefficient due to sideslip angle that features a change in sign and slope depending on β, as illustrated in Figure 5.42 for propellers rotating symmetrically inboard up. In this case, the main wing creates a restoring rolling moment at $\beta = 5°$. Compared to the case with circulation control and propellers off (Figure 5.41(a)), the main wing's C_l is considerably reduced. However, at higher sideslip angles, the main wing's rolling moment coefficient becomes positive and

reaches a similar value as in the propellers off case. Under these conditions, the effects of circulation control on the outboard wing dominate. The C_l contribution of the VTP is slightly destabilizing at low sideslip angles. However, with increasing sideslip angle, the C_l of the VTP decreases. It is mainly due to the contribution of the VTP that the airframe is laterally stable except for small sideslip angles. Moreover, the load shift of the propeller forces due to the sideslip, as seen in Figure 5.25, adds to the aircraft's lateral stability (dash-dotted line).

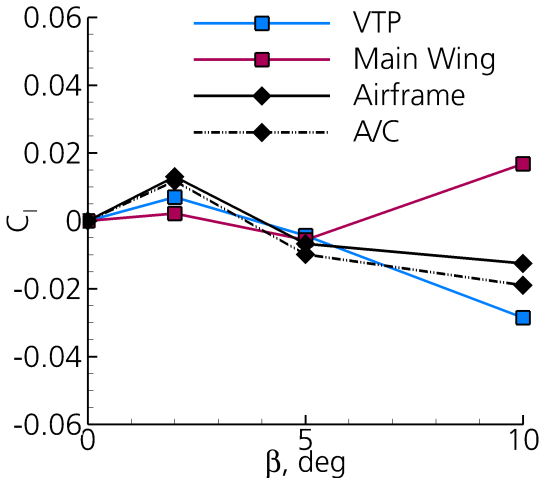

Figure 5.42: Rolling moment of components and entire aircraft depending on sideslip angle for symmetrically rotating propellers (I/B up), $C_\mu = 0.03$, and $\alpha = 0°$

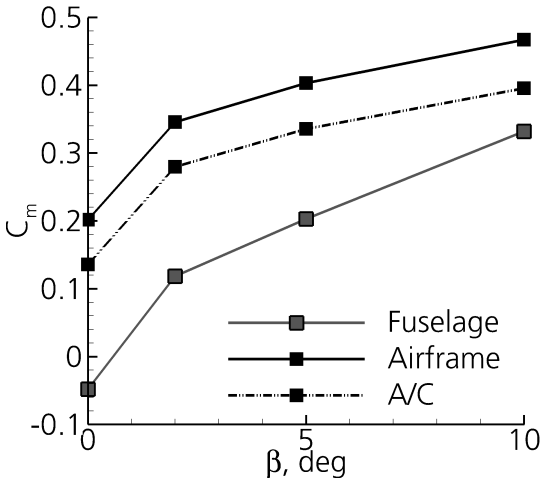

Figure 5.43: Pitching moment coefficient with respect to sideslip angle for symmetrically rotating propellers (I/B up), $C_\mu = 0.03$, and $\alpha = 0°$

It can be concluded that circulation control adversely affects the static lateral stability, particularly at high angles of attack and low sideslip angles. The propellers symmetrically rotating inboard up lead to a varying behavior with respect to the sideslip angle. At small sideslip angles ($\beta \leq 2°$), the aircraft tends to be laterally unstable. For $\beta > 2°$, lateral stability is increased due to the propellers. Analogous to the directional stability behavior, switching the rotational sense of the propellers to symmetric inboard down appears to lead to an increase in static lateral stability at $\alpha = 0°$ (not shown). The case with asymmetrically rotating propellers also reveals similar trends, as seen for the directional stability (not shown). Accordingly, static lateral stability decreases if the propeller on the windward side rotates in inboard up direction, whereas it increases if it rotates in inboard down direction. It shall be noted that with asymmetrically rotating propellers (and with circulation control), the airframe exhibits a notable rolling moment ($C_l = \pm 0.013$)[24] at otherwise symmetric flow conditions ($\beta = 0°$) due to the asymmetric load distribution of the main wing.

The adverse effect of powered lift on the static lateral stability was also documented by

[24]Further studies on the aileron design indicate that an aileron deflection of ±5 to ±7 degrees is required to trim the rolling moment at $\beta = 0°$ depending on the aileron layout.

Weiberg et al. [30]. During their wind tunnel experiment, they encountered a strong reduction in lateral stability in the case of deflected flaps with boundary layer control compared to the case without flap deflection and with no boundary layer control. Applying thrust led to higher variations and changes of sign of the rolling moment gradients. The behavior was considered "unsatisfactory".

5.2.4 Cross-Coupling of Static Longitudinal and Lateral Behavior

The pressure contour in Figure 5.37 points to another important aspect of the aircraft's static behavior with respect to crosswind. With the propellers rotating symmetrically inboard up, the low pressure zone at the lower end of the rear fuselage leads to forces, which also have a vertical component. As a result, the aircraft tends to pitch up. This is also manifested in the trend of the pitching moment coefficient with respect to the sideslip angle (Figure 5.43). The C_m-β curve indicates that the additional pitch up moment due to a change in sideslip is particularly strong at low sideslip angles with $\partial C_m/\partial\beta = 4.1$. For comparison, the static pitching moment derivative with respect to the angle of attack is $\partial C_m/\partial\alpha = -1.8$ in the linear range. At higher sideslip angles, the pitching moment increases further even though with a smaller gradient. The main driver of the increase in pitching moment is the fuselage contribution.

5.2.5 Dynamic Stability

As done for the longitudinal motion, this section discusses the influence of circulation control and the propellers on the aerodynamic properties with respect to the lateral dynamic stability. In lateral motion, three modes exist that are influenced by the dynamic derivatives with respect to a roll and a yaw rate. The aircraft's responses to a quasi-steady roll rate and a quasi-steady yaw rate are therefore investigated.

Roll Motion

The dynamic derivatives due to roll rate C_{lp} and C_{np} affect the dutch roll and the roll subsidence. The roll damping derivative C_{lp} is the only aerodynamic parameter that influences the roll subsidence. It also affects the damping of the dutch roll [90]. The derivatives are estimated via quasi-steady simulations of translatory motions that are super-imposed by roll motions around the aircraft's center of gravity.

Wing Contribution A roll motion induces vertical velocities along the spanwise axis, which increase with the distance to the roll axis. In the case of a positive roll motion, these velocities are positive on the port side and negative on the starboard side. Consequently, the positive roll motion leads to an increasing local angle of attack in negative spanwise direction and a decreasing local angle of attack in positive spanwise direction.

The resulting changes in local angles of attack alter the surface pressure distribution. Figure 5.44 depicts the difference in surface pressure distribution on the upper main wing surface due to a roll rate of $p = 15°/s$ at $\alpha = 6°$ in the case with circulation control and the propellers off. The main differences arise at the leading edge, where the suction peak is increased on the port side (blue color) and reduced on the starboard side (red color). As expected, the magnitude of these differences increases with an increasing spanwise distance to the center of gravity. The suction peak along the flap is adversely affected, as known from 2D α-sweep simulations.[25] Additional differences can be identified along the paths of the nacelle vortices, as they become stronger on the port side and weaker on the starboard side.

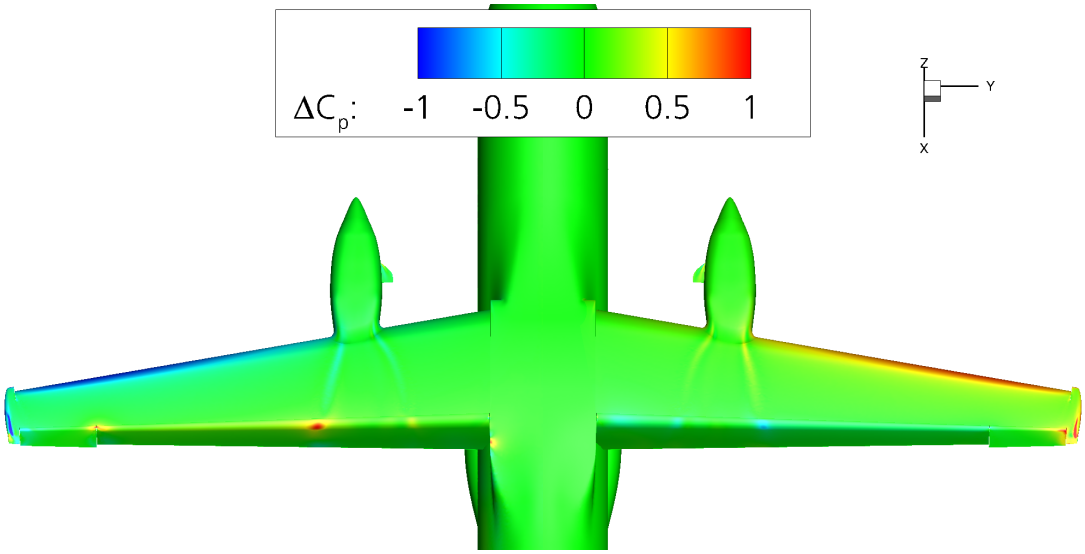

Figure 5.44: Differences in surface pressure coefficient due to a quasi-steady roll motion at $p = 15°/s$, $C_\mu = 0.03$ and $\alpha = 6°$ (propellers off)

Besides the change in magnitude of the suction peaks, the roll motion also alters the location of the leading edge suction peak. Figure 5.45 compares the resulting force vectors of the droop noses, the main elements of the wing, and the flaps of both sides for the cases without circulation control (Figure 5.45(a)) and with circulation control (Figure 5.45(b)). The red arrows symbolize the forces on the port side, which experiences an increase in local angle of attack. The green arrows represent the forces on the starboard side, which is exposed to a decrease in local angle of attack. As expected, the force vectors are generally larger in size if circulation control is active. Additionally, the directions of the droop noses' force vectors are altered compared to the case without circulation control due to the higher circulation. As a result, a significant part of the droop noses' forces act in horizontal direction. The differences in local angles of attack between the port and the

[25] If the angle of attack of an airfoil with circulation control is raised, the leading edge suction peak increases. This leads to a stronger adverse pressure gradient that in turn causes greater losses within the main wing boundary layer. The circulation control is therefore less effective and the flap suction peak decreases.

starboard side due to the roll motion lead to an asymmetric circulation distribution. Consequently, the droop noses' force vectors of the two wing sides differ from each other in terms of magnitude and direction. The difference is more pronounced when circulation control is active.
The forces of the flaps have a significant component in streamwise direction due to the large deflection. With circulation control, the force is slightly smaller on the port side compared to the force on the starboard side due to the influence of the differing local angles of attack (Figure 5.44). This effect is non-existent without circulation control, since, in this case, the flow is completely separated from the flap. In contrast to the case with circulation control, which shows the largest difference in forces between the two wing sides at the droop nose, the biggest difference in forces occurs at the main element in the case without circulation control.

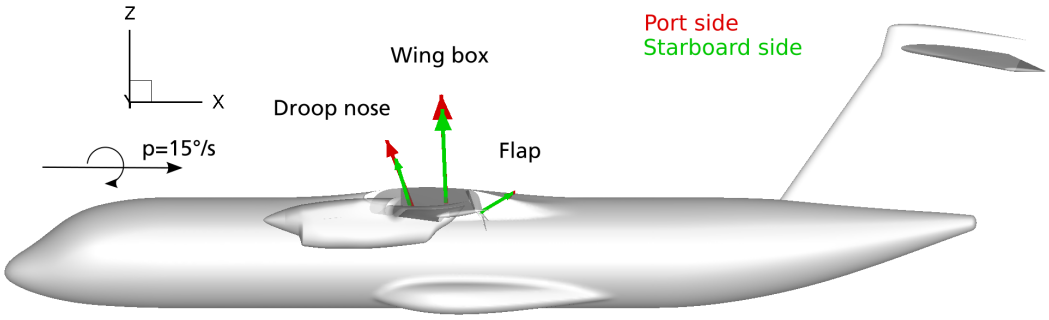

(a) Without circulation control

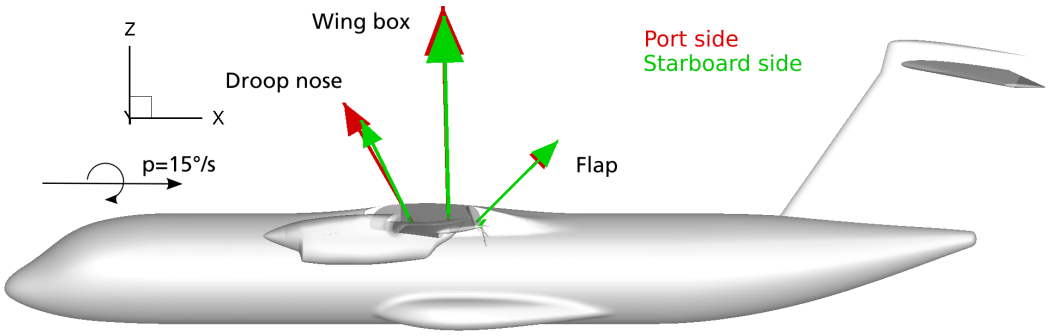

(b) With circulation control ($C_\mu = 0.03$)

Figure 5.45: Influence of circulation control on force vectors at $p = 15°/s$ and $\alpha = 6°$ (propellers off)

The difference in forces between the two wing sides generally results in a negative rolling moment, which dampens the roll motion. However, with circulation control, a significant part of the force difference between the wing sides points into horizontal direction and thus does not contribute to the rolling moment. Furthermore, the positive difference in vertical forces between the port wing and the starboard wing, caused by the droop nose and the main element, is slightly reduced by the flap. As a result, the main wing's

contribution to the roll damping derivative is smaller with circulation control than without circulation control. This characteristic agrees with the behavior of a representative airfoil (wing section). Preparatory studies have shown that the lift slope $C_{L'\alpha}$ of a wing section is reduced if circulation control is activated. The gradient $C_{Z'\alpha}$, which is more relevant for the roll damping derivative, is even more reduced with circulation control, compared to the case without circulation control. The roll damping derivative is also affected by the roll rate when circulation control is active. In this case, the roll damping derivative of the main wing decreases in magnitude with rising roll rate from $C_{lp,MW} = -0.85$ at $p = 10°/s$ to $C_{lp,MW} = -0.71$ at $p = 15°/s$. The non-linear behavior can be also explained by the characteristics of a wing section with regards to $C_{L'\alpha}$ and $C_{Z'\alpha}$. At constant C_μ, $C_{L'\alpha}$ and $C_{Z'\alpha}$ decrease non-linearily with rising angle of attack, as indicated by preparatory studies (not shown). For comparison, the roll damping derivative without circulation control is $C_{lp,MW} = -1.05 = const.$. With circulation control, propeller effects lead to an increase in magnitude of the roll damping derivative to $C_{lp,MW} = -0.94$ at $p = 15°/s$.

The large horizontal component of the forces and its difference between the two wing sides in the case with circulation control lead to an adverse yawing moment that turns the aircraft towards the starboard side. As a result, the main wing's yawing moment derivative due to roll rate doubles from $C_{np,MW} = -0.30$ without circulation control to $C_{np,MW} = -0.60$ when circulation control is active. However, with $C_{np,MW} = -0.58$, propeller effects do not substantially alter the yawing moment derivative due to roll rate.

Full Aircraft Table 5.5 summarizes the rolling and yawing moment derivatives due to roll rate of the entire aircraft. Comparing the rolling moment derivatives to the contributions from the main wing shows that the roll damping derivative C_{lp} is predominantly influenced by the main wing in all cases. The yawing moment derivative due to roll rate is, however, affected stronger by other components. Without circulation control and the propellers off, the VTP creates a negative yawing moment, which adds to the negative yawing moment generated by the main wing. In contrast, the VTP creates a positive yawing moment due to roll rate in the case with circulation control, which counteracts the negative yawing moment from the wing. Consequently, the influence of circulation control on the aircraft's yawing moment derivative due to roll rate is less than its influence on the main wing's yawing moment derivative due to roll rate. With the propellers on, the additional downwash causes a lower vertical position of the inner flap tip vortices and their influence seems to be less significant. As a result, the yawing moment derivative is increased due to the contribution of the VTP. In addition, asymmetric load distributions of the propeller affect the aircraft's dynamic moment derivatives by $\Delta C_{lp} = -0.02$ and $\Delta C_{np} = -0.06$.

C_μ	Propellers	α,deg	$p, deg/s$	C_{lp}	C_{np}
0	props off	6.0	15	-1.06	-0.39
0.03	props off	6.0	15	-0.74	-0.51
0.03	props on	6.0	15	-0.95	-0.81

Table 5.5: Dynamic moment derivatives of the full aircraft due to roll rate

Yaw Motion

The dynamic moment derivatives due to yaw rate (C_{lr} and C_{nr}) influence the dutch roll mode and spiraling [90]. They are estimated via quasi-steady yaw motions.

Wing Contribution In general, the main wing experiences additional velocities parallel to the roll axis due to a yaw motion that increase towards the wing tip and are point symmetric to the aircraft's center of gravity. The local dynamic pressure is thereby altered, which, in turn, leads to a change in the lift distribution. A positive turn therefore generally leads to a decrease in lift on the port side and an increase on the starboard side, with the differences increasing towards the wing tip in correlation to the relative free stream velocity. As a result, the force distribution of the main wing becomes asymmetric [90].

The asymmetric vertical force distribution leads to rolling moments that are summarized for the present configuration in Table 5.6 in terms of their derivatives C_{lr}. With circulation control, the rolling moment derivative of the main wing is significantly higher compared to the cases without circulation control. Since the change in lift distribution is mainly caused by the change in local freestream velocity due to the turn, this trend can be attributed to the increased effective camber and the resulting increased local lift coefficient due to circulation control (see Section 5.1.1). Consequently, the derivative is more than doubled due to circulation control ($C_{lr,MW}|_{CC}/C_{lr,MW}|_{noCC} = 2.06$) if the propellers are off. For comparison, the ratio of the lift coefficient of the wing-body model with and without circulation control at $\alpha = 6°$ and no yaw motion is $C_L|_{CC}/C_L|_{noCC} = 2.2$. The effect is slightly reduced with the propellers on.

Table 5.6 also depicts the main wing's contribution to the yawing moment derivative due to yaw rate. The table shows that the main wing's contribution to C_{nr} is negligible in all investigated cases. With the propellers on, the yawing moment derivative has an additional component from the propellers due to slightly asymmetric propeller loads. However, with the propellers' yawing moment derivative being $C_{nr} = -0.03$, this contribution is also negligible in all investigated cases.

C_μ	Propellers	α,deg	$C_{lr,MW}$	$C_{nr,MW}$
0	props off	6.0	0.51	-0.04
0.03	props off	6.0	1.05	-0.07
0.03	props on	6.0	0.95	-0.03

Table 5.6: Lateral dynamic derivatives of the main wing due to yaw rate

Fuselage and VTP Contribution Besides the changes in freestream velocity in spanwise direction, the circular flight path of the yaw motion also leads to varying cross flow velocities along the fuselage center axis. As a result, the fuselage and the VTP experience locally varying crosswind that counteracts the yaw rotation. The flow conditions at the rear fuselage and the VTP are therefore discussed complementary to the ones at constant crosswind (Section 5.2.2).

Figure 5.46(a) shows the evolution of the main wing's wake for the case with circulation control and the propellers off at $r = 15°/s$. In this case, the spanwise velocities that are directly induced by the yaw motion (Eq. 5.3) are of similar magnitude at the position of the VTP ($v_{yaw} = -4.8m/s$ at $\xi = 5.5$), as in the case of a sideslip angle of $\beta = 5°$.

$$v_{yaw} = -r \cdot (X - X_{c.g.}) \tag{5.3}$$

The visualization of the streamlines demonstrates that the wake is bent towards the center of the circular flight path, leading to similar wake-fuselage interactions, as seen for crosswind conditions (Figure 5.30(b)). Both inner flap tip vortices are transported to the port side. Even though the shift of the inner flap tip vortices is smaller with the yaw motion compared to the simulations with crosswind, it leads to positive induced spanwise velocities at the position of the VTP.

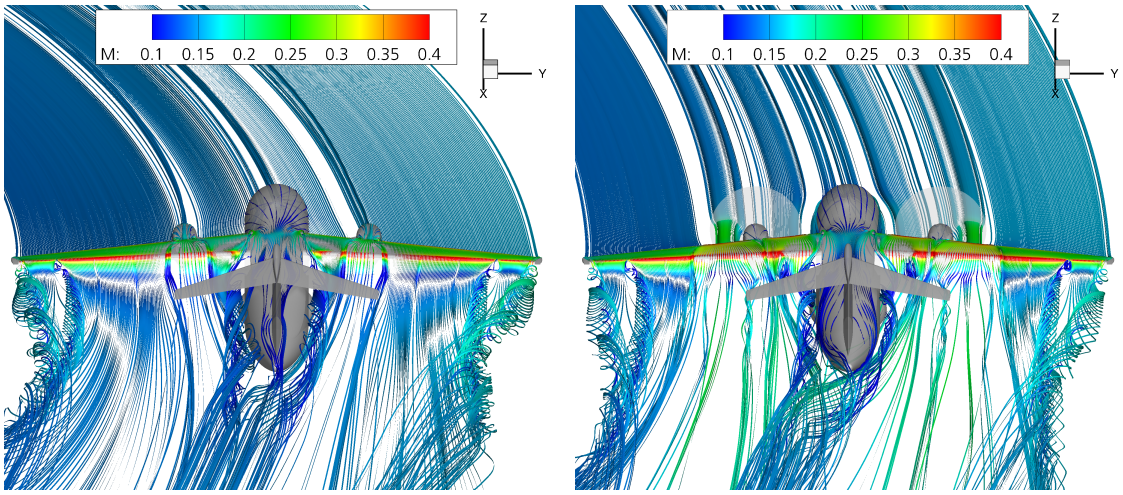

(a) Without propellers at $C_\mu = 0.03$, $\alpha = 6°$

(b) With symmetrically rotating propellers (inboard up) at $C_\mu = 0.03$, $\alpha = 0°$

Figure 5.46: Evolution of main wing wake with circulation control at $r = 15°/s$

The simulations with crosswind indicate that the case with circulation control and the propellers turning symmetrically inboard up at $\alpha = 0°$ is the most critical one regarding directional stability. This leads to the assumption that these particular conditions are also the most critical ones regarding the lateral dynamic stability. Figure 5.46(b) confirms that in this case (with circulation control, propellers rotating symmetrically inboard up, and $\alpha = 0°$), the slipstream interacts with the fuselage, as seen in the crosswind simulation

(Figure 5.35). The lower part of the slipstream on the starboard side is transported below the fuselage due to the same mechanisms. Furthermore, the evolution of the main wing's wake looks similar to the one at constant crosswind (Figure 5.35(b)). Below the rear fuselage, strong cross flow exists, which is accelerated by the slipstream and the inner flap tip vortex on the starboard side. An investigation of the flowfield at the rear fuselage (not shown) demonstrates that the flowfield closely resembles the one at constant crosswind, in particular regarding the positions of the slipstream and the inner flap tip vortices. It can be concluded that the mechanisms that lead to the flowfield at static sideslip act here as well.

The impact of the velocities, induced by this phenomena, on the yawing moment at the tail is depicted in Figure 5.47. It plots the yawing moment coefficient of the VTP and the fuselage with respect to the yaw rate for various conditions. At $\alpha = 6°$, all cases show a negative gradient of the VTP's yawing moment coefficient (Figure 5.47(a)), which means that they all dampen the yaw motion. Furthermore, the magnitudes of the yawing moment coefficient increase almost linearly. With circulation control and the propellers off (blue line), the gradient is notably reduced, which can be attributed to the positions of the inner flap tip vortices. With the propellers on (red line), the gradient is slightly increased, since the dynamic pressure at the lower part of the VTP is raised by the slipstream. However, similarly to the static lateral behavior, C_n becomes non-linear with respect to the yaw rate when circulation control is active and the propellers are on, if the angle of attack is lowered to $\alpha = 0°$. Under these conditions, the yawing moment coefficient increases at low yaw rates, which would support the yaw motion. With rising yaw rates, the slope becomes negative, which is thought to dampen the yaw motion.

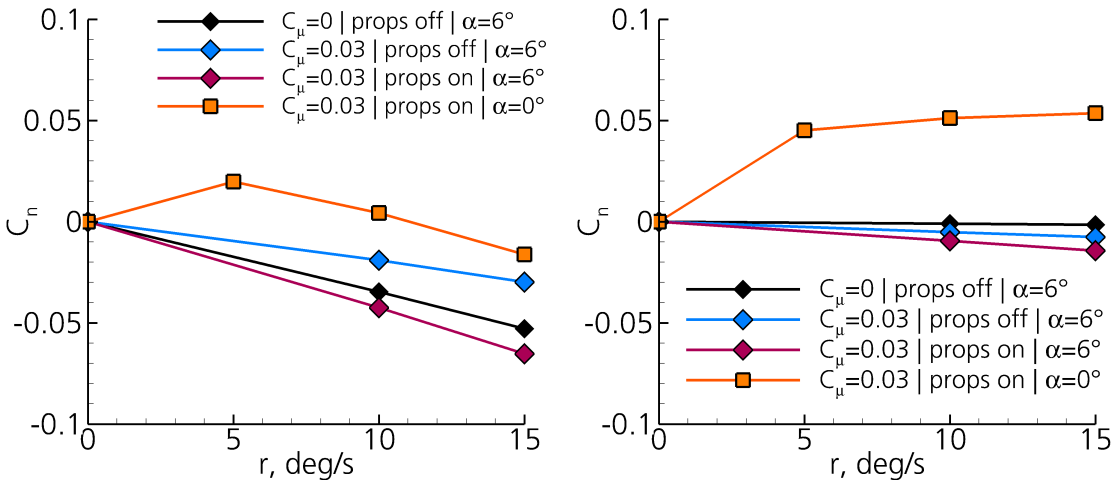

Figure 5.47: Influence of circulation control and the propellers on yawing moment with respect to the yaw rate

Table 5.7 summarizes the contributions of the VTP to the dynamic derivatives due to yaw rate. In addition to the yaw damping derivatives which result from the curve slopes in

C_μ	Propellers	α,deg	r,deg/s	$C_{lr,VTP}$	$C_{nr,VTP}$
0	props off	6.0	15	0.20	−0.74
0.03	props off	6.0	15	0.14	−0.44
0.03	props on	6.0	15	0.26	−0.93
0.03	props on	0.0	5	−0.15	0.80
0.03	props on	0.0	10	0.19	−0.63
0.03	props on	0.0	15	0.24	−0.83

Table 5.7: Lateral dynamic derivatives of the VTP

Figure 5.47(a), the table also shows the rolling moment derivatives. In all cases at $\alpha = 6°$, the VTP contributes significantly to the rolling moment derivative. With circulation control and the propellers off, the rolling moment derivative is reduced compared to the cases without circulation control, as seen for the yawing moment derivative. In contrast, the rolling moment derivative is increased with the propellers on. However, if the angle of attack is lowered to $\alpha = 0°$, the rolling moment derivative becomes negative at small yaw rates, whereas it is positive for $r \geq 10°/s$. These trends are therefore identical to the ones of the yaw damping derivatives.

The fuselage has little effect on the yawing moment coefficients at $\alpha = 6°$ (Figure 5.47(b)). The yawing moment decreases linearly, with the gradient being slightly higher with circulation control. The propellers also have a beneficial effect on the damping behavior. However, if the angle of attack is reduced to $\alpha = 0°$, the contribution from the fuselage has a destabilizing effect when circulation control is active and the propellers are on. At small yaw rates ($r \leq 5°/s$), the yawing moment of the fuselage increases considerably due to the yaw motion and the resulting wake-fuselage interaction. If the yaw rate is further increased, the additional yawing moment is rather small. The fact that, in this case, the contribution from the fuselage is significantly larger than the contribution from the VTP is unusual.
The rolling moment derivative of the fuselage is close to zero in all investigated cases, except for small angular velocities at $\alpha = 0°$, activated circulation control, and the propellers on. In this case, the rolling moment of the fuselage increases to $C_{lr} = 0.03$.

Full Aircraft Figure 5.48 shows the yawing moment distribution with respect to the yaw rate for the entire aircraft. As expected from the contributions of the components, the yawing moment distribution is nearly linear in all cases at $\alpha = 6°$. The aircraft reacts with a dampening yawing moment to a yaw motion, which is indicated by the negative slope. With circulation control, the gradient is reduced mainly due to the VTP. Propeller effects lead to an increase of the dampening. The influence of asymmetric propeller forces due to a yaw motion is thereby negligible with $|C_n| < 0.0025$.

At $\alpha = 0°$ and low yaw rates, the aircraft reacts to a yaw motion with a destabilizing yawing moment when circulation control is active and the propellers are on. The influence of both the VTP and the fuselage sums up to a substantial positive yawing moment at

$r = 5°/s$. With rising yaw rate, the yawing moment decreases due to the contribution of the VTP.

Simulations of a quasi-steady yaw motion of $r = 5°/s$ at $\alpha = 0°$ and $\beta = -5°$ (not shown) indicate that the aircraft's ability to dampen a yaw motion with circulation control active and the propellers on does not solely depend on the angle of attack and the yaw rate. It also depends on the sideslip angle. At a sideslip angle of $\beta = -5°$, the yaw damping derivative is strongly negative. In this case, the wake effect and the resulting positive yawing moments do not occur due to the yaw motion, but already exist when there is no rotation. Since the destabilizing effects are not caused by the yaw motion, the yaw damping derivative is not affected by these effects and is therefore negative. It is assumed that the change in sign of the yaw damping derivative is shifted towards higher yaw rates at positive sideslip angles.

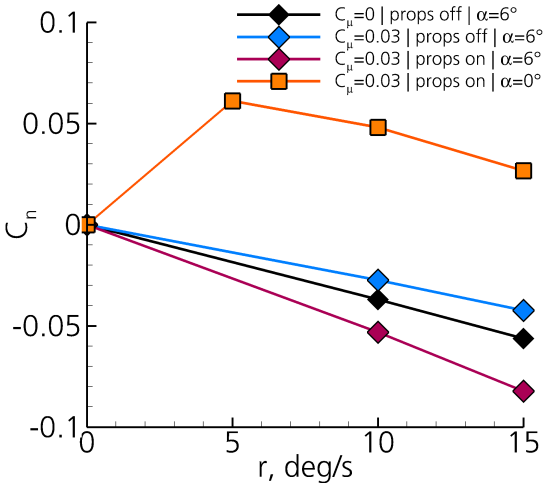

Figure 5.48: Influence of circulation control and propellers on aircraft's yawing moment with respect to the yaw rate

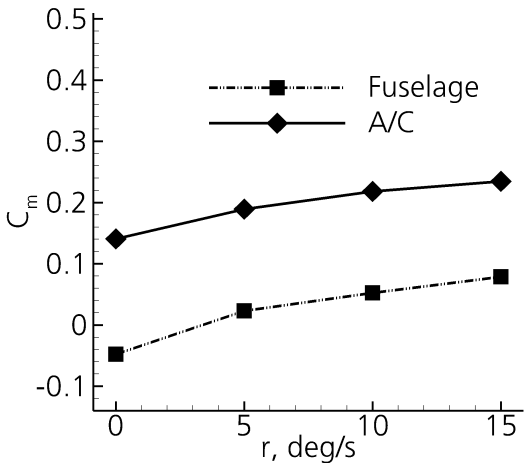

Figure 5.49: Pitching moment variation due to yaw rate at $C\mu = 0.03$, $\alpha = 0°$, and propellers on

Similar to the behavior under crosswind, the wake-fuselage interaction also leads to a buildup of a pitch up moment due to a yaw motion at $\alpha = 0°$ when circulation control is active and the propellers are on. Figure 5.49 demonstrates that the increase in pitching moment can clearly be attributed to the fuselage. However, the increase in the pitching moment is less significant compared to the case with crosswind. In all other cases, the pitching moment does not significantly change with respect to the yaw rate.

In summary, circulation control reduces the aircraft's yaw damping. The effect of the propellers is more complex and depends on several parameters. At $\alpha = 6°$, $\beta = 0°$, and propellers rotating inboard up, the yaw damping is increased. At $\alpha = 0°$, $\beta = 0°$, and propellers rotating inboard up, the yaw motion is not dampened at small yawing rates ($r \leq 5°/s$) due to similar aerodynamic phenomena observed under crosswind conditions. The conditions for undampened yaw motions also depend on the sideslip angle as simulations at $\beta = -5°$ indicate.

6 Conclusions and Outlook

In the present investigation, a full aircraft in high-lift configuration with circulation control and slipstream deflection was successfully simulated using a RANS approach. The comparison of cases with varying circulation control and propeller settings shows the influence of these lift augmentation measures on the aerodynamic properties of a state-of-the-art STOL aircraft configuration. By means of a detailed analysis of the flowfield, the characteristic behavior of the present configuration could be traced back to aerodynamic phenomena, and the sources of typical stability issues of this type of configuration could be identified. The most important findings are as follows:

- With circulation control and the propeller off, the integration of the nacelle in front of the main wing is the limiting factor for the maximum lift coefficient. The flow field analysis of the simulation results indicates high local angles of attack at the position of the nacelle, which arise due to circulation control. As a result, strong nacelle vortices evolve, which adversely affect the main wing boundary layer and the circulation control jet. The lift generation is therefore limited in proximity to the nacelle.

- The propeller leads to a permanent flow separation on the flap in the region of the slipstream throughout the entire range of angles of attack when circulation control is active. Despite the partial separation on the flap, the local wing load is raised even at the downwash side of the propeller due to the increase in local dynamic pressure and the large sectional $C_{L'(\alpha=0°)}$. The local lift can be further increased efficiently, as the circulation control acts as boundary layer control in the region of flap separation. The propeller slipstream also reduces the effect of the nacelle vortices due to the additional momentum in the near surface flow. The maximum angle of attack is thereby significantly increased. Stall occurs due to flow separation in the inboard region of the wing, where it is promoted by wing-body junction flow and propeller upwash. With circulation control and the propeller on, the maximum lift coefficient is increased by $\Delta C_L/C_L|_{noCC,T=0} = 94\%$ to $C_L = 4.52$. Altering the wing-body junction design or changing the rotational direction of the propeller has the potential to increase the maximum lift coefficient.

- Circulation control and the propeller have a large impact on the wing-body pitching moment. The resulting additional pitch down moment is counterbalanced to

some extent by the additional pitch up moment from the HTP that occurs due to increased downwash. The change in HTP trim angle is therefore moderate. However, the variations of flow conditions along the HTP span due to circulation control may generally affect longitudinal controllability, particularly when the propeller is on.
The longitudinal static stability is slightly improved by circulation control. The simulations demonstrate that the wake-fuselage interaction is the primary reason for the improved longitudinal static stability. In contrast, the propeller adversely affects the longitudinal static stability.

- The dynamic pitch damping is found to be slightly increased by circulation control and decreased by the propeller. However, the effect is rather marginal. Increasing the angle of attack leads to a moderate increase of the pitch damping derivative.

- Simulations of the full model under crosswind show a significant impact of circulation control and the propellers on the static stability in lateral motion. Circulation control reduces the directional stability due to the influence of the resulting strong inner flap tip vortices, which induce a notable sidewash at the position of the VTP. This effect increases with rising angle of attack. The influence of the propellers depends on several factors. In conjunction with circulation control, it depends on the combination of the rotational sense of the propellers, the angle of attack, and the sideslip angle. For the most part, the configuration retains directional stability. However, the simulations also indicate that with the propellers rotating symmetrically inboard up at a low angle of attack ($\alpha = 0°$) and a small sideslip angle ($\beta = 2°$), the static directional stability derivative becomes negative and thus destabilizing. The occurrence of the directional stability derivative being negative is shifted to higher sideslip angles at higher angles of attack. If the propellers rotate inboard down, the critical case regarding directional stability is also shifted to higher angles of attack ($\alpha = 10°$). The analysis of the flowfield extracted from the present simulations for the propellers rotating inboard up, $\alpha = 0°$, and $\beta = 5°$ demonstrates that the interaction of the inner flap tip vortex and the slipstream on the windward side leads to several effects, which result in destabilizing forces from the VTP and the fuselage under these conditions.

- Circulation control leads to a reduction of lateral static stability (dihedral effect). The trend is intensified at high angles of attack, with the stability derivative $C_{l\beta}$ becoming positive at $\alpha = 10°$. The results of the case with circulation control and the propellers off indicate that the reduced lateral stability is caused by asymmetric load redistribution at the outboard wing.
  The influence of the propellers again depends on several factors. If the propellers rotate inboard up, the static lateral stability is increased considerably at moderate sideslip angles, whereas it is reduced at low sideslip angles. Other combinations of rotational directions, except the case of asymmetrically rotating propellers with the one on the windward side rotating in inboard up direction, lead to an increase in static lateral stability.

- With the propellers on and rotating symmetrically inboard up, crosswind leads to a pitch up motion at small angles of attack due to the wake-fuselage interaction.
- The propellers rotating asymmetrically cause substantial rolling and yawing moments at otherwise symmetric conditions that adversely affect controllability. These modes of rotation are therefore thought to be not practical.
- The results of the quasi-steady simulations indicate that circulation control reduces roll damping, whereas propeller effects increase it. Furthermore, the yawing moment due to roll rate is notably increased by circulation control and propeller effects. When circulation control is active and the propellers are on, C_{np} is nearly doubled compared to the case without circulation control and the propellers off. The increased values of C_{np} are mainly caused by the horizontal components of the large pressure forces at the main wing, which arise at the droop nose due to the high circulation.
- The quasi-steady simulations of the yaw motion demonstrate similar flow phenomena already seen for the simulations under crosswind conditions. Circulation control therefore decreases the yaw damping. With the propellers on, the behavior strongly varies depending on several aspects. With the propellers rotating symmetrically inboard up, yaw damping reverses at small angles of attack and low yaw rates. The yaw motion also induces a pitch up moment under these conditions. The behavior can be attributed to similar flow phenomena, observed under crosswind conditions. Simulations at $\beta = -5^\circ$ indicate that the conditions for the occurrence of yaw damping reversal additionally depend on the sideslip angle.

The results show many parallels to the findings of previous experiments with similar high-lift configurations, in particular, with respect to the influence of powered lift on the longitudinal static stability [26, 30, 32] and the stability issues in lateral motion [30, 31]. On the one hand, these similarities underpin the reliability of the present results. On the other hand, the present results help to explain the sources of the stability issues found in past experiments.

Based on the findings regarding the influence of circulation control and the propellers on the aerodynamic behavior of the aircraft, detailed investigations of the flight mechanic behavior concerning stability and controllability can be performed [92]. The knowledge about the source of unfavorable effects provide the basis for potential improvements of the aerodynamic behavior, as shown for the maximum lift coefficient [4] and the directional stability [1]. These findings also suggest that the trend of electrification may be advantageous for the technologies of circulation control and slipstream deflection in two of the most critical aspects discussed. Due to electrification, distributing the propeller thrust to multiple smaller engines, known as distributed (electric) propulsion, becomes an option. Besides inherent beneficial consequences regarding safety (redundancy) and the beneficial impact on the maximum lift coefficient due to the use of slipstream deflection over a larger part of the main wing, the smaller engines would also reduce the strength of

the nacelle vortices when there is no propeller thrust. Circulation control would therefore be less affected by the nacelle vortices, and the adverse effects on the maximum lift coefficient in the case without thrust would be reduced. Distributed propulsion may also have a favorable impact on the stability in lateral motion. The intensity of the slipstream would be reduced if the propeller thrust is distributed over the entire wing span. Additionally, the redistribution of lift towards the outboard wing would lead to reduced inner flap tip vortices. Both effects are thought to have a significant favorable impact on the directional stability and the yaw damping.

Own Publications and Author Contributions

This section presents the author's own publications that are referenced within the thesis. The contributions to the following publications are as follows:

- [1]: D.K. conceived and performed the study, analyzed the data, and wrote the manuscript. All authors reviewed and approved the final manuscript.
- [2]: D.K. conceived and performed the study, analyzed the data, and wrote the manuscript. All authors reviewed and approved the final manuscript.
- [3]: D.K. conceived and performed the study, analyzed the data, and wrote the manuscript. All authors reviewed and approved the final manuscript.
- [4]: D.K. conceived the study. D.K. and Y.J.H. performed the study and analyzed the data. D.K. wrote the manuscript. All authors reviewed and approved the final presentation.
- [5]: D.K. and M.B. conceived and performed the study, analyzed the data, and prepared the presentation. Both authors reviewed and approved the final manuscript.
- [6]: D.K. conceived and performed the study, analyzed the data, and wrote the manuscript. All authors reviewed and approved the final manuscript.
- [7]: D.K. conceived and performed the study, analyzed the data, and wrote the manuscript. All authors reviewed and approved the final manuscript.

[1] D. Keller and R. Rudnik. Investigation and improvement of directional stability and control of a propeller-driven stol aircraft. *CEAS Aeronautical Journal*, 10(3):909–924, Sep 2019.

[2] D. Keller. Numerical Approach Aspects for the Investigation of the Longitudinal Static Stability of a Transport Aircraft with Circulation Control. In *New Results in Numerical and Experimental Fluid Mechanics IX*, volume 124 of *Notes on Numerical Fluid Mechanics and Multidisciplinary Design*, pages 13–22. Springer, 2014.

[3] D. Keller and R. Rudnik. Numerical Investigations of Aerodynamic Properties of a Propeller Blown Circulation Control System on a High Wing Aircraft. *CEAS Aeronautical Journal*, 7(3):441–454, 2016.

[4] D. Keller, Y. J. Hasan, and R. Rudnik. Nacelle strake design for short takeoff and landing configuration with turboprop engines. *Journal of Aircraft*, 55(6):2444–2453, 2018.

[5] M. Burnazzi and D. Keller. Numerical Assessment of a HighLift Configuration with Circulation Control and flexible Droop Nose. Speech at DLR Symposium "High-Lift System Research - Celebrating 10 Years of DLR-F15". URL: https://elib.dlr.de/119901, 2015.

[6] D. Keller and R. Rudnik. Numerical Investigation of Engine Effects on a Transport Aircraft with Circulation Control. *Journal of Aircraft*, 52(2):421–438, 2015.

[7] D. Keller and R. Rudnik. Aerodynamic assessment of potential rudder force augmentation due to circulation control based on a VTP rudder design for a STOL aircraft. In Rolf Radespiel and Richard Semaan, editors, *TU Braunschweig - Campus Forschungsflughafen, Berichte aus der Luft- und Raumfahrttechnik*, number 2017-14. Shaker Verlag, 2017.

Bibliography

[8] Acare. Acare flightpath 2050 - europe's vision for aviation. [online web site], URL: http://www.acare4europe.com/documents/latest-acare-documents/acare-flightpath-2050, [retrieved 14th April 2017].

[9] A. B. Bauer and A. G. Munson. Airframe Noise of the DC-9-31. Contractor Report CR-3027, NASA, 1978.

[10] G. K. Korbacher. Aerodynamics of powered high-lift systems. Annual Review of Fluid Mechanics, pages 319–358. 1974.

[11] V. Brunet, J. Dandois, and C. Verbeke. Recent Onera Flow Control Research on High-Lift Configurations. *Aerospace Lab*, 6(5), 2013.

[12] M. Salikuddin, W. H. Brown, and K. K. Ahuja. Noise from a circulation control wing with upper surface blowing. *Journal of Aircraft*, 24(1):55–64, 1987.

[13] S. E. Munro and K. K. Ahuja. Aeroacoustics of a High Aspect-Ratio Jet. In *Proc. 9th AIAA/CEAS Aeroacoustics Conference and Exhibit*, number 2003-3323, Hilton Head, South Carolina, USA, May 2003.

[14] M. Pott-Pollenske and K. C. Pfingsten. Aeroacoustic Performance of an Airfoil with Circulation Control. In *Proc. 16th AIAA/CEAS Aeroacoustics Conference*, number 2010-3881, Stockholm, Sweden, 2010.

[15] J. Delfs and B. Faßmann and N. Lippitz and M. Lummer and M. Mößner and L. Müller and K. Rurkowska and S. Uphoff. SFB 880: aeroacoustic research for low noise take-off and landing. *CEAS Aeronautical Journal*, 5(4):403–417, 2014.

[16] L. Prandtl. Über Flüssigkeitsbewegung bei sehr kleiner Reibung. In *Proc. 3. Internationaler Mathematik Kongress*, Heidelberg,Germany, 1904.

[17] M. Knight and M. Bamber. Wind tunnel tests on airfoil boundary control using a backward opening slot. NACA Technical Note 323, Langley Field, Va, 1929.

[18] H. M. Lyon and R. Hills. Lift Increase by Boundary-Layer Control. Dept. Note W.T. 391, R.A.E., 1939.

[19] H. M. Lyon, E. G. Barnes, and J. E. Adamson. Further Experiments on Boundary-Layer Control as a Means of Increasing Lift. Report B. A. 1669, R.A.E., 1941.

[20] J. Williams. An Analysis of Aerodynamic Data on Blowing Over Trailing Edge Flaps for Increasing Lift. Technical Report C.P. No. 209, Aeronautical Research Council, 1955.

[21] J. M. Riebe. A correlation of two-dimensional data on lift coefficient available with blowing-, suction-, slotted-, and plain-flap high-lift devices. NACA Research Memorandum L55D29a, 1955.

[22] H. Hagedorn and P. Ruden. Wind Tunnel Investigations of a Wing with Junkers Slotted Flap and the Effect of Blowing through the Trailing Edge of the Main Surface over the Flap. L.G.L. Bericht A. 64, Institut für Aeromechanik und Flugtechnik der Technischen Hochschule Hannover, 1938.

[23] W. Schwier. Versuche zur Auftriebssteigerung durch Ausblasen von Luft an einem symmetrischen Profil mit Wölbungsklappe grosser Tiefe. Bericht 41/14/27, Aerodynamische Versuchsanstalt Göttingen, 1941.

[24] von der Decken J. Aerodynamics of Pneumatic High-Lift Devices. Lecture Series AGARD-LS-43-71, AGARD, 1971.

[25] Ph. Poisson-Quinton and L. Lepage. Survey of French Research on the Control of Boundary Layer and Circulation. In *Boundary Layer and Flow Control*, volume 1. Pergamon Press LTD., London, UK, 1961.

[26] M. P. Fink, B. W. Cocke, and S. Lipson. A Wind-Tunnel Investigation of a 0.4-Scale Model of an Assault Transport Airplane With Boundary-Layer Control Applied. Research Memorandum L55G26a, NACA, 1956.

[27] J. A. Weiberg, R. N. Griffin Jr., and G. L. Florman. Large-Scale Wind-Tunnel Tests of an Airplane Model with an Unswept, Aspect-Ratio-10 Wing, Two Propellers, and Area-Suction Flaps. Technical Note 4365, NASA, 1958.

[28] R. N. Griffin Jr., C. A. Holzhauser, and J. A. Weiberg. Large-scale wind-tunnel tests of an airplane model with an unswept, aspect-ratio-10 wing, two propellers, and blowing flaps. Memorandum 12-3-58A, NASA, 1958.

[29] J. A. Weiberg and V. R. Page. Large-Scale Wind-Tunnel Tests of an Airplane Model with an Unswept, Aspect-Ratio-10 Wing, Four Propellers, and Blowing Flaps. Technical Note D-25, NASA, 1959.

[30] J. A. Weiberg and C. A. Holzhauser. STOL characteristics of a propeller-driven, aspect-ratio-10 wing, straight-wing airplane with boundary-layer control flaps, as estimated from large-scale wind-tunnel tests. Technical Note D-1032, NASA, 1961.

[31] R. C. Innis and H. C. Quigley. A Flight Test Examination of the Operating Problems of V/STOL Aircraft in STOL-Type Landing and Approach. Technical Note D-862, NASA, 1961.

[32] H. C. Quigley and R. C. Innis. Handling qualities and operational problems of a large four-propeller stol transport airplane. NASA Technical Note D-1647, Ames Research Center, Moffett Field, Ca, Januar 1963.

[33] H. C. Quigley, R. C. Innis, and C. A. Holzhauser. A flight investigation of the performance, handling qualities, and operational characteristics of a deflected slipstream stol transport airplane having four interconnected propellers. NASA Technical Note D-2231, Ames Research Center, Moffett Field, Ca, March 1964.

[34] C. A. Holzhauser and R. C. Innis. A flight and simulator study of the handling qualities of a deflected slipstream stol sea- plane having four propellers and boundary-layer control. Technical Note D-2966, NASA, 1965.

[35] L. B. Gratzer and T. J. O'Donnell. Development of a blc high-lift system for high-speed airplanes. *Journal of Aircraft*, 2(6):477–484, 1965.

[36] J. H. Nichols and M. J. Harris. Fixed Wing CCW Aerodynamics with and without Supplementary Thrust Deflection. Technical Report N88-17607, David W. Taylor Naval Ship Research and Development Center, 1987.

[37] A. J. Pugliese and R. J. Englar. Flight testing the circulation control wing. In *Proc. Aircraft Systems and Technology Meeting*, number 79-1791, New York, NY, USA, 1979.

[38] R. J. Englar. Development of the A-6/Circulation Control Wing Flight Demonstrator Configuration. Technical Report DTNSRDC/ASED-79/01, David W. Taylor Naval Ship Research and Development Center, 1979.

[39] R. J. Englar and G. G. Huson. Development of advanced circulation control wing high-lift airfoils. *Journal of Aircraft*, 21(7):476–483, 1984.

[40] J. D. Stephenson, J. A. Jeske, and G. H. Hardy. Lateral-directional stability and control characteristics of the Quiet Short-Haul Research Aircraft (QSRA). Technical Memorandum 102250, NASA, 1990.

[41] W. E. Milholen II, G. S. Jones, D. T. Chan, and S. L. Goodliff. High-Reynolds Number Circulation Control Testing in the National Transonic Facility (invited). In *Proc. 50th AIAA Aerospace Sciences Meeting including the New Horizons Forum and Aerospace Exposition*, Nashville, TN, USA, 2012.

[42] J. Lichtwardt, E. Paciano, D. Marshall, and K. Jameson. STOL Performance of Cal Poly's AMELIA. In *Proc. 51st AIAA Aerospace Sciences Meeting including the New Horizons Forum and Aerospace Exposition*, number 2013-976, Grapevine, TX, USA, 2013.

[43] A.V. Petrov. Aerodynamics of stol airplanes with powered high-lift systems. In *Proc. ICAS 2012 Congress*, Brisbane, Australia, September 2012.

[44] R.C. Swanson, C.L. Rumsey, and S.G. Anders. Progress Towards Computational Method for Circulation Control Airfoils. In *Proc. 43rd AIAA Aerospace Sciences Meeting and Exhibit*, number 2005-89, Reno, Nevada, USA, 2005.

[45] E. M. Lee-Rausch, V. N. Vatsa, and C. L. Rumsey. Computational Analysis of Dual Radius Circulation Control Airfoils. In *Proc. 3rd AIAA Flow Control Conference*, number 2006-3012, San Francisco, California, USA, 2006.

[46] C.L. Rumsey and T. Nishino. Numerical study comparing RANS and LES approaches on a circulation control airfoil. *International Journal of Heat and Fluid Flow*, 32:847–864, 2011.

[47] K. C. Pfingsten, C. Jensch, K. W. Körber, and R. Radespiel. Numerical Simulation of the Flow Around Circulation Control Airfoils. In *Proc. First CEAS European Air and Space Conference*, Berlin, Germany, 2007.

[48] Y. Liu, L. Sankar, R. J. Englar, K. K. Ahuja, and R. Gaeta. Computational Evaluation of the Steady and Pulsed Jet Effects on the Performance of a Circulation Control Wing Section. In *Proc. 42nd AIAA Aerospace Sciences Meeting and Exhibit*, number 2004-56, Reno, Nevada, USA, 2004.

[49] C. Jensch, K.C. Pfingsten, R. Radespiel, M. Schuermann, M. Haupt, and S. Bauss. Design aspects of a gapless high-lift system with active blowing. In *Proc. Deutscher Luft- und Raumfahrtkongress*, Aachen, Germany, 2009.

[50] C. Jensch, K.C. Pfingsten, and R. Radespiel. Numerical investigation of leading edge blowing and optimization of the slot and flap geometry for a circulation control airfoil. In *New Results in Numerical and Experimental Fluid Mechanics VII*, volume 112, pages 183–190. Springer, 2010.

[51] M. Burnazzi and R. Radespiel. Design and Analysis of a Droop Nose for Coanda Flap Applications. *Journal of Aircraft*, 51(5):1567–1579, 2014.

[52] M. Burnazzi and R. Radespiel. Synergies between Suction and Blowing for Active High-Lift Flaps. *CEAS Aeronautical Journal*, 6(2):305–318, 2015.

[53] K.C. Pfingsten, R.D. Cecora, and R. Radespiel. An experimental investigation of a gapless high-lift system using circulation control. In *Proc. CEAS/KATnet II Conference on Key Aerodynamic Technologies*, Bremen, Germany, 2009.

[54] D. D. Marshall and K. K. Jameson. Overview of Recent Circulation Control Modeling Activities at Cal Poly. In *Proc. 48th AIAA Aerospace Sciences Meeting Including the New Horizons Forum and Aerospace Exposition*, number 2010-348, Orlando, USA, 2010.

[55] J. Pham and D. D. Marshall. Improved Meshing Technique for the Engine Exhaust of an Over-the-Wing Engine and Circulation Control Wing Configuration. In *Proc. 49th AIAA Aerospace Sciences Meeting including the New Horizons Forum and Aerospace Exposition*, number 2011-1042, Orlando, FL, USA, 2011.

[56] V. Ciobaca and J. Wild. An overview of recent dlr contributions on active flow-separation control studies for high-lift configurations. *Aerospace Lab*, 6(12), 2013.

[57] M. Pitkin. Free-Flight-tunnel Investigation of the Effect of Mode of Propeller Rotation Upon the Lateral-stability Characteristics of a Twin-engine Airplane Model with Single Vertical Tails of Different Size. Advance Restricted Report NACA-ARR-3J18, NACA, 1943.

[58] J. Stüper. Effect of Propeller Slipstream on Wing and Tail. Technical Memorandum NACA-TM-0874, NACA, 1938.

[59] H. H. Sweberg. The Effect of Propeller Operation on the Air Flow in the Region of the Tail Plane for a Twin-engine Tractor Monoplane. Advance Restricted Report NACA-ARR-L381, NACA, 1942.

[60] F. M. Rogallo and R. S. Swanson. Wind-tunnel Tests of a Twin-engine Model to Determine the Effect of Direction of Propeller Rotation on the Static-stability Characteristics. Advance Restricted Report NACA-ARR-L295, NACA, 1942.

[61] J. Mannée. Windtunnel Investigation of the Influence of the Aircraft Configuration on the Yawing and Rolling Moments of a Twin-Engined Propeller Driven Aircraft with one Engine Inoperative. Technical report, Amsterdam, 1962.

[62] M.J.T. Schroijen, L.L.M. Veldhuis, and R. Slingerland. Propeller Empennage Interaction Effects on Vertical Tail Design of Multiengine Aircraft. *Journal of Aircraft*, 47:1133–1140, 2010.

[63] L. B. Gratzer. Analysis of Transport Applications for High-Lift Schemes. Lecture Series AGARD-LS-43-71, AGARD, 1971.

[64] H. Coandă. Device for deflecting a stream of elastic fluid projected into an elastic fluid, September 1 1936. US Patent 2,052,869.

[65] Ph. Poisson-Quinton. Recherches théoretiques et éxperimentales sur le contrôle de couche limite. In *Proc. 7th Congress of Applied Mechanics, Aerospace Science and Technology*, London, 1948.

[66] W. Heinze, C. M. Österheld, and P. Horst. Multidisziplinäres Flugzeugentwurfsverfahren PrADO - Programmentwurf und Anwendung im Rahmen von Flugzeug-Konzeptstudien. In Deutsche Gesellschaft für Luft-und Raumfahrt (DGLR), editor, *DGLR-Jahrbuch 2001*, volume 3, pages 1701–1712. Bonn, 2001.

[67] T. W. Weiss and W. Heinze. Multidisciplinary Design of CESTOL Aircraft with Powered Lift System. In *TU Braunschweig - Campus Forschungsflughafen, Berichte aus der Luft- und Raumfahrttechnik*, number 2013-3. Shaker Verlag, 2013.

[68] M. Kintscher, M. Wiedemann, H. P. Monner, O. Heintze, and T. Kühn. Design of a smart leading edge device for low speed wind tunnel tests in the European project SA-DE. *International Journal of Structural Integrity*, 2(4):383–405, 2011.

[69] A. Schmitz and P. Horst. A new curvature morphing skin: manufacturing, experimental and numerical investigations. In *Proc. 16th European Conference on Composite Materials*, Seville, Spain, 2014.

[70] A. Rudenko, H. P. Monner, and M. Rose. A Process Chain for Structural Optimization of a Smart Droop Nose for an Active Blown High Lift System. In *Proc. 22nd AIAA/ASME/AHS Adaptive Structures Conference*, number 2014-1414, Washington D.C., USA, 2014.

[71] CentaurSoft. Centaur hybrid grid generation system. [online web site], URL: http://www.centaursoft.com, [retrieved 19th November 2012].

[72] A. K. Michler. Aircraft control surface deflection using rbf-based mesh deformation. *International Journal for Numerical Methods in Engineering*, 88(10):986–1007, 2011.

[73] H. Schlichting. *Grenzschicht-Theorie*. G. Braun, Karlsruhe, 1982.

[74] S. Melber-Wilkending. Numerische Untersuchung aerodynamischer Effekte im Flügelrumpfübergang einer Hochauftriebskonfiguration. PhD thesis, DLR-Forschungsbericht 2014-21, TU Braunschweig / DLR Braunschweig, 2014.

[75] T. Schwarz. Ein blockstrukturiertes verfahren zur simulation der umströmung komplexer konfigurationen. PhD thesis, DLR-Forschungsbericht 2005-20, TU Braunschweig, 2005.

[76] W. Schröder. *Fluidmechanik*. Verlag Mainz, 2004.

[77] J. Blazek. *Computational Fluid Dynamics: Principles and Applications*. Elsevier, 2001.

[78] O. Reynolds. On the dynamical theory of incompressible viscous fluids and the determination of the criterion. *Phil. Trans. R. Soc. A*, 186:123–164, 1895.

[79] D. Wilcox. *Turbulence Modeling for CFD*. DCW Industries, Inc., 1994.

[80] P.R. Spalart and S.R. Allmaras. A One–Equation Turbulence Model for Aerodynamic Flows. In *Proc. 30th Aerospace Sciences Meeting and Exhibit*, number 92–439, Reno, NV, USA, 1992.

[81] C.L. Rumsey. Apparent transition behavior of widely-used turbulence models. *International Journal of Heat and Fluid Flow*, 28:1460–1471, 2007.

[82] D. D. Knight and N. J. Saffman. Turbulence Model Predictions for Flows with Significant Mean Streamline Curvature. In *Proc. 16th Aerospace Sciences Meeting*, number 78-258, Huntsville, USA, 1978.

[83] P.R. Spalart and M. Shur. On the sensitization of turbulence models to rotation and curvature. volume 1 of *Aerospace Science and Technology*, pages 297–302. 1997.

[84] M.L. Shur, M. K. Strelets, and P. R. Spalart. Turbulence Modeling in Rotating and Curved Channels: Assessing the Spalart-Shur Correction. *AIAA Journal*, 38:784–792, 2000.

[85] V. Togiti and B. Eisfeld. Assessment of g-Equation Formulation for a Second-Moment Reynolds Stress Turbulence Model. In *Proc. 22nd AIAA Computational Fluid Dynamics Conference*, number 2015-2925, Dallas, TX, USA, 2015.

[86] Various authors. TAU-Code User Guide. Technical Report Release 2013.2.0, DLR, Institut für Aerodynamik und Strömungstechnik, Braunschweig, Deutschland, September 2013.

[87] A. Jameson, W. Schmidt, and E. Turkel. Numerical Solutions of the Euler Equations by Finite Volume Methods Using Runge-Kutta Time-Stepping Schemes. In *Proc. 14th Fluid and Plasma Dynamics Conference*, number 81-1259, Palo Alto, CA, USA, 1981.

[88] P. L. Roe. Approximate riemann solvers, parameter vectors, and difference schemes. *J. Computational Physics*, 43:357–372, 1981.

[89] A. Jameson and E. Turkel. Implicit Schemes and LU-Decomposition. *Mathematics of Computation*, 37(156):385–397, 1981.

[90] R. Brockhaus, W. Alles, and R. Luckner. *Flugregelung*. Springer Berlin Heidelberg, 2011.

[91] A.-R. Hübner. Experimentelle und numerische Bestimmung der dynamischen Derivative. PhD thesis, Forschungsbericht 2009-26, German Aerospace Center, 2009.

[92] J.H. Diekmann. Flugmechanische Charakteristika von propellergetriebenen Flugzeugen mit aktiven Hochauftriebssystemen. PhD thesis, DLR-Forschungsbericht 2017-54, German Aerospace Center, 2017.

[93] C.L. Rumsey, J. P. Slotnik, M. Long, R. A. Stuever, and T. R. Wayman. Summary of the First AIAA CFD High-Lift Prediction Workshop. *Journal of Aircraft*, 48:2068–2078, 2011.

[94] C.L. Rumsey and J. P. Slotnik. Overview and Summary of the Second AIAA High-Lift Prediction Workshop. *Journal of Aircraft*, 52:1006–1025, 2015.

[95] C.L. Rumsey, J. P. Slotnik, and A. J. Sclafani. Overview and Summary of the Third AIAA High Lift Prediction Workshop. *Journal of Aircraft*, 56, 2018.

[96] R. Rudnik and S. Melber-Wilkending. DLR Contribution to the 2nd High Lift Prediction Workshop. In *Proc. 52nd Aerospace Sciences Meeting*, number 2014-0915, National Harbor, Maryland, USA, 2014.

[97] R. Rudnik, D. Rekzeh, and J. Quest. HINVA - High lift INflight VAlidation - Project Overview and Status. In *Proc. 50th AIAA Aerospace Sciences Meeting including the New Horizons Forum and Aerospace Exposition*, number 2012-0106, Nashville, TN, USA, 2012.

[98] D. Rohlmann and S. Keye. Stall Maneuver Simulation of an elastic Transport Aircraft based on Flight Test Data. In *Proc. 33rd AIAA Applied Aerodynamics Conference*, number 2015-2570, 2015.

[99] J. J. Thibert. The GARTEUR high lift research programme. AGARD-CP-515 - High-Lift System Aerodynamics, Delft, The Netherlands, 1993.

[100] R. Rudnik. CFD Assessment for 3D High Lift Flows in the European Project EUROLIFT. In *Proc. 21st AIAA Applied Aerodynamics Conference*, number 2003-3794, Orlando, FL, USA, 2003.

[101] R. Rudnik. Evaluation of cfd methods for transport aircraft high lift systems. *The Aeronautical Journal*, 109(1092):53–64, 2005.

[102] H. v. Geyr, N. Schade, J.W. v. d. Burg, P. Eliasson, and S. Esquieu. CFD Prediction of Maximum Lift Effects on Realistic High-Lift-Commercial-Aircraft-Configurations within the European Project EUROLIFT II. In *Proc. 25th AIAA Applied Aerodynamics Conference*, number 2007-4299, 2007.

[103] P. Iannelli. Comparison of optimization strategies for high-lift design. *Journal of Aircraft*, 54(2):642–658, 1895.

[104] J. W. Slater. Examining Spatial (Grid) Convergence. [online web site], URL: https://www.grc.nasa.gov/WWW/wind/valid/tutorial/spatconv.html, [retrieved 20th June 2018].

[105] P. J. Roache. Perspective: A method for uniform reporting of grid refinement studies. *J. Fluids Eng*, 116(3):405–413, 1994.

[106] B. G. Allan, G. S. Jones, and J. C. Lin. Reynolds-Averaged Navier-Stokes Simulation of a 2-D Circulation Control Wind Tunnel Experiment. In *Proc. 49th AIAA Aerospace Sciences Meeting including the New Horizons Forum and Aerospace Exposition*, number 2011-25, Orlando, Florida, USA, 2011.

[107] R. H. Nichols. Algorithm and Turbulence Model Requirements for Simulating Vortical Flows. In *Proc. 46th AIAA Aerospace Sciences Meeting and Exhibit*, number 2008-337, Reno, USA, 2008.

[108] M. J. Churchfield and G. A. Blaisdell. Numerical Simulations of a Wingtip Vortex in the Near Field. *Journal of Aircraft*, 46(1):230–243, 2009.

[109] T. Sarpkaya. Effect of the Adverse Pressure Gradient on Vortex Breakdown. *AIAA Journal*, 12:602–607, 1974.

[110] C. O. Marquez Gutierrez, A. Stürmer, C. Clemen, and A. Grimminger. Validation of Actuator Disk Simulations of CROR Propulsion Systems at Low-Speed Flight Conditions. In *Proc. 30th AIAA Applied Aerodynamics Conference*, number 2012-2787, New Orleans, USA, 2012.

[111] C. Lenfers, N. Beck, and M. Bauer. Propeller and active high lift wing interaction in experiment and simulation. *New Results in Numerical and Experimental Fluid Mechanics X*, 132:51–61, 2016.

[112] Marco Burnazzi, Jakob Thiemeier, and Rolf Radespiel. Numerical stall behavior investigation of an aircraft equipped with coanda flap and droop nose. In Andreas Dillmann, Gerd Heller, Ewald Krämer, Claus Wagner, and Christian Breitsamter, editors, *New Results in Numerical and Experimental Fluid Mechanics X*, pages 3–16, Cham, 2016. Springer International Publishing.

[113] M. Burnazzi. Design of Efficient High-Lift Configurations with Coanda Flaps. PhD thesis, Forschungsbericht 2016-11, TU Braunschweig, 2016.

[114] W. A. Tucker. Wind-Tunnel Investigation of Effect of Wing Location, Power, and Flap Deflection on Effective Dihedral of a Typical Single-Engine Fighter-Airplane Model with Tail Removed. Technical Note TN-1061, NACA, 1946.

[115] J. Williams, S. F. J. Butler, and M. N. Wood. The Aerodynamics of Jet Flaps. Reports and Memoranda 3304, Aeronautical Research Council, 1961.

[116] R. E. Kuhn. On the Prediction of the Lateral/Directional Characteristics of Distributed Jet STOL Configurations. Reports and Memoranda NADC-81275-60, Naval Air Development Center, 1982.

[117] U.S. Government Publishing Office. Federal aviation regulations, part 25. In *ELECTRONIC CODE OF FEDERAL REGULATIONS, URL: https://www.ecfr.gov*. [retrieved 2015-5-11].

[118] S. Gudmundsson. *General Aviation Aircraft Design*. Butterworth-Heinemann, 2014.

A Referenced Wind Tunnel Tests and Flight Experiments

Model-ID	Type of experiment	no. of propellers	rotational sense of propellers	BLC system	TED deflections	references
AR10W2-BS	wind tunnel	2	asymmetric	I/B suction, O/B blowing	$\delta_f = 50°$, $\delta_a = 30°$	Fink [26]
AR10W2-S	wind tunnel	2	asymmetric	suction	$\delta_f \leq 70°$, $\delta_a = 30°$	Weiberg [27]
AR10W2-B	wind tunnel	2	asymmetric	blowing	$\delta_f \leq 80°$, $\delta_a = 30°$	Griffin [28], Weiberg [30]
AR10W4-B	wind tunnel	4	asymmetric	blowing	$\delta_f \leq 80°$, $\delta_a = 30°$	Weiberg [29, 30]
YC-134A	flight test	2	asymmetric	suction	$\delta_f \leq 60°$, $\delta_a = 30°$	Innis [31]
NC-130B	flight test	4	asymmetric	blowing	$\delta_f \leq 90°$, $\delta_a = 30°$	Quigley [32]
BR 941	flight test	4	symmetric (I/B down)	-	$\delta_F \leq 98°$, $\delta_a \leq 65°$	Quigley [33]
UF-XS	flight test	4	asymmetric	blowing	$\delta_f \leq 55°$, $\delta_a = 0°$	Holzhauser [34]

Table A.1: Overview of models, similar to present configuration, which were used in experiments and flight tests

B Stall Behavior

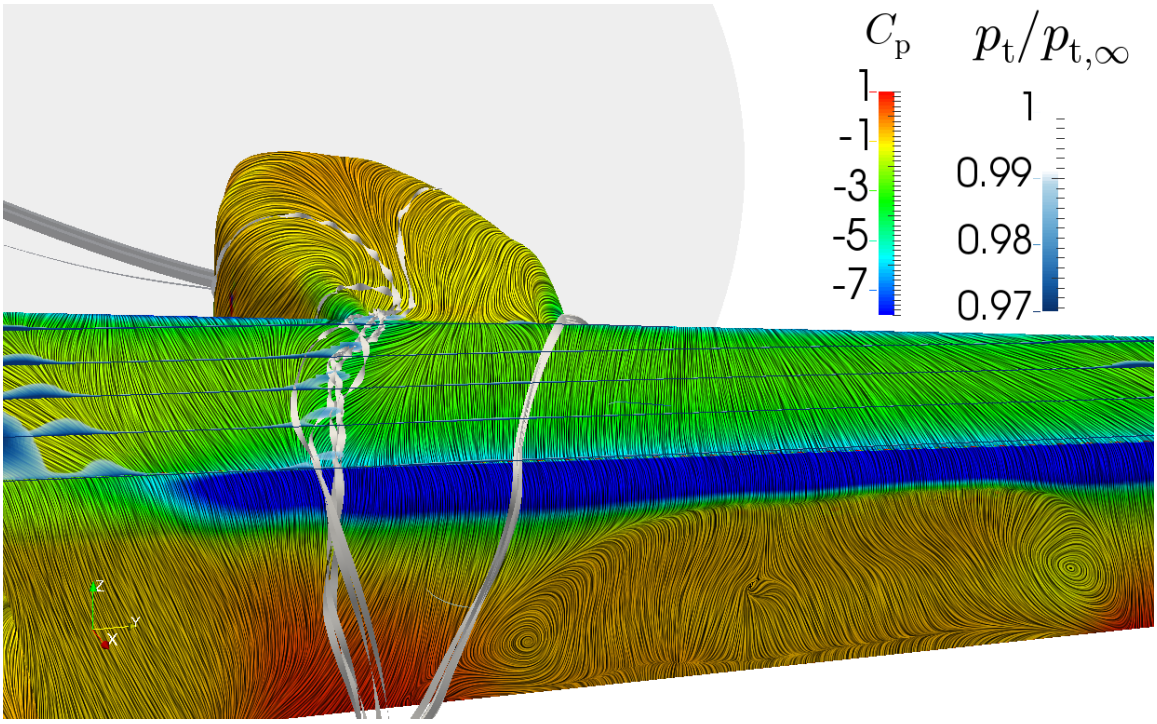

Figure B.1: Visualization of nacelle vortices by streamlines and total pressure loss at $C_\mu = 0.03$, $\alpha = 10°$, and propeller on

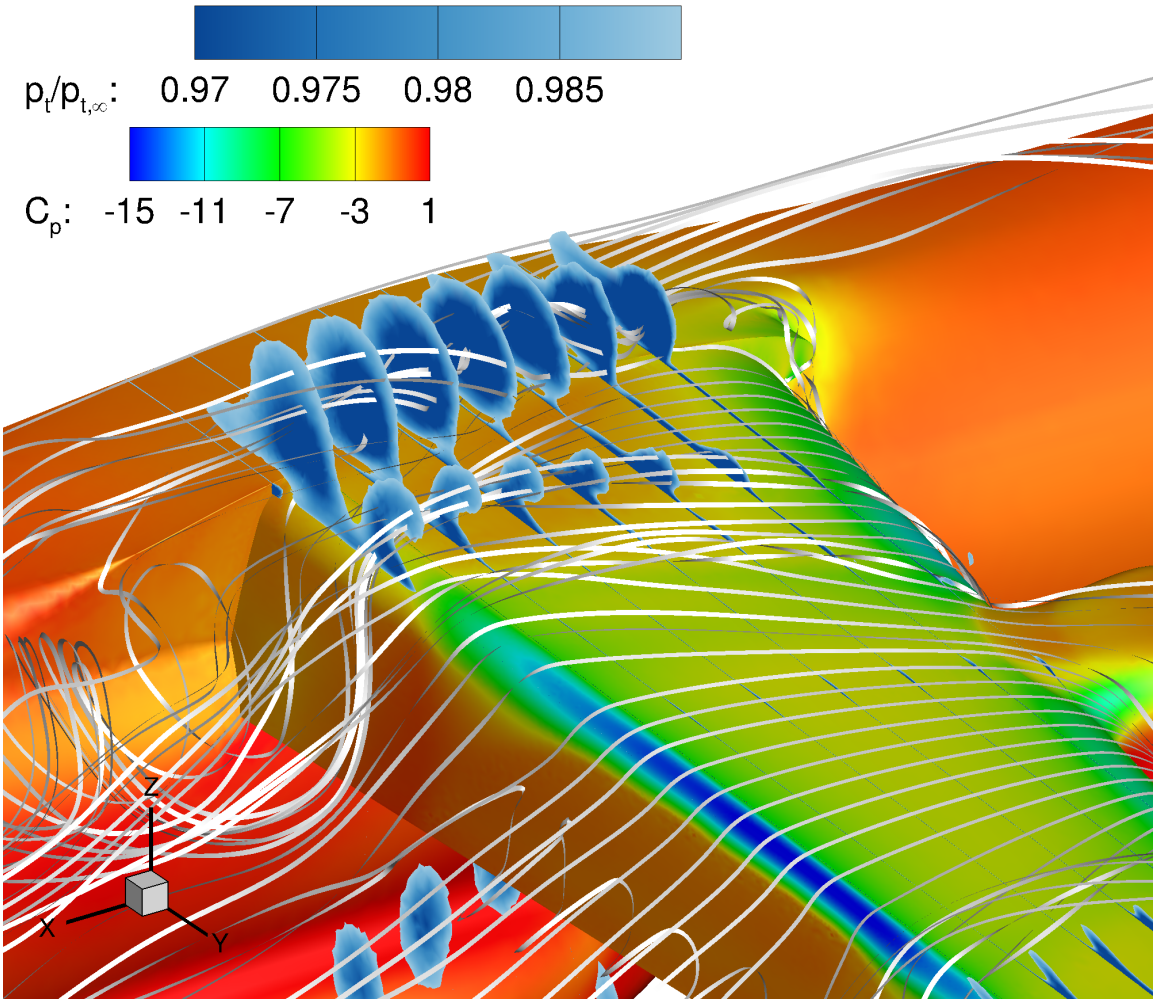

Figure B.2: Begin of stall at the wing root visualized by total pressure loss and streamlines ($C_\mu = 0.03$, $\alpha = 19°$, and propeller on)

C Lateral Stability

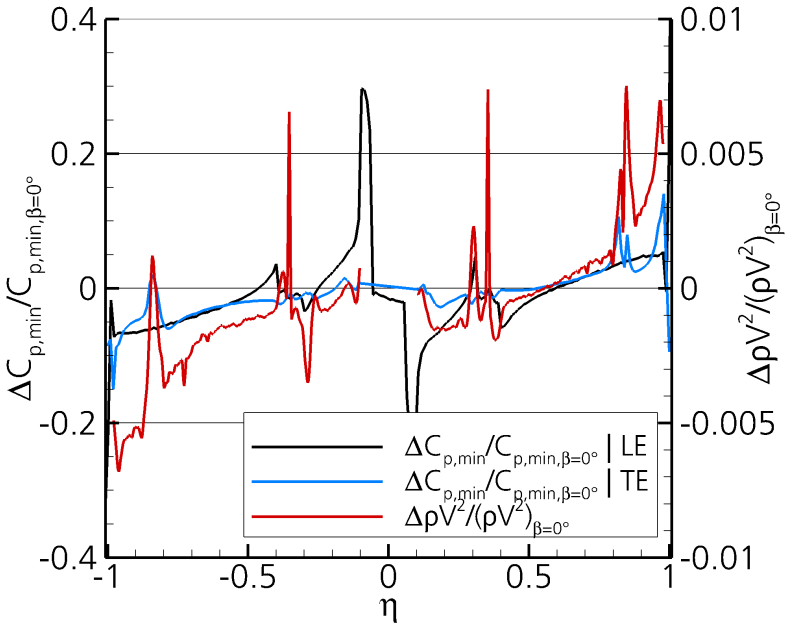

Figure C.1: Change in spanwise jet momentum distribution and suction peak distributions due to crosswind $C_\mu = 0.03$, props off, $\alpha = 0°$, and $\beta = 5°$ (LE = leading edge, TE = trailing edge)

D Directional Stability

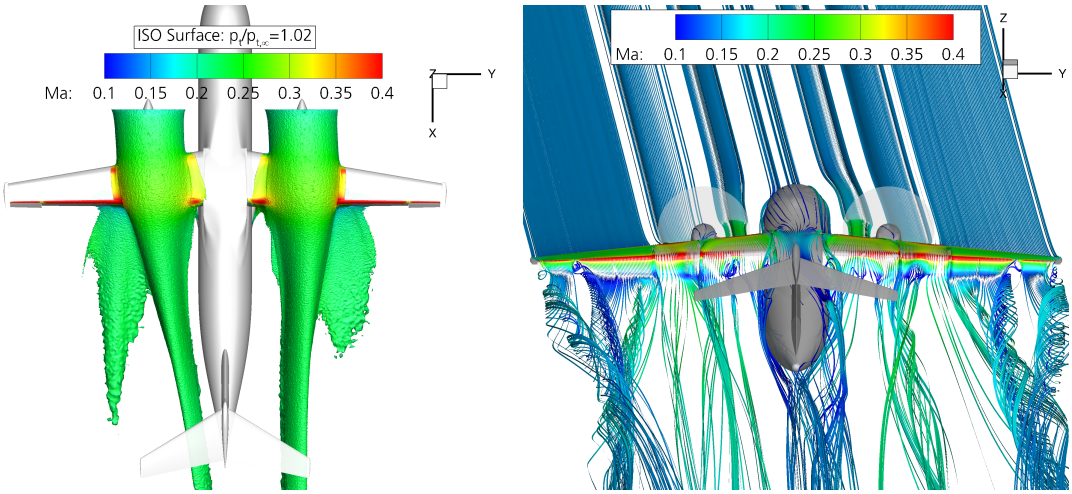

(a) Slipstream (b) Main wing boundary layer

Figure D.1: Evolution of main wing wake with symmetrically rotating propellers (inboard down) at $C_\mu = 0.03$, $\alpha = 0°$, and $\beta = 5°$

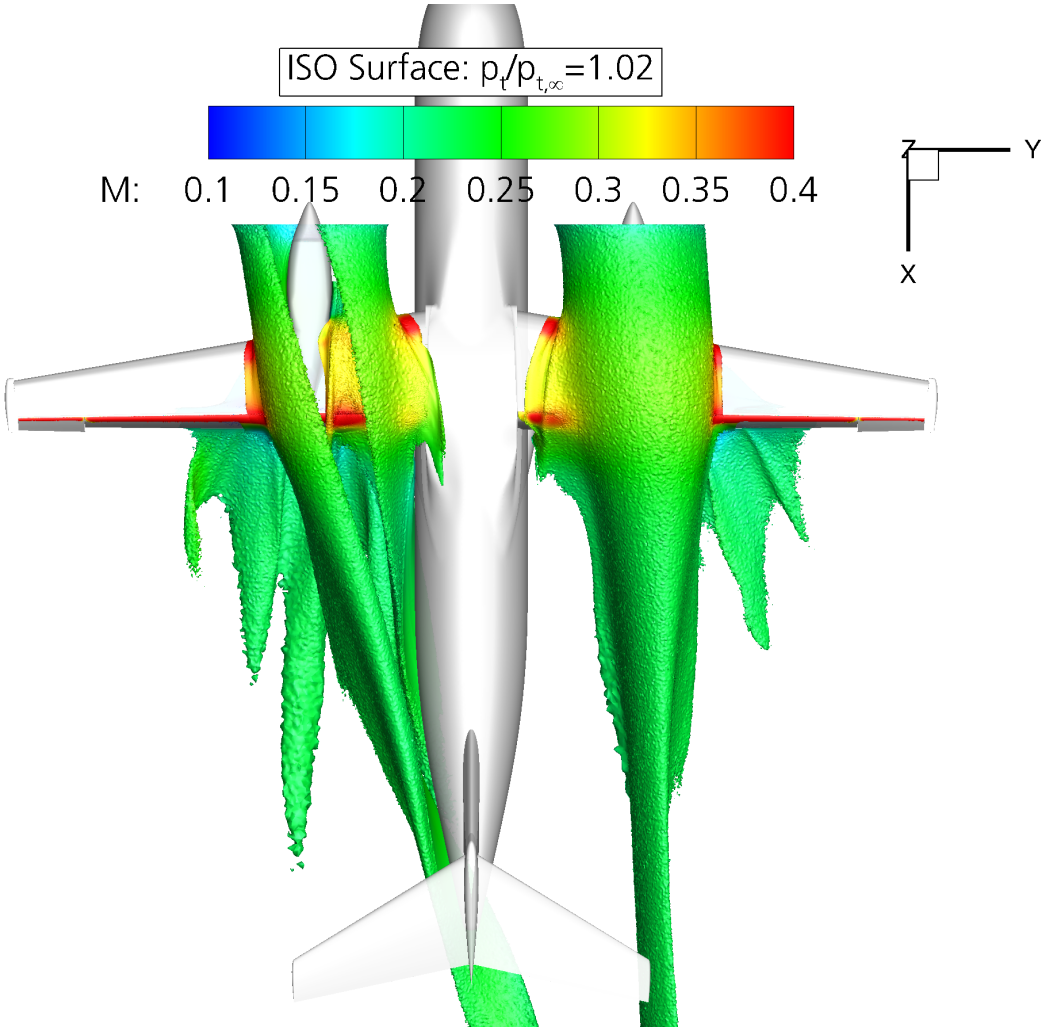

Figure D.2: Slipstream evolution with symmetrically rotating propellers (inboard down) at $C_\mu = 0.03$, $\alpha = 10°$, and $\beta = 10°$

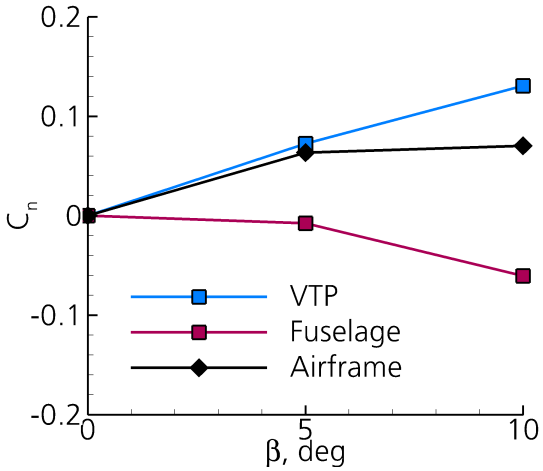

Figure D.3: Yawing moment with respect to sideslip angle for symmetrically rotating propellers (inboard down) at $C_\mu = 0.03$ and $\alpha = 10°$